Applying Non-Canonical Amino Acids for Investigation of Vibrational Energy Transfer and Dynamic Allostery in a Synaptic Protein Domain

Dissertation
zur Erlangung des Doktorgrades
der Naturwissenschaften

vorgelegt beim Fachbereich Physik
der Johann Wolfgang Goethe - Universität
in Frankfurt am Main

von Katharina Barbara Eberl
aus Limburg

Frankfurt 2020
(D 30)

vom Fachbereich Physik der
Johann Wolfgang Goethe - Universität als Dissertation angenommen.

Dekan:

Gutachter:

Datum der Disputation:

Publications and Presentations

Some of the results of this thesis have been published in a journal or been presented on a conference already. The following list gives an overview of manuscripts (published, submitted, and in preparation) and conference contributions.

Publications

T. Baumann*, M. Hauf*, F. Schildhauer*, **K. B. Eberl***, P. M. Durkin, E. Deniz, J. G. Löffler, C. G. Acevedo-Rocha, J. Jaric, B. M. Martins, H. Dobbek, J. Bredenbeck, and N. Budisa
Site-Resolved Observation of Vibrational Energy Transfer Using a Genetically Encoded Ultrafast Heater
Angewandte Chemie (International ed. in English), vol. 58, no. 9, pp. 2899–2903, 2019
*shared lead authors
awarded **VIP** status by the reviewers

T. Baumann*, M. Hauf*, F. Schildhauer*, **K. B. Eberl***, P. M. Durkin, E. Deniz, J. G. Löffler, C. G. Acevedo-Rocha, J. Jaric, B. M. Martins, H. Dobbek, J. Bredenbeck, and N. Budisa
Ortsaufgelöste Beobachtung von Schwingungsenergietransfer mit einem genetisch codierten ultraschnellen Heizelement
Angewandte Chemie, vol. 131, pp. 2925-2930, 2019
*shared lead authors

E. Deniz, **K. B. Eberl**, and J. Bredenbeck
Note: An automatic liquid nitrogen refilling system for small (detector) Dewar vessels
Review of Scientific Instruments, vol. 89, no. 11, p. 116101, 2018
selected as **Editor‘s Pick**

F. Lehner, D. Kudlinzki, C. Richter, H. M. Müller-Werkmeister, **K. B. Eberl**, J. Bredenbeck, H. Schwalbe, and R. Silvers
Impact of Azidohomoalanine Incorporation on Protein Structure and Ligand Binding
Chembiochem, vol. 18, no. 23, pp. 2340–2350, 2017

K. B. Eberl, H. M. Müller-Werkmeister, M. Essig, and J. Bredenbeck
Allostery in PDZ3: Using Unnatural Amino Acids as Site-Specific Reporters in IR Spectroscopy to Probe Allosteric Pathways
Biophysical Journal, vol. 108; no. 185A, 2015

K. B. Eberl, C. Bonifer, and J. Bredenbeck
Solvatochromism and Vibrational Dynamics of the Non-Canonical Amino Acid Azidohomoalanine by FTIR and 2D-IR Spectroscopy
in preparation, designated journal: PCCP

Preliminary List of Authors: **K. B. Eberl**, P. Quoika, D. Üresin, J. Schmidt-Engler, G. Wille, H. M. Müller-Werkmeister, and J. Bredenbeck
Working Title: **Application of the Non-Canonical Amino Acid Azidohomoalanine as a Highly Sensitive Probe for FTIR and 2D-IR Spectroscopy on an Allosteric Protein Domain**
in preparation, designated journal: PCCP

Preliminary List of Authors: **K. B. Eberl**, E. Deniz, J. G. Löffler, H. M. Müller-Werkmeister, P. M. Durkin, N. Budisa, and J. Bredenbeck
Working Title: **Mapping Vibrational Energy Transfer between a Ligand and an Allosteric Protein Domain with Non-Canonical Amino Acids and Ultrafast Infrared Spectroscopy**
in preparation

Preliminary List of Authors: E. Deniz, J. G. Löffler, **K. B. Eberl**, P. M. Durkin, R. Kaml, L. Valino-Borau, A. Gulzar, S. Wolf, N. Budisa, G, Stock, and J. Bredenbeck
Working Title: **Vibrational Energy Transfer Across β-Sheets Outcompetes Transfer Along the Backbone in a Hairpin Peptide**
in preparation, designated journal: JACS

Conference Contributions

Bunsentagung 2020 in Gießen, Germany
Poster presentation:
J. G. Löffler, **K. B. Eberl**, E. Deniz, T. Baumann, F. Schildhauer, P. M. Durkin, N. Budisa, and J. Bredenbeck
Investigation of Vibrational Energy Transfer Pathways in a Protein-Ligand Complex by Ultrafast Spectroscopy and Non-Canonical Amino Acids

Bunsentagung 2020 in Gießen, Germany
Oral presentation:
E. Deniz, J. G. Löffler, **K. B. Eberl**, P. M. Durkin, R. Kaml, N. Budisa, and J. Bredenbeck
Through-Bond/Through-Contact Efficiency of Vibrational Energy Transfer in a Hairpin Peptide

International Conference on Ultrafast Phenomena 2019 in Hamburg, Germany
Poster presentation:
J. G. Löffler, **K. B. Eberl**, E. Deniz, H. M. Müller-Werkmeister, T. Baumann, M. Hauf, F. Schildhauer, P. M. Durkin, N. Budisa, and J. Bredenbeck
Vibrational Energy Transfer in Peptides and Proteins studied with Non-canonical Amino Acids and Time-Resolved IR Spectroscopy

Biennial Meeting of the German Biophysical Society 2018 in Düsseldorf, Germany
Poster presentation:
K. B. Eberl, J. Schmidt-Engler, P. Quoika, C. Bonifer, J. G. Löffler, H. M. Müller-Werkmeister, M. Essig, and J. Bredenbeck
Azidohomoalanine as Site-Specific Probe for Steady State and 2D-IR Spectroscopy on an Allosteric Protein

Biennial Meeting of the German Biophysical Society 2018 in Düsseldorf, Germany
Talk presentation:
K. B. Eberl, E. Deniz, J. G. Löffler, T. Baumann, M. Hauf, F. Schildhauer, P. Durkin, N. Budisa, and J. Bredenbeck
Mapping Vibrational Energy Transfer in Peptides and Proteins with Non-Canonical Amino Acids and Ultrafast Infrared Spectroscopy

TRVS (Time-resolved vibrational spectroscopy) 2017 in Cambridge, UK
Poster presentation:
K. B. Eberl, J. G. Löffler, P. Durkin, E. Deniz, D. Üresin, H. M. Müller-Werkmeister, T. Baumann, M. Hauf, F. Schildhauer, N. Budisa, and J. Bredenbeck
Vibrational energy transfer between peptide ligand and protein studied with non-canonical amino acids

Bunsentagung 2017 in Kaiserslautern, Germany
Oral presentation:
K. B. Eberl, J. G. Löffler, P. Durkin, E. Deniz, D. Üresin, H. M. Müller-Werkmeister, T. Baumann, M. Hauf, F. Schildhauer, N. Budisa, and J. Bredenbeck
Investigation of Vibrational Energy Transfer in Various Biological Systems Using a Pair of Non-Canonical Amino Acids

Bunsentagung 2017 in Kaiserslautern, Germany
Poster presentation:
J. G. Löffler, **K. B. Eberl**, E. Deniz, P. Durkin, N. Budisa, and J. Bredenbeck
Vibrational Energy Transfer in Tryptophan Zippers

Bunsentagung 2016 in Rostock, Germany
Poster presentation
K. B. Eberl, P. Quoika, H. M. Müller-Werkmeister, J. G. Löffler, M. Essig, and J. Bredenbeck
Allostery in PDZ3: Azidohomoalanine as Site-Specific Probe for IR Spectroscopy

Biophysical Society 59th Annual Meeting 2015 in Baltimore, US
Oral presentation:
K. B. Eberl, H. M. Müller-Werkmeister, M. Essig, and J. Bredenbeck
ALLOSTERY IN PDZ3: using unnatural amino acids as site specific reporters in IR spectroscopy to probe allosteric pathways

Contents

Chapter 1

Motivation

Proteins are the machines of cells and their activity is crucial for life. Transmission of communication signals between distinct proteins but also within one protein is essential to ensure functionality of countless cellular processes. The transduction of perturbational effects at one site of a protein, causing structural and/or dynamical changes at a distant site, is called allostery [1–4]. Formerly, allostery was mainly associated with major conformational changes [1, 2] but later a more dynamical view onto allostery evolved and the investigation of allosteric signaling without big conformational changes received more attention [1–5]. The idea of allosteric pathways composed of conserved and energetically coupled amino acids (AA), that mediate the signal transmission between the distant sites, arose [1]. These pathways were associated with pathways of efficient anisotropic energy flow in a protein by several theoretical studies [4, 6–9]. The energy flow along these networks links allosteric signaling to vibrational energy transfer (VET) [2, 9]. The majority of research works on allostery in absence of big conformational changes applied theoretical methods because experimental approaches are very sparse [5, 6, 8–37]. In order to comprehend this ubiquitous and essential biological process of information transfer, the development of new powerful experimental tools and techniques is urgently required. The present dissertation aims for contributing such new tools.

VET in proteins is inherently anisotropic due to the protein geometry, which can be described as a network of connected sites containing long-range channels and dead-ends [38–40]. Hence, all globular proteins exhibit channels for efficient energy flow, which have been suggested to be important for protein functions such as fast dissipation of excess heat, regulation of chemical reactions, ligand binding, enzyme kinetics, and allosteric signaling [9, 38, 39, 41–46]. Transfer of vibrational energy is mediated by covalent bonds but also by non-covalent contacts [8, 9, 39, 46–50]. VET can be investigated by time-resolved infrared (IR) spectroscopy, in which a femtosecond laser pump pulse injects vibrational energy into the molecular system

at a distinct site, either by direct IR excitation or by UV-Vis excitation followed by relaxation, and a subsequent IR probe pulse detects the propagation of this vibrational energy [41, 44, 47, 48, 51–70]. The time delay between these two laser pulses is varied in order to observe vibrational energy spreading with time. In earlier works, IR excitation of a high frequency mode was used to inject energy [56, 60, 68]. The excited high-frequency mode serves as a heater for the molecule and transfers energy to anharmonically coupled lower-frequency modes. These lower-frequency modes are more delocalized and carry the vibrational energy through the molecule [38, 39, 71]. In order to map VET through a whole protein, a high amount of vibrational energy needs to be injected into the system. A chromophore, that converts the energy of a visible photon into vibrational energy is required, like the heme cofactor, which has been used successfully as a heater [47, 48, 52, 58]. Since only a few proteins contain a naturally occurring chromophore, investigation of VET in proteins is strongly limited. A protein-compatible chromophore, which can be applied versatilely, is needed to study anisotropic VET in proteins and to map long range energy transfer pathways. The azulene chromophore is ideally suited as a heater as it undergoes ultrafast internal conversion upon photoexcitation of the first electronically excited state without any structural changes and it converts almost all injected energy into vibrational energy within less than a picosecond [41, 54, 70, 72–75]. Azulene has already been applied to study VET in carbon-chain-bridged azulene-anthrazen compounds [41, 54, 72] and in small peptides [70]. Implemented into the non-canonical amino acid (ncAA) β-(1-azulenyl)-L-alanine (AzAla), the azulene moiety can be incorporated site-specifically into proteins [76, 77]. After injection, the arrival of the vibrational energy at a distinct site of the protein can be easily sensed by a VET sensor in form of an ncAA incorporated at this position. A combination of azulene as a VET heater and the ncAA Azidohomoalanine (Aha) as a VET sensor has been applied successfully for small peptides in the work of Henrike M. Müller-Werkmeister, which preceded the research for this thesis in the lab of Jens Bredenbeck [70, 78]. The heater-sensor pair combined with transient IR (TRIR) spectroscopy revealed a high potential to map VET also along larger distances, as it would be needed for the application in a protein.

The vibrational frequency of chemical bonds is specific for the chemical structure and highly sensitive to even subtle conformational and dynamical changes in the bond's proximity [79]. The vibrational frequency of a bond can be measured by IR spectroscopy, *e. g.* by Fourier transform IR (FTIR) spectroscopy [80, 81]. IR spectroscopy exhibits an outstanding ultrafast time resolution, enabling observation of dynamical processes in molecules on a picosecond time scale. Therefore, it is an excellent approach to study the ultrafast transfer of vibrational energy in molecular systems and proteins. With two-dimensional (2D)-IR spectroscopy the relaxation of vibrationally excited states and structural fluctuations around the oscillating bond on a picosecond to millisecond timescale can be detected [81–83]. However, the excellent time resolution of IR spectroscopy is accompanied with broadened spectra

and limited spectral resolution [84]. For larger molecules with numerous bonds, vibrational bands are overlapping and site resolution is submerged. This is the case for proteins, whose spectra are dominated by backbone absorptions. Furthermore, strong water absorption superimposes some spectral regions of the protein spectrum. To overcome the limited site resolution of IR spectroscopy in proteins, an IR label can be introduced. An IR label are small chemical groups, which absorb in a spectrally clear region of the protein/water spectrum (between 1800 and 2500 cm^{-1}). Implemented as an ncAA, they can be cotranslationally incorporated into a protein at a requested site. Hereby, they provide site-resolved information out of a protein for IR spectroscopy [79, 85–89]. Organic azides (N_3) have an outstanding potential as an IR label. They feature a small size, a relatively large extinction coefficient (350-400 $M^{-1}cm^{-1}$), and a high sensitivity to changes in local environment [90, 91]. Implemented into an ncAA, the asymmetric stretching mode of the azido moiety absorbs around 2100 cm^{-1} in a narrow band [70, 91–107]. One azido containing ncAA is Aha [70, 91, 100–108]. It can be incorporated into proteins as methionine (Met) analogue [100, 108] and exhibits a simple band shape. That makes Aha our IR labeling ncAA of choice as a tool for studying allostery in proteins.

The different methods to study dynamic allostery developed in the course of this dissertation based on FTIR, 2D-IR and TRIR spectroscopy of Aha have been examined by applying them to the PDZ3 domain of the postsynaptic density protein PSD-95, which is a small protein-protein interaction domain [109, 110] and a showcase example for allostery without big conformational changes. The great majority of studies on PDZ3 allostery is based on theoretical approaches [5, 6, 8–29], which predict partly differing networks of coupled amino acids as allosteric pathways. The few experimental works available are almost entirely applying NMR (nuclear magnetic resonance) spectroscopy or double mutation cycles combined with binding constant determination methods [5, 11, 22, 29–37]. They are not able to experimentally proof or reject the diverse theoretical predictions entirely. Therefore, new approaches are strongly required to reveal allosteric signaling in PDZ3.

In order to exploit the full potential of Aha as a site-specific IR reporter for proteins, it is essential to understand the influence of electrostatics and hydrogen bonding on Aha's vibrational frequency, band shape, and vibrational dynamics. However, the effect of diverse solvents displaying various local environments on Aha's vibration has not been investigated systematically, yet. In this thesis FTIR and 2D-IR spectroscopy was used to study the vibrational wavenumber, band shape, lifetime, and spectral diffusion of three different Aha derivatives in a broad set of 16 solvents in dependency on the solvent properties (see **chapter 4.1**).

Afterwards, Aha was introduced into PDZ3 (PSD-95) at 15 positions (15 mutants) (see **chapter 4.2**). Some mutation sites are located on and some off different theoretically predicted allosteric communication pathways [5, 6]. Correct folding and

functionality in terms of ligand binding were tested for all PDZ3-Aha mutants. FTIR spectra of the Aha's asymmetric stretching vibration were measured on the PDZ3-Aha mutants in presence and absence of the native ligand (see **chapter 4.2.4**). Vibrational frequency and band shape are uncovered and their connection to Aha's solvent exposure is investigated. Since ligand binding triggers allosteric effects, Aha's potential to detect subtle structural changes upon ligand binding is exploited. The observed changes are compared to the predicted signaling pathways and the potential of Aha's vibrational band to reveal allosteric pathways in proteins is discussed.

Furthermore 2D-IR spectra of selected PDZ3-Aha mutants with and without ligand were measured (see **chapter 4.2.5**). To the best of our knowledge, the detected time resolved 2D-IR spectra, are the first ever measured on an Aha labeled protein. Vibrational lifetimes, spectral diffusion and ligand induced dynamical changes of the vibrational lifetime are analyzed and compared to Aha's solvent exposure and to the theoretically predicted allosteric pathways.

The application of the heater-sensor pair AzAla-Aha in combination with ultrafast TRIR spectroscopy to measure VET in a protein in a native environment is demonstrated (see **chapter 4.3**). The measurement setup and routine were optimized in order to detect even tiny VET signals. Inter- and intramolecular VET via covalent bonds and also via H-bonds from a bound ligand to different sites of PDZ3 and vice versa was measured on a timescale of a few picoseconds. The arrival time and the amount of vibrational energy at a distinct site are analyzed in relation to the positions and distance of AzAla and Aha. Ultrafast TRIR spectroscopy in combination with the heater-sensor pair reveal a high potential to map pathways of efficient VET, which have been linked to allosteric communication. They will finally offer the opportunity to experimentally scrutinize the variety of theoretical predictions.

Chapter 2

Introduction

2.1 Allostery

Allostery ('allo-steric = other-space') is a ubiquitous phenomenon in biology in which the effect of a perturbation at one site of a protein triggers changes at a distant site [1–4]. This perturbation is most often associated with a ligand binding event and the induced changes can be structural and/or dynamical. Allostery is commonly involved in protein activity regulation.

First of all allostery was investigated in proteins, which perform extensive structural changes upon ligand binding (*e.g.* haemoglobin). The initial allosteric models are, thus, based on a structural and static image [1, 2]. For a long time two predominant models for the mechanism of allostery were proposed, the conformational selection (CS) model, in which a preexisting equilibrium between a tensed (T) and a relaxed (R) allosteric state is shifted upon ligand binding, and the induced fit (IF) model, in which ligand binding induces a conformational change in response to the perturbation [1, 2, 4]. However, in the view of an energy landscape perspective the CS and IF model can be merged. If the ensemble of existing conformations are populated depending on their energies [1] and ligand binding causes a change in free energy that shifts the conformational equilibrium [3], then CS and IF are two extreme scenarios only differing in the energy gap between the T and R state and their relative population [2]. In the IF model only the T state is populated without ligand, whereas in the CS model both states are populated. If the R state is easily accessible also without ligand, conformational changes upon ligand binding may not be visible. This ensemble view demonstrates the statistical nature of allosteric coupling [1].

Allostery has not only been associated with conformational changes but also with changes in conformational entropy in the form of modified backbone and side-chain dynamics upon ligand binding [1–4].

As a mechanism of signal propagation the idea of an allosteric pathway consisting of conserved and energetically coupled amino acids, which are mediating the information transmission between the distant sites, emerged [1]. Even the coexistence of multiple of these pathways is imaginable [4, 8, 12, 18]. From a chemical view onto allostery a perturbation at one site is transferred to other regions of the protein through specific interactions between the atoms (chemical bonds, hydrogen bonds, van-der-Waals interactions, *etc.*) [4]. These allosteric pathways were linked to pathways of efficient anisotropic energy flow by a number of theoretical studies [4, 6–8, 42] allowing excess energy from ligand binding to be guided along the pathway and to cause structural and/or dynamical changes at a distant position in the protein [4]. The energy flux across these networks was suggested to relate allosteric signaling to vibrational energy transfer [2, 9].

2.2 Spectroscopic Methods

Chemical bonds are fundamental modules of all molecules and their vibrational modes are highly characteristic for their chemical structure [79]. Additionally, the frequency of the vibrational mode usually is affected by the local environment especially by electrostatics and hydrogen bonding [79]. Hence, investigation of the frequency and frequency variation gives insights into structure and dynamics of the molecular systems [82]. Infrared (IR) spectroscopy can visualize vibrational normal modes, if there is a change in the dipole moment during the vibration [80] as IR absorption arises from the interaction of an electromagnetic field with the molecular dipole moment [81]. IR spectroscopy has a large application range from small molecules and molecular complexes to cells and tissues [80, 111]. One of its main benefits is, that organic samples can be studied under native conditions [111]. Moreover, IR spectroscopy is one of few methods that can directly observe hydrogen bonding and report on its strength [80, 81, 112].

There are two main types of vibrations in the mid IR region (4000-1000 cm^{-1}) [80, 113, 114]. Bending vibrations, which involve a change of the bond angle, and stretching vibrations providing a change in bond length. The latter can be simplified and modelled with an harmonic oscillator with two atoms as point masses (m_1, m_2) and the chemical bond as a spring connecting them (**equation 2.2.1**).

$$\nu = \frac{1}{2\pi c}\sqrt{\frac{k(m_1 + m_2)}{m_1 m_2}} \tag{2.2.1}$$

The vibrational frequency (ν), therefore, depends on the bond strength (represented by the spring constant k) and the masses of the involved atoms. That

makes a vibrational frequency very sensitive to its environment because the environment can influence the bond strength. For example hydrogen bonding can elongate and this way weaken a bond causing a red shift of the vibrational frequency. The frequency dependence on mass can be exploited to identify chemical groups by directed isotope labeling [80, 113, 114].

Schrödinger's equation (**equation 2.2.2**) for an harmonic oscillator ($\hat{H}$ - Hamiltonian operator, $\psi(t)$ - wave function, E - energy eigenvalue) gives discrete possible energy levels: $E_n = h\nu \cdot (n + \frac{1}{2})$ with $n = 0$, 1, 2,...; $n = 0$ is denoted as vibrational ground state, $n = 1$ as first excited state, and so on [113].

$$\hat{H} \left|\psi(t)\right\rangle = E \left|\psi(t)\right\rangle \tag{2.2.2}$$

However, the use of the harmonic oscillator is limited because it can not account for the dissociation of the molecule caused by intense excitation. Therefore, the anharmonic oscillator, which includes dissociation, is a more suitable model and can be described as Morse potential (**equation 2.2.3** and **figure 2.2.1**) with r_0 as equilibrium distance, D_e as dissociation energy, and a as the width of the potential [113, 115].

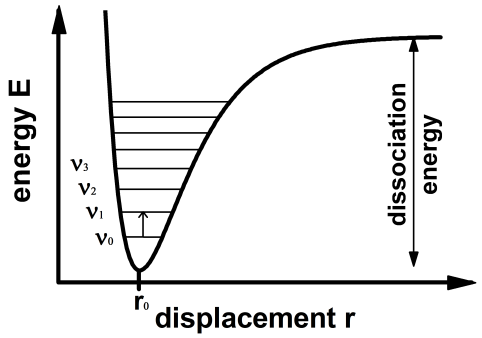

Figure 2.2.1: Scheme of a Morse potential with its vibrational states (ν_0, ν_1, ν_2, ...) and dissociation energy.

$$E_{pot} = D_e[1 - e^{-a(r-r_0)}]^2 \tag{2.2.3}$$

2.2.1 FTIR Spectroscopy

Static IR spectra can be recorded by a Fourier transform infrared (FTIR) spectrometer using a Michelson-interferometer with a movable mirror to constructively or destructively interfere polychromatic light for faster detection of an IR spectrum

[113, 115–117]. The recorded spectrum reveals information about *i. a.* chemical structure, change of protonation state, electron transfer reaction, hydrogen bonding, electric field, and conformational freedom [112].

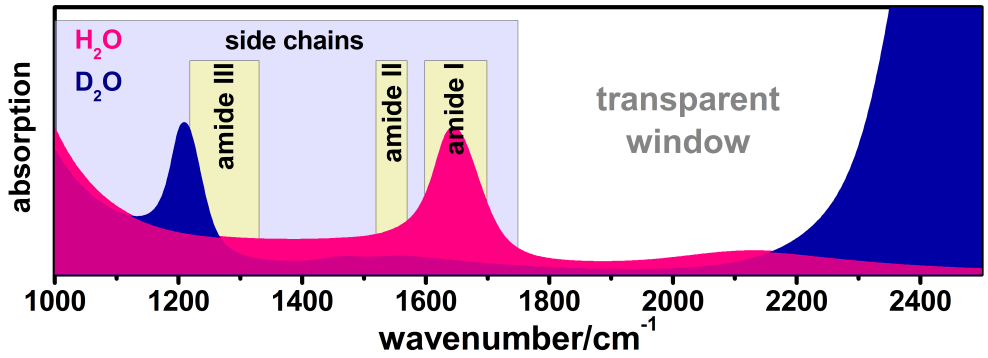

Figure 2.2.2: FTIR spectra of H_2O and D_2O and a schematic depiction of the major protein absorptions (amide I-III and side chains) in the mid IR range from 1000 to 2500 cm^{-1}.

Furthermore, IR spectroscopy exhibits an excellent picosecond (ps) time resolution, making it a highly precise and versatile technique to study dynamics of molecular systems [84]. However, this excellent time resolution comes along with broadened spectra and corresponding limited spectral resolution. For larger molecules/molecular complexes like proteins, which have many similar oscillating bonds, vibrational bands are overlapping and site resolution is submerged. IR spectra of proteins in aqueous solution are dominated by the backbone peptide bond absorption, whose chemical groups absorb in specific spectral regions, and solvent water absorption (**figure 2.2.2**) [80, 81, 112, 117, 118]. The stretching vibration of the peptide C=O groups cause a strong absorption in the region of 1600 to 1700 cm^{-1} and depend on secondary structure elements (α-helices, β-sheets, and turns). Despite superposition, the C=O stretching vibration gives insight into the global protein architecture. The corresponding broad band is called amide I band, but it almost coincidences with the HOH bending motion of H_2O (*ca.* 1590-1700 cm^{-1}). Isotope labeling of H_2O to D_2O shifts water absorption out of the amide I region. N-H bending coupled to C-N stretching gives rise to the amide II band (1520-1560 cm^{-1}) and single N-H bending and C-N stretching to the amide III band (1220-1330 cm^{-1}). Most side chain vibrations are overlapping and absorb between 720 and 1750 cm^{-1} [112, 115, 118, 119]. Only the side chain of cysteine absorbs at 2550 to 2600 cm^{-1} in H_2O [112, 118]. Accordingly, a transparent window arises between 1800 and 2500 cm^{-1} in the IR spectra of proteins in water. Only a relatively small, but broad band from H_2O, which is a combination band of libration and bending, is centered around 2000 cm^{-1} [120]. Despite spectral convolution, FTIR difference spectroscopy is very sensitive to the detection of conformational changes in proteins [80]. In order to overcome the limited site resolution, an IR reporter could be introduced, which absorbs in the region of the transparent window. A versatile

approach is the side-specific incorporation of ncAAs containing a strongly IR absorbing group into proteins (see **chapter 2.4**) [79, 85–89]. That way site-resolved information out of a protein can be gained by IR spectroscopy.

2.2.2 Transient IR Spectroscopy

In order to observe molecular processes on timescales faster than a detector is able to measure, an artifice is applied. A femtosecond (fs) laser pulse (pump pulse) excites the sample and after a tunable time delay (population time) a second femtosecond laser pulse probes the state of the system (probe pulse). By changing the time delay between the two pulses dynamical evolution of the molecular system is revealed. Depending on the frequency of the pump and probe pulse different processes can be investigated [70, 105, 121–123]. A simple case is the transient IR (TRIR) spectroscopy, where a visible (VIS) pump pulse electronically excites the sample and an IR pulse probes the induced changes in dependence of the past time (**figure 2.2.3**). VIS excitation triggers a process and is used to study non-equilibrium conformational dynamics [81, 124]. Photo cycles, charge transfer, chemical reactions, vibrational energy transfer, and diverse other processes can be studied this way.

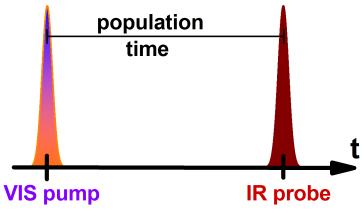

Figure 2.2.3: TRIR pulse sequence. Pump-probe pulse sequence of a TRIR experiment with a visible excitation pulse and an IR probe pulse after a variable population time.

2.2.3 2D-IR Spectroscopy

By exciting a sample with an IR pulse and also probing it in the IR range, molecular systems and their dynamics can be investigated in equilibrium [82, 124]. Replacing the spectrally broad IR pump pulse by a tunable spectrally narrow IR pump pulse and scanning the pump frequency in addition to the population time, adds another dimension to the spectrum (**figure 2.2.4 a**). This method is called two-dimensional infrared (2D-IR) spectroscopy. Spectrally narrow pump pulses, which are Lorentzian shaped in the frequency domain and exponentially decaying in the time domain, can be generated by an adjustable Fabry Perot filter [124, 125]. The 2D-IR signal is detected as a difference signal between the pumped IR spectrum

and the IR spectrum without previous IR excitation. 2D-IR spectra typically consist of a negative (blue) and a positive (red) band (**figure 2.2.4 c+d**). The negative band arises from ground state bleaching (less absorption) and stimulated emission and is connected to the transition between the vibrational ground state (ν_0) and the first excited state (ν_1) (**figure 2.2.4 b** blue arrows) and is referred to as bleach. The positive band belongs to the transition from the first (ν_1) to the second excited state (ν_2) (**figure 2.2.4 b** red arrow) and is called excited state absorption (ESA). Due to vibrational anharmonicity it is shifted to lower frequencies [124].

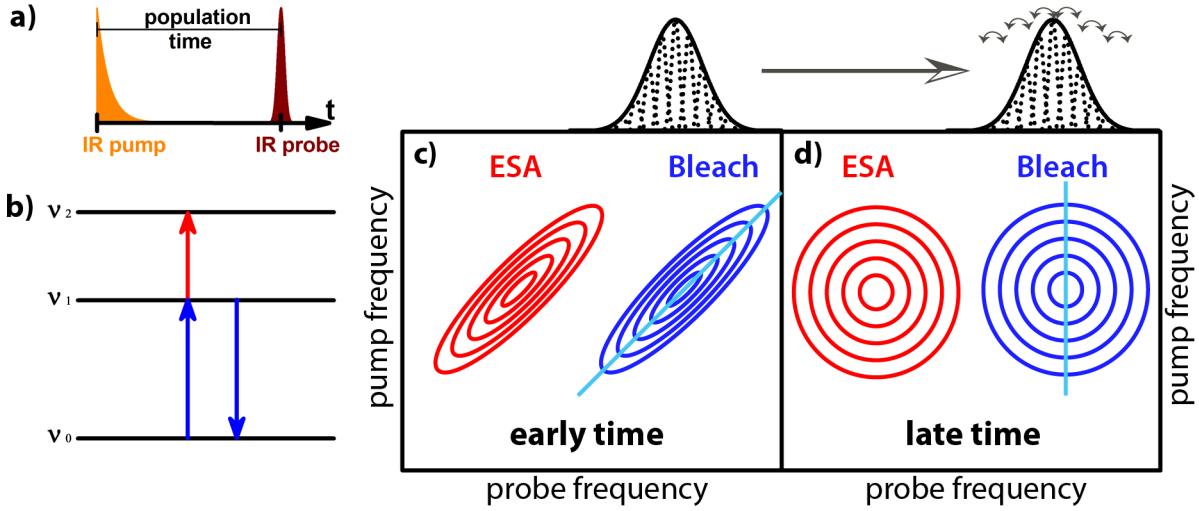

Figure 2.2.4: **(a)** Pulse sequence of a 2D-IR experiment, **(b)** the involved vibrational transitions, and **(c)** scheme of a 2D-IR spectrum at a short and **(d)** a long population time. The transition between the ground state (ν_0) and the first (ν_1) vibrationally excited state (ground state bleaching and stimulated emission) and the corresponding 2D-IR signal are colored blue. The excitation from the first (ν_1) to the second (ν_2) vibrational state (ESA) and its signal are marked red. The tilt of the bleach signal is marked by a cyan line as center line slope and a schematic depiction of a one dimensional vibrational band consisting of several distinct conformational sub bands, which are interchanging, is depicted above.

2D-IR spectroscopy probes the decay of vibrationally excited states and the time dependent frequency evolution of an ensemble of molecules caused by equilibrium structural fluctuations on a ps to ms timescale [81–83]. 2D-IR spectroscopy is useful to understand vibrational properties like spectral diffusion, intermode coupling, conformational variations, chemical exchange, and structural disorder [81, 83, 114, 126]. Additional off-diagonal signals (cross-peaks) can arise, revealing coupling of different vibrational modes as well as incoherent and coherent population transfer by anharmonic interactions or chemical exchange [82, 83, 114, 124]. 2D-IR spectroscopy on protein backbone, which studies mainly the amide I absorption, detects protein structure, solvation, folding, and protein-ligand/protein interactions [81, 88, 127]. One big advantage of 2D-IR spectroscopy is, that the signal size scales quadratically with the extinction coefficient and, therefore, solvent background absorption is reduced relative to the sample signal [84, 91].

2.2.3.1 Spectral Diffusion

Since the vibrational frequency is very sensitive to the local environment, vibrational bands usually consist of many sub bands representing different conformational states (inhomogeneous line broadening) (**figure 2.2.4** above **c+d**) [82, 83, 91, 114, 124, 126, 128]. If the IR pump excitation is immediately followed by the IR probe pulse, the fluctuational motions of a molecular system do not have enough time to proceed and are quasi frozen within the observed time scale. The excitation frequency of an oscillator, therefore, is the same as the frequency, which is measured with the probe pulse, and the 2D-IR peak is elliptically elongated along the diagonal of the spectrum (**figure 2.2.4 c**). Molecular dynamics of the molecule itself or changes in interactions to surrounding solvent molecules spectrally shift the initially excited vibrational frequency when population time passes. The previous correlation between pump and probe frequency gets lost. For an ensemble of molecules, this means, that the elliptically shaped band becomes more circular and less tilted (**figure 2.2.4 d**). This change in peak shape as a function of population time is called spectral diffusion and is an excellent reporter of solvation dynamics.

The frequency-frequency correlation function (FFCF) is the link between experimental observables and molecular dynamics: $c_1(t) = \frac{\delta(t)}{T_2} + \sum_i \triangle_i^2 e^{-\frac{t}{\tau_i}}$ with $\triangle_i$ as frequency fluctuation amplitude and with τ_i as correlation time of the i-th component [82]. The $\frac{\delta(t)}{T_2}$ term gives a Lorentzian contribution to the line shape, which describes homogeneous broadening (pure dephasing time, vibrational lifetime, and orientational relaxation). To extract the FFCF from a 2D-IR spectrum diverse approaches are available. For the center line slope (CLS) method a line is fitted through the peak maxima of a series of cuts through the 2D-IR spectrum parallel to the probe axis (cyan line in **figure 2.2.4 c+d**). The time evolution of the inverse slope of this line can be estimated by a sum of exponentials ($\sum_i \triangle_i^2 e^{-\frac{t}{\tau_i}}$) and gives the normalized FFCF without homogeneous contributions, because the homogeneous part does not depend on the population time. Often, the last term of the sum has a correlation time of $\tau_i = \infty$ leading to a constant offset describing an inhomogeneous contribution, which is not decaying within the time scale of the experiment. The CLS value at $t = 0$ gives the inhomogeneous contribution to the line broadening of an IR spectrum and the difference of this value to 1 describes the homogeneous contribution (but this part might also include very fast decaying inhomogeneous contributions causing an error). A big advantage of the CLS method is, that an estimation on the line shape is not needed and it is, therefore, more robust to experimental noise than other approaches for analyzing spectral diffusion.

2.3 Vibrational Energy Transfer

Efficient and rapid energy dissipation of excess energy in proteins is essential to avoid chemical band ruptures [46]. Vibrational energy transfer (VET) in proteins is mediated by backbone as well as non-covalent contacts [8, 39, 42, 46–50, 129, 130]. Energy flows anisotropically along distinct channels [38]. These channels are supposed to play an important role in protein function like in regulation of chemical reactions, ligand binding/dissociation, photosensing, photosynthesis, enzyme kinetics, signal communication, and allostery [9, 38, 39, 41–45]. For this reason, VET has been investigated by several theoretical [6, 8, 16, 25, 39, 40, 45, 46, 49, 50, 54, 55, 67, 68, 71, 72, 130–137] and experimental studies [41, 44, 47, 48, 51–70]. Energy flow in proteins can be considered from different aspects, as an energy flow through the residues of a protein or an energy flow through its vibrational states. Consequently, energy transport channels can be regarded as extended networks of residues or of vibrational states through which energy readily flows [38]. Energy flow along vibrational states can be described as transport among protein's collective oscillations or normal modes. Normal modes are defined in a way that all atoms of the mode are oscillating around an equilibrium position with the same frequency. They can be extended over several atoms or be localized [38, 39].

In folded proteins energy flows anisotropically and shows anomalous subdiffusion due to protein's geometry. Energy flow can be described as a random-walk in a labyrinth and can be compared with flow on a percolation cluster, which is a network of connected sites providing both long-range channels and dead-ends [38–40]. The energy flows readily along strongly connected long-ranging paths and is slowed down at dead-end traps. In a protein possible dead-ends are side chains and their different lengths give rise to the anisotropy of energy flow [38–40, 49].

VET in a protein requires transitions among vibrational states (intramolecular vibrational energy redistribution (IVR)) [38, 39, 41, 51, 71]. These transitions arise from anharmonic interactions between the vibrational modes. Relaxation of an excited high-frequency mode of a protein transfers energy into anharmonically coupled lower-frequency, more delocalized heat carrying modes, from which the energy is further redistributed to other coupled low-frequency modes [38, 39, 71] (**figure 2.3.1**). If energy of a high-frequency localized mode relaxes into a low-frequency mode, the rest of the energy must be transferred to another high/intermediate-frequency localized mode with a similar frequency as the initially excited mode. However, localized modes with similar frequency tend to rarely overlap in space and are, therefore, only weakly coupled. This weak coupling slows down IVR into low-frequency modes and makes it the rate-determining step of VET in several systems [38, 39, 54, 57, 68, 71, 132, 134]. Normal modes, which are extended over the whole protein, exhibit frequencies below 150 cm^{-1} [39, 71]. In principle, the higher

its vibrational frequency, the more localized a normal mode is. The amid I band of a protein's backbone, however, forms an exception, being relatively delocalized.

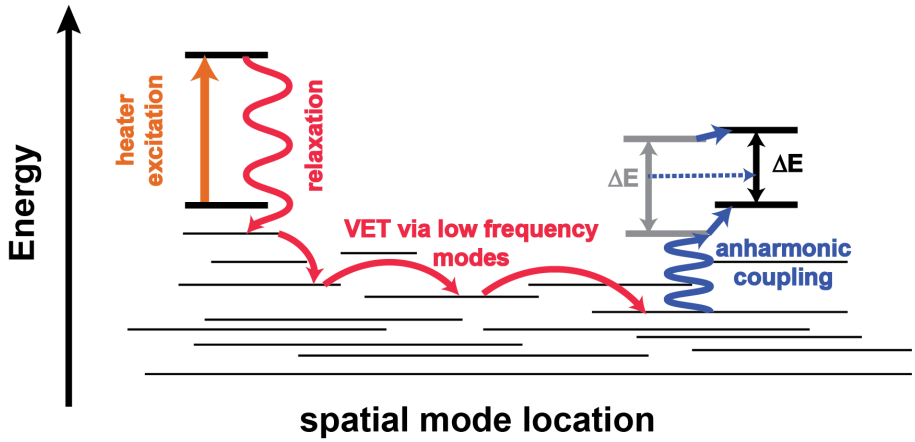

Figure 2.3.1: Scheme of VET and IVR. After excitation of a high-frequency mode the energy is transferred to anharmonically coupled, delocalized low-frequency modes and further transferred among them. The heating of low-frequency modes can change the energy gap between the vibrational states of anharmonically coupled high-frequency modes.

The transport speed was found to strongly depend on the type of the initially excited mode [61, 63, 68]. Variations up to a factor of 4 were detected for the same system. Relaxation of the initially excited mode populates different lower-frequency modes depending on initial mode's frequency, localization, and its anharmonic coupling to other bands. Therefore, different transporting modes are predominantly contributing to VET.

Both ballistic and diffusive behavior has been found for VET in experimental studies [54, 55, 61–63, 68, 69, 72]. Ballistic transport implicates the free propagation of a vibrational wave packet with the energy $\hbar\omega$ along a strongly delocalized vibrational state spanning the whole molecule. It can be extremely speedy and efficient and requires ordered molecular structures. The observed evident variation in ballistic transfer velocities is probably caused by the type of chain mode used for energy transfer. Diffusive VET includes Brownian-like energy exchange and occurs in less ordered structures. Usually diffusive transport is slower than ballistic one.

In molecular systems in solution, additional to intramolecular VET, vibrational energy is also transferred to solvent molecules [41, 46, 51–53, 55, 59, 70, 135]. In experimental studies the intramolecular VET through the molecular systems from the initially excited mode to the probed mode was found to dominate instead of energy diffusion through the solvent despite longer through chain distances [54, 63]. However, some theoretical studies suggested that tightly bound water molecules in the protein interior or at interfaces of dimeric proteins might contribute to channels of efficient VET [136, 137].

Experimentally measuring VET along an α-helical peptide chain using an azobenzene moiety as heater revealed a thermal diffusivity of 2 $\text{Å}^2/ps$ for the α-helix [55]. Excitation of a peptide C=O oscillator in the same system showed a thermal diffusivity of 8 $\text{Å}^2/ps$ [67]. Transport speeds between 1 and 14.4 $\text{Å}/ps$ were found for various organic oligomeres [61, 63, 135]. The arrival time of a VET signal scales with the intermode distance, but also depends on the involved modes [56, 57]. VET was observed experimentally for up to a distance of 60 Å for a highly ordered oligomeric structure, which displayed ballistic transport [63].

The distance dependency and the velocity of VET has already been applied to assign IR bands [60], to determine structural changes [65], and to estimate the degree of hydration of a sample [66].

VET has been experimentally triggered by exciting several modes as potential heater. The vibrational bands of CN, azide, and CO were used to inject vibrational energy into organic molecules [56, 57, 61–63]. These chemical groups are widespread in organic molecules, however, the excitation of an IR band injects only a small amount of vibrational energy. In order to observe VET through a whole protein a higher amount of vibrational energy is required. Naturally occurring heme cofactors [47, 48, 52, 58] and metallo ligands [44] have been excited electronically and served as VET heater, but observing VET is limited to systems holding such a chromophore. To overcome this limitation an azobenzene moiety was incorporated into an α-helical peptide [55, 59, 67–69]. It undergoes ultrafast cis-trans isomerization upon visible excitation but involves a structural change, besides heat injection. Another possible heater, the azulene moiety undergoes ultrafast internal conversion upon photoexcitation without any structural changes and converts almost all injected energy into vibrational energy. It was applied to investigate VET in bridged azulene-anthrazen compounds [41, 54, 72] and to study VET in peptides [70]. In the shape of a non-canonical amino acid, the azulene chromophore exhibits a high potential as a heater in order to map VET in proteins.

2.4 Non-Canonical Amino Acids

Proteins are the machines of cells and their tasks are essential for life. They consist of one or multiple chains of amino acids (AAs) which are folded and arranged in a three dimensional structure to achieve an operating mode. In order to investigate and manipulate their structure, function, and dynamics many additional functionalities have been incorporated with the help of non-canonical amino acids (ncAA) with special moieties like halogeno, keto, cyano, azido, nitroso, nitro, and silyl groups, and acetylenic and heavy-atom containing side chains [138, 139]. Also ncAAs, which contain reporter groups for IR-, NMR-, and fluorescence-spectroscopy

and X-ray crystallography, have been introduced into proteins to study ligand binding, protein stability, activity, folding, charge transfer, and even cellular processes. New or enhanced catalytic functions and improved pharmaceutical properties can also be achieved by ncAAs [90, 92, 100, 101, 103, 107, 139–142].

There are different approaches to incorporate ncAAs into proteins and peptides depending on the ncAA and the protein/peptide of choice:

- For peptides and small proteins (up to 50 AA) solid phase peptide synthesis (SPPS) is an advantageous method as it can incorporate nearly every ncAA even toxic ones. It can be combined with semisynthetic approaches like native chemical ligation to produce larger proteins containing ncAAs.
- *In vitro* synthesis is performed in a cell-free translation system with truncated tRNAs which are enzymatically ligated to chemically aminoacylated nucleotides. It is technical demanding and yields are quite low [79, 86, 138–140, 143].
- There are two main approaches for recombinant expression of ncAA equipped proteins *in vivo*, the selective pressure incorporation (SPI) and the stop codon suppression (SCS). NcAAs have been successfully incorporated into proteins in *i. a. E.coli*, yeast, *C.elegans*, and mammalian cells [79, 86, 138–140, 143, 144]. A wild type aminoacyl tRNA synthetase in combination with a chemical defined growth medium and auxotrophic strains are employed in the SPI approach. In absence of a certain endogenous AA the cells are forced to make a miss-incorporation with an ncAA which is a close structural analogue to this endogenous AA. The ncAA is introduced at every position of the former endogenous AA and, therefore, a residue-specific labeling is achieved.
- Site-specific incorporation can be achieved by genetically encoding an ncAA with the SCS approach. The least occurring stop codon (TAG) in *E.coli,* the so called amber stop codon, is the most used codon for the genetically encoded introduction of ncAAs. An orthogonal aminoacyl-tRNA synthetase (aaRS)/t-RNA pair incorporates the ncAA of choice in response to the stop codon. For this the exogenous tRNA containing the cognate anticodon needs to be selectively aminoacylated with the ncAA by an evolved synthetase and must not interfere with the endogenous tRNAs and aaRSs. The heterologous *M.jannaschii* TyrRS (*Mj*TyrRS)/*Mj*tRNA^{Tyr} pair [145] is an established and frequently used orthogonal aaRS/t-RNA pair for SCS in *E.coli*. Orthogonal aaRSs are evolved using a gene library in combination with several steps of positive and negative selection. Many structurally distinct ncAAs have been incorporated via this method [79, 86, 93, 138–140, 143, 146].
- Another possibility of introducing desired functionalities into a protein is the post-translational modification of reactive AA side chains like cysteine [79, 86, 138–140, 143].

2.4.1 Azidohomoalanine

In order to overcome sensitivity limitations due to signal superposition in IR spectroscopy on proteins and extract site-selective information, vibrational labels can be introduced. The criteria for choosing an ideal IR label for proteins are [79, 85–89]: (1) The IR label's absorption needs to be in the transparent window of a protein/buffer spectrum (between 1800 and 2500 cm^{-1}). (2) Its transition dipole moment/extinction coefficient should be preferably large. (3) Its transition should be simple and largely decoupled from the rest of the molecule. (4) Its vibrational frequency should be highly sensitive to changes in the local environment. (5) It needs to be stable in buffer solution. (6) Incorporation of the label into a protein should be easy (*e. g.* as ncAA). (7) It should be small to minimize perturbations.

Different vibrational labels have been introduced into proteins. They have been successfully applied to study electrostatics, hydrogen bonding, conformational changes, stability, folding, protein dynamics, changes during enzyme's catalytic or photo cycles, and various other processes [70, 79, 85, 86, 88, 89, 96, 99, 101, 105, 107, 142, 147–157]. Every label has its advantages and disadvantages. Isotope labeling (most often of the CO groups of the peptide backbone (-$^{13}C^{18}O$)) was the first approach applied. It is completely non-perturbing but limited to small proteins because incorporation is done with peptide synthesis and the IR bands are shifted in a region in which also many side chains absorb. Additionally, its extinction coefficient (ε) is low [79, 84, 88, 89]. The nitrile (CN) [87, 106, 152–162] and the thiocyanate (SCN) [142, 148–151, 158, 159, 163–166] moiety exhibits a separated absorption with a larger ε and cause only small perturbations [79, 84, 88, 167]. Organic azides (N_3) [70, 91–107] are similarly small, but show a 2 to 4 times larger extinction coefficient [97, 168] than nitriles [79, 84, 86, 88–90]. Conjugated metal-carbonyl complexes exhibit an exceedingly high extinction coefficient but they are also much larger in size and, therefore, more perturbing [79, 169].

The combination of its small size, its relatively high extinction coefficient (350-400 $M^{-1}cm^{-1}$) [90, 91], and its sensitivity to changes in the local environment mark the outstanding potential of azido containing ncAAs as IR reporters. Their asymmetric stretching mode absorbs around 2100 cm^{-1} in a narrow band [90, 91]. Different azido ncAAs have been successfully incorporated into peptides or proteins: azidophenylalanine (N_3Phe) and its derivatives [92–99, 106, 170], azidoproline (N_3Pro) [171], azidoalanine (N_3Ala) [147, 172], and azidohomoalanine (Aha) (**figure 2.4.1**) [70, 91, 100–108]. Furthermore, azides have been applied as RNA/DNA IR reporters [90, 126] and can be used for click chemistry to attach additional groups like metal carbonyls, fluorescent dyes, or spin labels [90, 108, 169]. Aromatic azido ncAAs are often bothered by a pronounced Fermi resonance between the asymmetric stretching vibration and a combination band (N_3 symmetric stretching (~1200-1350 cm^{-1}) and aromatic ring mode at ~1000 cm^{-1}) [86, 95–

98, 168, 170, 173–175], which is complicating the IR spectrum. Fermi resonance can be eliminated by ^{15}N isotope labeling [79, 86, 175] or adding an additional CH_2 group between the phenyl ring and the azido group [97]. However, the size of N_3Phe and its derivatives is large compared to other azido ncAAs. N_3Pro is a structure-control and -probing element at the same time due to the azido-gauche effect, which leads to a conformation with strong intramolecular electrostatic interactions between the azide and the methylamide carbonyl O-atom. The backbone interaction affects the asymmetric stretching frequency [171]. N_3Ala also seems to be impacted by the azido-gauche effect and two different backbone interactions (hydrogen bonding between the inner N-atom of the azide and the N-terminal amide H-atom and an electrostatic interaction between the carbonyl oxygen's atom nonbonding orbital and the azido group's antibonding orbital). However, interpretation of the influence of local environment on the spectrum seems to be much easier than for N_3Pro [172, 176]. As Aha contains an additional CH_2 group at the C_β position, the azido group is more separated from the polar peptide backbone [177]. It can be incorporated into peptides and proteins via SPPS or SPI as methionine (Met) analogue because its electron density map is similar enough to that of Met to be incorporated instead [100, 108]. Removal or retention of N-terminal Aha (introduced in response to the Met start codon) depends on the penultimate residue [178]. That makes Aha our azido containing ncAA of choice to investigate local environment and dynamics in proteins.

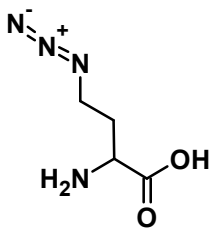

Figure 2.4.1: Chemical structure of unprotected azidohomoalanine (upAha).

2.4.1.1 Solvatochromism

To tap Aha's full potential as a site-specific reporter of the local environment in a protein, it is essential to understand the dependency of its vibrational frequency and band shape on electrostatics and hydrogen bonding to the surrounding solvent molecules (solvatochromism).

Some previous studies on solvatochromism of aliphatic azides have been conducted by different groups already. Vibrational Stark effect spectroscopy, which is used to measure the sensitivity of the vibrational frequency to an electric field (electrochromism) [85, 88, 149, 150, 156, 158, 159, 179–183], revealed a much smaller Stark tuning rate (a measure of this sensitivity) of organic azides than for nitriles

or thiocyanates despite azide's larger extinction coefficient [79, 85, 181]. In 2008 Oh and coworkers [147] measured FTIR spectra of an N_3Ala dipeptide in aprotic DMSO, THF, and protic H_2O and found similar band maximum frequencies for the aprotic solvents and a blue shifted maximum for H_2O. They suggested that the azido stretching frequency is rather determined by hydrogen bonding to the solvent than by the solvent's dielectric properties. Three years later Wolfshorndl *et al.* [184] published an extensive study on solvatochromism of an aliphatic (5-azido-1-pentanoic acid (AzPen*)) and an aromatic azide (3-(*p*-azidophenyl)-1-propanoic acid) as model compounds and found a negligibly low sensitivity of the stretching frequency maximum of the aliphatic N_3 to solvent polarity, in contrast to a weak but nonzero sensitivity for the aromatic N_3. The aromatic N_3 was perturbed by Fermi resonance and that might cause this higher sensitivity. Stretching frequencies of both azides are distinctly blue shifting due to hydrogen bonding, but astonishingly the frequency in water is the highest of all solvents investigated, including solvents which are stronger hydrogen bond donors like HFIP. They attributed this behavior to the higher hydrogen bond donor density in water compared to the other solvents used and concluded that the N_3 asymmetric stretching vibration is an excellent and highly specific water sensor [184].

Ab initio calculations in combination with classical and quantum mechanical (QM)/ molecular mechanics (MM) molecular dynamic (MD) simulations investigated the impact of hydrogen bonding between azidomethane or an N_3Ala dipeptide and surrounding water molecules onto the azide's asymmetric stretching frequency. Only the inner and the terminal nitrogen (not the central) of the azido group actively participate in hydrogen bonding interactions with water. Depending on the angle of the hydrogen bonding interaction with an H_2O molecule a blue shift of the stretching frequency for a σ-hydrogen bond and a red shift for a π-hydrogen bond is induced. Also a linear correlation of the N_3 frequency and the N≡N bond lengths was found. For more than one hydrogen bond the frequency shift is determined by competing contributions from blue shifting σ-hydrogen bonds and red shifting π-hydrogen bonds. The additional peptide bonds of the N_3Ala dipeptide seem to have a smaller influence on the vibrational frequency than hydrogen bonding interaction with water and do not seem to concern the solvation structure of the water around the azido group despite an intramolecular hydrogen bonding interaction of the N-terminal amide H-atom with the inner N atom of the azido group [176]. Two years later the same group performed further theoretical calculations on the N_3Ala dipeptide and a tripeptide and predicted an intramolecular electrostatic n$\rightarrow\pi^*$ interaction between the carbonyl oxygen's nonbonding orbital (n) and the azido group's antibonding orbital (π^*) additional to the hydrogen bond between the N-terminal amide H-atom and the inner N-atom of the azido group caused by azido gauche effect [172].

To the best of our knowledge, a comprehensive study of solvatochromism of Aha itself is still absent despite being essential to understand Aha's vibrational fre-

quency and band shape in a protein.

2.4.1.2 Time Resolved IR

Despite the high potential of 2D-IR spectroscopy on proteins for studying structural dynamics and dynamical heterogeneity on a ps timescale [81, 82, 114, 124, 185] and the fact that it also benefits from the use of ncAAs as IR label [94, 153, 154, 186, 187] only few 2D-IR experiments on aliphatic azide containing ncAAs have been performed yet. Biexponential relaxation with vibrational lifetimes of 0.1/1.1 ps for N_3Ala and 0.1/1.0 ps for N_3Pro in H_2O were found and an Aha labeled ligand exhibited a vibrational lifetime of 1 ps in D_2O [91, 188]. Different N_3Pro conformers in $CHCl_3$ show biexponential lifetimes of 1.0-1.6 ps/9.6-14.4 ps depending on their conformation [171]. Correlation times for spectral diffusion of 1-3 ps were found for N_3Ala, N_3Pro and the Aha labeled ligand [91, 188]. But, to the best of our knowledge, the influence of solvent properties on the vibrational lifetime and spectral diffusion have not been investigated methodically for aliphatic azide containing ncAAs yet.

2.4.1.3 Application in Proteins

Some previous studies have applied Aha as site-specific IR reporter for local environment in proteins. In 2010 Taskent-Sezgin *et al.* [100] incorporated Aha at two different positions into the N-terminal domain of the ribosomal protein L9(NTL9), which is a model for protein folding and stability. Changes in Aha's absorption spectrum between the folded and unfolded state of the protein domain were detected and differences in frequency and band shape between water exposed or buried positions in the hydrophobic core were found [100]. Later also the time scale for the ordering of the polypeptide backbone relative to side chains was investigated using T-jump time resolved IR spectroscopy in combination with Aha and isotope labeling [101]. QM/MM MD simulations on the two NTL9 mutants revealed the statistical distribution of hydrogen bonded water molecules. Despite the Aha is pointing into the hydrophobic pocket in one of the mutants, hydrogen bonds are formed to some water molecules, too, but in different angles and distribution compared to the solvent exposed mutant. The Aha seems to be not flexible enough to allow the formation of hydrogen bonds in ideal angles. Strongly blue shifting backbone interactions with the carbonyl O-atom are only found for this Aha, which is incorporated at the N-terminal position [177].

Thermal unfolding of the nSH3 domain of the protein CrkII has been investigated with several IR labels (isotope label, cyano-phenylalanine, N_3Phe, and Aha) [106].

The protein-protein interaction domain PDZ2 from human tyrosin-phosphatase 1E has been studied by the Hamm group with different Aha labeling strategies. A

peptide ligand was labeled with Aha at four different sites. One mutant showed a frequency shift and one a splitting of the band into two peaks upon binding to the protein domain. Time resolved 2D-IR spectroscopy revealed similar lifetimes for all bound and unbound Aha ligands, but differing spectral diffusion [91]. By improving their experimental setup the group was able to detect tiny 2D-IR signals, too small to be detected by a normal FTIR spectrometer [84]. Determination of the dissociation constant of two Aha labeled ligands with the PDZ2 domain was possible using its solvatochromic shift detected by 2D-IR spectroscopy at a single population time [107]. Later the PDZ2 domain itself was labeled and covalently linked to a photoswitch, which was intended to mimic conformational transitions upon ligand binding. Regrettably, a shift induced by illumination could only be found in one of six mutants. Quantum chemistry calculations revealed an electronic interaction involving charge transfer between the azido group and the sulfonate group of the photoswitch [102]. 2D-IR spectra at a single time point uncovered a frequency shift of one Aha PDZ2 mutant upon binding of two different ligands. MD simulations suggested that fewer solvent contacts and newly built polar contacts with side chains of the bound ligand are causing this shift [103]. Incredibly tiny signals were measured with 2D-IR spectroscopy on an Aha labeled protein but due to the small signal size only one population time was detected and, therefore, time resolved information is lacking. To the best of our knowledge, time resolved 2D-IR spectra have not been measured on an Aha labeled protein, yet.

2.4.2 Azulenylalanine

Azulene (Azu) is a planar aromatic 10 π conjugated molecule, consisting of a fused cyclopentadien and cycloheptatriene ring [189–191] (**figure 2.4.2**). It exhibits a weak electronic transition from the ground state to the first excited state ($S_0 \rightarrow S_1$) at about 500-700 nm (ε = 400cm^{-1}M^{-1}), a stronger $S_0 \rightarrow S_2$ transition at about 340 nm, and the most pronounced transition at about 275 nm ($S_0 \rightarrow S_3$) [75, 76, 189, 191, 192]. Usually, photoemission of organic molecules only takes place from the lowest electronically excited state (Kasha's rule) [191]. Azulene forms an exception of this rule. Its first excited state (S_1) decays almost radiationless and an anomalous fluorescence from S_2 at about 375 nm occurs with a quantum yield of about 0.02-0.031 and a fluorescence lifetime of *ca.* 2-3 ns [74, 75, 191–193]. The S_1 state decays ultrafast within 1 ps via internal conversion through a conical intersection between S_0 and S_1 [70, 73–75]. Thereby almost the complete photon energy of 2.1 eV is converted into vibrational energy [70].

The ncAA β-(1-azulenyl)-L-alanine (AzAla) contains the Azu moiety for incorporation into peptides and proteins. AzAla is a pseudoisoteric tryptophan (Trp) analogue [76, 194] and it can be synthesized via malonic ester condensation [190]. It has been introduced into proteins successfully via selective pressure incorporation, using Trp auxothroph expression host bacterium *L.lactis* [76].

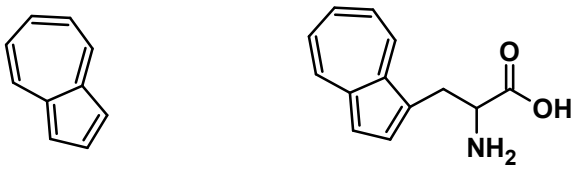

azulene (Azu)

b-(1-azulenyl)-L-alanine (AzAla)

Figure 2.4.2: Chemical structure of azulene (Azu) and β-(1-azulenyl)-alanine (AzAla).

Azu's ability for ultrafast conversion of a 600 nm photon's energy into vibrational energy in combination with its weak environmental dependence [77, 194] and its excellent photostability makes Azu a highly capable heater to induce vibrational energy transfer (VET) in molecules [41, 54, 70]. Its potential as a tool for the real time investigation of VET has already been applied for bridged Azu-anthrazen compounds [41, 54] and small peptides [70].

In addition, Azu/AzAla and derivatives are powerful fluorescence labels [77, 189, 194]. Their absorption and fluorescence is separated from Trp and is only weakly environment dependent. Therefore, mild intrinsic quenchers like Met, histidine (His) and imidazole can be used [77, 194].

2.5 PDZ Domains

The PDZ domain is one of the most abundant protein-protein interaction domains in numerous organisms from bacteria to humans. They conduct numerous functions in cells, like transport, localization, and assembly of target proteins into branched supramolecular signaling complexes, aggregation of receptors at the plasma membrane and contribute to the signaling specificity of many receptors [109, 110, 195]. In the human genome over 500 PDZ domains have been discovered in more than 300 different proteins (status: 2009) and in mouse genome even more than 900 (status: 2010) have been found [195, 196]. PDZ domains are almost exclusively occurring in cytoplasmic proteins [109] and PDZ containing proteins are divided into three families on basis of their modular organization [109, 110, 197]. Multi-PDZ domains contain only PDZ domains, MAGUK (membrane-associated guanylate kinase) proteins are composed of 1 to 3 PDZ domains, followed by one SH3 domain and one Gk domain (both domains are also protein-protein interaction domains), and the last family comprises proteins with PDZ domains combined with other domains [109, 110, 197].

PDZ domains contain 80 to 100 AAs arranged in a globular structure [109, 110, 195, 197–199]. Despite strongly differing sequence (down to 20 % sequence identity) different PDZ domains exhibit highly conserved three-dimensional structure

similarities. They consist of 5 to 6 β-sheets and 2 to 3 α-helices which can vary in length. Their ligand is bound into an elongated groove at the surface which is formed by the βB-strand, the αB-helix, and the carboxylate binding loop (L1) of PDZ [109, 195] (**figure 2.5.1**). The ligand is attached as an antiparallel β-sheet with the βB-strand of PDZ and the carboxylate binding loop (L1) binds the free carboxyl-terminus of a target protein with PDZ's characteristic KXXXGLGF sequence.

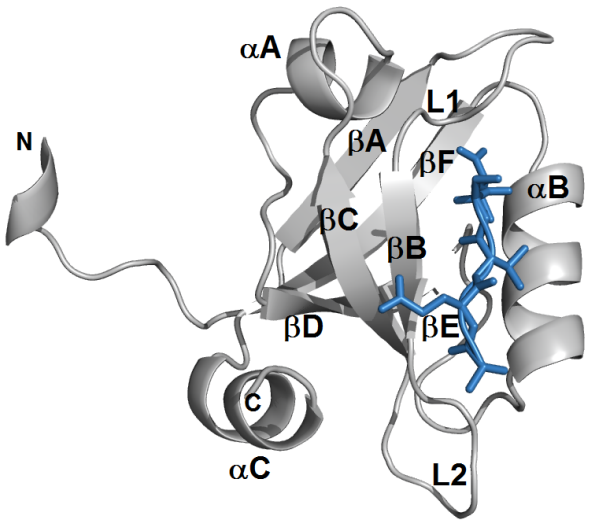

Figure 2.5.1: Structure of PDZ3(PSD-95) (grey) with ligand (blue) (PDB 1BE9 shorten by 13 AA).

Beyond the carboxyl-terminus of various proteins, PDZ domains can also bind internal peptide motifs such as the β-finger in neuronal nitric oxide synthetase (nNOS) or even lipids with an affinity in the micromolar range [109, 110, 195, 197–199]. In the past PDZ domains have been classified into two major groups according to their binding specificity: class I with a S/T-X-Ψ-COOH motif (X-any, Ψ - hydrophobic residue) and class II with the Ψ-X-Ψ-COOH motif [109, 196–198, 200]. However, later the class model needed to be expanded by additional classes and even later studies came to the result that this kind of classification is not far-reaching enough because of the complex pattern of overlapping binding specificities of PDZ domains [198, 200].

Tandem arrangements of several PDZ domains or of PDZ domains with other adjacent domains can affect their binding specificities [197, 200, 201]. For some PDZ containing proteins it has been shown that ligand binding at the binding site of one domain can regulate ligand interaction for an adjacent domain in a multi domain protein via allosteric interaction [202–204]. Since deregulation of PDZ interactions was connected to several diseases, such as cancer, PDZ domains could be worthwhile drug targets, however it is challenging to discover drug-like inhibitors for them [195, 198].

In 1999 Lockless and Ranganathan [5] developed a method, which uses evolutionary data of a protein family, to detect statistical coupling between AA positions for the PDZ domain family via multiple sequence alignment (MSA). They revealed unexpected long-range interactions between remote sites of the protein and proofed with the help of double mutant cycles that their statistical energy function is a good indicator of thermodynamic coupling [5]. This turned out to be the starting point of numerous theoretical [5, 6, 8–29] and some experimental [5, 11, 22, 29–37] studies on allostery without big conformational changes on PDZ domains. Mainly two different PDZ domains have been studied as model systems for allostery: the PDZ3 domain of the postsynaptic density protein PSD-95 (here referred to as PDZ3) [5, 6, 9, 10, 13–24, 26, 29, 31, 32, 35–37] and the second PDZ domain of human protein tyrosine phosphatase hPTP1E (sometimes also referred to as PTP-1E) [8, 11, 12, 15, 16, 18, 20, 24, 25, 27, 28, 30, 33, 34, 205]. Since the large majority of studies is based on theoretical approaches and only few experimental methods are available like NMR (nuclear magnetic resonance) spectroscopy and double mutation cycles combined with binding constant determination, new approaches to experimentally confirm or reject these theoretical predictions are urgently needed to understand allosteric communication.

2.5.1 PDZ3 of PSD-95

PSD-95 is a scaffolding protein and is found directly beneath the postsynaptic membrane [109, 206]. It is involved in the organization of the synaptic structure and is essential for synaptic plasticity [109, 207]. PSD-95 is a MAGUK protein and consists of three PDZ domains (PDZ1-PDZ2-PDZ3) followed by an SH3 and a Gk domain, which can operate either alone or in tandem [109, 110, 201, 206]. The PDZ1-PDZ2 domains and the PDZ3-SH3-Gk domain can form two distinct structural supramolecules cooperating together [109, 201, 206, 208]. Several binding partners for the different structural elements of PSD-95 are known. The PDZ1-2 domain can bind to the glutamate receptor NMDA NR2 subunit which allows Ca^{2+} influx into the cell or to shaker type K^{+} channels, which are both attaching PSD-95 to the membrane [109, 197, 208–210], or to nNOS [208]. The binding partners of PDZ3 are, therefore, complexed at the postsynaptic membrane. The PDZ3 domain can bind Neuroligins (Nlg), a neuronal adhesion molecule which forms an intercellular junction by interacting with β-Neurexins from an adjacent cell in the brain (**figure 2.5.2**) [200, 209]. Other interaction partners of the PDZ3 domain are the cysteine-rich protein (CRIPT) [208, 211], Citron [212], DHHC5 [206], and one isoform of the NO-sensitive guanylyl cyclase (NO receptor) [213]. They are bound canonical, which means at their C-terminal sequence [206, 208].

Often small C-terminal sequences of PDZ3 binding partners, usually CRIPT, are used for ligand binding studies. For these small peptides it makes hardly any

difference for binding kinetics if PDZ3 is used solely or combined with the adjacent domains. However, for full length CRIPT the dissociation is significantly slower from full length PDS-95 compared to PDZ3 only. This hints at the presence of non-canonical interactions of CRIPT outside PDZ3 [208].

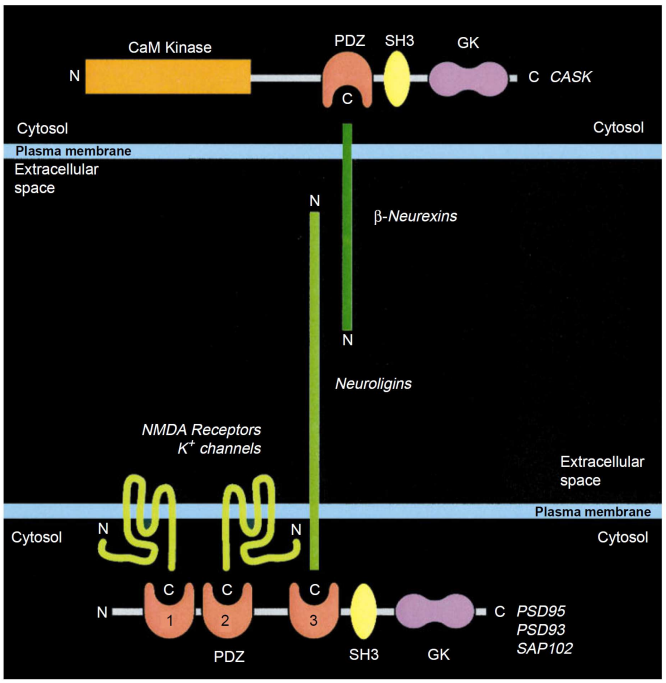

Figure 2.5.2: Model of intercellular junction formation of PSD-95 with NMDA receptors and Neuroligins. From Science 277 (5331), M. Irie, Y. Hata, M. Takeuchi, K. Ichtchenko, A. Toyoda, K. Hirao, Y. Takai, T. W. Rosahl, T. C. Südhof, Binding of Neuroligins to PSD-95, 1511-1515 [209]. Reprinted with permission from AAAS.

Comprehensive ITC (isothermal calorimetry) studies on PDZ3 revealed an optimal C-terminal sequence of X-T-X-V for the ligand [214]. PDZ3 binds its ligand via a one-step binding mechanism whereas many other PDZ domains exhibit a two-step binding with an induced fit mechanism [215–217]. For PDZ3 an MD simulation predicted three existing conformations in the apo state (state without ligand), from which the peptide ligand chooses the one with the smallest aperture of the binding site for binding via a conformational selection mechanism [17].

Interdomain allosteric regulation processes have been found for PDZ domains in other MAGUK proteins, which are very similarly structured as PSD-95: Disc Large (Dlg) and PSD-93. Ligand binding of CRIPT to the PDZ3 domain of Dlg regulates the interaction of the adjacent SH3-Gk domains with its binding partner. It was suggested, that the linker, which connects the PDZ3 domain to the SH3 domain might interact with the SH3 domain [202]. Also in PSD-93 the binding of the Gk domain to its binding partner can be inhibited by the intramolecular PDZ domains [203]. In PTP-BL, a protein tyrosine phosphatase, the PDZ2 domain ligand inter-

action is regulated by the presence of PDZ1 via a specific interaction of PDZ1 with PDZ2 at the site opposite to the ligand binding groove [204].

1996 Doyle *et al.* [210] resolved the crystal structure of PDZ3 of brain synaptic PSD-95 without ligand (PDB: 1BFE) and bound to the nonameric C-terminal CRIPT sequence (TKNYKQTSV) (PDB: 1BE9) (**figure 2.5.1**). One peptide is bound per PDZ3 with a very well resolved C-terminal end. The PDZ3 structure undergoes only very little conformational changes upon ligand binding with an RMSD (root mean square deviation) for the C_α atoms of 0.9 Å with small changes in the flexible loop L_2 (behind the βB-sheet) and a 180° rotation of the His372 side chain [210].

2.5.1.1 PDZ Allostery

Lockless and Ranganathan used the highly conserved and functionally important binding site residue His372 (numbered 76 in [5]) to reveal residues, which are statistically coupled to this AA, using a MSA of 274 eukaryotic PDZ domains. Only a few AA positions showed a significant coupling to His372, some are in His372's proximity but others are unexpectedly long range coupled. Thermodynamic double mutant cycle (DMC) analysis combined with an assay based on fluorescence detection, which determines binding rates, was applied to 14 double mutants to compare thermodynamical coupling energies with the calculated statistical coupling. The mutational study confirmed the prediction of energetically coupled AAs. A set of these coupled AAs was chosen to predict a connected pathway of AAs through the protein from His372 along the αB-helix side chains of Ala376 and Lys380, across the binding pocket to Phe325 and later on to Ala347 and Leu353 in the protein core on the other site of the protein, which might be the basis for efficient energy conduction (**figure 2.5.3a**) [5].

Nine years later Chi *et al.* [31] applied a different fluorescence method with a stopped-flow technique for determining binding constants of mainly the same PDZ3 double mutants. However, their thermodynamical coupling energies differed a lot from the ones measured by Lockless and Ranganathan [5] due to unknown reasons. The observed coupling in Chi *et al.* [31] could be explained by a distance relationship with stronger coupling for close residues than for long range coupling. Nevertheless, they found that the type of mutation has an impact on the coupling constant [31]. A computational DMC also proposed that coupling energies depend on the type of mutation and that averaging all kinds of mutations is required to get reliable results. No correlation between computational DMC and the statistical coupling analysis prediction could be found and DMC coupling was predicted to be distance dependent [13]. Experimental DMC in combination with fluorescence spectroscopy and a stopped-flow technique of 31 PDZ3 and PDZ2 PTP-BL mutants in turn proposed a wire of long range communication, distinct for both PDZ domains, and without a clear distance dependency [35].

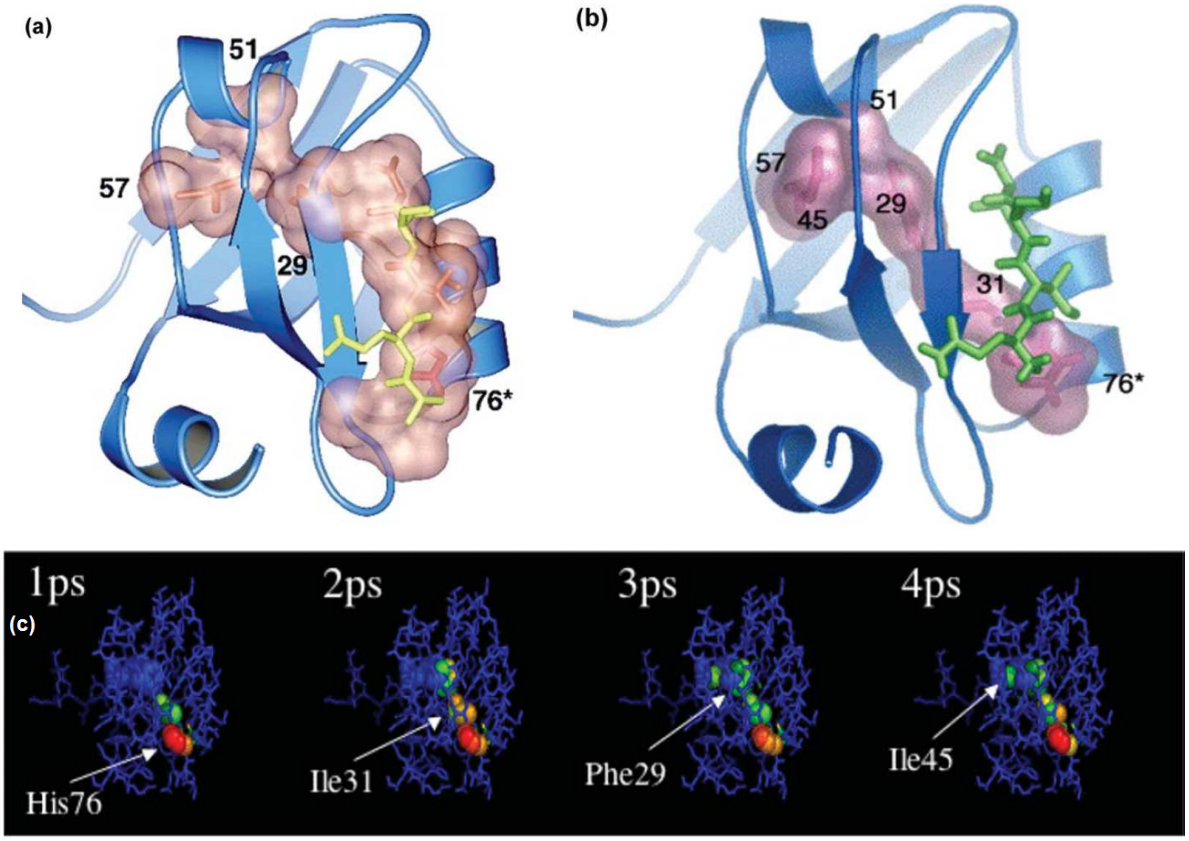

Figure 2.5.3: Theoretically predicted allosteric pathways in PDZ3. Pathway proposed by **(a)** evolutionary statistical method of [5] and **(b)** signaling pathway proposed by anisotropic thermal diffusion method of [6]. The numbering is +296 compared to the crystal structure of [210]. **(c)** Heat propagation revealed by anisotropic thermal diffusion MD simulations. Reprinted from Journal of Molecular Biology, 351, Nobuyuki Ota and David A. Agar, Intramolecular signaling pathways revealed by modeling anisotropic thermal diffusion, 345-354, Copyright 2005, with permission from Elsevier [6].

An extensive experimental single mutation study, in which 83 AAs of PDZ3 were mutated to each other AA, suggested a sector of 20 functionally important residues within the PDZ3 fold [36]. Interestingly, it turned out that mutations of only few positions have an impact on changing the binding specificity of PDZ3 from class I to II and that these mutations can be divided into class-bridging mutations, which allow class I and class II ligand binding, and in class-switching mutations, which directly change from class I to II binding specificity. Former are likely to have occurred first in evolution. Only one double mutation of Gly330Thr and His372Ala is sufficient for complete class changing [22, 36].

In 2004 NMR measurements on PDZ2 hPTP1E revealed that the side chain methyl dynamics change upon ligand binding at two distant surfaces [33]. An overall rigidification of the protein upon ligand binding was detected. The idea arose that dynamic fluctuations and ps-ns dynamics in PDZ domains might play a role in

allosteric signal transduction as well. A later study showed that the backbone dynamic is not affected by the change in side chain dynamics upon ligand binding [34]. A normal mode analysis of apo and holo PDZ3 found that only one to two normal modes are needed to explain structural differences upon ligand binding matching the NMR results. It was suggested that thermal fluctuations of PDZ domains prepare them for binding [29].

Ota and Agard [6] applied a non-equilibrium MD simulation approach called anisotropic thermal diffusion (ATD) to PDZ3. PDZ3 was energy minimized and equilibrated to 10 K and then the His372 side chain was temperature coupled to a 300 K bath. The heat diffusion appeared to be highly anisotropic and a pathway of most efficient thermal diffusion was revealed (**figure 2.5.3b and c**). The observed pathway is similar to the one found in [5], but it takes the more direct path between His372 and Phe325 across Ile327. Heating another residue instead revealed a more isotropic pattern of energy transfer. Van-der-Waals interactions (and not electrostatic interactions) were found to be the main element of these signaling interactions [6]. Another non-equilibrium MD approach named pump-probe molecular dynamics also perturbed the His372, but found a pathway along the same site of the binding pocket [10] like the pathway of Lockless and Ranganathan [5]. Further non-equilibrium MD simulations with different approaches revealed other coupling patterns showing that simulation conditions have a significant impact on the proposed pathways [13, 14, 19].

The impact of the third α-helix, which is special for PDZ3, on allosteric signaling has been a matter of several studies. Petit *et al.* [37] used NMR spectroscopy and isothermal titration calorimetry (ITC) to investigate the difference in behavior between PDZ3 and a truncated version PDZ3-α3. ITC measurements yield a 21x lower binding constant for PDZ3-α3 compared to full length PDZ3 for an Ac-TKNYKQTSV ligand with the main change being entropic not enthalpic. In NMR spin relaxation experiments a shorter ligand (Ac-NYKQTSV) was used, which does not show any contacts to the α3-helix. Without ligand the side chain flexibility is significantly increased for the truncated PDZ3 compared to full-length, but the backbone dynamics are similar for both. Ligand binding modulates the side chain dynamics pattern back to the one of full length PDZ3. In further ITC studies by another group PDZ3 and PDZ3-α3 with a much shorter ligand (KQTSV) exhibit similar binding constants for both PDZ3s [214]. This suggested, that the enormous change in the binding constant between PDZ3 and PDZ3-α3 in the Petit *et al.* publication [37] might rather be caused by direct interactions of the longer ligand to the α3-helix. Chi *et al.* [32] also investigated this phenomenon with ITC and NMR. Ligand binding of a YKQTSV ligand revealed a 6x lower binding constant for PDZ3-α3. Their NMR measurements using a longer GSKNYKQTSV ligand show direct contacts of the K_{-7} and Q_{-3} ligand residues to the α3-helix. They proposed that the α3-helix forms a part of an extended binding surface outside the canonical binding groove. The acetylated N-terminus of the Peptit ligand or the used temper-

ature might be reasons for this differing result [32]. Despite the hints that at least the strong change in the binding constant is rather caused by direct interaction between the ligand and the α3-helix than by an allosteric effect, the 21-fold change in the binding constant is used to be cited in the majority of later publications on allostery in PDZ domains. Nevertheless, the additional α3-helix of PDZ3 seemed to affect side chain dynamics in PDZ3. In another NMR study the conserved Tyr397 residue in the α3-helix was phosphorylated, which caused an equilibrium between a docked and an undocked conformation of α3 with weakened interactions of PDZ3 with the adjacent SH3 domain. This might be a biologically relevant allosteric regulation process [218]. Furthermore, some computational simulations predicted clear differences in the AA networks of PDZ3 and PDZ3-α3 [15, 20, 21].

Atomistic MD simulations suggested, that ligand binding causes a change in electrostatic interactions and an AA network along the α3-helix consisting of almost entirely charged AAs was predicted [23]. The small overall change of enthalpy is explained by cancellation of local redistributions. A combination of MD simulation and Fourier filtering found stiffening of PDZ domains in the THz region upon ligand binding and proposed that specific THz-frequency vibrational modes might play a role in the allosteric communication [24]. Also the existence of multiple communication pathways, which are intrinsically displaced, has been suggested by a theoretical approach [18].

Several computational studies found differing pathways for PDZ3 from PSD-95 and PDZ2 from hPTP1E with the same method applied for both PDZ domains [14, 15, 18, 20, 24]. Only one study [16] predicted a similar network with a Gaussian network model for all 12 PDZ domains calculated. The dynamic response of PDZ2 (hPTP1E) in the ps-ns time range upon structural changes similar to ligand binding was studied using a covalently linked azobenzene photoswitch in combination with femtosecond TRIR spectroscopy and MD simulations. Structural reorganization on ns time scales without a dominant barrier similar to a downhill folding scenario along multiple pathways was found [25, 30]. Later the same PDZ domain has also been target of Aha incorporation in the same research group [91, 102, 103, 107].

Chapter 3

Experimental Section

3.1 Samples

3.1.1 Ahas and its Derivatives

Commercially available unprotected Aha (upAha), Boc-protected Aha (bocAha), and Fmoc-protected Aha (fmocAha) from Iris BIOTECH GmbH were dissolved in commercially available solvents. Hexafluoroisopropanol (HFIP) from Carl Roth GmbH&Co. KG and n-heptane, cyclohexane, tetrachloromethane (CCl_4), tetrachloroethylene (PCE), chloroform ($CHCl_3$), tetrahydrofuran (THF), dichloromethane (DCM), acetonitrile, dimethylformamide (DMF), dimethyl sulfoxide (DMSO), formamide, methanol, and 2,2,2-trifluoroethanol (TFE) from Merck KGaA were utilized. D_2O was bought from Euriso-Top GmbH. For the H_2O samples MilliQ H_2O was used.

3.1.2 Peptides

Several peptides were employed in this thesis. As a native PDZ3 ligand the C-terminal peptide of CRIPT [208, 211] was utilized as a heptamer (acNYKQTSV) (called Hepta) (structure in **figure 3.1.1**). The numbering of the ligand residues is the same as commonly applied in previous publications: $N_{-6}Y_{-5}K_{-4}Q_{-3}T_{-2}S_{-1}V_0$ [210, 214]. One portion of the Hepta was synthesized by Marie Anders-Maurer (Harald Schwalbe group, Institut für Organische Chemie, Johann Wolfgang Goethe-Universität Frankfurt, Germany) via solid phase peptide synthesis and the other portion was purchased from PANA Tecs biochemical solutions. For the VET measurements two different PDZ3 ligands were used: the Azu containing ligand (AzuCaKQTSV) (named AzuLig) was bound to the Aha labeled PDZ3 mutants and the

Aha containing ligand (YKQTAhaV) (called AhaLig) is the binding partner of the AzAla labeled PDZ3 mutants in the VET measurements. The optimum position for the azulene moiety in the ligand was determined by Martin Essig in his Bachelor thesis using *in silico* docking simulations [219]. As the $_{-1}$ position is quite tolerant to substitution [214], this position was chosen to substitute the S_{-1} with an Aha residue. For the VET measurements also an Aha-AzAla dipeptide (DiPe) was used as the simplest test case for the VET pair. A longer PDZ3 ligand-like peptide with both AzAla and Aha (AzAla-KQAhaSV) (VETLig) was utilized as a test peptide for VET in a ligand-like peptide. All peptides used for the VET measurements (AzuLig, AhaLig, DiPe, and VETLig) were synthesized by our collaboration partner Patrick Durkin from the group of Nediljko Budisa, Institut für Chemie, Technische Universität Berlin, Germany. Disadvantageously, AzuLig was impure and shorter fragments of the N-terminus were expected to exist in the solution.

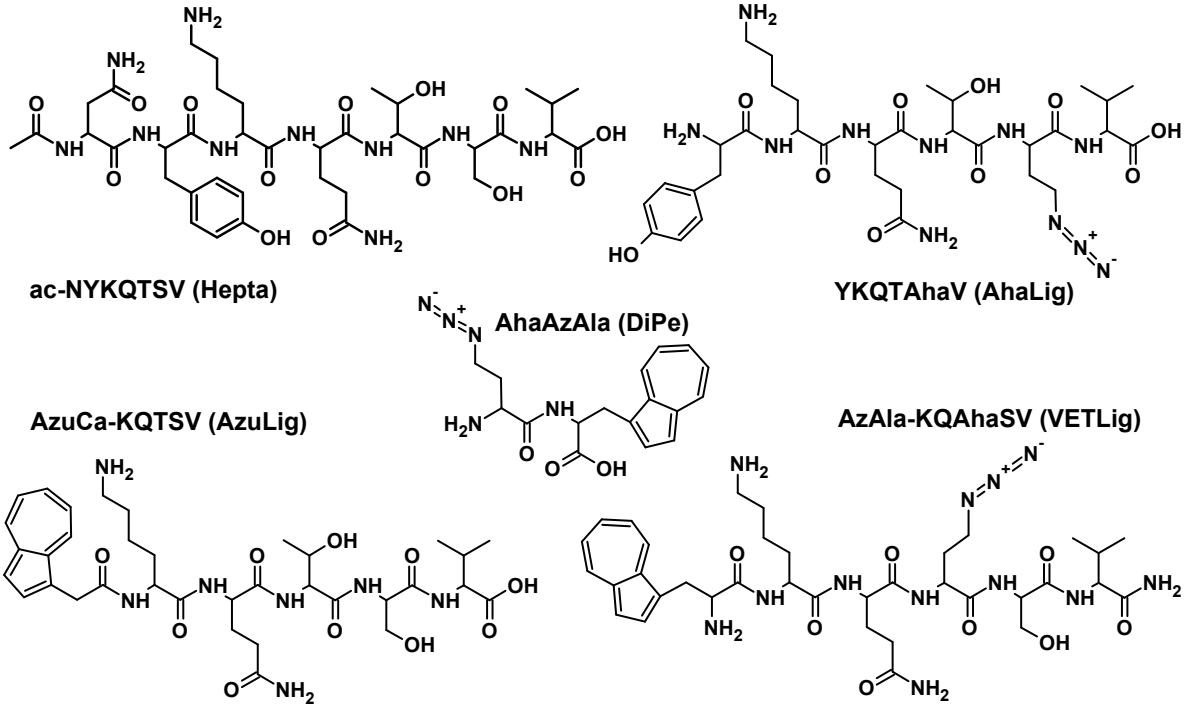

Figure 3.1.1: Chemical structures of the used peptides.

3.1.3 PDZ3

PDZ3 (residues 303-402) of PSD-95 from *Rattus norvegicus* is numbered as in the crystal structure of Doyle *et al.* [210].

3.1.3.1 PDZ3 Expression and Purification

Wild Type and PDZ3-Aha

Mutagenesis, expression, and purification of wild type (WT) PDZ3 and the Aha mutants were conducted by Sabrina Oesteritz.

For protein expression the methionine-auxotrophic *E.coli* strain B834 was utilized with a pGDR11 vector coding for the PDZ3 construct. Directly in front of the PDZ3 residues 303-402 the vector contains a His-tag and a TEV-cleavage site, so that the His-tag, which is used for protein purification, can be removed from the PDZ3 sequence afterwards by a TEV-polymerase leaving only one N-terminal G at the 302 position. This is important for removing the additional Aha at the Met start codon position. For the different mutants each point mutation was introduced with the Site-Directed Mutagenesis kit of GeneArt.

The final WT sequence (the subsequently introduced Aha mutation sites are colored magenta) of the used PDZ3 domain is:
^{302}GGEE DIPRE ^{311}PRRIV IHRGS ^{321}TGLGF NIIGG ^{331}EDGEG IFISF ^{341}ILAGG PADLS ^{351}GELRK GDQIL ^{361}SVNGV DLRNA ^{371}SHEQA AIALK ^{381}NAGQT VTIIA ^{391}QYKPE EYSRF ^{401}EA

The cells were grown overnight in LB medium (10 g/l tryptone/peptone, 5 g/l yeast extract, 7.5 g/l NaCl) inoculated with ampicillin. For Aha incorporation the medium was changed to a Met free M9 medium (for 7 liters: 1.4 l M9 salt (5x concentrated; 15 g KH_2PO_4, 42.25 g Na_2HPO_4 x $2H_2O$, 2.5 g NaCl, 5 g NH_4Cl), 28 g glucose, 14 ml 1 M $MgSO_4$, 700 µl 1 M $CaCl_2$, 1.4 ml trace element solution (10 mM $CoCl_2$, 4 mM $CuSO_4$, 90 mM $FeCl_3$, 5 mM H_3BO_3, 50 mM $MnCl_2$, 10 mM Na_2MoO_4, 25 mM $ZnCl_2$), 70 mg thiamine, 70 mg biotine, 700 mg ampicillin) with 50 mM Aha. The WT continued growing in LB medium. About 6-8 hours after the medium exchange at an optical density (OD) of 1.4-1.5, PDZ3 expression was induced by addition of IPTG (isopropyl-β-D-1-thiogalactopyranoside). 18-21 hours later cells were harvested and disrupted by ultrasound. PDZ3 was purified with an Ni-NTA affinity column to which the His-tag binds and which can be eluted with imidazole. Afterwards the His-tag was cleaved by the HisTagged TEV-polymerase and both were separated from PDZ3 by an additional Ni-NTA column and PDZ3 was finally purified via a gel filtration. The protein concentration was determined by a Lowry assay after concentrating. PDZ3 was stored at -70 °C in a 50 mM NaPi buffer at pH 6.8.

All PDZ3-Aha and WT measurements were performed in a 50 mM NaPi buffer at pH 6.8. The PDZ3-Aha samples were concentrated using Vivaspins (5000 MWCO, Santorius AG) and a small centrifuge (Hettich Zentrifuge, Micro 120) with 1000 rpm at 7 °C.

PDZ3-AzAla

Our collaboration partners from the group of Nediljko Budisa, Institut für Chemie, Technische Universität Berlin, Germany, developed an AzAla specific orthogonal pair consisting of an aminoacyl-tRNA synthetase (aaRS) and its cognate tRNA in order to incorporate AzAla into a protein via stop codon suppression (SCS) [105]. They scanned a gene library of *M.jannaschii* TyrRS (*Mj*TyrRS) in combination with three rounds of positive and negative selection to evolve the aaRS.

With this approach they incorporated AzAla site-specifically into PDZ3 at two positions (two mutants: Phe325AzAla and Phe340AzAla). A C-terminal Gly-Ser-$(His)_6$-tag was encoded to the PDZ3 sequence. This C-terminal His-tag is used to separate the truncated PDZ3 (termination at the stop codon instead of AzAla incorporation) from the full length PDZ3-AzAla. The final sequence (the subsequently introduced AzAla mutation sites are colored blue) is:
^{300}M ^{301}GGGEE DIPRE ^{311}PRRIV IHRGS ^{321}TGLGF NIIGG ^{331}EDGEG IFISF ^{341}ILAGG PADLS ^{351}GELRK GDQIL ^{361}SVNGV DLRNA ^{371}SHEQA AIALK ^{381}NAGQT VTIIA ^{391}QYKPE EYSRF ^{401}EAGSH HHHHH

PDZ3-AzAla was expressed in *E.coli* strain BL21(DE3). The cells were grown on a ZYP-5052 autoinduction medium and AzAla was added after 1 h to a final concentration of 1 mM. The cells were harvested by centrifugation, resuspended in lysis buffer, and lysed by high pressure homogenization. The lysate was loaded onto an Ni-NTA column (binds His-tag of the full length PDZ3-AzAla) and purified via an ÄKTA column. The PDZ3-AzAla samples were stored in 50 mM NaPi pH 7.5 buffer with 10 % glycerol at -70 °C.

PDZ3-AzAla expression and purification were carried out by Tobias Baumann, Matthias Hauf, and Fabian Schildhauer from the group of Nediljko Budisa, Institut für Chemie, Technische Universität Berlin, Germany, Germany. Afterwards Sabrina Oesteritz from the Bredenbeck group determined the protein concentration by a Lowry assay.

3.1.3.2 PDZ3 Characterization

All PDZ3-Aha mutants were characterized by circular dichroism (CD) and isothermal titration calorimetry (ITC).

Circular Dichroism

CD spectra were recorded with a spectropolarimeter J-720 from Jasco in a range from 260 to 178 nm, a scanning speed of 200 nm/min, an accumulation of 32, and a path length of 55 μm.

Prior to the data analysis, the CD spectra of the buffer was subtracted as background and then the secondary structure composition was estimated applying a concentration independent method by Raussens *et al.* [220, 221].

Table 3.1: Concentration of the PDZ3 samples for the CD measurements determined by Lowry assay.

	c/mg/ml
WT1	1.18
WT2	1.42
WT3	1.89
Ala347Aha	2
Ala376Aha	1.5
Ala378Aha	2
Ala390Aha	1.55
Gly322Aha	1
Gly329Aha	0.75
Ile327Aha	1.41
Ile338Aha	1
Ile341Aha	1.99
Leu342Aha	1.5
Leu353Aha	3.2
Lys380Aha	1
Ser398Aha	1.8
Val362Aha	2
Val386Aha	2

Isothermal Titration Calorimetry

The VP-ITC MicroCalorimeter from MicroCal (Volker Dötsch group, Institut für Biophysikalische Chemie, Johann Wolfgang Goethe-Universität Frankfurt, Germany) was used for ITC measurements with the following parameters:

Table 3.2: Instrument parameters for the ITC measurements.

ITC parameters	
number of injections	28
stirring speed	307 s^{-1}
temperature	25 °C
first injection 5 μl and all following 10 μl volume	
duration	20 s
spacing	250 s

ITC data were analyzed with the MicroCal ITC analysis software in Origin 7, assuming a one site binding model. The initial concentration of the PDZ3 samples was adjusted according to the concentration determined by the Lowry assay. All protein samples were degased directly before the experiment. The protein concentration changes due to degasing. For fitting the data, therefore, the protein concentration was adjusted to get a stoichiometry of about 1, as it is known to be

true for PDZ3 with canonical ligands [214]. The concentration of the ligands without Azu was determined by UV-Vis spectroscopy using the 280 nm absorption of the tyrosine residue. The denoted ligand concentrations are the concentrations in the syring before titration. The WT/PDZ3-Aha+Hepta ITC data were measured in a 50 mM NaPi H_2O pH 6.8 buffer.

Table 3.3: Concentration of the PDZ3-Aha mutants and WT plus Hepta for the ITC measurements.

	c_{PDZ3}/mM	c_{Hepta}/mM	reference power/$\mu Cal/s$
WT1	0.22	2	10
WT2	0.13	1.4	15
Ala347Aha	0.10	1.58	15
Ala376Aha	0.09	2	10
Ala378Aha	0.10	1.51	15
Ala390Aha	0.165	2	10
Gly322Aha	0.10	1.58	15
Gly329Aha	0.08	1.46	30
Ile327Aha	0.12	2	10
Ile338Aha	0.11	1.37	15
Ile341Aha	0.185	2	10
Leu342Aha	0.11	1.58	15
Leu353Aha	0.145	2	10
Lys380Aha	0.13	1.58	15
Ser398Aha	0.19	2	10
Val362Aha	0.13	1.58	15
Val386Aha	0.11	1.37	15

For the WT/PDZ3-Aha+AzuLig ITC measurements a fraction of DMSO was added to the 50 mM NaPi H_2O pH 6.8 buffer in order to predissolve AzuLig. In the ITC measurement of Ile341Aha + old ligand 6 % DMSO and for all others with new AzuLig 2 % DMSO were added. Since the concentration of new AzuLig could not be determined due to the impurity with shorter fragments of the N-terminus, the AzuLig concentration was adjusted in the analysis in a way that the binding parameter matches the results of a former ITC measurement with pure AzuLig (old ligand) for the Ile341Aha sample. The AzuLig concentrations for the other mutants were adjusted to this value via comparing UV-Vis absorptions.

Table 3.4: Concentration of the PDZ3-Aha mutants and WT plus AzuLig for the ITC measurements.

	c_{PDZ3}/mM	c_{AzuLig}/mM	reference power/$\mu Cal/s$
Ile341Aha + old ligand	0.2	2	10
Ile341Aha	0.12	1.4	30
WT	0.17	1.4	30
Ala376Aha	0.14	1.4	30
Gly322Aha	0.16	1.16	30
Gly329Aha	0.10	1.16	30
Ile327Aha	0.17	1.4	30
Ile338Aha	0.17	1.4	30

For PDZ3-AzAla samples a 50 mM NaPi pH 6.8 buffer without DMSO was used for the ITC measurements.

Table 3.5: Concentration of the PDZ3-AzAla mutants and WT plus AhaLig and Hepta for the ITC measurements.

	c_{PDZ3}/mM	c_{ligand}/mM	reference power/$\mu Cal/s$
Phe325AzAla+Hepta	0.04	1.46	30
Phe340AzAla+Hepta	0.045	1.46	30
WT+AhaLig	0.10	1.32	30
Phe325AzAla+AhaLig	0.05	1.32	30
Phe340AzAla+AhaLig	0.06	1.32	30

Mass Spectrometry

In order to determine the Aha labeling efficiency of the PDZ3-Aha samples, MALDI spectra were measured by Dr. Ute Bahr from the group of Prof. Dr. Karas, Institut für Pharmazeutische Chemie, Johann Wolfgang Goethe-Universität Frankfurt, Frankfurt. The WT-PDZ3 was used as internal reference (**figure 3.1.2** as an example). However, due to the very small mass difference of 5 Da between Aha and Met, the peaks of the Aha labeled and Met labeled sample strongly overlap in a combination peak. An estimation of the Aha labeling efficiency was performed using the mass of this combination peak in relation to the expected mass of the PDZ3-Aha mutant. However, this approach gives only a very rough estimate for the labeling efficiency, which might differ by a factor of 2.

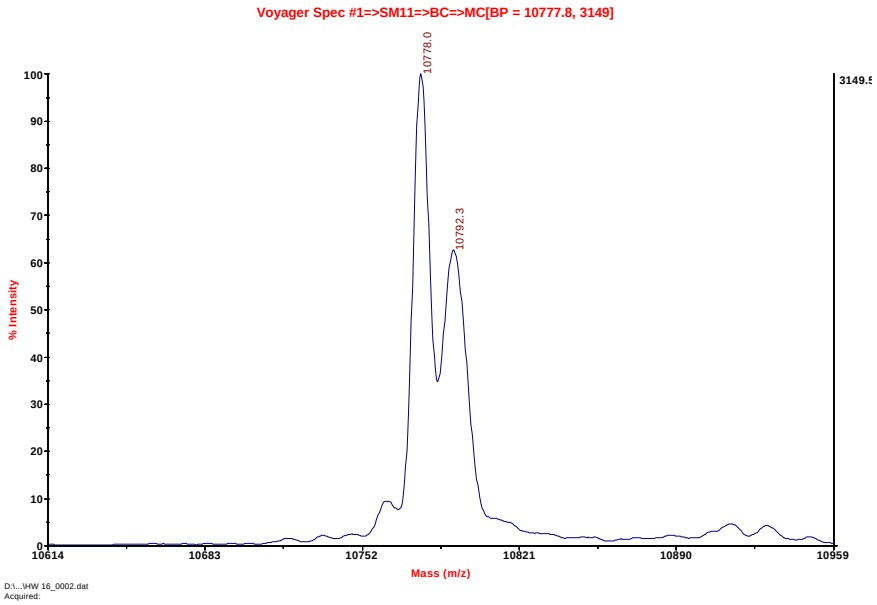

Figure 3.1.2: MALDI spectrum of an Ile327Aha sample with WT as internal reference. For this sample an Aha labeling efficiency of 74 % was estimated. The spectrum was measured by Ute Bahr from the group of Prof. Dr. Karas, Institut für Pharmazeutische Chemie, Johann Wolfgang Goethe-Universität Frankfurt.

Rene Zangl and Maximilian Gauger from the group of Prof. Dr. Nina Morgner, Institut für Physikalische Chemie, Johann Wolfgang Goethe-Universität Frankfurt were able to measure ESI spectra with a much higher resolution (**figure 3.1.3** as an example). In this case the ESI spectrum of the Ile327Aha sample was compared to the ESI spectrum of a pure Ile327Met sample. The spectrum of Ile327Aha was fitted by two Gaussians for the Aha labeled fraction and the Met labeled part. This way a much more accurate value for the Aha labeling efficiency could be determined. Unfortunately, ESI spectra only exist for a few PDZ3-Aha samples. For them Aha labeling efficiencies between 46 and 88 % were found. The PDZ3-Aha samples can be assumed to contain a fraction of Met labeled sample. Since PDZ3-Met does not absorb in the range of 2100 cm^{-1}, it is not seen in the IR spectra in this spectral range. Anyway, it reduces the possible signal size in a VET measurement and complicates calculation of the VET efficiency.

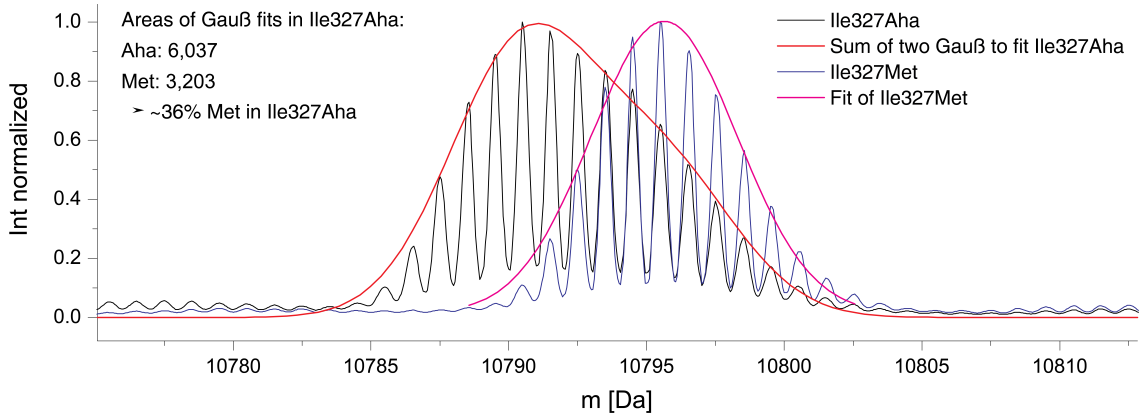

Figure 3.1.3: ESI spectrum of an Ile327Aha and an Ile327Met sample. For this Ile327Aha sample an Aha labeling efficiency of 64 % was estimated. The spectrum was measured by Rene Zangl and Maximilian Gauger from the group of Prof. Dr. Nina Morgner, Institut für Physikalische Chemie, Johann Wolfgang Goethe-Universität Frankfurt.

3.1.3.3 Solvent Accessible Surface Area

For the calculation of the solvent accessible surface area (SASA) of the AA positions, at which an Aha is incorporated later, the program free SASA running on python basis was used [222]. The crystal structures of Doyle *et al.* [210] were utilized (PDB: apo-1BFE, holo-1BE9). The SASAs were scaled on the size of the AA at that position [223].

3.2 FTIR

All FTIR spectra were measured on a Bruker Tensor 27 FTIR spectrometer with a resolution of 1 cm^{-1}. A CaF_2 flow cell [224] with a Teflon spacer in different thicknesses determining the path length was first flushed with the solvent as background and afterwards with the sample in the solvent to ensure identical path lengths and same absorption of the CaF_2 windows for the background and the investigated sample. All samples were centrifuged before the FTIR measurements to prevent scattering.

3.2.1 Aha

If possible the Aha concentration of the three Ahas was adjusted to 50 mM. For the less soluble Aha/solvent samples Aha was dissolved up to saturation. The samples with lower concentrations than 50 mM are: upAha in TFE; fmocAha in TFE, formamide, PCE, CCl_4, and n-heptane; bocAha in acetonitrile, CCl_4, cyclohexane, and n-heptane. Some samples were even not soluble enough to show a sufficiently large IR signal: upAha in acetonitrile, formamide, PCE, CCl_4, n-heptane, $CHCl_3$, DCM, THF, hexane, and cyclohexane; fmocAha in H_2O, hexane, and cyclohexane; bocAha in hexane.

Spectra were measured with a path length of 100 μm for aqueous solutions and 250 μm for all other solvents. The solvent background was subtracted from the sample spectrum. All FTIR measurements were performed at room temperature (RT).

3.2.2 PDZ3-Aha

For the FTIR measurements on the PDZ3-Aha mutants a Teflon spacer with 100 μm path length was used. The PDZ3 concentration was set to 3-10 mM and the Hepta concentration was adjusted to be at a 1.3-1.5 fold excess to ensure fully bound PDZ3. Additional IR measurements of Ala376Aha+Hepta point out, that in the used IR measurement total saturation might not have been achieved. But the data quality of these additional data was poor and a significant spectral change is also visible in the presented data (saturation is at least larger than 90 %). Therefore, the other spectrum was utilized for further analysis. A long pass filter cutting the spectra below 4 μm was used. The temperature was set to 25 °C with a thermostat. The buffer background was subtracted from the sample spectrum. A 5^{th} order polynomial was extrapolated to the spectrum in the range from 1950 cm^{-1} to 2300 cm^{-1} (signal manually excluded) and subtracted as additional background correction.

The second derivative of the corrected spectrum in the Aha signal range was calculated to find the number of sub bands in the Aha absorption band. Accordingly, the sum of 1-4 pseudo-Voigt (psVoigt) functions composed of the sum of a Gaussian and a Lorentzian function was fitted to the Aha band.

Equation 3.2.1 gives the equation for one psVoigt function with x_c as the band maximum, ω as the FWHM, m as the Lorentz ratio, A as the area of the peak, and y_0 as an offset. For the sum of multiple psVoigt functions only one offset y_0 in total was used. For a few spectra the fitting borders needed to be set to flank at 10 % or 20 % of the signal sizes to prevent perturbation caused by background issues. Therefore, A and ω are not analyzable for them.

$$y = y_0 + A[m\frac{2}{\pi}\frac{\omega}{4(x-x_c)^2+\omega^2} + (1-m)\frac{\sqrt{4ln2}}{\sqrt{\pi}\omega}\cdot e^{-\frac{4ln2}{\omega^2}(x-x_c)^2}] \tag{3.2.1}$$

3.3 2D-IR

A 5 W Titan:Sapphire oscillator/regenerative amplifier system from Spectra Physics (Mai Tai Sp oscillator, Empower pump laser, Spitfire Ace) with a repetition rate of 3 kHz, a wavelength of 800 nm, and a pulse duration of 97 fs (full width at half maximum (FWHM)) was operated to run two two-stage home-built optical parametric amplifiers (OPAs) in combination with a difference frequency generation (DFG). OPAs combined with other nonlinear optical processes are used to convert the 800 nm light from the laser source into tunable broadband light from the visible to the infrared [225–227]. The 800 nm beam from the laser enters the OPA and is split into two beams via a beam splitter (**figure 3.3.1**). The smaller portion is reflected and severs as seed pulse in the optical parametric process. It is focused to a YAG or a Sapphire plate to generate white light continuum [225, 226, 228–230]. Afterwards it is focused into a β-barium borate (BBO) type II crystal and serves as seed for the optical parametric amplification. The second fraction from the 800 nm beam is split again into two portions. The smaller one, called *Pump1*, is focused into the same BBO crystal. The seed beam and the *Pump1* beam enter the BBO collinearly and are adjusted to achieve spacial and temporal overlap. The first stage optical parametric process takes place and generates the *Signal* (1.1 to 1.6 μm) and *Idler* (1.6 to 3 μm) beam. The desired wavelength of *Signal* and *Idler* can be adjusted by changing the phasematching conditions, especially the angle of the crystal, the angle of the incoming beams and their timing. *Signal* and *Idler* are separated via a dichroic mirror after leaving the BBO and the *Signal* is sent back into the BBO crystal afterwards. There it meets the third part of the 800 nm beam and a second optical parametric amplification takes place using the *Signal* pulse from the first amplification as seed. The two-stage optical parametric amplification yields higher pulse stability than a single-stage OPA. The, thus, generated

Signal and *Idler* pulses are guided into an interferometer, where they are split and merged again within a $AgGaS_2$ crystal (AGS). Their spacial and temporal overlap can be optimized. A DFG process takes place in the AGS crystal and mid IR light tunable from 2.4 to 12 μm is generated. *Signal* and *Idler* can also be used to create visible light by employing other crystals and nonlinear optical processes [225–227].

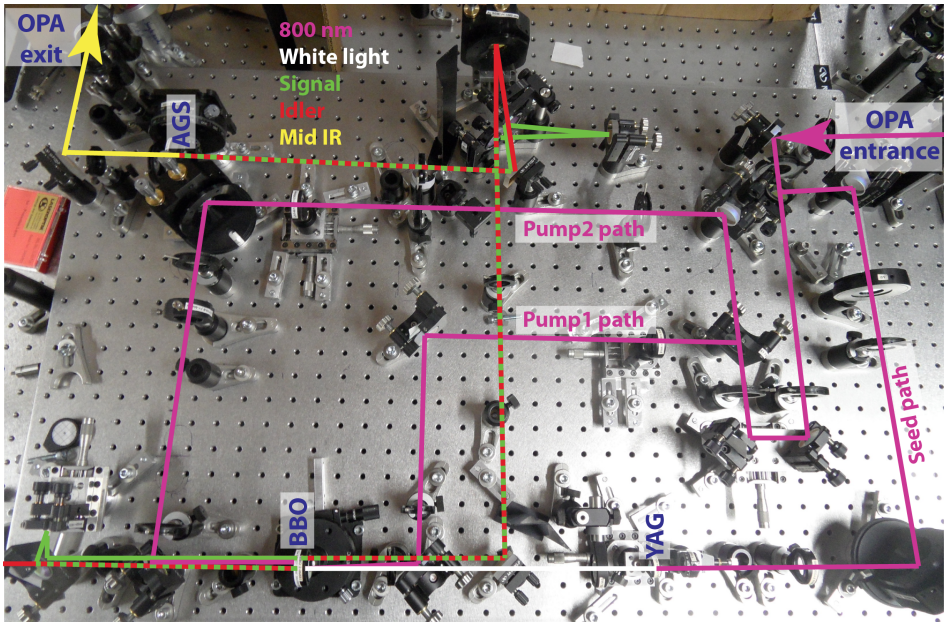

Figure 3.3.1: OPA setup. View onto a home-built two-stage OPA with attached DFG. The beam-pathways are drawn in magenta (800 nm), white (white light), green (*Signal*), red (*Idler*), and yellow (Mid IR).

For the 2D-IR spectroscopy experiments described here the two OPAs exhibit broad band mid infrared pulses centered around 4740 nm. The pulse of the first OPA (1.9 μJ) was split into a probe pulse and a reference pulse to correct data for intensity fluctuations of the laser. Both probe and reference were guided through the sample, dispersed with a spectrometer (Triax 180, HORIBA Jobin Yvon, 210 l/mm grating) and detected on a 2x64 pixel mercury cadmium telluride (MCT) detector (Infrared Associates). To achieve running times of over 50 hours, a home-built automatic liquid nitrogen refilling system was applied, which restocks the MCT detector periodically with liquid nitrogen [231].

The simplest implementation of a 2D-IR experiment (described in **chapter 2.2.3**) is the pulsed frequency-domain experiments, where a spectrally narrow pump pulse excites the sample and a 2D-IR spectrum is recorded by scanning the pump frequency. The pump pulse can be produced by a Fabry Perot filter, which generates a Lorentzian shaped narrow pulse in the frequency-domain, but an exponentially decaying relatively long pulse in the time-domain.

To achieve a better time resolution and bigger signal sizes another implementation for the 2D-IR spectroscopy was used, the time-domain Fourier transform 2D-

IR spectroscopy [83, 124, 125]. In the time domain Fourier transform experiment not only one pump pulse is generated, but two. The pump light of the second OPA (10 μJ) is guided into an interferometer with a flexible arm (**figure 3.3.2**), which produces a pair of intense pump pulses with a tunable time delay called the coherence time. The interferometer arm is continuously moved during data acquisition to scan the coherence time. A part of the mid-IR output of the interferometer is collimated onto a pyroelectric detector to record interferograms of the pump pulse pair during every scan of the interferometer from which the relative phase of the pump pulses is determined. About 2 cm above the mid IR pathway the beam of a HeNe laser is also guided through the interferometer and its interference is observed with two photodiodes. This way the delay change of the pump pulses is traced [232]. The two pulses are guided along a flexible delay line to adjust the population time (time between pump pulses and probe pulse). Scatter suppression is achieved by a periodic pseudo inversion of the phase between pump and probe pulses, for which a synchronized wobbling Brewster window (ZnSe) in front of the interferometer periodically modulates the population time of the pump beams by half of a period of the mid IR central frequency $t \pm \frac{\pi}{\omega_0}$. Data at a population time of t and $t \pm \frac{\pi}{\omega_0}$ are detected. The modulation is running with one quarter of the laser repetition rate (250 Hz) [232, 233]. Both implementations of a 2D-IR experiment basically provide the same information [124, 125]. In order to suppress contributions from rotational diffusion a magic angle polarization between probe and pump pulses was chosen.

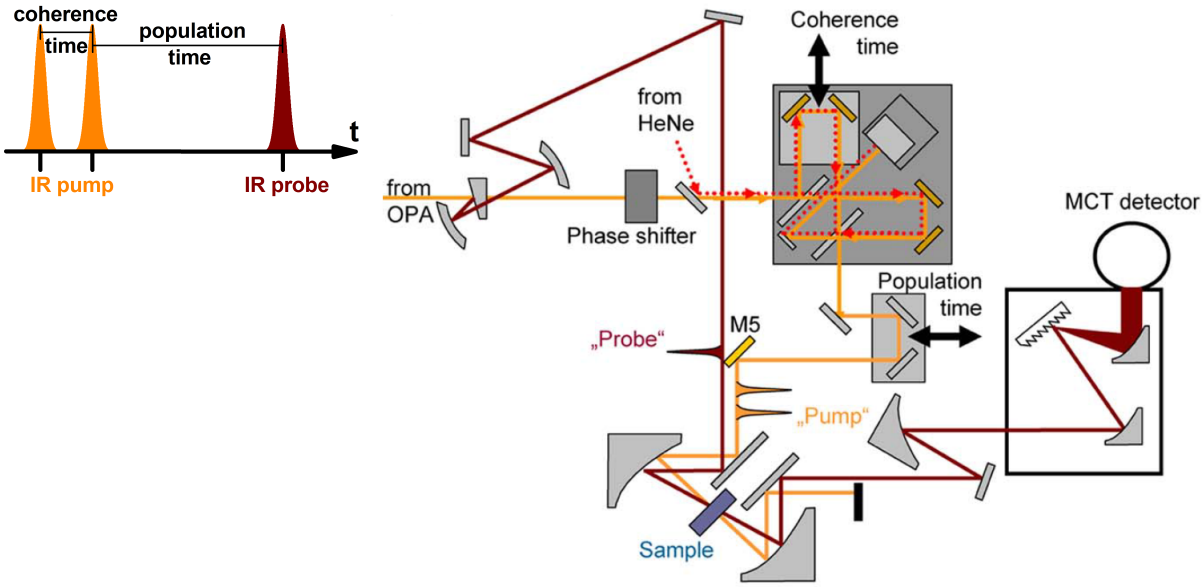

Figure 3.3.2: Fourier transform 2D-IR experiment. **Left:** Fourier transform 2D-IR pulse sequence. **Right:** 2D-IR setup. The pathway of the pump pulses is colored orange and the probe pathway brown. The setup figure was reprinted with permission from Journal of the Optical Society of America B, 28, 171-178, Jan Helbing and Peter Hamm, Compact implementation of Fourier transform two-dimensional IR spectroscopy without phase ambiguity [232].© 2011 Optical Society of America.

For data analysis the spectrum at a population time of -20 ps was subtracted as a background for all data. Since the wavelength calibration of the 210 l/mm grating was incorrect the probe wavelengths were calibrated manually. For this a diagonal line (slope=1) was fitted to the scattering along the diagonal in the 2D-IR spectra of the PDZ3 measurements at 0.1 ps population time. Averaging of the offset of the two axes revealed a value of 40.9 cm^{-1}, which was added to the probe axis wavenumber for calibration.

3.3.1 Aha

In the 2D-IR experiments of upAha, bocAha, and fmocAha in different solvents the same concentrations and path lengths as for the FTIR measurements were chosen. All samples were centrifuged before the 2D-IR measurements to prevent scattering and absorption was controlled via FTIR before the experiment. The temperature was set to RT or 8 °C as denoted.

3.3.1.1 Data Analysis

In case the azide signal have already vanished at the last population time, the spectrum of the latest time point was subtracted to correct for heating of the solvent. For the measurements in H_2O, D_2O, and CCl_4 a 5th order-polynomial was fitted to the spectrum along the pump axis at every probe pixel (signal region excluded) and subtracted from the data to additionally correct for solvent heating.

Vibrational lifetimes were analyzed by global analysis using a MATLAB based toolbox [187]. A global analysis with a sequential model and four components was performed on the pump cut (probe spectrum at one pump wavenumber) at the probe minimum at different population times. The same was done for the sum of the pump slices in the signal range to ensure that none of the components originates from spectral diffusion. As a second analysis method for the vibrational lifetimes, a two dimensional Gaussian was fitted to the bleach signal and its amplitude and its volume were determined. The time evolution of the amplitude and volume were extrapolated with a biexponential function to reveal the vibrational lifetimes.

In order to analyze the line shape, a Gaussian was fitted to every pump slice in the region of the bleach signal at each population time (borders were set to approximately FWHM). Then a line was fitted along the maxima of these Gaussians. The decay of the inverse slope of this line was extrapolated with a monoexponential function including an amplitude and a linear offset. For this analysis a MATLAB based line shape analysis toolbox was used, which was written by Sebastian Lenz in course of a lab internship [234].

3.3.2 PDZ3-Aha

A path length of 100 μm was chosen for the PDZ3 samples with and without ligand. The PDZ3 concentration was set to 10 mM and the Hepta concentration to 15 mM. The samples were centrifuged before the measurements to prevent scattering and an FTIR spectrum was recorded as a control. For the 2D-IR measurements the temperature was adjusted to 8 °C.

3.3.2.1 Data Analysis

Data were processed the same way as the Aha data in aqueous solution. The last time point was subtracted and a polynomial of 5th order was fitted to the spectrum along the pump axis at every probe pixel (signal region excluded) and subtracted from the data to additionally correct for solvent heating.

For vibrational lifetime analysis also the MATLAB based global analysis tool-box was used [187] with a sequential model and four components. The pump cut at the wavenumbers of the maximum of the fitted psVoigt functions of the FTIR data was used. As the spectral resolution of the 2D-IR data is lower (*ca.* 3.9 cm^{-1} in this spectral range) than that of the FTIR data (1 cm^{-1}) and the calibration is slightly shifted, the pump pixel with the next larger wavenumber than the psVoigt maximum wavenumber was used for the global analysis.

For the line shape analysis also the toolbox of Sebastian Lenz [234] was employed with the same proceeding as for the Aha 2D-IR data.

3.4 Vibrational Energy Transfer

3.4.1 Experimental Setup

A similar laser setup as for the 2D-IR measurements was used for the VET experiments: a 3 W Titan:Sapphire oscillator/regenerative amplifier laser system from Spectra Physics (Millennia, Tsunami, Empower pump laser, Spitfire Ace) with a repetition rate of 1 kHz, a wavelength of 800 nm, and a pulse duration of 100 fs (FWHM) was utilized to run two two-stage home-built OPAs. The OPA, which generates the probe/reference beam, was combined with a DFG in order to generate mid IR light. The mid IR light from this OPA was split into a probe and a reference beam, which were guided through the sample, dispersed with a spectrometer (Triax 180, HORIBA Jobin Yvon, 150 l/mm grating), and detected on a 2x32 pixel MCT detector (Infrared Associates). The probe beam detects the sample spectrum

and the reference beam is used to correct for fluctuations of the MIR pulses. The detector signal was amplified and integrated via a home-built electronic. To achieve running times of over 50 hours of the detector, a home-built automatic liquid nitrogen refilling system was used [231]. In the second OPA the *Signal* beam from the second stage of the optical parametric process was frequency doubled with a type I BBO crystal. Tunable light in the range of 613 nm was generated. To separate the remaining *Signal* light from the 613 nm light, a 600 nm bandpass filter was used in the former work of Henrike M. Müller-Werkmeister [70, 78]. However, the quantity of 613 nm light absorbed by this filter was relatively high. In order to enhance the amount of 613 nm light available for the experiment, this filter was replaced by a series of 6 dichroic mirrors (Layertec GmbH: 108634; HR s,p 400-700>99.7). The amount of 613 nm light used to pump the sample was adjusted with an ND filter wheel. A mechanical chopper blocked every other pump pulse such that the pump-on/pump-off difference spectrum was obtained. The polarization of the pump pulse was set to magic angle with respect to the probe pulse via a half-wave plate/polarizer combination in order to suppress contributions from rotational diffusion. The lens, which focuses the pump pulse into the sample was replaced by a lens with a longer focal length (Thorlabs: LA4184; f=500 mm) to gain a more proper focus (diameter 200 μm).

The sample was placed between two CaF_2 windows, which are separated by a Teflon spacer giving the sample thickness. This sample cell was placed in a home-built movable sample holder (picture see **figure 4.3.2**). The sample cell is rotated (motor: RS Components GmbH: 399-0035, 24vdc, 485rpm) and moved upwards and downwards (motor: Newport Spectra Physics GmbH: CONEX-LTA-HL) during the VET measurement. This way the sample volume, which is excited, is exchanged between the laser shot and the whole sample volume is used. Protein denaturation and bleaching are retarded.

The spatial overlap between the pump and the probe beam was adjusted with a DiPe test sample. This way the VET signal size could be checked before each measurement. The pump beam is mechanically blocked behind the sample and additionally by a filter to prevent a contribution of scattered pump light to the measured signal via a higher order reflection of the spectrometer. The time zero between pump and probe pulse was determined before every measurement using the cross phase modulation signal in water.

For the VET measurements of AzuLig and Ile341Aha+AzuLig in the amide I, histidine, and amide II region the probe OPA was set to a central wavenumber of 6135 nm, 6470 nm, and 6803 nm, respectively. The pump pulse was temporally stretched via two CaF_2-rods to a pulse duration of about 550 fs. The pump pulse's energy was set to 12 μJ.

With this measurement conditions also the first Aha VET signal of Ile327Aha+ AzuLig was measured. Additional optimization of the laser setup was required to

improve the data quality and obtain an Aha VET signal for mutants with a larger distance between heater and sensor. The CaF_2-rods were removed to receive a pump pulse, which is shorter in time (pulse duration *ca.* 200 fs FWHM) and gives a sharper starting point for the VET. To prevent sample damage, the pump power was reduced to 6 μJ. Furthermore, the path of the light from the probe/reference beam was changed to gain more light at the detector and improve signal to noise ratio. Previously, the main part of the light from the probe OPA was split off using a BaF_2 wedge. This part of the mid IR light was not further used for the VET measurements and was, therefore, wasted. The beam path was exchanged by a path with an IR beamsplitter to divide the mid IR pump light into the probe and the reference part (see **figure 4.3.3**). This way, the biggest part of the light from the OPA could be used for the measurement, which was about 0.2 μJ for each beam. Focus sizes of 66x60 μm and 86x65 μm FWHM for probe and reference beam at the sample were measured after the rebuilding.

For the VET measurements in the azide region, the probe OPA was set to a central wavenumber of 4735 nm and a pulse energy of 6 μJ was used for the majority of experiments. After necessary reparation of the laser system, the size of the Aha VET signal was smaller and, therefore, the pump energy needed to be increased to 8 μJ for the measurements afterwards (Gly329Aha+AzuLig and Ile341Aha+AzuLig(2)) to achieve the same signal sizes for the DiPe test sample than before. For the measurement recorded later (Ile341Aha+AzuLig(3), Gly322Aha+AzuLig, Ala367-Aha+AzuLig(2), Lys380Aha+AzuLig, WT+AzuLig(3), and VETLig in GdmCl) the pump energy was reduced to 6 μJ again, but the measurement quality and the signal sizes were worse for these data compared to the data measured before.

The analysis of the VET data was carried out with MATLAB R2012a. The spectrum at a delay of -20 ps between pump and probe pulse was subtracted as background. For the VET measurements in the Aha region, a representative water heating signal was calculated by averaging all spectra at long delays (data points after 54 ps), at which the observed VET signal is solely caused by water heating. This averaged water signal was fitted with an amplitude and an offset to the spectra at every single population time and subtracted. The Aha VET signal remained. In order to compress the information of the Aha VET signal and reduce noise, the probe pixel containing the signal were summed to get time dependent amplitude transients. To prevent signal cancellation, the pixels with a positive Aha signal were added and pixels with a negative Aha signal were subtracted.

3.4.2 Samples

All samples were centrifuged before the VET measurements to prevent scattering. UV-Vis (Hitachi U-2000 spectrophotometer) and FTIR (Burker Tensor 27 FTIR

spectrometer) spectra of the mounted VET samples were measured directly before each VET experiment.

3.4.2.1 Peptides

The solvents, concentrations, and spacer thicknesses of the peptide samples are summarized in **table 3.6**. For the VETLig H_2O GdmCl measurements 8 M guanidine hydrochloride (GdmCl) were added to the sample.

In the case of the VETLig in D_2O, the probe OPA central wavenumber was set to 4800 nm instead of 4735 nm to achieve a more ideal illumination of the detector.

Table 3.6: Composition of the peptide VET samples.

sample	solvent	% DMSO	$c_{peptide}$	spacer thickness
DiPe	H_2O	2	*ca.* 10 mM	94.3 μm
VETLig H_2O	H_2O 50mM NaPi	2	*ca.* 5 mM	94.3 μm
VETLig H_2O GdmCl	H_2O	2	*ca.* 10 mM	94.3 μm
VETLig D_2O	D_2O	6	*ca.* 10 mM	150 μm

3.4.2.2 PDZ3-Aha

VET in Azide Region

The protein concentration of the PDZ3-Aha+AzuLig samples was adjusted to 10 mM according to the Lowry assay. The AzuLig concentration was initially set to 13 mM according to its UV-Vis absorption. However, due to the impurity of AzuLig with shorter N-terminal fragments, the real AzuLig concentration was lower than the protein concentration (for detailed analysis see **chapter 4.3.4.4**). A 94.3 μm Teflon spacer was used for setting the sample thickness. AzuLig was predissolved in DMSO and added to the protein solution resulting in a volume fraction of 2 % DMSO in the 50 mM NaPi H_2O pH 6.8 buffer.

VET in Amide Region

For the measurements in the amide I, His, and amide II region a D_2O 50 mM NaPi buffer, pD 7.2, containing 6 % DMSO (Ile341Aha+AzuLig)/14 % DMSO (AzuLig) and a sample thickness of 50 μm was used. For the Ile341Aha+AzuLig measurements the concentration of Ile341Aha was adjusted to 5 mM according to the Lowry assay and the AzuLig concentration was about 6-7 mM. For the AzuLig VET measurements the AzuLig concentration was about 30 mM, but a part of the sample precipitated during the measurement causing strong scattering.

3.4.2.3 PDZ3-AzAla

The PDZ3-AzAla samples were concentrated to about 10 mM in 50 mM NaPi pH 7.5 buffer with 10 % glycerol. AhaLig was predissolved in DMSO and added to the PDZ3-AzAla sample resulting in a volume fraction of 2 % DMSO. Resulting AhaLig concentrations determined via the Aha FTIR absorption (ε= 375 $cm^{-1}M^{-1}$ [235]) were 3.5 mM and 5.5 mM for the F325AzAla+AhaLig and F340AzAla+AhaLig samples, respectively. For the measurement of F325AzAla without ligand 2 % pure DMSO were added.

3.5 Software for Data Analysis

The following software was used for data analysis: MATLAB R2012a, OriginPro 8.5.0G SRO, Pymol 1.3, UCSF Chimera 1.6.2, LabView 16.0f6 (64-bit), and OPUS 6.5.

Chapter 4

Results & Discussion

4.1 Azidohomoalanine

Since Aha is our IR reporting ncAA of choice to detect site-resolved information within a protein, it is essential for the data interpretation to understand Aha's solvatochromism and vibrational dynamics in diverse solvents displaying different local environments. Therefore, a broad set of 16 solvents with distinct properties was chosen to investigate its effect on vibrational wavenumber, band shape, vibrational lifetime, and spectral diffusion of three different Aha derivatives, unprotected Aha (upAha), bocAha, and fmocAha (structures in **figure 4.1.3**).

4.1.1 Solvatochromism of Aha

Some of the pictured FTIR spectra were measured by Christian Bonifer, supervised by the author, during a practical course [236], which was part of his chemistry master degree program.

4.1.1.1 Concentration Effects

FTIR spectra of all soluble Aha/solvent samples were measured at different concentrations to exclude concentration dependent effects onto the azido's asymmetric stretching wavenumber and band shape. Only in two very nonpolar aprotic solvents (PCE and CCl_4) these effects were found (**figure 4.1.1**). In cases in which there was change in the IR band at the lower concentration, the sample was further diluted to proof that a concentration is achieved at which no further changes upon dilution occur. The spectra of fmocAha in CCl_4 (**figure 4.1.1 top right**) at different concentrations clearly reveal a discrepancy in the band maximum position

and shape. A very similar picture shows for fmocAha in PCE (**figure 4.1.1 bottom right**). At a higher concentration of fmocAha, the absorption band seems to be strongly affected by intermolecular interactions among the fmocAha molecules such as dimerization or clustering. For further data analysis the spectra at the lower concentration were used to exclude these influences on the vibrational band. In contrast, the absorption band of bocAha in CCl_4 (**figure 4.1.1 top left**) is independent of the solute concentration. However, in PCE the absorption band of bocAha consists of multiple bands (**figure 4.1.1 bottom left**), whose pattern is not reproducible. Another kind of incident seems to occur there. Hence, these data were excluded from further analysis.

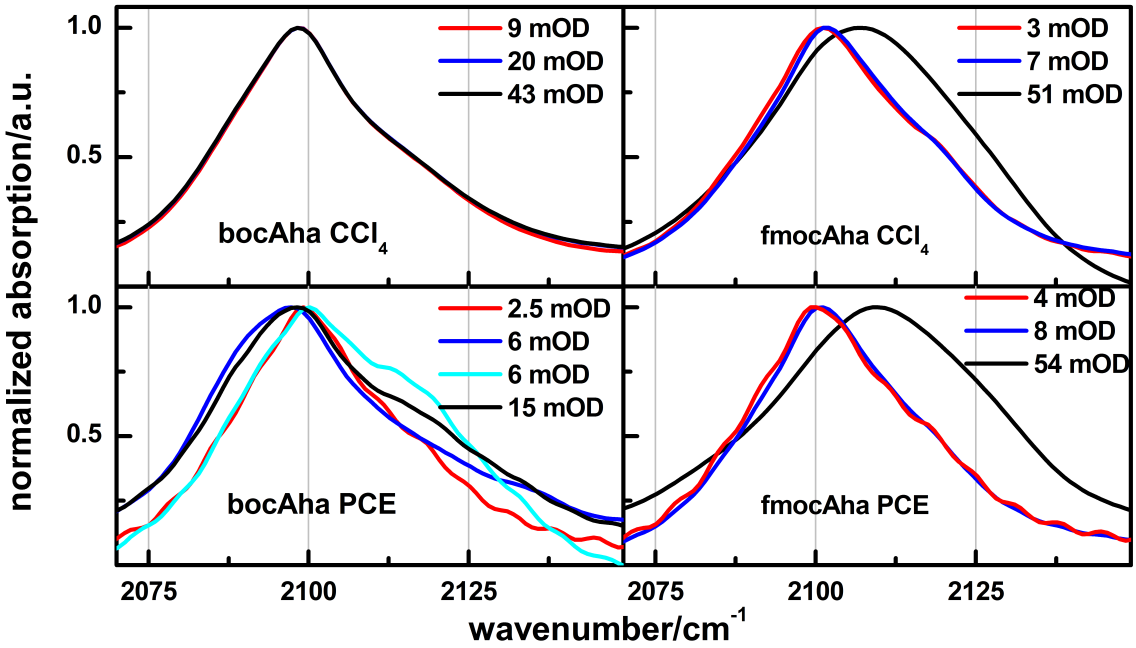

Figure 4.1.1: FTIR spectra of bocAha and fmocAha in varying concentrations dissolved in PCE and CCl_4. Spectra are normalized (arbitrary numbers - a.u.) and their original signal size is denoted in the legend in mOD, which scales with the concentration.

4.1.1.2 Different Solvents

The measured FTIR spectra of all evaluable Aha/solvent samples are plotted in **figure 4.1.2** (grouped by solvent) and **figure 4.1.3** (grouped by solute). It is striking that many bands show asymmetries with a pronounced flank on their blue site (at high wavenumbers). In some cases even a small additional band at about 2150 cm^{-1} can be seen. This phenomenon is specially distinct for upAha. This band has not been assigned yet, but since no cross peak was detected in the 2D-IR measurements (see **chapter 4.1.2**), it is unlikely to be caused by Fermi resonance.

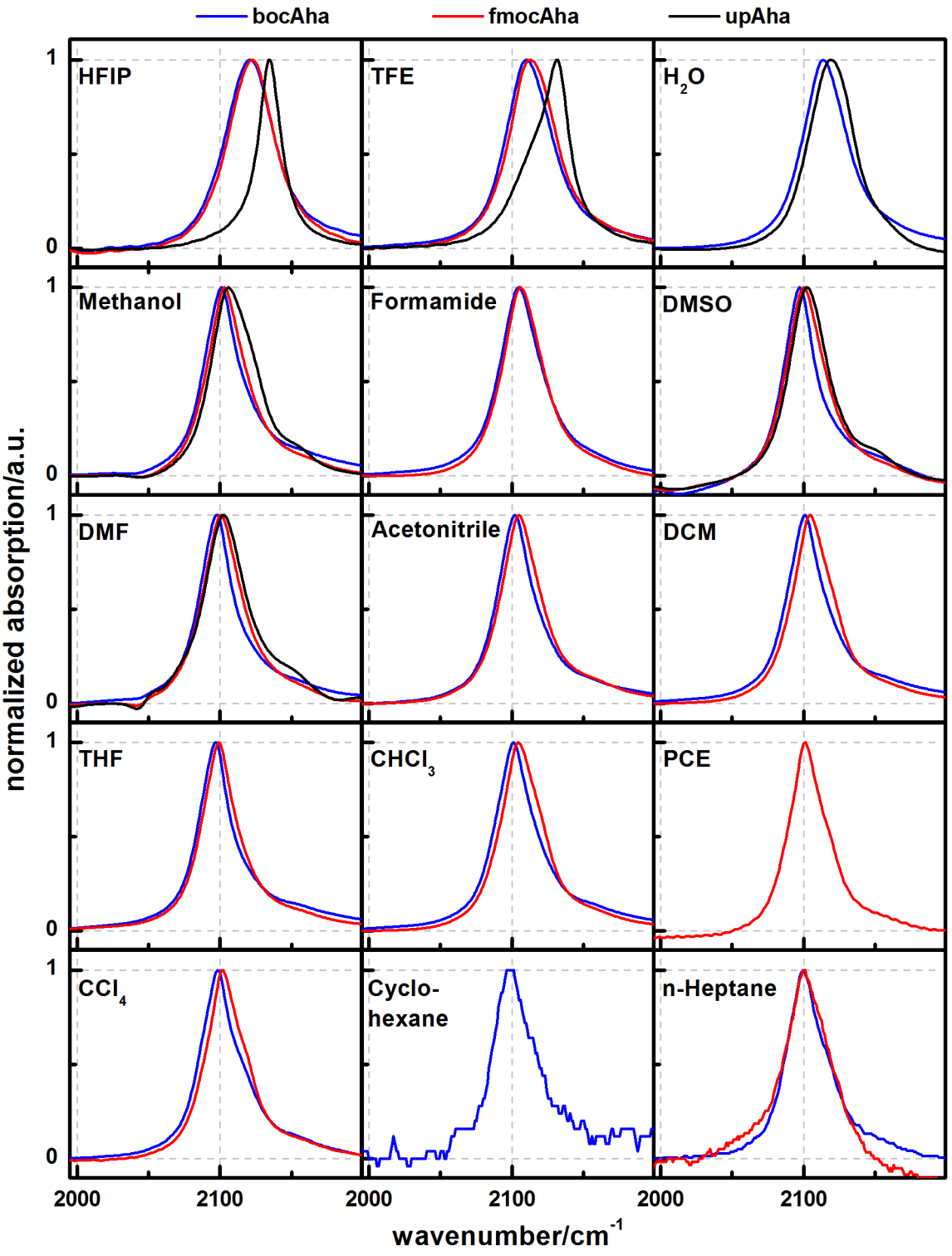

Figure 4.1.2: Asymmetric stretching band of bocAha, fmocAha, and upAha in different solvents sorted by the solvent.

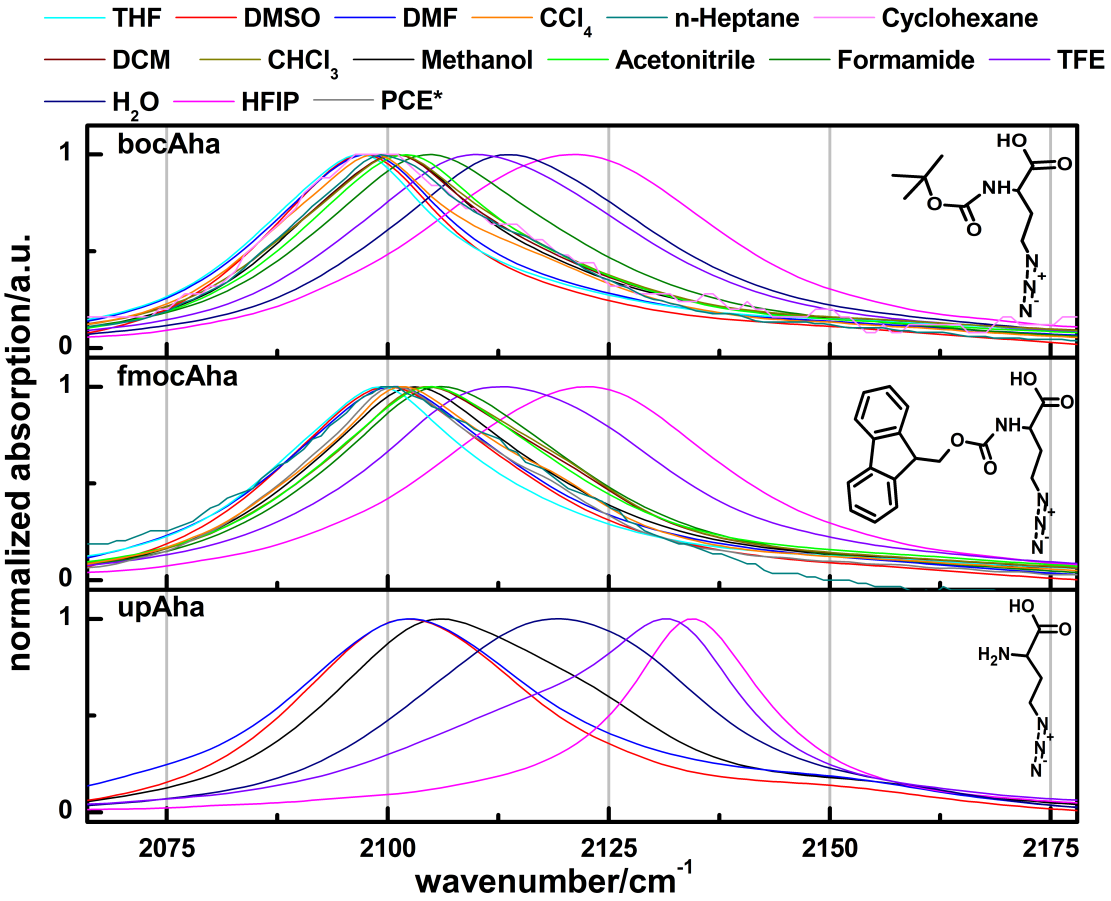

Figure 4.1.3: Structure of bocAha **(top)**, fmocAha **(middle)**, and upAha **(bottom)** and its asymmetric stretching band in different solvents sorted by the solute. The solvent legend is sorted by the order of the band position of bocAha in this solvent (from left to right).

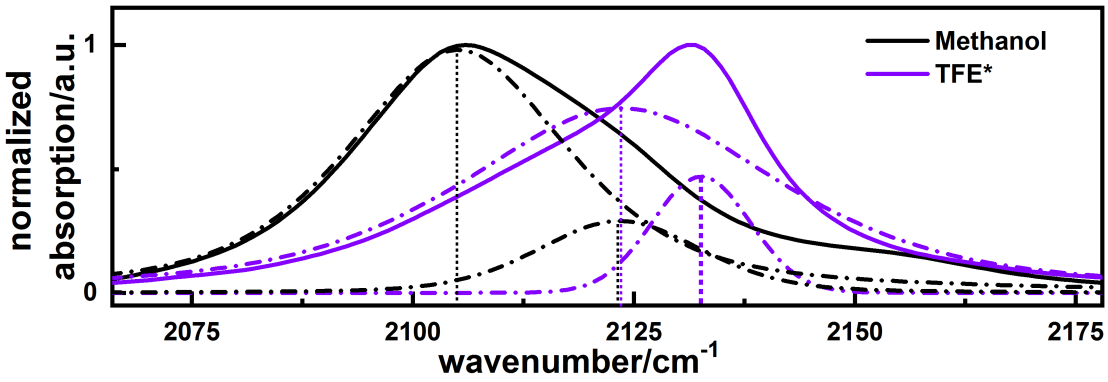

Figure 4.1.4: Fit of the two peaks of the upAha azide band in methanol and TFE.

In addition to this small side band in the flank, the main band of upAha in methanol and TFE, which are both relatively strong protic solvents, consists of two large partially overlapping sub bands (**figure 4.1.4**). One peak shows similar characteristics in position and shape with the bands of bocAha and fmocAha in the same solvent.

The second peak is strongly blue shifted and much narrower. This might be due to different conformations and is discussed further below. For upAha in methanol the peak on the red side (at low wavenumbers) is more pronounced and in TFE it is vice versa. For upAha in HFIP only one narrow band at a very high wavenumbers is detected.

4.1.1.3 Solvent Mixtures

FTIR spectra of upAha and bocAha in DMSO/H_2O and THF/H_2O mixtures were measured and the wavenumbers of the band maximum position (band maximum) were compared (**figure 4.1.5**). Despite an offset, both Ahas show a similar dependency of the band maximum on the H_2O content. In the DMSO/H_2O as well as in the THF/H_2O mixture a concave progression is observed with the THF/H_2O graph being more curved. This curve shape could be caused by selective clustering of aprotic solvent around the Aha molecules. The measured curve shapes are in accordance with the literature, even though the degree of curvature varies with the used aliphatic azido compound [90, 147, 184].

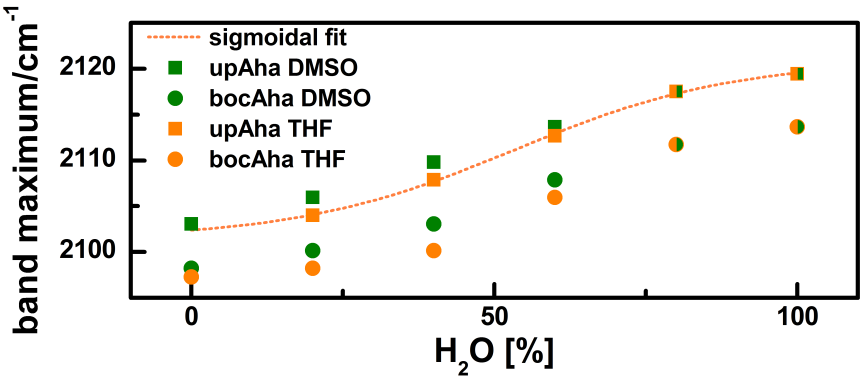

Figure 4.1.5: Band maxima of upAha (squares) and bocAha (circles) in a DMSO/H_2O (green) and a THF/H_2O (orange) mixture in dependency on the H_2O content of the sample. The dotted line gives a sigmoidal fit of the upAha data in the THF/H_2O mixture.

UpAha is not soluble in the most aprotic solvents and data are lacking. In order to gain an additional data point for upAha in aprotic solvents, a sigmoidal curve was fitted to the THF/H_2O data to estimate the band maximum of upAha in 0 % H_2O (*i. e.* in THF).

4.1.1.4 Band Position

From the FTIR spectra of the Aha/solvent samples the band maxima were picked to analyze the influence of different solvent properties on the band position (**figure 4.1.6**, **table 4.1**). Data for AzPen* from Wolfshorndl *et al.* [184] were added to

compare an aliphatic azide, which is simple composed, to Aha containing amino acids.

In **figure 4.1.6 a**, it becomes clear, that for all aprotic solvents the band maximum is at a similar position for each azido compound regarded. Only small blue shifts (4-6 cm^{-1}) could be obtained in acetonitrile, DCM, and $CHCl_3$ compared to the other aprotic solvents. In protic solvents on the other hand much bigger solvatochromic shifts are found, also strongly deviating between the different azido compounds. **Figure 4.1.6 b**, in which the band positions are "normalized" to the band maximum of the bocAha/solvent samples, gives a better view onto the band position of the four compounds with respect to the moiety bound to the azido group. In aprotic solvents all bands of fmocAha are slightly blue shifted in a similar way compared to the ones of bocAha in the same solvent whereas the bands of AzPen* are used to be slightly red shifted compared to bocAha.

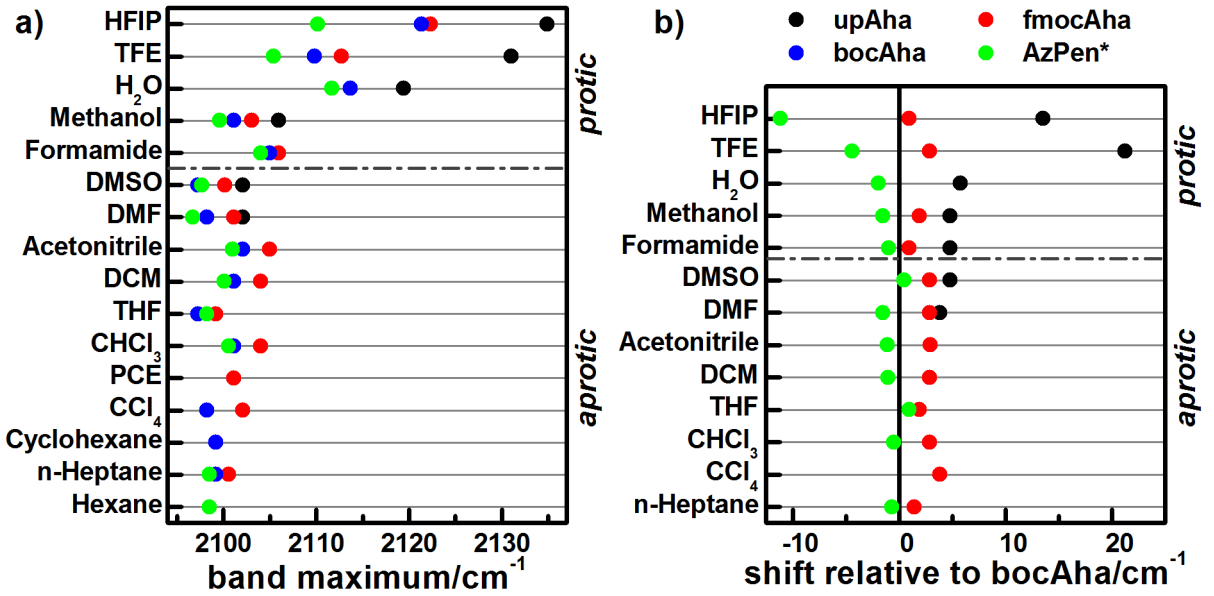

Figure 4.1.6: Aha band maxima. **(a)** Band maxima of the different Aha/solvent and AzPen*/solvent samples in comparison. **(b)** Difference between the band maxima of bocAha and upAha/fmocAha/AzPen* in respective solvent. For both figures the data for AzPen* are taken from Wolfshorndl *et al.* [184], the protic solvents **(top)** are sorted descending by their hydrogen bond donor acidity and the aprotic solvents **(bottom)** are arranged descending by their dielectric constant.

However, in protic solvents, particularly in strongly hydrogen bonding ones, the positions of the band maxima are strongly differing and highly dependent on the moiety bound to the azido group. The AzPen* band is much less blue shifted in halogenated strongly protic solvents compared to the Ahas. The trend in the band position of bocAha and fmocAha is similar, but even for the upAha, which only deviates in having an unprotected amine group, a big discrepancy to the protected

Ahas was detected. This effect could be correlated to the observed additional narrow and stronger blue shifted peak of upAha in methanol, TFE, and HFIP. The lower-wavenumber peak in methanol and the higher-wavenumber peak in TFE are chosen to depict the band maximum.

Table 4.1: Collection of the measured band maxima of all Aha/solvent samples. The value for upAha in THF (in brackets) is an estimated value.

solvent	upAha/cm^{-1}	fmocAha/cm^{-1}	bocAha/cm^{-1}
HFIP	2134.9	2122.3	2121.4
TFE	2131.0	2112.7	2109.8
H_2O	2119.4		2113.7
D_2O	2119.4		
Methanol	2105.9	2103.1	2101.1
Formamide		2105.9	2105.0
DMSO	2102.1	2100.1	2097.3
DMF	2102.1	2101.1	2098.2
Acetonitrile		2105.0	2102.1
DCM		2104.0	2101.1
THF	(2102.4)	2099.2	2097.3
$CHCl_3$		2104.0	2101.1
PCE		2101.1	
CCl_4		2102.1	2098.2
Cyclohexane			2099.2
Heptane		2100.6	2099.2

This additional strongly blue shifted band of upAha in methanol, TFE, and HFIP might be caused by a second structural conformation. As the only disagreement between the Ahas is the existence/absence of the protection of the amide group it could be suggested that protonation/deprotonation of the amino group might play a role for this second conformational state. Protonation has also been suggested previously to be the reason for an arising second blue shifted band in the IR spectrum of an N-terminal Aha in a small protein domain (NTL9) at a lower pH value [100]. To check this assumption FTIR spectra of upAha in aqueous buffer at pH values from 4 to 10 were recorded (**figure 4.1.7**). Only a very small shift in the band maxima caused by the protonation/deprotonation of the amino group is found. Therefore, protonation can be excluded to be the reason for the two bands of upAha in stronger protic solvents. Also for the previously published double band of N-terminal Aha in NTL9 the shift is likely caused predominantly by changed intramolecular interactions of the azido group with the backbone or small structural changes of the protein and not by the electrostatic effects of protonation alone [101].

Possible explanations for the second state of upAha in strongly protic solvents are altered intramolecular interactions and a changed arrangement of intermolecular hydrogen bonds to the solvent. As mentioned in **chapter 2.4.1** theoretical studies predicted that the solvatochromic shift of an N_3Ala dipeptide and Aha in NTL9 in H_2O is a delicate balance of blue- and red-shifting contributions of the hydrogen

bonding interactions with solvent molecules, intramolecular hydrogen bonding between the inner N-atom of the azido group and the N-terminal amide H-atom, and intramolecular electrostatic interactions between the azido group and the carbonyl O-atom [172, 176, 177]. For upAha compared to bocAha/fmocAha the absence of a protection group might lead to a different conformation of the solvent around the upAha with another angle distribution of upAha/solvent hydrogen bonds and might also cause changes in intramolecular interactions.

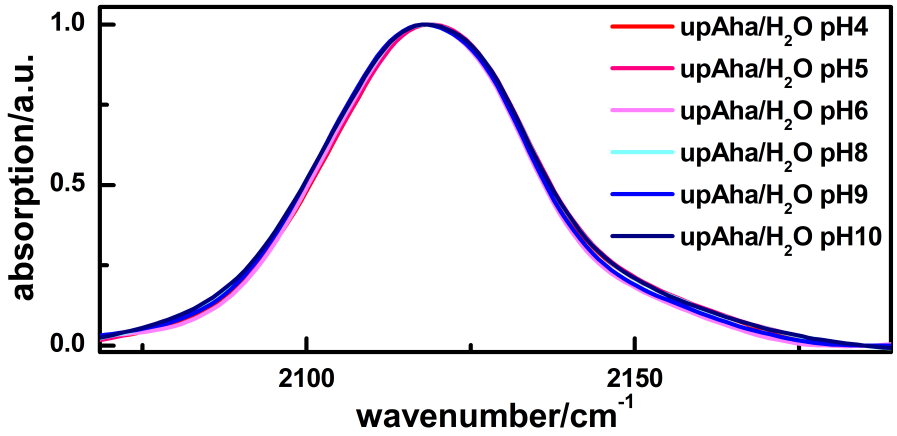

Figure 4.1.7: FTIR spectra of the asymmetric stretching vibration of upAha in H_2O at different pH values.

4.1.1.5 Band Shape

Table 4.2: FWHM of the asymmetric stretching band of the three Ahas in different solvents. The protic solvents (**top**) are sorted descending by their hydrogen bond donor acidity and the aprotic solvents (**bottom**) are arranged descending by their dielectric constant.

solvent	upAha/cm^{-1}	fmocAha/cm^{-1}	bocAha/cm^{-1}
HFIP	20.0	37.8	39.6
TFE		37.9	37.4
H_2O	37.5		36.0
Methanol		32.2	30.9
Formamide		33.6	34.9
DMSO	33.8	34.0	33.4
DMF	37.3	33.3	29.7
Acetonitrile		33.5	31.6
DCM		33.3	32.0
THF		29.6	28.0
$CHCl_3$		33.3	32.5
PCE		31.4	
CCl_4		32.4	33.6
Cyclohexane			
Heptane			33.2

Besides the band position, also the band shape and especially its width were analyzed. Fitting a pseudo Voigt function to the asymmetric stretching vibration revealed that the bands are almost exclusively Lorentzian shaped and, thus, a Lorentzian was used to estimate the FWHM (**table 4.2**). Bands with two peaks were excluded from the analysis. The FWHM of all Ahas are in a similar range (29-40 cm^{-1}), except the FWHM of upAha in HFIP (20 cm^{-1}). Overall the band widths in protic solvents are a bit broader than in aprotic ones and increase with the hydrogen bond donor acidity of the solvent. This might be caused by a larger variation in possible conformational sub states caused by hydrogen bonding.

4.1.1.6 Kamlet-Taft Model

In order to further analyze the band maxima of the Ahas and its correlation to solvent properties, two theoretical models are applied.

Linear solvation energy relationship links solvent properties to many types of physiochemical properties and reactivity parameters, *i. a.* absorption and fluorescence frequency, NMR chemical shift, reaction rate, equilibrium constant, enthalpy, *etc.* [237–240]. A frequently used model is the Kamlet-Taft relationship, which is based on a set of empirically determined solvatochromic parameters (**equation 4.1.1**).

$$XYZ_{KT} = XYZ_0 + a \cdot \alpha + b \cdot \beta + s \cdot (\pi^* + d \cdot \delta) + h \cdot \delta_H + e \cdot \xi \tag{4.1.1}$$

XYZ is the physiochemical property measured and XYZ_0 gives a constant offset. α is a measure of the solvent hydrogen bond donor acidity and describes the solvent's ability to donate a proton in a solvent-to-solute hydrogen bond. β scales the solvent hydrogen bond acceptor acidity, the ability to accept a proton/donate a free electron pair in a hydrogen bond. π^* is an index of the solvent's dipolarity/polarizability and δ gives a solvent class dependent polarizability correction factor. The Hildebrand solubility factor δ_H describes the change in solute-solvent interactions caused by creation of a cavity and is important when monitoring chemical reaction. ξ is a scale for the coordinate covalency, which is diverse for different types of bases. a, b, s, d, h, and e are the fitted coefficients, which give the relative susceptibility of XYZ to the correlated solvent property scale [237–240]. Suitable to the observed sample and its physiochemical properties the relationship is reduced to the required terms. In case of the solvatochromic shift of the vibrational frequency of aliphatic azides the Hildebrand solubility factor is negligible. As the aliphatic azido group itself is just a hydrogen bond acceptor and not a donor, only the hydrogen bond donor acidity of the solvent plays a role and $b \cdot \beta$ and $e \cdot \xi$ can be neglected. Since no aromatic solvents are used and also the parameter is not certain, the polarizability correction factor is neglected, too. This results in:

$$\tilde{\nu}_{KT} = \tilde{\nu}_0 + a \cdot \alpha + s \cdot \pi^* \tag{4.1.2}$$

a, s, and $\tilde{\nu}_0$ are fitted to achieve minimal aberration of the Kamlet-Taft wavenumber ($\tilde{\nu}_{KT}$) and the experimentally observed band maximum ($\tilde{\nu}_{exp}$) for the three Ahas and also for AzPen*. All methanol/solute data turned out to be outliers. Possible explanations are that the solvatochromic parameters of methanol are inaccurate or that different solvatochromic effects occur in methanol. Therefore, the data of the methanol/solute samples are excluded, preventing perturbation of the fit. After determining the fitting coefficients on the basis of the data for all other solvents, $\tilde{\nu}_{KT}$ for methanol was calculated from these coefficients and added to the diagram subsequently (**figure 4.1.8**).

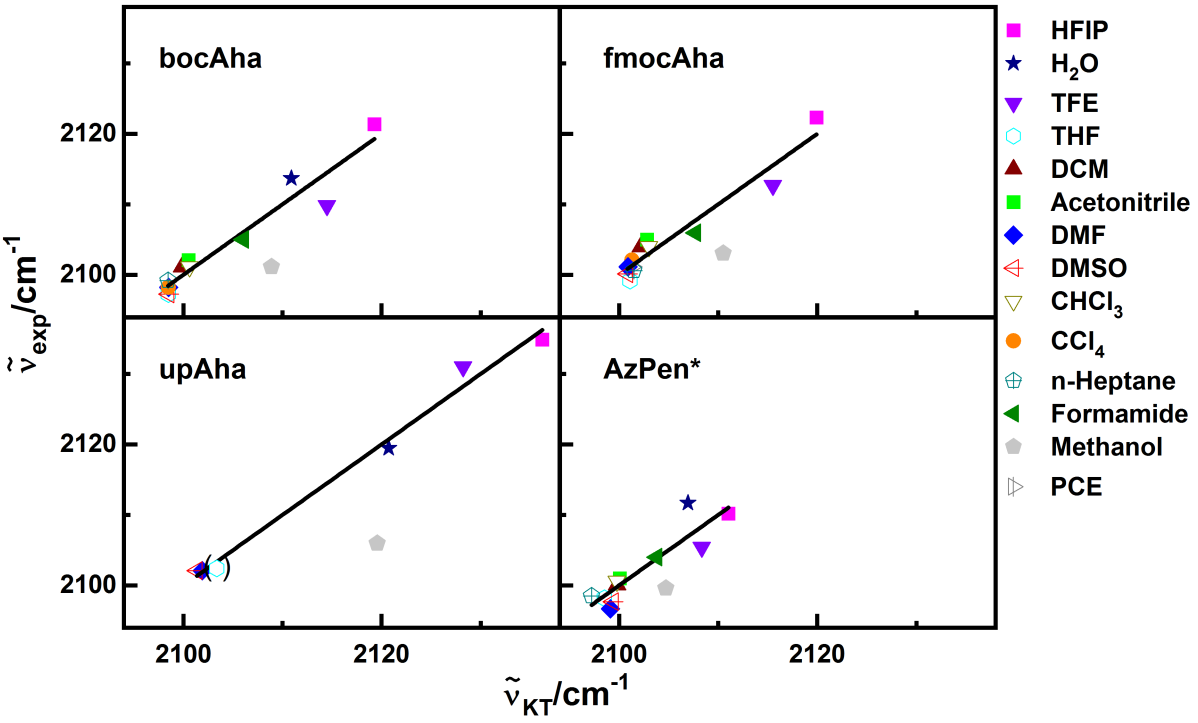

Figure 4.1.8: Kamlet-Taft fit for the three Ahas and AzPen*. The methanol data were excluded from the fit and added later (details see in text). Values for the experimental band maximum for AzPen* are taken from reference [184].

Table 4.3: Fitted Kamlet-Taft coefficients for the aliphatic azides.

	a	s	$\tilde{\nu}_0$/cm^{-1}	R^2
bocAha	11±1	0±2	2098±2	0.93
fmocAha	9.6±0.9	-0.6±0.9	2101±2	0.93
upAha	16±1	-9±2	2111±2	0.99
upAha (+THF)	17±1	-5±2	2106±2	0.99
AzPen*	6±2	2±2	2097±3	0.83

Table 4.3 displays the fitted coefficients and the R^2 value as an index of the fit quality. The prefactor s is very small and close to zero (except for upAha), meaning the band maximum is rarely affected by the dipolarity/polarizability of the solvent. In contrast, the value of a, which gives the susceptibility to the hydrogen donor ability of the solvent, is positive and variable for the four aliphatic azides. This means, that the band maximum of aliphatic azides is impacted by the hydrogen donor ability of the solvent, the strongest effect can be obtained for upAha, followed by bocAha/fmocAha and AzPen*. This totally reflects the trend observed in **figure 4.1.6**. The values for the offset $\tilde{\nu}_0$ are also in accordance with the relative position of the band maximum in aprotic solvents among the aliphatic azides (red to blue: AzPen*, bocAha, fmocAha) as seen above.

The fitting coefficients of upAha are deviating from the other azido compounds. The values in the upper row of **table 4.3** are from a fit with the directly measured $\tilde{\nu}_{exp}$ only. Unfortunately, upAha is only soluble in two aprotic solvents DMSO and DMF, whose π^* values do not differ much. Data points for aprotic solvents (α=0) are missing to correctly estimate the prefactor s. Thus, the band maximum of upAha in THF, calculated from the THF/H_2O mixture, was added to the Kamlet-Taft fit (**table 4.3** row below upAha). The result for a is very similar, but s and $\tilde{\nu}_0$ are differing and they seem to have compensated each other before due to the lack of data points. The newly fitted values seem to be more comparable to the other azido compounds and the fit seems to be more reasonable. Nevertheless, additional data points are still needed to correctly estimate these coefficients for upAha. Hence, the estimated values for upAha need to be considered with care.

4.1.1.7 Onsager Field Theory

As a second model for linear solvation energy relationship the Onsager field theory, which is based on the vibrational Stark effect, was applied to the data of the three Ahas and AzPen*. In the Onsager field theory the solute-induced polarization of the solvent induces an electric field. The electric field is sensed by the solute again involving a change in its vibrational dipole moment $\triangle\vec{\mu}$, which can often be described as Stark tuning rate $|\triangle\mu|$[cm^{-1}(V m^{-1})$^{-1}$] [88, 166, 183, 241, 242] (in case that the angle between the change in dipole moment of vibration $\triangle\vec{\mu}$ and the transition dipole moment direction is zero [85]). The solvatochromic shift of the band maximum $\triangle\tilde{\nu}$ [cm^{-1}] is caused by the vibrational Stark effect and can be described as [85, 166, 183, 241, 242]:

$$\triangle\tilde{\nu} = \frac{-\triangle\vec{\mu} \cdot \triangle\vec{F}_{Onsager}}{h \cdot c} \tag{4.1.3}$$

The solvent field $\vec{F}_{Onsager}$ [V m^{-1}] is given as:

$$\vec{F}_{Onsager} = \frac{\vec{\mu}_0}{4\pi\varepsilon_0 a^3}\left[\frac{2\left(\varepsilon-1\right)\left(n^2+2\right)}{3\left(2\varepsilon+n^2\right)}\right] \tag{4.1.4}$$

With ε - dielectric constant of the solvent, ε_0 - permittivity, n - refractive index of the solute ($n_{methyl-2-azidoacetate} = 1.44$), $\vec{\mu}_0$ - permanent dipole moment of the solute in vacuum ($\vec{\mu}_{0-methyl-azide} = 2.17D$) [243], a - Onsager spherical cavity radius defined as $a = \frac{V\cdot 3}{4\pi}$ with V as Onsager spherical volume $V = \frac{M_W}{\rho\cdot N_A}$ including M_W - molecular weight, ρ - density ($\rho_{methyl-azide} = 0.869g/cm^{-1}$) [243], and N_A - Avogadro constant.

Because the refractive index, the density, and the permanent dipole moment of the Ahas and AzPen* are unknown, substitute values of organic azides (methyl-2-azidoacetate and methyl-azide [243]) were used. Including the molecular weights of all four compounds gives an idea of their different field ranges, even though the calculated solvent fields are not accurate in their values.

Hydrogen bonding is not embedded in the Onsager field theory because this theory only regards the solvatochromic dipole contribution and is, therefore, not accurate enough to describe such close distance interactions, which also involve quadrupole contributions [88]. Therefore, protic solvents must be considered separately. For aprotic solvents hardly any solvatochromic shift in dependency on the solvent field can be found (**figure 4.1.9**). This is very well in accordance with the observed absence of a significant solvatochromic shift caused by the dipolarity/polarizability of the solvent. Three aprotic solvents (acetonitrile, DCM, and $CHCl_3$) show a blue shifted (4-6 cm^{-1}) band maxima compared to all other aprotic solvents, which is not correlated to the solvent field and can also be seen in **figure 4.1.6** as discussed above. Looking at the Kamlet-Taft solvatochromic parameters of these three solvents, a very tiny but nonzero α is found (but not for the other aprotic solvents) [237, 240], which means, that these solvents are actually a bit protic in a Kamlet-Taft picture. This might cause the blue shifted wavenumber compared to the other aprotic solvents. For the other aprotic solvents in total a very small variation of about 2 cm^{-1} was observed.

Only the pure aprotic solvents (α=0) were used to fit a linear curve: $\tilde{\nu} = \tilde{\nu}_0 + |\triangle\vec{\mu}| \cdot \vec{F}_{Onsager}$. **Table 4.4** gives the estimated $\tilde{\nu}_0$ and Stark tuning rates $|\triangle\tilde{\mu}|$ for the different solutes. Despite the very small total shift (2 cm^{-1}) in combination with a spectral resolution of only 1 cm^{-1} and a poor fit quality with a high error range, the results for the Stark tuning rate for all aliphatic azides are in a similar range (1-3·10^{-9} cm^{-1}(V m^{-1})$^{-1}$). Therefore, it is reasonable, that the Stark tuning rate is in fact in this range and that the band maximum is slightly blue shifting with decreasing polarity in aprotic solvents for the Ahas and AzPen*. But it needs to be kept in mind that the value for the Stark tuning rate is not certain and gives only the

trend, because refractive index, density, and permanent dipole moment were taken from substitution compounds. However, compared to methyl thiocyanate (MeSCN) in mostly the same solvents, which shows a total solvatochromic shift of 8.5 cm^{-1} in dependency on the solvent field in aprotic solvents [166], solvatochromic shifts of the Ahas and AzPen* in aprotic solvents are small.

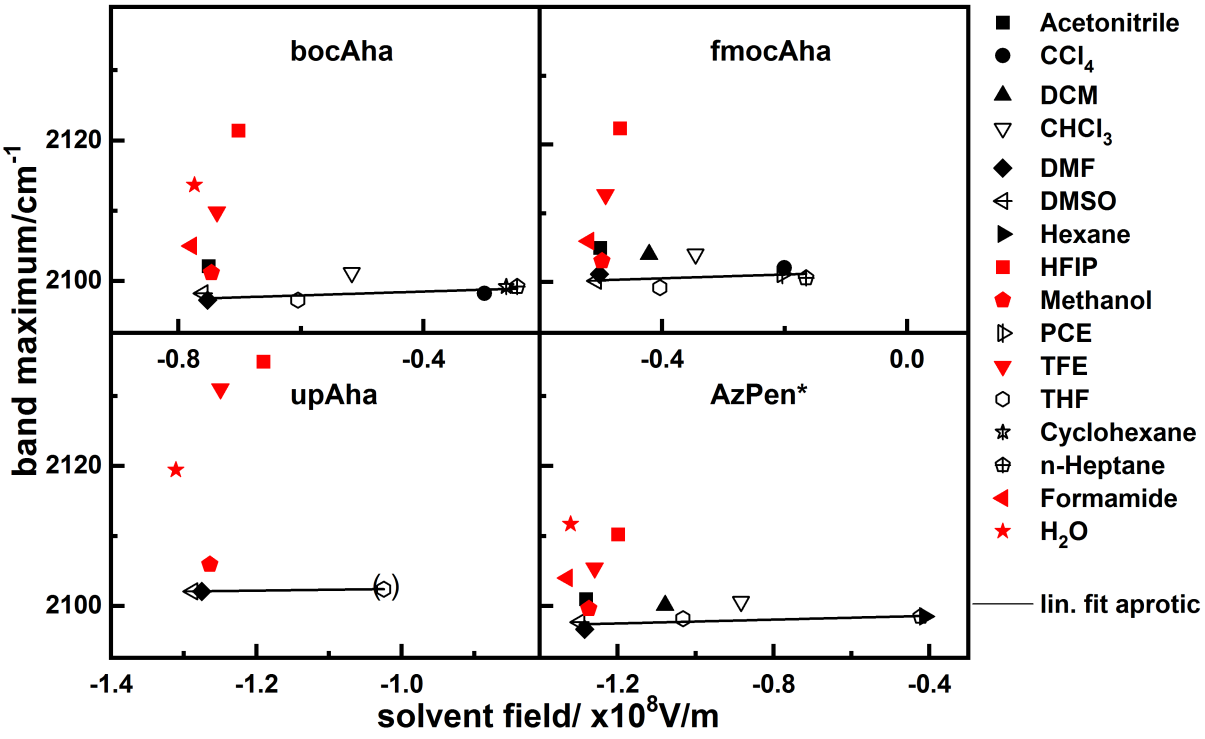

Figure 4.1.9: Onsager plots for the three Ahas and AzPen*. Band maximum of the Ahas and AzPen* in dependency on the solvent field. The data points derived from aprotic solvents are colored black (either filled or unfilled) and from protic solvents red. The data points from the pure aprotic solvents are fitted by a linear curve (black line). The data of AzPen* were taken from reference [184].

Table 4.4: Fitted Stark tuning rates and $\tilde{\nu}_0$ for the aliphatic azides.

	$\tilde{\nu}_0$ /cm^{-1}	$\lvert\triangle\vec{\mu}\rvert$ /cm^{-1}(V m^{-1})$^{-1}$	R^2
bocAha	2099.6±0.6	(3±2)·10^{-9}	0.505
fmocAha	2102±1	(3±3)·10^{-9}	0.002
upAha	2103.7±0.1	(1.2±0.1)·10^{-9}	0.996
AzPen*	2099.1±0.6	(1.4±0.6)·10^{-9}	0.527

4.1.1.8 Hydrogen Bonding

As much bigger shifts of the band maxima are observed for protic solvents than for aprotic ones, hydrogen bonding seems to have a much stronger effect on solvatochromic shifts than dipolarity/polarizability and solvent field for the aliphatic

azides and needs to be treated separately. Wolfshorndl *et al.* [184] analyzed the correlation between the hydrogen bond donor acidity (α), which is a measure of hydrogen bond strength, and the band maximum (**figure 4.1.10 left**). They compared it to the correlation of the hydrogen bond density (ρ) with the band maximum (**figure 4.1.10 right**). Since water exhibits the biggest blue shift for the band maximum of AzPen*, they found the correlation between the band maximum and the hydrogen bond density to fit their data better. It shows a linear dependency, when fluorinated solvents are excluded. They explained this required elimination of the fluorinated solvents by possibly longer-living 1:1 complexes and that these solvents are not biological relevant. They concluded that the N_3 asymmetric stretching vibration is a reporter of local hydrogen bond donor density, a specific water sensor, and a vibrational indicator for hydration [184].

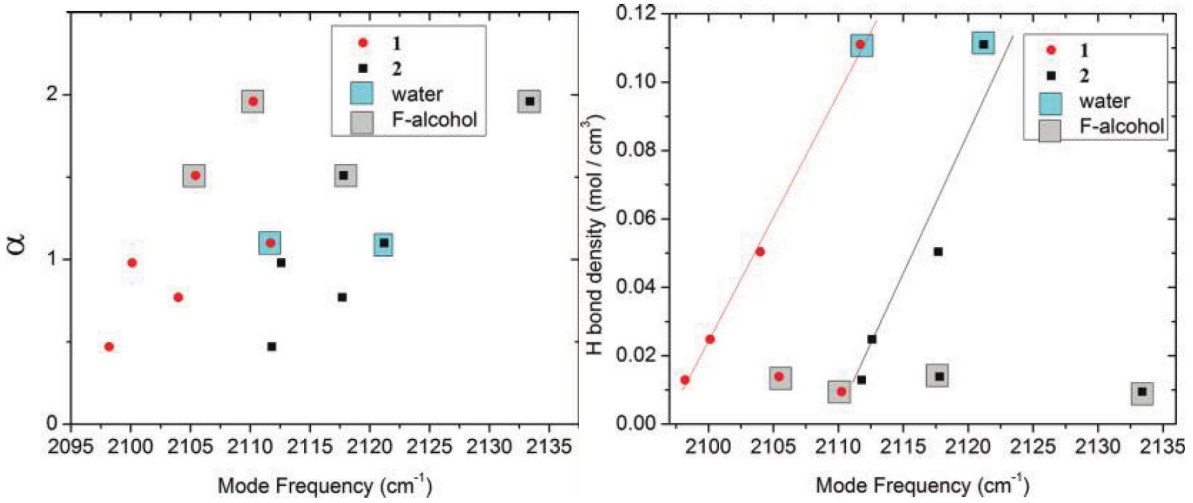

Figure 4.1.10: Dependency of AzPen*'s band maximum on hydrogen bonding. **Left:** hydrogen bond donor acidity of the solvent as a function of the mode frequency (which is the band maximum) of AzPen*. **Right**: hydrogen bond density of the solvent as a function of the mode frequency. 1 (red) is AzPen* and 2 (black) is 3-(*p*-azidophenyl)-1-propanoic acid. Reprinted with permission from The Journal of Physical Chemistry B, 116, 1172-1179, Marta P. Wolfshorndl, Rachel Baskin, Ishita Dhawan, and Casey H. Londergan, Covalently Bound Azido Groups Are Very Specific Water Sensors, Even in Hydrogen-Bonding Environments [184]. Copyright 2012 American Chemical Society.

None of the Ahas shows an outstanding blue shifted band maximum in H_2O. They all reveal the largest shift for HFIP which is the strongest hydrogen bonding solvent. A better correlation between the band maximum and the hydrogen bond donor acidity than for the hydrogen bond density is, therefore, found (**figure 4.1.11**). If the data points of the fluorinated solvents (HFIP and TFE) were excluded analogously to the approach of [184], the remaining 2-3 data points would also inevitably show linear behavior. However, considering all data points as valid information, the relation to the hydrogen bond donor acidity is in better accordance with a linear fit than the correlation to the hydrogen bond donor density. The linear fit gives similar slopes for bocAha and fmocAha and a smaller slope for upAha (**table 4.5**).

Here, again, it can be seen that different aliphatic azido compounds show variable solvatochromic shifts in protic solvents. As discussed above altered orientation, angle, and number of the hydrogen bonded solvent molecules or changes in solute's intramolecular interactions caused by the different moieties bound to the aliphatic azide might be an explanation.

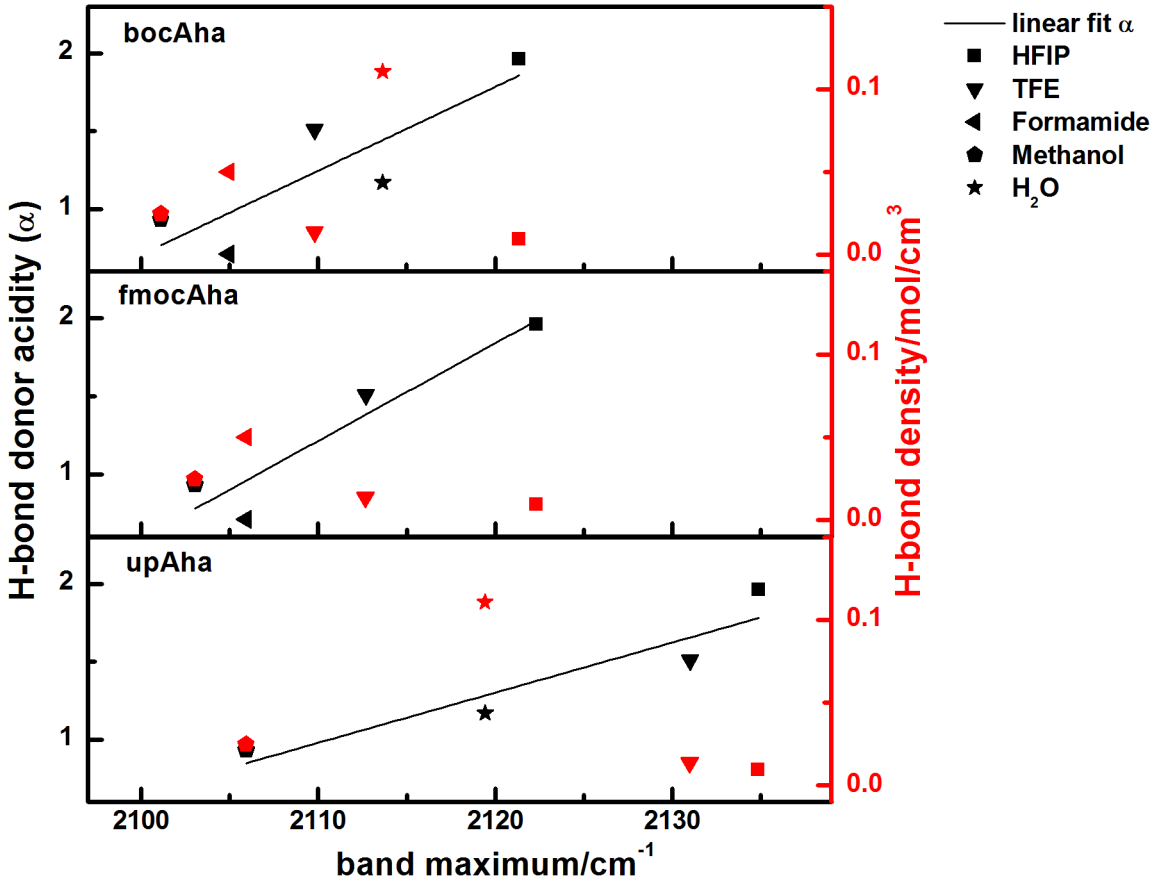

Figure 4.1.11: Correlation of the band maximum of the Ahas with the hydrogen donor acidity (α) (black symbols) and with the hydrogen bond donor density (ρ) (red symbols) and linear fit of the correlation with α (black line).

Table 4.5: Parameters of the linear fit of the correlation between band maximum and the hydrogen bond donor acidity (α).

	slope	R^2
bocAha	0.05±0.02	0.65
fmocAha	0.06±0.01	0.84
upAha	0.03±0.01	0.82

4.1.1.9 FTIR Aha Discussion

Both linear solvation energy relationship models show that the asymmetric stretching wavenumber of Aha and AzPen* is hardly sensitive to the dipolarity/polarizability

of the solvent and the solvent field. In a broad range of solvent fields only a total solvatochromic shift of 2 cm^{-1} was obtained. The observed total solvatochromic shift of upAha (33 cm^{-1}), bocAha (24 cm^{-1}), and fmocAha (23 cm^{-1}) is almost exclusively caused by hydrogen bonding. However, it needs to be kept in mind that the orientation of the transition dipole moment and the change in dipole moment can be different in a protein compared to in solution, which might affect solvatochromic wavenumber shifts caused by the solvent field. In solution hydrogen bonding solely causes blue shifting of the band maximum. As MD simulations predicted additional possible red shifting for distinct hydrogen bonding angles, this might also be found in a protein environment, in which hydrogen bonding might be forced to non-ideal angles, as it has been suggested for the NTL9 domain, previously [176, 177].

The most convenient model system for the application in a protein seems to be bocAha or fmocAha, because they exhibit the most similar structure compared to an Aha in a protein. Moreover, both show a very similar solvatochromic behavior confirming their suitability as a model system. In contrast to CN [183] and SCN [166], which are reporters of solvent field/dipolarity/polarizability and hydrogen bonding simultaneously, aliphatic azides seem to be almost exclusively sensors of hydrogen bonding in solvents. The total shift of MeSCN in various solvents (similar ones as used here) of 23 cm^{-1} is caused by competing contributions of solvent field/dipolarity/polarizability and hydrogen bonding [166]. The Ahas exhibit a similarly large total shift, which is almost exclusively caused by hydrogen bonding, which means, that Aha is a much more sensitive sensor of hydrogen bonding than MeSCN. Furthermore, Aha's solvatochromism might be easier to interpret because of the near-complete absence of competing contributions. Therefore, aliphatic azides are very sensitive to even slight changes in hydrogen bonding networks. On the other side this advantage makes them unsuitable as vibrational sensors for the electric field in a protein.

Incorporated into a protein, total variations of the band maximum of 18 cm^{-1} have been observed up to now for the SCN label and the CN label [106, 142, 148–155, 157–161, 163, 166]. This is a bit less than the solvent induced total shift detected (23 cm^{-1}) [166]. However, for Aha in protein shifts of up to 45 cm^{-1} for the band maximum were observed [100, 101, 103, 106], which is more than the total solvent induced shift of bocAha, fmocAha, and upAha. As mentioned before, this might be caused by different hydrogen bond angle distributions in a protein compared to solution, which is also influencing the solvatochromic shift of CN and SCN [176, 177, 244]. Providing a more than two times larger variance in the band position in a protein compared to the SCN and CN label marks the Aha as highly sensitive for detecting changes in local protein environment.

4.1.2 2D-IR Spectroscopy Aha

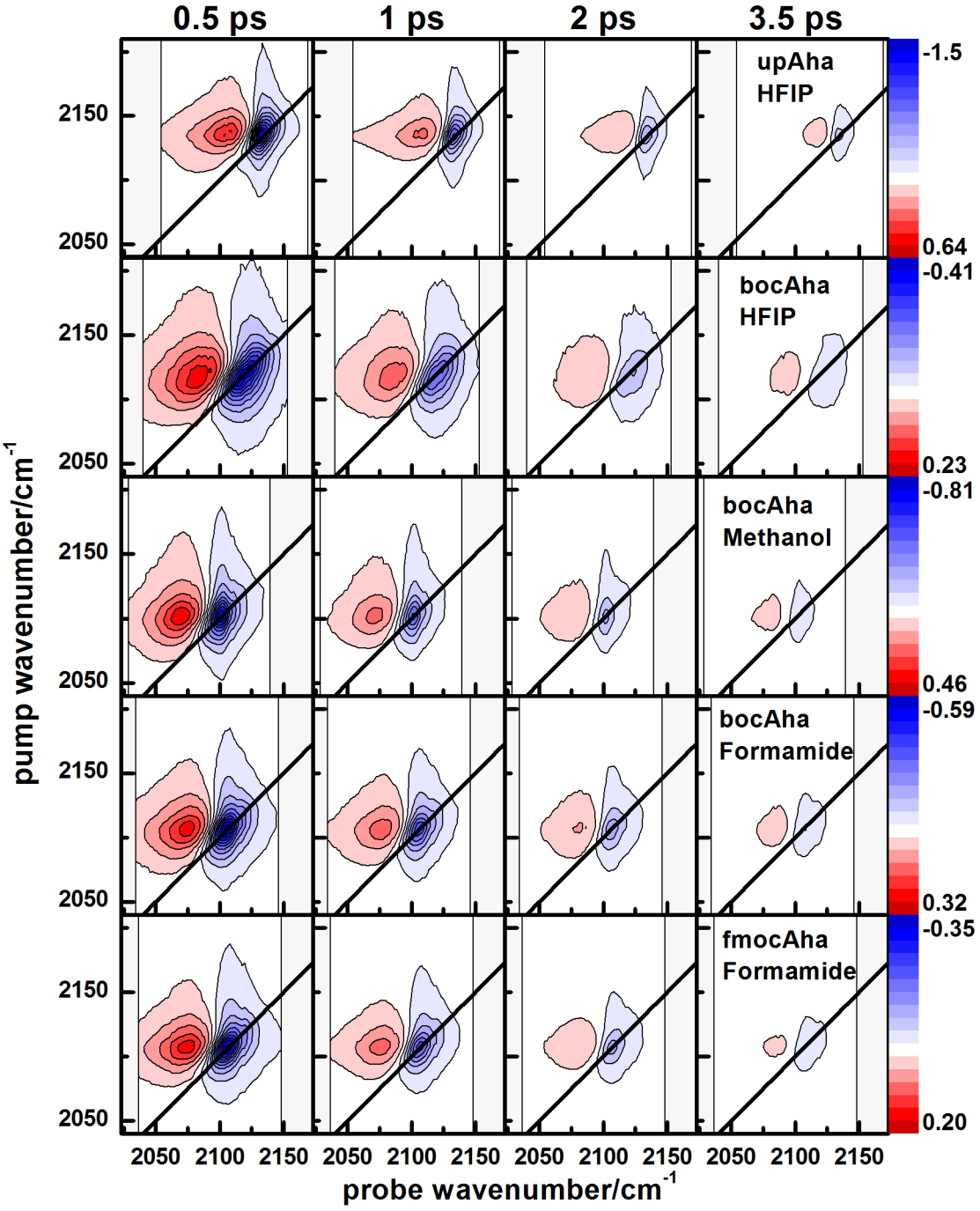

Figure 4.1.12: 2D-IR spectra of different Aha/solvent samples at 0.5, 1, 2, and 3.5 ps population time. The black line gives the diagonal. The thin vertical lines mark the borders of the spectrum. All spectra are measured at room temperature (RT).

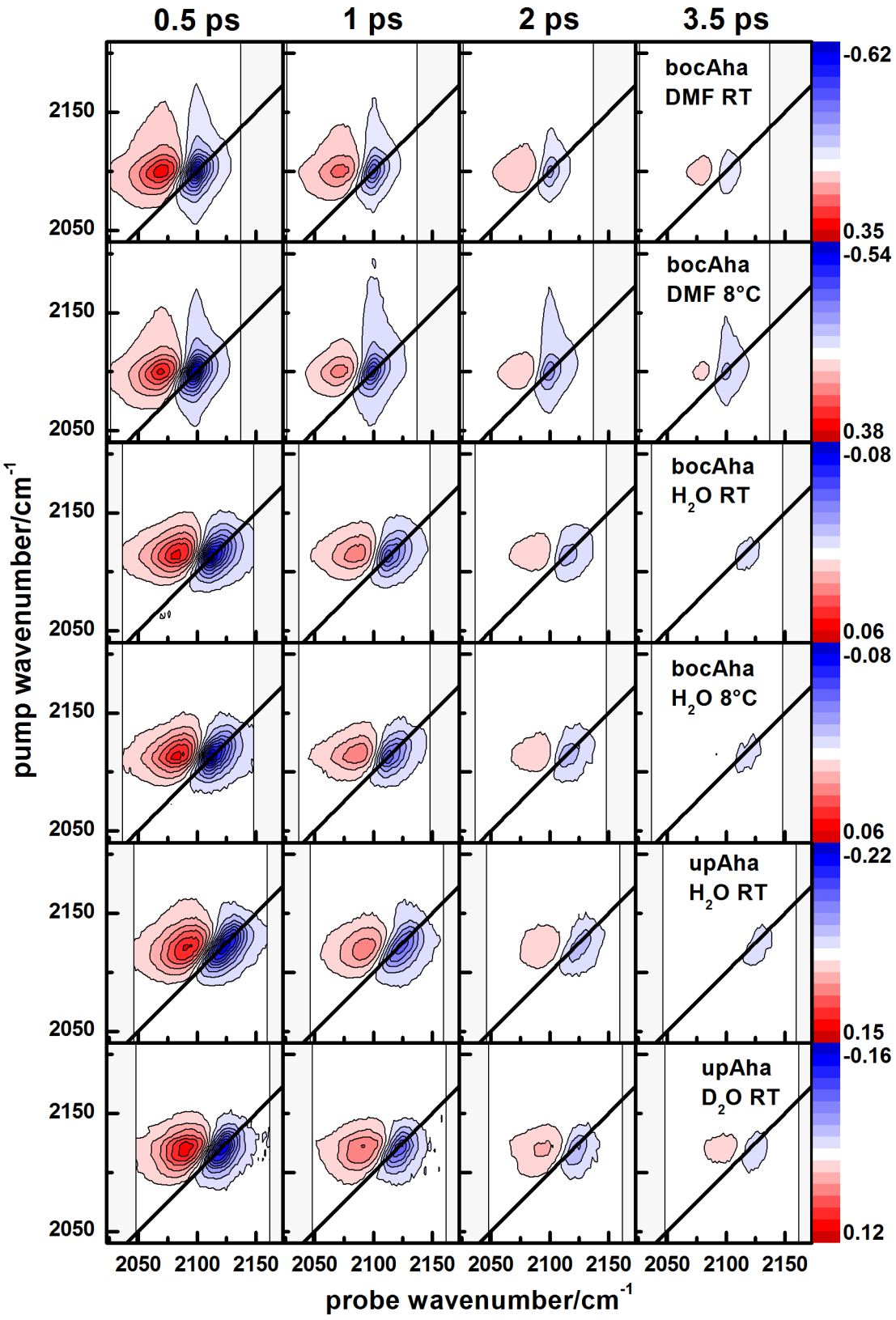

Figure 4.1.13: 2D-IR spectra of different Aha/solvent samples at 0.5, 1, 2, and 3.5 ps population time. The black line gives the diagonal. The thin vertical lines mark the borders of the spectrum. Spectra are measured at 8 °C or at RT as labeled.

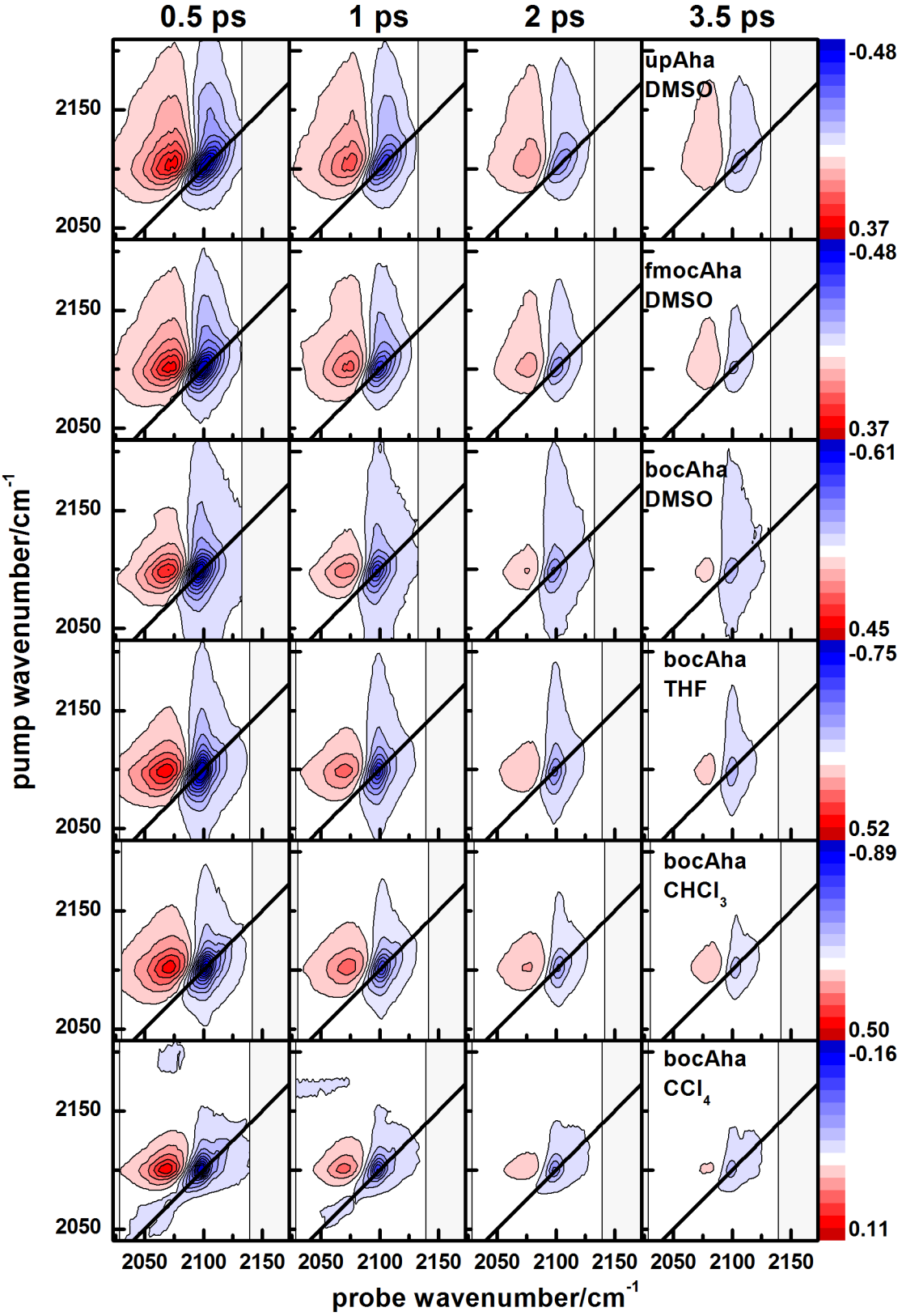

Figure 4.1.14: 2D-IR spectra of different Aha/solvent samples at 0.5, 1, 2, and 3.5 ps population time. The black line gives the diagonal. The thin vertical lines mark the borders of the spectrum. All spectra are measured at RT.

Fourier Transform 2D-IR spectra of selected Aha/solvent samples were measured (**figures 4.1.13**, **4.1.14**, **4.1.12**) to study vibrational lifetimes and time dependent solvent-solute fluctuations of the Ahas in different solvents. The spectra are composed of the typical negative (blue) (ground state bleaching and stimulated emission) and positive (red) band (excited state absorption) (see **chapter 2.2.3**). No cross peaks between the main band and the small additional side band at about 2150 cm^{-1} appear in the 2D-IR spectra. This points out, that the additional band seems not to be caused by Fermi resonance.

4.1.2.1 Vibrational Lifetime Analysis

Different approaches to estimate the vibrational lifetime of the Aha/solvent samples from the 2D-IR data were executed. At first a two dimensional Gaussian was fitted to the bleach signal at every population time. Both its maximum absorption and its integral were extracted and a population time dependent biexponential function with a flexible offset was fitted to them. Due to the signal size some 2D-IR data sets could be fitted by the 2D-Gaussian up to 20 ps population times, but others only up to 5.6 ps. To test for reproducibility, all data were fitted only up to 5.6 ps additionally and the results were compared. The strongly differing lifetimes caused by the fitting range showed that the fit is not very stable. To fix the problem of not having enough data points at later population times, the offset was set to zero, as the vibration should decay to zero. This approach neglects longer living heating signals of the solvent. However, it makes the fit much more reproducible when changing fitting conditions. The fits up to 5.6 ps with zero offset are similar to the fits up to later time points with a flexible offset. For the fits up to later time points the results are independent of the offset. Using the absorption maximum or the integral of the fitted 2D Gaussian, leads to similar results.

As a second approach a cut of the 2D spectrum at the pump wavenumber corresponding to the maximum bleach signal was extracted and analyzed with a global analysis [187] using a sequential model and four exponential components (*1-4* with the monoexponential lifetimes τ_1-τ_4). This approach leads to much more reliable and stable results, which are hardly dependent on fitting borders (less than 8 % aberration in vibrational lifetime of components *2-4*). As the change in band shape (spectral diffusion) can also cause contributions to the global analysis, additionally, the sum of all cuts in the bleach region was estimated and analyzed by global analysis with the same conditions. Results were deviating less than 10 % for components *2-4*, so that it can be assumed that none of the obtained lifetimes is a spectral diffusion correlation time.

Therefore, the global analysis approach was further used for the vibrational lifetime analysis. All resulting spectra of the four components (**figure 4.1.15**) (amplitudes and lifetimes in appendix **table A.1**) show a positive band on the red side

and a negative one on the blue side, except for component *1*, which shows diverse band shapes. The spectra of component *2* and *3* are very similar and the negative signal of component *4* is also at the same position as those of *2* and *3*, but its positive band is less red shifted compared to *2* and *3*. As the lifetime of *1* is smaller than 1 fs and the one of *2* between 80 and 280 fs, both components can be assigned to perturbed free induction decay and are, therefore, not analyzed further. Vibrational lifetimes of *3* and *4* are summarized in **table 4.6**. The lifetime of *3* (τ_3) is in a range of 0.7 to 1.1 ps for all Aha/solvent samples and gives the vibrational lifetime of the azide's asymmetric stretching vibration. It is in consistence to previously measured vibrational lifetimes of azides in the literature [91, 188].

While the azide ion has been object of several 2D-IR spectroscopy experiments and theoretical simulations [120, 128, 188, 245–248], only few 2D-IR studies on ncAAs containing an aliphatic azide group have been performed yet. The vibrational relaxation lifetime of the azide ion in H_2O was measured to be in the range of 0.6-1.3 ps [188, 245, 247]. The vibrational lifetime of the azide ion was found to be significantly longer in aprotic solvents compared to protic ones, which shows the importance of hydrogen bonding for the relaxation [245, 247]. Interestingly, the azide ion's vibrational frequency is shifted in D_2O compared to H_2O and the vibrational lifetime is extended. This is known as the solvent isotope effect [245, 248]. Vibrational relaxation and the solvent isotope effect have been matter of some theoretical studies [120, 248]. Two pathways for the vibrational decay in H_2O/D_2O were suggested: direct relaxation of the azide to its vibrational ground state accompanied by energy transfer to the solvent and intramolecular vibrational energy redistribution (IVR) to the symmetric stretching mode (and transfer to the solvent afterwards) [120, 248]. Charge fluctuation of the ion was found to enhance the relaxation rate in both pathways [120].

For organic azides the symmetry is broken and the charges are no longer equally distributed [188, 249]. Thus, slightly longer vibrational relaxation lifetimes were obtained for N_3Ala and N_3Pro in H_2O (biexponential: 0.1/1.1 ps and 0.1/1.0 ps, respectively) compared to the azide ion measured at the same experimental setup (monoexponential: 0.6 ps) [188]. A vibrational lifetime of 1 ps for an Aha labeled ligand peptides was measured in D_2O for the free ligand as well as for the ligand bound to a protein [91].

Our measurements show, that the vibrational lifetime of Aha (τ_3) changes only little in dependency on solvent properties. It seems to be a bit longer in very nonpolar aprotic solvents (1-1.1 ps) and a bit shorter in H_2O/D_2O (0.7-0.8 ps). Also no solvent isotope effect was found, neither for the wavenumber (**table 4.1**) nor for the vibrational lifetime τ_3. In contrast to the azide ion, in which hydrogen bonding to the solvent is important for fast relaxation [245, 247], hydrogen bonding to the solvent seems not to be equally important for vibrational relaxation of Aha. As Aha exhibits additional vibrational modes compared to the azide ion, a preferred

intramolecular vibrational relaxation via IVR along alternative modes, which does not directly involve solvent modes, seems to be likely. Temperature was also found to have only little influence on Aha's vibrational lifetime. As to be expected relaxation is a little bit slower at 8 °C compared to RT.

Observed vibrational lifetimes are very similar for the different Ahas, even for bocAha and upAha in HFIP, which are differing strongly in band position and width. Lee *et al.* [171] obtained biexponential lifetimes of 1.0-1.6 ps/9.6-14.4 ps for different N_3Pro conformers in $CHCl_3$. The vibrational mode of the conformers with electrostatic interactions between the azido moiety and the backbone decayed more slowly than the conformers with a free azido group. They concluded, that IVR across these electrostatic interactions is less efficient. For our data of bocAha and upAha in HFIP it means, that the observed similar lifetimes might indicate, that the difference in band position and width that we detected is rather not caused by a differing backbone interaction. The suggested explanation of different hydrogen bonding angles to solvent molecules seems to fit the observed lifetimes better.

Table 4.6: Vibrational lifetime of component *3* and *4* from the global analysis fit of the Aha/solvent samples at RT and 8 °C.

solvent	**bocAha**		**fmocAha**		**upAha**	
	τ_3/**ps**	τ_4/**ps**	τ_3/**ps**	τ_4/**ps**	τ_3/**ps**	τ_4/**ps**
HFIP RT	0.87	4.2			0.89	4.6
H_2O 8 °C	0.74	2.0			0.71	2.1
H_2O RT	0.70	1.8				
D_2O 8 °C					0.79	2.9
Methanol RT	0.98	3.6				
Formamide RT	0.91	3.3	0.84	3.3		
DMSO RT	0.86	5.0	0.91	5	0.89	5.1
DMF 8 °C	0.95	3.8				
DMF RT	0.87	3.5				
THF RT	0.9	5.4				
$CHCl_3$ RT	1.0	6.5				
CCl_4 RT	1.1	6				

Component *4* was assigned to a hot ground state because of its spectrum. Heated solvent around the azido group slightly changes the anharmonic potential of Aha's asymmetric stretching mode and lowers the needed energy for excitation. Therefore, excitation from the ground state to the first excited state is red shifted for the hot state compared to the unheated spectrum. For a difference spectrum this leads to a positive band, which is a bit red shifted compared to the also present bleach of the "cold" ground state. The decay of the hot ground states is determined by solvent cooling and, therefore, depends on the properties of the solvent only. As expected hydrogen bonding solvents are found to cool faster than aprotic ones and for aprotic solvents cooling gets more slowly with a descending dielectric constant. Only HFIP and DMF are outliers. Their cooling is a bit faster at RT than at 8 °C.

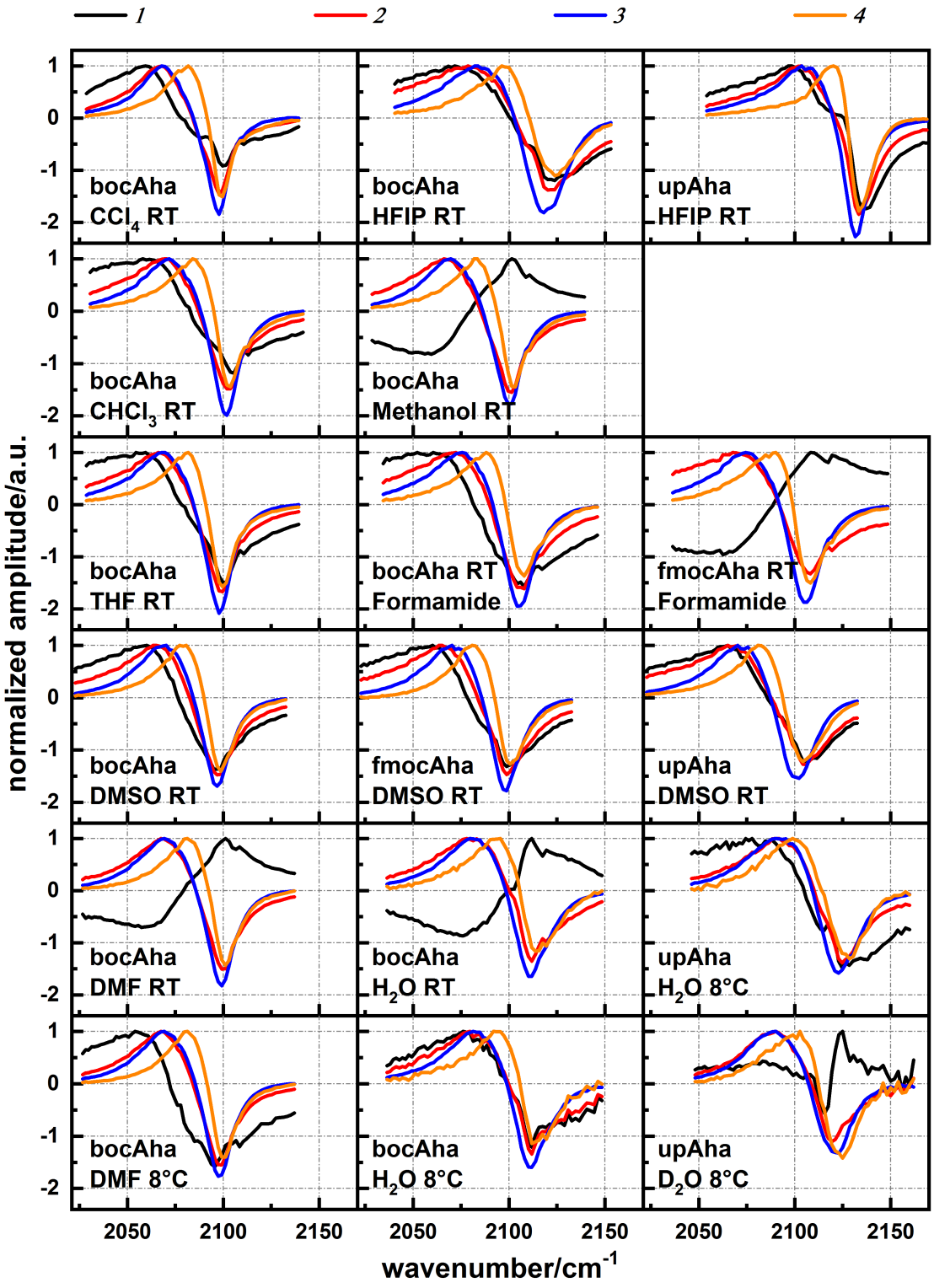

Figure 4.1.15: Global analysis spectra of the four components for the Aha/solvent 2D-IR spectra. The positive amplitude was normalized to 1 (normalization factor and lifetimes in **table A.1**). Data are measured at 8 °C or RT as labeled.

4.1.2.2 Line Shape Analysis

The center line slope of the bleach signal was analyzed in order to investigate time-dependent fluctuations of the solute-solvent interactions and inhomogeneous/homogeneous line broadening. In the signal range of the bleach (borders set to FWHM) a Gaussian was fitted to each cut parallel to the probe axis to find the maximum of the bleach at this pump frequency. Then a line was fitted along these maxima, which gives the tilt of the bleach signal (**figure 4.1.16 a-h**). The slope of the fitted line was determined. The time evolution of the inverse slope (CLS) (**figure 4.1.16 i+j**) can be estimated by an exponential function giving the normalized frequency-frequency correlation function (FFCF) without homogeneous contributions (see **chapter 2.2.3.1**). In this case a monoexponential function with an amplitude $\triangle$ and an offset δ is sufficient.

$$CLS = \triangle \cdot e^{-t/\tau_c} + \delta \tag{4.1.5}$$

The time constant τ_c is the vibrational frequency correlation decay. The offset δ is an on the timescale of the experiment (determined by the vibrational lifetime of the Ahas) static inhomogeneous contribution. At the population time zero the CLS value is $\triangle + \delta$, which describes the inhomogeneous part of the bandwidth and consequently $1 - (\triangle + \delta)$ gives the homogeneous part (which might be disturbed by a very fast decaying inhomogeneous part).

The observed correlation times for the Ahas are around 2 ps (**table 4.7**), which is longer than the vibrational lifetime of the Aha's asymmetric stretching vibration. Therefore, the signal disappears faster than the tilt of the band decays, which means that fitting of the correlation decay at later population times is difficult and errors are getting large. This makes the fit very sensitive to the chosen fitting borders and less reliable. Fitting borders were tried to be set to FWHM for every sample, but differing line shape makes it impossible to achieve exact equality of fitting conditions. Therefore, the results contain relatively high uncertainties (about 30 % possible) and need to be interpreted with care.

In case of τ_c this means that only the conclusion can be drawn, that the correlation decay of all Aha/solvent samples is in a similar range. For H_2O and D_2O correlation decay seems to be a bit faster than for the other solvents. The smaller value for bocAha in HFIP needs to be considered with special care because in this case the fit was particularly unstable and, thus, it is not possible to make a deduction.

For bocAha δ, $\triangle$, and, thus, $\triangle + \delta$ appear to be a bit larger in protic solvents (except methanol) compared to the aprotic solvents. Hence, the inhomogeneous part of the line broadening seems to be bigger for protic solvents (except methanol) as a consequence of hydrogen bonding. The static inhomogeneous contribution seems

to be smaller for D_2O compared to H_2O in case of upAha. Among the three Ahas bigger deviations can be found for δ and $\triangle$, which are both larger for upAha and fmocAha compared to bocAha. Only upAha in HFIP is an exception as there δ, $\triangle$, and, thus, $\triangle + \delta$ are significantly smaller than for bocAha in HFIP. This means that in HFIP the bandwidth is more dominated by inhomogeneous broadening in the case of bocAha in comparison to upAha. This is in total accordance with the much narrower bandwidth of upAha in HFIP, which was obtained in the FTIR spectrum (**chapter 4.1.1.5**). That might be due to a more fixed conformational state of hydrogen bonding to the solvent than it is the case for the protected bocAha and a reduction of longer living static inhomogeneous interactions.

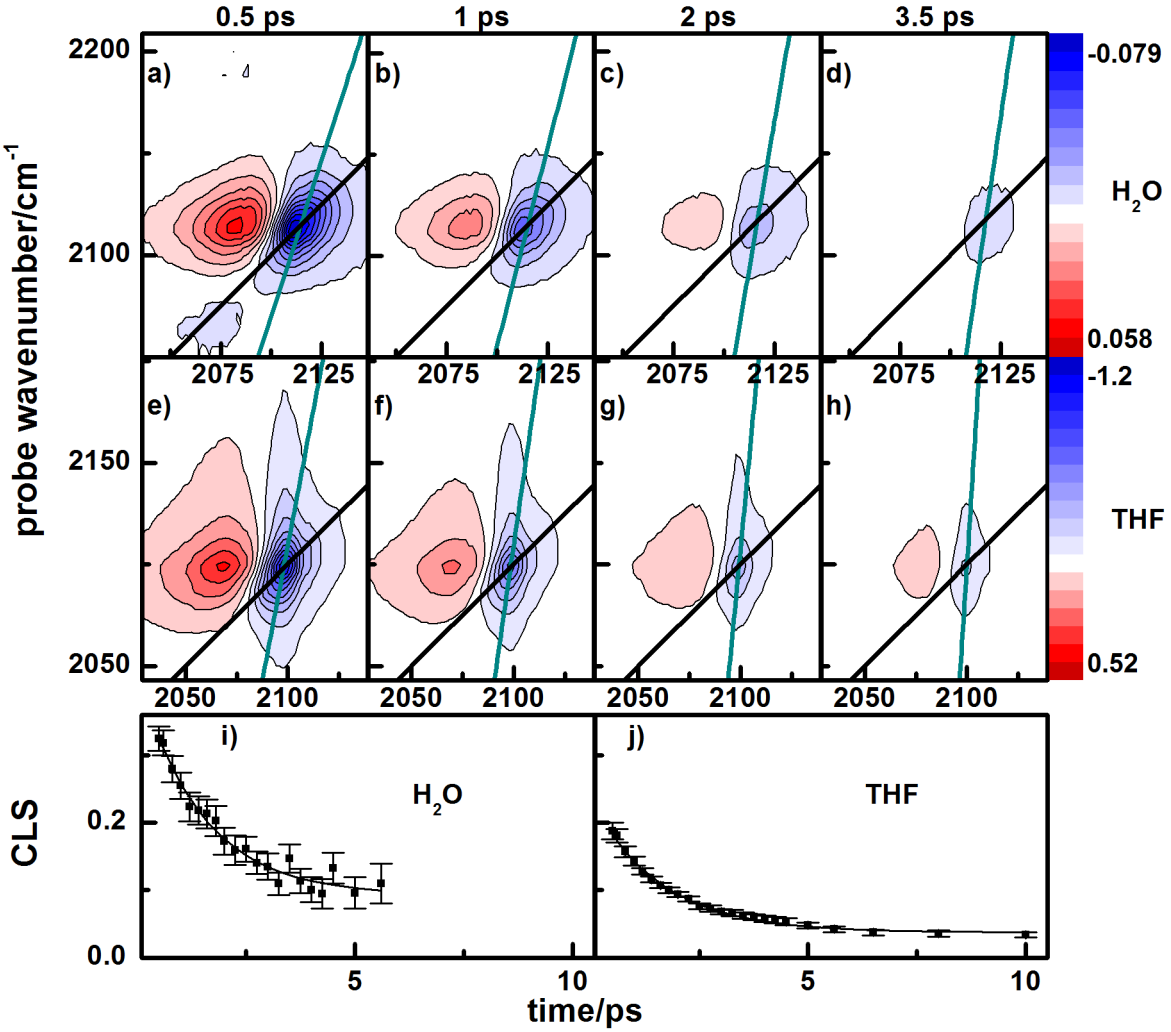

Figure 4.1.16: 2D-IR spectra of bocAha in **(a-d)** H_2O and **(e-h)** THF at 0.5, 1, 2, and 3.5 ps population time. The black line gives the diagonal and the cyan line is the tilt of the bleach band. **(i)** and **(j)** gives the CLS decay fitted by a monoexponential function for both samples.

Spectral diffusion of the azide ion has also been object of previous studies. In D_2O and reverse micelles a biexponential vibrational frequency correlation decay of 80 fs and 1.3 ps/1.2 ps in combination with a longer living inhomogeneous part

Table 4.7: Fit parameters of the CLS decay of the different Aha/solvent samples with the vibrational frequency correlation decay τ_c, the amplitude Δ, the static offset δ, and the time range of the exponential fit Γ. Uncertainties are high and results need to be considered with care.

solvent	bocAha					fmocAha					upAha				
	τ_c/ps	δ	Δ	δ+Δ	Γ/ps	τ_c/ps	δ	Δ	δ+Δ	Γ/ps	τ_c/ps	δ	Δ	δ+Δ	Γ/ps
HFIP RT	1.6	0.14	0.34	0.48	0.5-10						2.2	0.06	0.27	0.33	0.5-10
H_2O 8 °C	1.5	0.14	0.37	0.51	0.5-3.5						1.4	0.32	0.34	0.66	0.5-4.2
H_2O RT	1.5	0.09	0.33	0.42	0.5-5.6										
D_2O 8 °C											1.5	0.18	0.31	0.49	0.5-4.5
Methanol RT	2.1	0.03	0.17	0.20	0.5-10										
Formamide RT	1.8	0.08	0.29	0.37	0.5-10	1.8	0.11	0.34	0.45	0.5-10					
DMSO RT	1.7	0.08	0.25	0.33	0.5-6.5	1.5	0.11	0.35	0.46	0.5-6.5	1.6	0.14	0.47	0.61	0.5-6.5
DMF 8 °C	2.1	0.06	0.24	0.30	0.5-6.5										
DMF RT	2	0.05	0.23	0.28	0.5-6.5										
THF RT	1.6	0.04	0.20	0.24	0.5-10										
$CHCl_3$ RT	2.2	0.04	0.22	0.26	0.5-15										
CCl_4 RT	2.4	0.08	0.23	0.31	0.5-6.5										

was found [246, 250]. The measured spectral diffusion was interpreted as fluctuations of the vibrational force constant from the making and breaking of hydrogen bonds to D_2O [246]. Another theoretical study correlated the spectral diffusion to more collective dynamics like electric field fluctuations [128]. Okuda *et al.* [188] obtained correlation times of 1.3 ps, 1.5 ps, and 1.0 ps for the azide ion, N_3Ala, and N_3Pro in H_2O, respectively. The static inhomogeneous contribution for the organic azides was much larger compared to the one of the ion. They assigned the correlation time to hydration dynamics of the solute and concluded that the structure around the ionic and non-ionic azide group is similar. For an Aha containing peptide ligand a correlation decay of 3 ps was discovered for both the unbound and the bound form. However, a static inhomogeneous contribution was only seen in the bound form [91]. Compared to our data, in which an offset is found for every free Aha/solvent sample, it is surprising that they did not find an offset for the unbound peptide. Tucker *et al.* [126] detected a correlation time of 1.5 ps for 2'-azido-2'-deoxyuridine in H_2O. In THF no change of the tilt could be seen on the timescale of the experiment discovering a much longer correlation time in this aprotic solvent. This finding is in contrast to our measured correlation decays, which are similar in aprotic and protic solvents. All in all, observed correlation decays in literature are much more differing than the found vibrational lifetimes. This is caused by the fact that the vibrational lifetime is shorter than the correlation decay time and the possible fitting ranges of the latter are varying between the particular experiments. Okuda *et al.* fitted the CLS of the azide ion, N_3Ala, and N_3Pro between 0 and 2 ps [188], Bloem *et al.* fitted the inverse CLS of the Aha peptide up to 3 ps [91] and in this dissertation the fit was applied between 0.5 and 3.5-10 ps depending on the spectra (**table 4.7**). This might play a part in contributing to the differing calculated correlation times. The correlation decay in literature (1-3 ps) which was almost exclusively measured in water or heavy water has been assigned to making and breaking of hydrogen bonds. With regard to the data presented in this dissertation, in which similar correlation times have also been measured for all aprotic solvents this conclusion is compromised.

4.1.2.3 2D-IR Aha Discussion

Since the vibrational lifetime of Aha was found to be relatively short (0.7 to 1.1 ps) compared to the correlation time (~2 ps) of spectral diffusion, which makes analysis of the latter challenging, Aha's potential as a 2D-IR label is limited despite its large extinction coefficient. Additionally, its vibrational lifetime is not very sensitive to solvent properties. In contrast the CN label in water exhibits lifetimes in a range of 1-5 ps [86] and MeSCN even has vibrational lifetimes of 32-158 ps in different solvents being sensitive to polarity and hydrogen bonding [166] making them both being more powerful 2D-IR labels than Aha.

4.2 Aha in PDZ3

Aha was incorporated into the PDZ3 domain of PSD-95 at 15 different positions (15 mutants) to get a broad set of environments and conditions for the label. Some of the mutation sites were chosen because of being involved in allosteric communication pathways in the theoretical work of Ota and Agard [6] or Lockless and Ranganathan [5], others because of being not part of the pathways as a negative control. All mutants were characterized for correct folding and functionality in terms of ligand binding. FTIR spectra of the Aha's asymmetric stretching vibration were measured for the pure PDZ3 and for PDZ3 bound to its native ligand, the C-terminal sequence (acNYKQTSV) of the CRIPT peptide [208, 211]. Additionally, 2D-IR spectra were recorded for the free and ligand bound state for a selection of mutants.

The ITC data of WT and Ile341Aha have previously been published by us [104]. Some of the pictured FTIR, CD, and ITC data were measured by the author as part of a bachelor thesis [235] and by Patrick Quoika, supervised by the author, in course of his bachelor thesis [251].

4.2.1 Selection of Mutation Sites

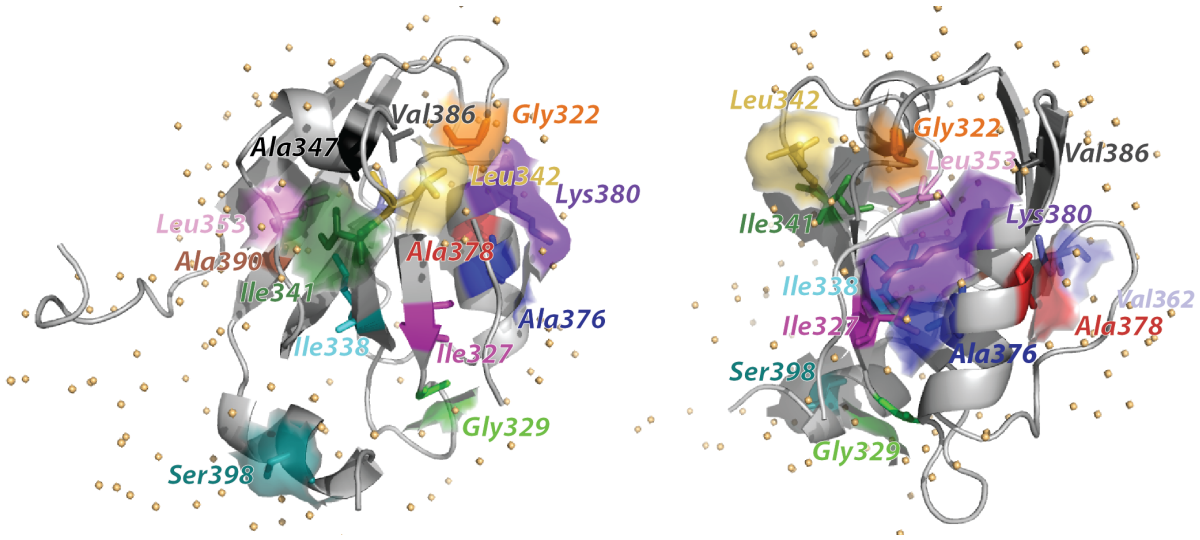

Figure 4.2.1: Two views onto the mutation sites in PDZ3 of PSD-95 (PDB: 1BE9 shorten by 13 AA). The transparent surfaces gives the solvent exposure of the mutation sites.

The PDZ3 domain of PSD-95 consists of 6 β-sheets and 3 α-helices. Mutation sites were chosen to be part of different secondary structure elements (**table 4.8**). The selection and description is based on the crystal structure of PDZ3 by Doyle *et al.*

[210] (**figure 4.2.1**). **Gly322** is localized in the carboxylate binding loop following the first β-sheet (βA). This loop is part of the binding site groove and highly conserved especially its Gly322-Leu323-Gly324-Phe325 motif (one of the early names of PDZ domains was "GLGF repeats" due to this motif). It is important for ligand recognition and tightly binds the C-terminal carboxylate of the peptide ligand via hydrogen bonds. **Gly322** itself is not directly involved in ligand binding but might be important for the shape of the loop. **Ile327** and **Gly329** are part of the βB-sheet. The ligand is bound to this β-sheet via antiparallel backbone interactions. Two hydrogen bonds of the backbone of **Ile327** are formed to the Tyr_{-2} residue of the ligand. **Gly329** is not involved in ligand binding directly but its backbone forms a hydrogen bond to His372, which is a highly conserved residue lying in the αB-helix on the other side of the binding pocket and this might stabilize the binding pocket. **Ile338** and **Ile341** are localized in the βC-sheet, which is oriented antiparallel to the βB-sheet. **Leu342** is the first residue of the following loop and **Ala347** is situated in the first α-helix (αA). **Leu353** is part of the loop afterwards and **Val362** is the first residue following the βD-sheet. We chose three residues of the αB-helix, which is part of the binding pocket, **Ala376**, **Ala378**, and **Lys380**. **Val386** and **Ala390** are situated in the last β-sheet (βF). The third α-helix, which is special for the PDZ3 domain of PSD-95 contains the **Ser398** residue.

The mutation sites exhibit different degrees of solvent exposure, which were calculated as solvent accessible surface area (SASA) for the mutation sites using free SASA (**table 4.8**).

Table 4.8: Localization and water exposure (in terms of normalized SASA) of the PDZ3 Aha mutation sites with (PDB: 1BE9) and without ligand (PDB: 1BFE).

	structure element	**normalized SASA PDB: 1BFE**	**normalized SASA PDB: 1BE9**
Gly322	carboxylate binding loop	0.412	0.513
Ile327	βB	0.097	0
Gly329	βB	0.192	0.089
Ile338	βC	0	0
Ile341	βC	0.233	0.231
Leu342	loop	0.519	0.503
Ala347	αA	0.007	0.0016
Leu353	loop	0.093	0.090
Val362	loop	0.018	0.017
Ala376	αB	0.364	0.040
Ala378	αB	0.167	0.219
Lys380	αB	0.669	0.543
Val386	βF	0	0
Ala390	βF	0	0
Ser398	αC	0.546	0.564

Originally some of the mutation sites were chosen because they are predicted to be allosterically coupled in the study of Ota and Agard [6] (**Ile327**, **Ile341**, **Ala347**,

Leu353) or Lockless and Ranganathan [5] (**Gly322**, **Gly329**, **Ala347**, **Leu353**, **Val362**, **Ala376**, **Lys380**, **Val386**) and the others because they are not part of these networks (**Ile338**, **Leu342**, **Ala378**, **Ala390**, **Ser398**). However, in the publication of Ota and Agard [6] **Ala347** and **Leu353** only appear in the final figure, which compares their network to the publication of Lockless and Ranganathan [5]. No data are shown for these residues, so it is not completely clear if they really are part of their found anisotropic energy transfer pathway. Anyhow, if more of the studies on allostery in PDZ3 are considered, about half of all residues of PDZ3 have been proposed to be part of at least one pathway or network of somehow coupled AAs (**table 4.9**). Since most of these deviating networks derive from theoretical studies and only a few are predicted by thermodynamical mutation cycles the need of new experimental methods to study dynamical allostery in PDZ3, which sheds light on the variety of network variants, becomes obvious. Of the Aha mutation sites chosen only **Ser398** has not been predicted to be part of a network in any of these studies.

Table 4.9: Predicted networks of allosterically coupled AAs from different studies. [5, 6, 10, 13–16, 18, 19, 26] are theoretical (black) and [5, 31, 35, 36] are experimental works (blue). [5] is the theoretical and [5]* is the experimental part of the publication of Lockless and Ranganthan. All experimental studies are mutational studies in which different residues were mutated and their impact on the binding parameters was determined. Therefore not all AA sites of the protein were considered and the found couplings are only a section. In some studies coupling to His372 was investigated (marked with a capital X) and in others a complete scan was made. In [14] overall pairwise coupling was investigated. The frequency of a residue to be predicted being a coupled residue is counted in the last column. The bold residues give the chosen Aha mutation sites.

	[5]	[5]*	[6]	[10]	[31]	[13]	[14]	[16]	[15]	[35]	[36]	[18]	[19]	[26]	
Glu310						x									1
Arg312												x			1
Ile314									x						1
Ile316								x							1
Arg318						x	x								2
Glu319						x									1
Ser320						x									1
Gly322	**x**	**x**													**2**
Leu323						x	x				x				3
Gly324											x				1
Phe325	x	x	x	x			x	x		x	x	x		x	10
Asn326								x							1
Ile327			**x**			**x**		**x**	**x**	**x**	**x**	**x**			**7**
Val328											x			x	2
Gly329	**x**	**x**		**x**	**x**	**x**					**x**	**x**		**x**	**8**
Gly330	x	x									x			x	4
Glu331						x								x	2
Gly333						x								x	2

	[5]	[5]*	[6]	[10]	[31]	[13]	[14]	[16]	[15]	[35]	[36]	[18]	[19]	[26]	
Glu334						x								x	2
Gly335	x	x												x	3
Ile336	x	x					x	x			x		x	x	7
Ile338									**x**		**x**	**x**	**x**		**4**
Ser339														x	1
Phe340										x					1
Ile341			**x**							**x**	**x**	**x**		**x**	**5**
Leu342														**x**	**1**
Pro346							x	x							2
Ala347	**x**		**x?**				**x**		**x**		**x**	**x**	**x**		**7**
Leu353	**x**		**x?**						**x**		**x**	**x**			**5**
Asp357								x							1
Gln358														x	1
Ile359											x			x	2
Leu360														x	1
Ser361														x	1
Val362	**x**	**x**			**x**		**x**		**x**		**x**				**6**
Asp366														x	1
Leu367							x		x		x	x		x	5
Arg368														x	1
Asn369														x	1
Ala370														x	1
Ser371														x	1
His372	X	X	X	X		x			x	x	x	x	x	X	11
Glu373														x	1
Gln374														x	1
Ala375							x				x			x	3
Ala376	**x**	**x**		**x**	**x**	**x**					**x**			**x**	**7**
Ile377														x	1
Ala378							**x**			**x**				**x**	**3**
Leu379							x				x	x			3
Lys380	**x**	**x**		**x**					**x**					**x**	**5**
Asn381														x	1
Gly383														x	1
Gln384						x									1
Val386	**x**	**x**							**x**						**3**
Ile388											x	x			2
Ala390													**x**		**1**
Gln391								x							1
Glu396									x						1

	[5]	[5]*	[6]	[10]	[31]	[13]	[14]	[16]	[15]	[35]	[36]	[18]	[19]	[26]	
Tyr397												x	x		2
Phe400						x							x		2

4.2.2 Characterization of PDZ3-Aha Mutants

Correct folding and the functionality in terms of ligand binding of the PDZ3-Aha mutants were characterized by different methods and compared to wild type (WT) PDZ3 data.

4.2.2.1 CD PDZ3-Aha

Correct folding and secondary structure composition of a protein in solution can be determined via the circular dichroism (CD) technique [220, 252–254]. The different absorption of left- and right-hand circularly polarized light of an intrinsically chiral sample results in an elliptical polarization. This change in polarization is reported in terms of ellipticity ($\Theta = tan^{-1}(\frac{b}{a})$) [deg] with a as major and b as minor axis of the ellipse [252–254]. As the peptide bonds of distinct secondary structure elements of a protein, like α-helices, β-sheets, and turns, show different wavelength dependent ellipticities in the far-UV region (<250 nm), secondary structure composition can be estimated from CD data [220, 252, 254]. Results for WT and mutants can be compared and hereby proper folding of the mutants can be proven.

Since concentrations determined by Lowry assay [255] are not accurate enough for secondary structure determination for commonly used CD analysis [220, 252, 254] the concentration independent method of Raussens *et al.* [220] was applied. This method includes a normalization by a single wavelength value followed by the analysis of each secondary structure element with a quadratic model based on one or two wavelength values. The results are a bit less accurate than from commonly used methods, however uncertainties in concentration and path length are canceled out.

For better comparison of the estimated secondary structure composition (**table 4.10**) three WT spectra at different concentrations were measured, analyzed, and the results were averaged. The obtained results fit the secondary structure composition of the crystal structure. Applying the standard deviation of the analysis method, only the α-helix amount of the Gly329Aha mutants is outside the error range of the WT. Also the CD spectrum of Gly329Aha (**figure 4.2.2**) shows a little deviating shape compared to the WT spectra. The total folding of this mutant seems to be a bit perturbed by the Aha mutation. CD data of all other mutants are inconspicuous within the scope of accuracy of this analysis method. However, the

sensitivity is not very high and small local perturbations of the structure around the mutation site cannot be excluded by this method.

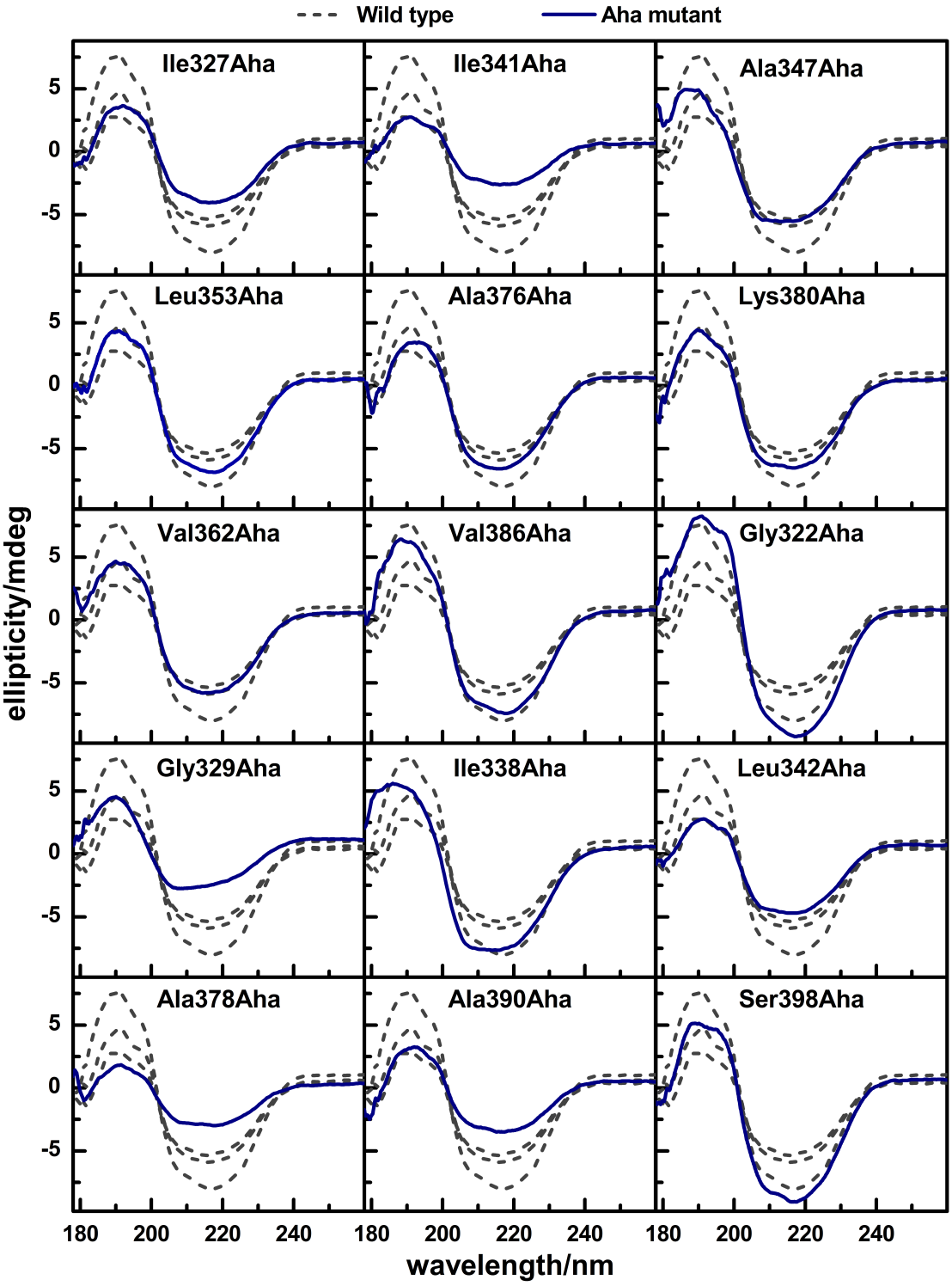

Figure 4.2.2: CD spectra of all PDZ3-Aha mutants (solid blue) in comparison to CD spectra of WT at three different concentrations (dashed grey). As high voltage should not be larger than 700 V (**figure A.0.1**), spectra at wavelengths smaller than 182.7 nm need to be considered with care.

Higher accuracies could be achieved by precise concentration determination via costly amino acid analysis [252] or measuring of temperature dependent unfolding via CD spectroscopy. Nonetheless, very small local perturbation could only be seen by X-ray or NMR structure determination because the CD technique always gives a measure of the overall structure and is not site-resolved.

Table 4.10: Secondary structure analysis of the PDZ3 CD data with the concentration independent method of Raussens *et al.* [220, 221]. Three WT measurements with different protein concentrations were averaged and the standard deviation of the method was added.

	α-helix/%	β-sheet/%	turn/%	random/%	sum/%
PDB: 1BE9	18.8	32.7			
WT1	12.1	30.2	12.5	37.0	91.7
WT2	15.2	29.6	12.5	35.8	93.1
WT3	19.9	25.8	12.5	34.9	93.1
WT average	**15.7±11.9**	**28.5±11.1**	**12.5±4.15**	**35.9±10.3**	
Ala347Aha	16.2	28.1	12.5	36.5	93.3
Ala376Aha	11.2	30.8	12.5	36.7	91.2
Ala378Aha	13.8	29.1	12.5	368	92.2
Ala390Aha	21.4	25.7	12.5	34.5	94.0
Gly322Aha	17.6	27.7	12.5	34.4	92.3
Gly329Aha	31.8	20.0	12.5	33.3	97.6
Ile327Aha	20.0	25.3	12.5	34.6	92.4
Ile338Aha	14.9	28.5	12.5	36.8	92.7
Ile341Aha	22.8	23.5	12.5	34.3	93.2
Leu342Aha	13.8	28.7	12.5	36.7	91.7
Leu353Aha	14.0	29.0	12.5	36.3	91.8
Lys380Aha	13.3	29.4	12.5	36.6	91.9
Ser398Aha	11.5	30.3	12.5	36.6	91.0
Val362Aha	18.3	27.5	12.5	35.4	93.7
Val386Aha	18.3	27.5	12.5	35.4	93.7

4.2.2.2 ITC PDZ3-Aha with Hepta

Isothermal titration calorimetry (ITC) is the only method that can directly quantify binding constants of biological interactions by measuring the heat emerged through association of a protein and its ligand. Furthermore, it quantifies the enthalpy $\triangle H$, the stoichiometry N, the Gibbs free energy $\triangle G$, the entropy $\triangle S$, and the change in heat capacity [256–260]. The ligand is placed into a syringe and titrated stepwise into the protein sample cell. Binding of the ligand to the protein is accompanied by the release or absorption of heat. A heat-flux calorimeter determines the power which is needed to preserve a constant temperature difference between the sample cell and a reference cell during ligand titration. Integration of the peak gives the required heat per titration step [256, 257, 260]. From the evolution of required heat per step $\triangle H$, N, and the association constant k_a can be calculated. Gibbs free energy $\triangle G$, the entropy $\triangle S$, and the binding constant k_d are given by the following thermodynamic principles [256, 259, 261]:

$$\triangle G = -RT \cdot ln(k_a) = \triangle H - T\triangle S \tag{4.2.1}$$

$$k_d = \frac{1}{k_a} \tag{4.2.2}$$

ITC measurements of WT PDZ3 and all 15 PDZ3-Aha mutants in combination with a C-terminal CRIPT peptide with the sequence acNYKQTSV (named Hepta) were conducted (**figure 4.2.3** and **4.2.4**) and binding parameters were determined (**table 4.11**). The WT PDZ3 experiment was repeated to prove reliability of the data and a negligible deviation between the two measurements was found. A dissociation constant of 2.9 μM was detected for the WT, which is about 3 times smaller than the dissociation constant determined by Saro *et al.* [214] of $k_d = 9.9 \pm 1.4\,\mu M$ (with $\triangle H = -7.3 \pm 0.1\,kcal/mol$; $T\triangle S = -0.5 \pm 0.1 kcal/mol$). This might be due to the fact, that the α3 helix of PDZ3 was truncated in their work. The main change of k_d seems to be caused rather by the binding entropy than the enthalpy.

Most of the PDZ3-Aha mutants exhibit similar binding constants like the WT (**figure 4.2.5**). Surprisingly, Gly322Aha binds Hepta with an even higher binding constant than the WT, despite being part of the highly conserved recognition sequence of the carboxylate binding loop. Ile327Aha, Ala376Aha, and Gly329Aha show significantly lower binding affinities compared to WT. The backbone of Ile327 is directly involved in binding of the ligand via hydrogen bonding and Gly329 forms a hydrogen bond to His372 which is then hydrogen bonded to the ligand [210]. Therefore, a reduced binding affinity is expected. CD spectra showed that the folding of Gly329Aha seemed to be perturbed, which might also decrease the binding affinity. Ala376Aha is part of the binding pocket. Even if it is not directly involved in ligand binding, very small local changes at this site can have an effect on binding. Ala347Aha and Val386Aha, which are distant from the binding site, also show a small change in the binding constant. Ala347Aha is placed in the αA-helix, which shows a small structural change upon ligand binding in NMR spectroscopy [104].

Since deviations in binding affinity of the observed magnitude are hardly altering the ratio of bound ligand for an 1.3-1.5 ligand excess at concentrations in a mM range, sufficient binding ability of all mutants can be assumed. Despite similar binding affinities, the deviations of $\triangle H$ and $\triangle S$ are higher and seem to compensate each other. Saro *et al.* also discovered this kind of enthalpic coupling for double mutations of an artificial ligand, but did not found an explanation for it [214].

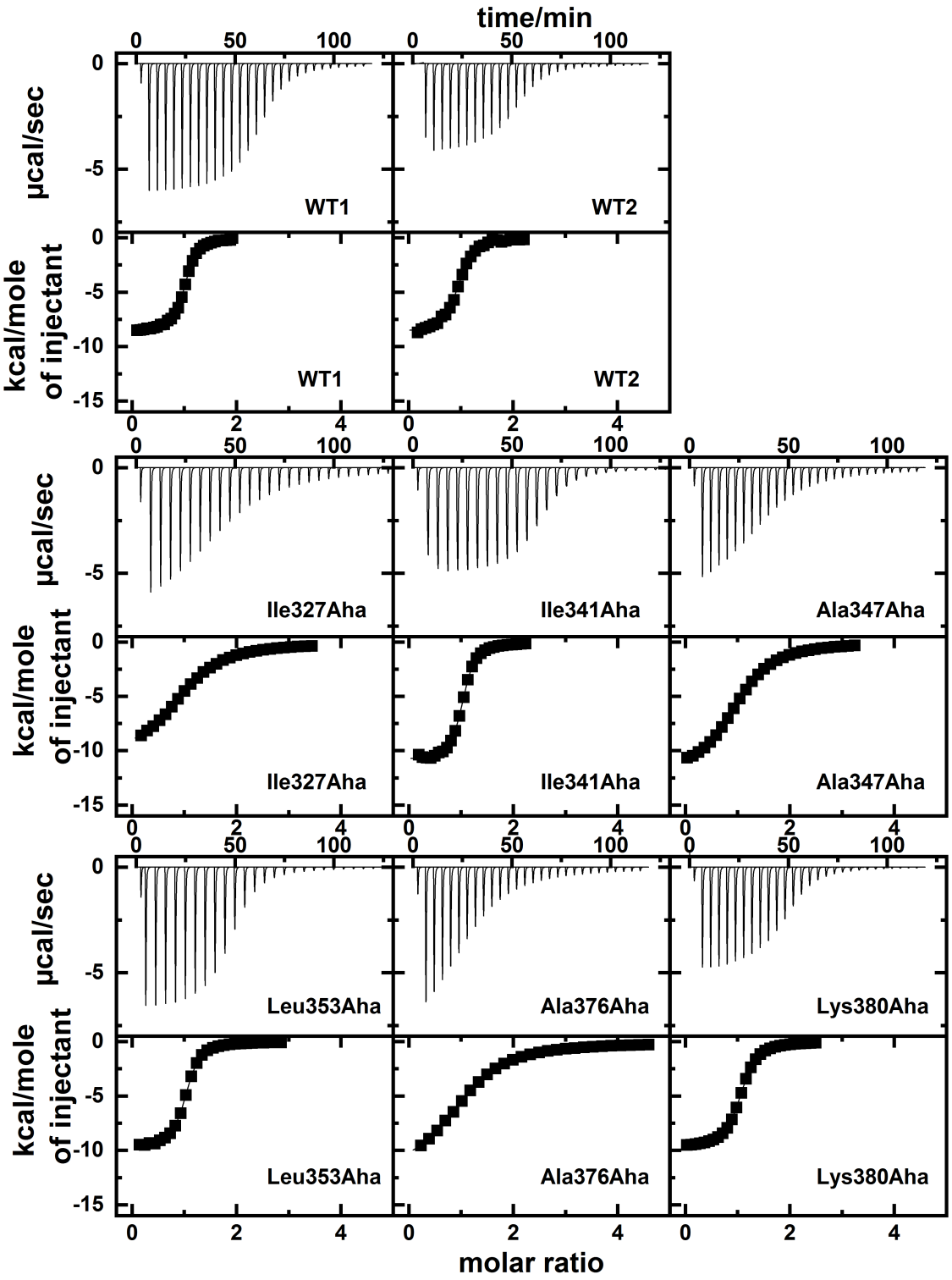

Figure 4.2.3: ITC data of different PDZ3-Aha mutants and WT PDZ3 + Hepta.

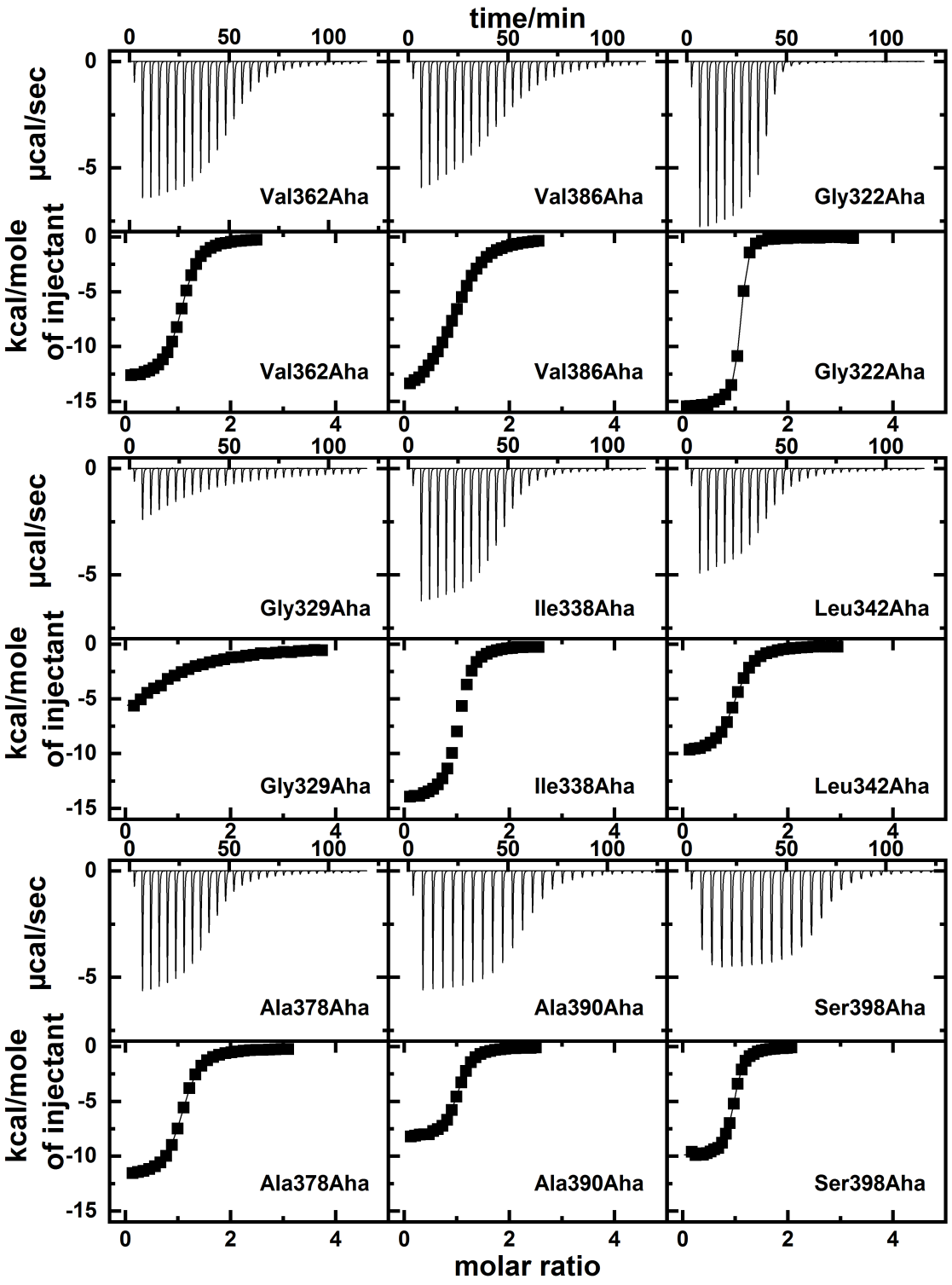

Figure 4.2.4: ITC data of different PDZ3-Aha mutants + Hepta.

Table 4.11: Binding parameters of WT PDZ3 and the Aha mutants with Hepta determined by ITC.

	k_a /μM^{-1}	k_d /μM	N	ΔH/cal/mol	ΔS/cal/mol
WT1	0.35±0.02	2.9±0.2	1.00±0.002	-8550±30	-3.33
WT2	0.35±0.03	2.9±0.3	0.945±0.005	-8700±70	-3.83
Ala347Aha	0.072±0.001	13.9±0.2	1.03±0.01	-12130±50	-18.5
Ala376Aha	0.0442±0.0008	22.6±0.5	1.07±0.01	-12460±90	-20.5
Ala378Aha	0.36±0.02	2.8±0.2	1.06±0.01	-11950±70	-14.6
Ala390Aha	0.337±0.007	2.97±0.07	1.00±0.01	-8350±20	-2.7
Gly322Aha	2.7±0.02	0.37±0.03	1.05±0.01	-15330±50	-22
Gly329Aha	0.019±0.002	53±6	0.938±0	-9700±200	-12.9
Ile327Aha	0.0405±0.0006	24.7±0.4	1.03±0.01	-10710±50	-14.8
Ile338Aha	0.49±0.02	2.04±0.09	1.01±0.01	-14210±40	-21.6
Ile341Aha	0.40±0.02	2.5±0.2	1.01±0.001	-10870±40	-10.8
Leu342Aha	0.27±0.01	3.7±0.2	0.993±0.004	-10080±50	-8.95
Leu353Aha	0.402±0.008	2.49±0.05	1.00±0.01	-9690±20	-6.87
Lys380Aha	0.349±0.008	2.87±0.07	0.905±0.002	-9690±30	-7.13
Ser398Aha	0.53±0.03	1.9±0.2	0.954±0.002	-9990±40	-7.30
Val362Aha	0.298±0.005	3.36±0.06	1.06±0.002	-12990±30	-18.5
Val386Aha	0.115±0.004	8.7±0.4	0.992±0.005	-14400±90	-25.1

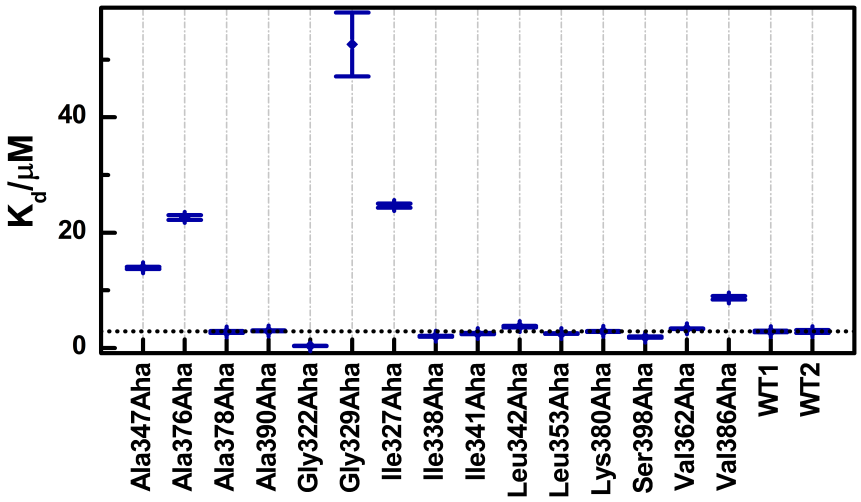

Figure 4.2.5: Comparison of the dissociation constants of the different PDZ3-Aha mutants and WT PDZ3 determined by ITC.

4.2.3 Crystal Structures PDZ3-Aha

The crystal structures of 5 of the 15 PDZ3-Aha mutants, investigated in this thesis, have been resolved by coworkers. The structure of Ile341Aha was determined by our collaboration partners from the Harald Schwalbe group, Institut für Organische Chemie, Johann Wolfgang Goethe-Universität Frankfurt, Germany, and has already been published in [104]. The structures of Val362Aha, Ile338Aha, Ala376Aha, and Val386Aha were measured by Deniz Üresin and Georg Wille from

the Bredenbeck group in course of Deniz Üresin's master thesis (not published yet). To convey a complete picture, the results from these works are discussed here as well, even if determination of the X-ray structures of the PDZ3-Aha mutants was not part of this thesis.

4.2.3.1 Crystal Structure Ile341Aha

The X-ray structure of Ile341Aha (PDB: 5mz7) was resolved with a resolution of 1.5 Å and is equipped with 4 molecules in the asymmetric unit. An alignment of every chain from the Ile341Aha structure with the WT structure (PDB: 1BFE) shows only very small changes in the overall structure (**table 4.12** and **figure 4.2.6**). The main changes are visible in the carboxylate binding loop L1, the flexible loop L2, and the α3 helix. These three elements show a higher conformational flexibility in the WT structure as well as in the Ile341Aha structure. Therefore, deviations in these regions are expected and could also derive from the position of the chain in the asymmetric unit. They do not originate from the mutation. In two chains the L2 conformation matches the WT structure. Only minor structural changes around the mutation site were found [104].

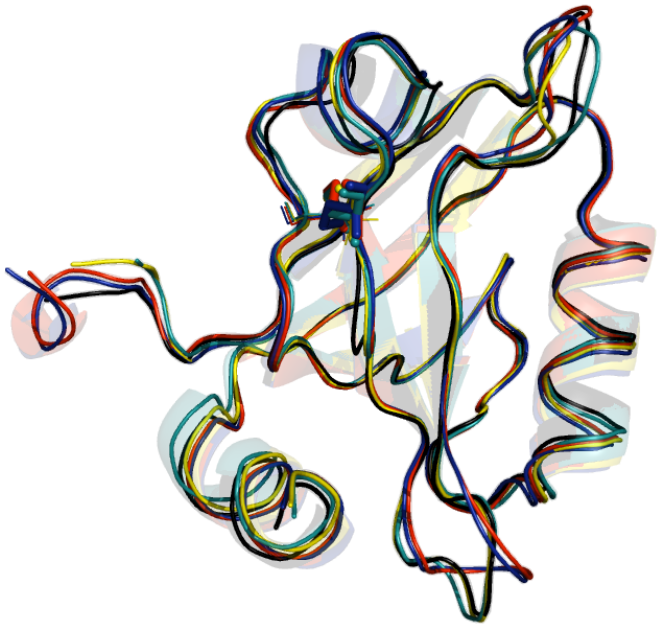

Figure 4.2.6: C_α alignment of chain A-D of the X-ray structure of Ile341Aha (PDB: 5mz7) with the WT PDZ3 (PDB: 1BFE). The WT is colored black, Ile341Aha chain A red, chain B blue, chain C yellow, and chain D cyan. The Aha is depicted in sticks.

In the alignment of the four chains among each other (**table 4.12**) the flexible elements L1, L2, and α3 show the highest aberrations as well. However, the overall

fold of the protein is very similar and highly conserved. The Aha incorporation is only minimally invasive [104].

Table 4.12: Alignment parameters of chain A-D of the crystal structure of Ile341Aha (PDB: 5mz7) between themselves and to WT PDZ3 (PDB: 1BFE). The root mean square deviation (RMSD) of all heavy atoms and the C_α RMSD were calculated.

	RMSD	RMSD C_α
ChainA-WT	0.544	0.491
ChainB-WT	0.621	0.551
ChainC-WT	0.530	0.473
ChainD-WT	0.538	0.485

	RMSD	RMSD C_α
ChainB-ChainA	0.321	0.314
ChainC-ChainA	0.482	0.417
ChainD-ChainA	0.476	0.422

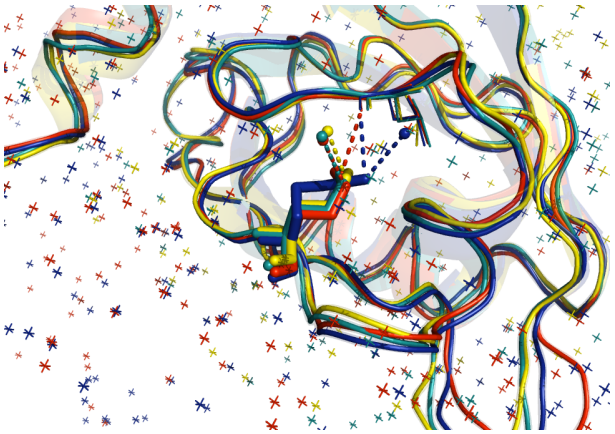

Figure 4.2.7: C_α alignment of chain B-D of the X-ray structure of Ile341Aha (PDB: 5mz7) with chain A at the mutation site. Chain A is colored red, chain B blue, chain C yellow, and chain D cyan. Aha is depicted as sticks, bound water molecules as spheres and non-covalent interactions of the Aha side chain with other groups of PDZ3 and solvent water molecules as dashed lines.

NMR measurements on Ile341Aha, WT, and Ile341Met, which were conducted by our collaboration partners from the Schwalbe group, also revealed that changes between Ile341Aha and WT are mainly located in proximity of the mutation site and are small [104]. In contrast to the crystal structure only one orientation of the L2 loop was found in solution. Chemical shift perturbations for Ile341Met are very similar to the ones of Ile341Aha, suggesting that the small changes compared to WT are caused by the mutation site and not the type of mutation. The Aha incorporation has only minor effects on the internal flexibility of the protein. Ligand binding of the Hepta ligand is very similar in Ile341Aha and WT and only a very small destabilization of the mutant complex was found.

The Aha side chain points towards the interior of the protein similar to the Ile341 orientation in the WT in the X-ray structure. Its orientation is very similar in chain A, C, and D and a bit twisted in chain B (**figure 4.2.7** and **figure 4.2.8**). All azido groups form a hydrogen bond between their terminal N-atom and a water molecule at a distance of 3.1 to 3.5 Å. For chain A, C, and D the hydrogen bonded

water molecule is at a similar position. The Aha side chain in chain A and B might form an electrostatic interaction with the carbonyl O-atom of the opposing Leu353 backbone. For chain C and D the distance might be a bit too large for this kind of interaction because of slightly different orientations of Leu353 and the Aha side chain. To the best of our knowledge these kind of electrostatic interaction with an opposing backbone group (instead of with its own backbone carbonyl O-atom) has not been described for Aha in a protein before.

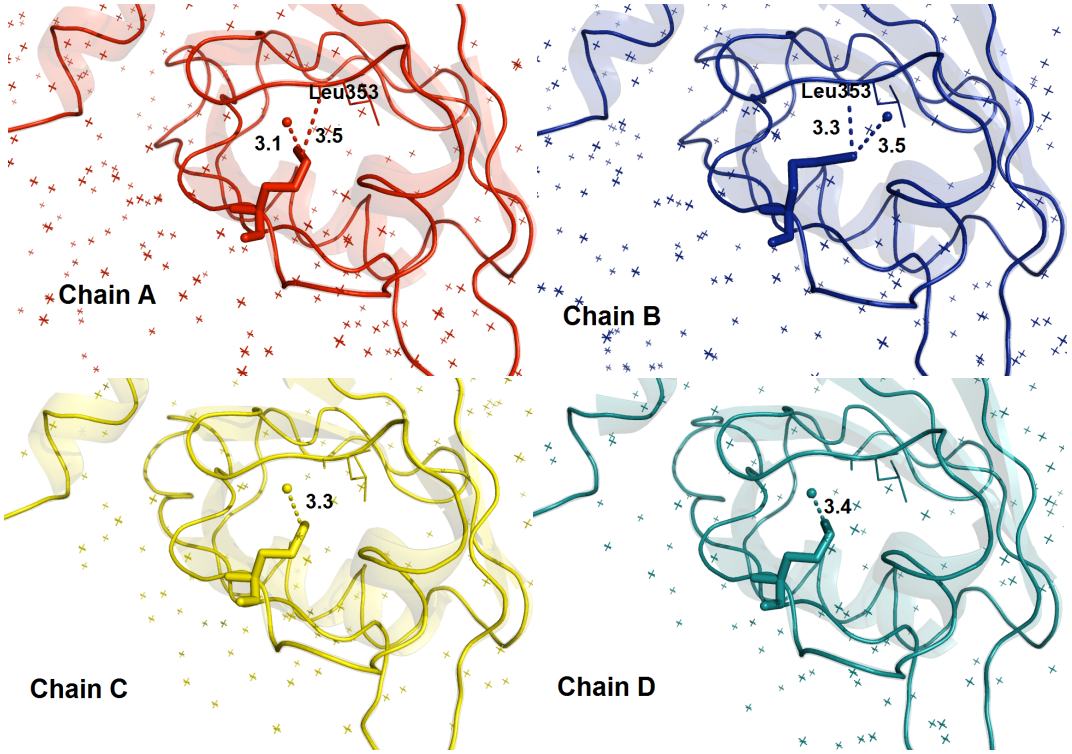

Figure 4.2.8: Non-covalent interactions of the Aha side chain in the Ile341Aha crystal structure of chain A (red), chain B (blue), chain C (yellow), and chain D (cyan) (PDB: 5mz7). Aha is depicted as sticks and non-covalent interactions to other atoms in PDZ3 and solvent water (spheres) molecules are shown as dashed lines.

4.2.3.2 Crystal Structure Val362Aha

Table 4.13: Alignment parameters of chain A-D of the crystal structure of Val362Aha between themselves and to WT PDZ3 (PDB: 1BFE).

	RMSD	RMSD C_α
ChainA-WT	0.595	0.518
ChainB-WT	0.706	0.663
ChainC-WT	0.528	0.505
ChainD-WT	1.00	0.962

	RMSD	RMSD C_α
ChainB-ChainA	0.395	0.392
ChainC-ChainA	0.448	0.390
ChainD-ChainA	0.662	0.577

The crystal structure of Val362Aha has a resolution of 1.72 Å and consists of four molecules in its asymmetric unit. An itemized alignment of the four chains with

the WT structure reveals that the overall structures are very similar (**table 4.13** and **figure 4.2.9**). The main changes are again in the flexible loops L1 and L2. Partly, the structures seem to have a small parallel offset. The conformational structure around the mutation site is largely unperturbed upon Aha incorporation.

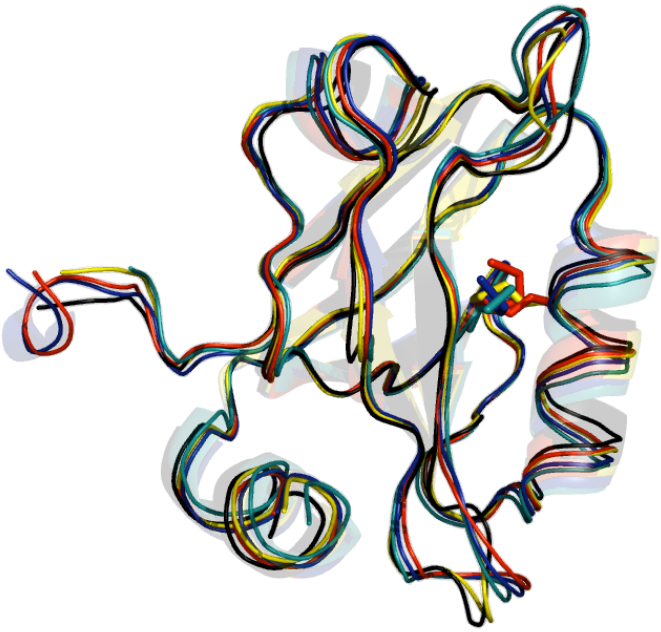

Figure 4.2.9: C_α alignment of chain A-D of the X-ray structure of Val362Aha with the WT PDZ3 (PDB: 1BFE). The WT is colored black, Val362Aha chain A red, chain B blue, chain C yellow, and chain D cyan. The Aha is depicted in sticks..

Figure 4.2.10: C_α alignment of chain B-D of the X-ray structure of Val362Aha with chain A at the mutation site. Chain A is colored red, chain B blue, chain C yellow, and chain D cyan. Aha is depicted as sticks and non-covalent interactions of the Aha side chain with other groups of PDZ3 as dashed lines.

The alignment of the four Val362Aha chains among each other shows high similarities and again the main differences are found in L1 and L2 (**table 4.13**). The α3-helix of chain D shows small changes, which might be caused by its location at the edge of the asymmetric unit.

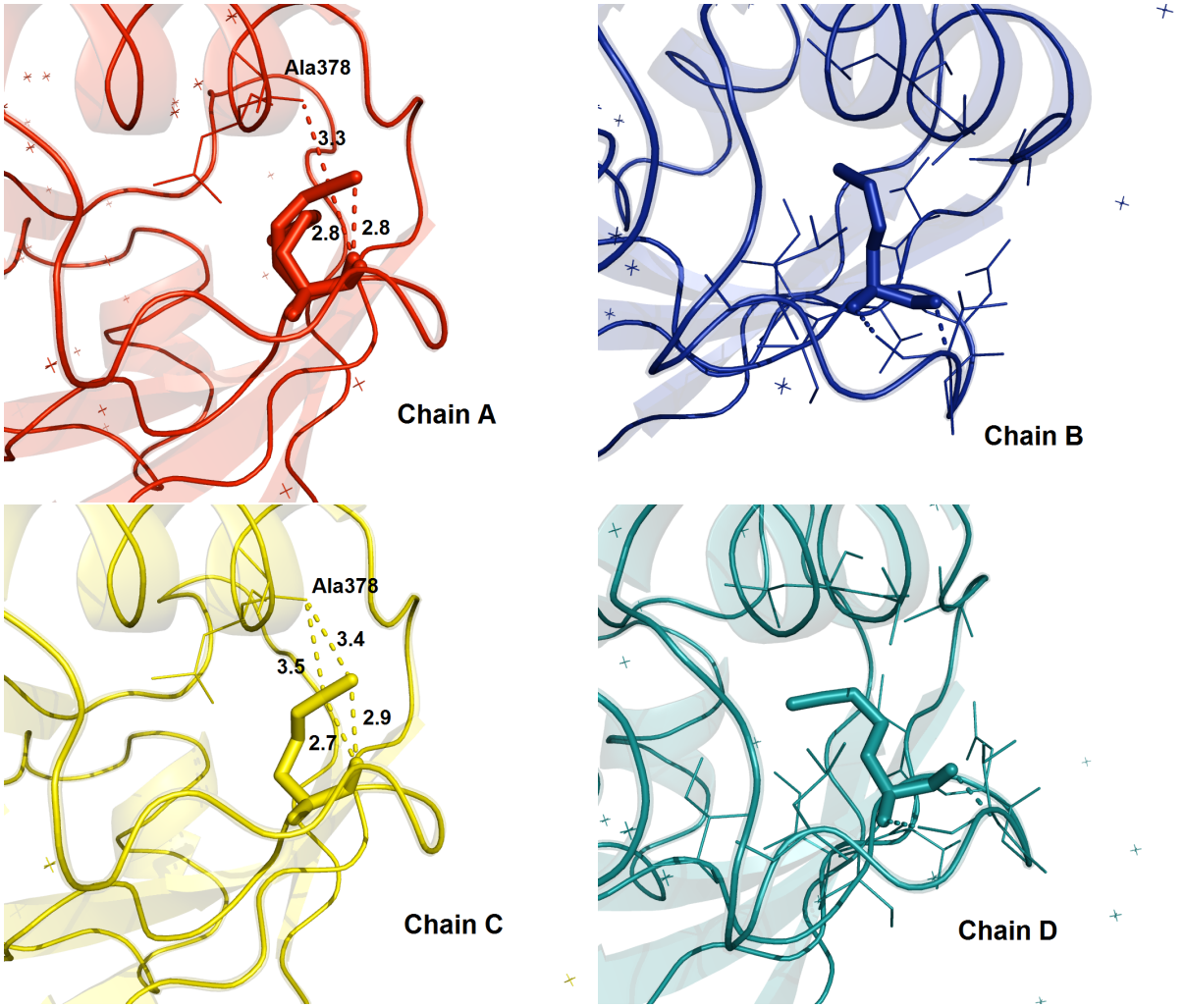

Figure 4.2.11: Non-covalent interactions of the Aha side chain in the Val362Aha crystal structure of chain A (red), chain B (blue), chain C (yellow), and chain D (cyan). Aha is depicted as sticks and non-covalent interactions to other atoms in PDZ3 are shown as dashed lines.

The Aha orientation seems to be compressed compared to the original Val side chain at this position (**figure 4.2.10** and **figure 4.2.11**). The rough orientation of the Aha side chains is similar in chain A and C, in which it points more in the direction of the protein surface, and in chain B and D, in which it points to the protein interior. Chain A shows multiple Aha conformations. One conformation of the Aha side chain is strongly bended, so much that it forms an electrostatic interaction with the carbonyl O-atom of its own backbone (2.8 Å). At the same time an electrostatic interaction to the carbonyl O-atom of the opposing Ala378 backbone is formed on the other site of the Aha side chain (3.3 Å). The azido group

is tucked between these two carbonyl O-atoms. The second orientation of the Aha side chain in chain A does not form any non-covalent interactions. In chain C the tucking of the Aha side chain between the carbonyl O-atoms of Ala378 and its own backbone can be found as well. In chain B and D the side chain of Aha does not form any non-covalent interactions. It is oriented into the protein interior while the Leu379 side chain is turned to give place for it.

4.2.3.3 Crystal Structure Ile338Aha

With a resolution of 1.43 Å and four molecules in an asymmetric unit, the X-ray structure of Ile338Aha also shows mainly accordance with the WT structure (**table 4.14** and **figure 4.2.12**). The main deviations are again seen in L1 and L2. For this mutant also minor changes around the mutation site in the βC-sheet are found.

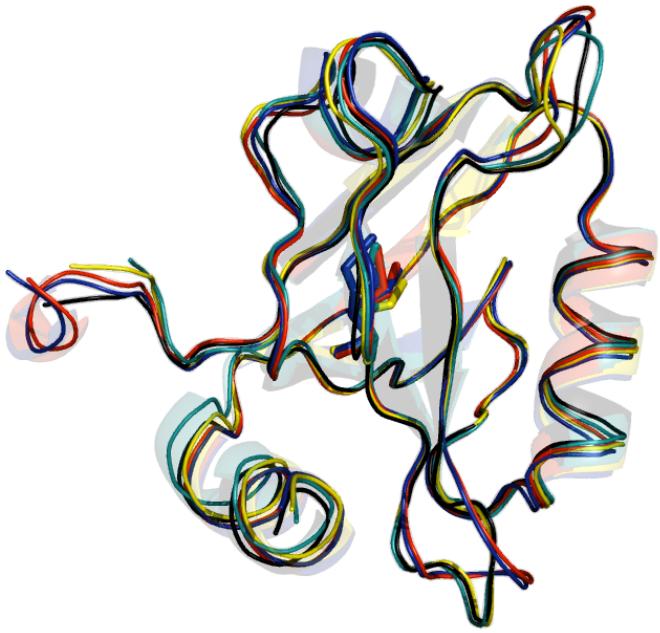

Figure 4.2.12: C_α alignment of chain A-D of the X-ray structure of Ile338Aha with the WT PDZ3 (PDB: 1BFE). The WT is colored black, Ile338Aha chain A red, chain B blue, chain C yellow, and chain D cyan. The Aha is depicted in sticks.

Table 4.14: Alignment parameters of chain A-D of the crystal structure of Ile338Aha between themselves and to WT PDZ3 (PDB: 1BFE).

	RMSD	**RMSD C_α**
ChainA-WT	0.584	0.510
ChainB-WT	0.632	0.564
ChainC-WT	0.517	0.445
ChainD-WT	0.497	0.409

	RMSD	**RMSD C_α**
ChainB-ChainA	0.325	0.275
ChainC-ChainA	0.543	0.456
ChainD-ChainA	0.454	0.411

The alignment of the four chains among each other revealed high similarities with the largest changes in L1 and L2 and for chain D in the α3-helix (**table 4.14**).

Two rough main orientations of the Aha side chain exist, being oriented along the original Ile side chain directions (**figure 4.2.13**). The orientation along the Ile -CH_2-CH_3 end is preferred compared to the -CH_3 end. For the former a nearly continuous distribution of slightly different conformations is found, suggesting that there is plenty of space at this position. Chain A, B, and C exhibit multiple sub conformations of the Aha side chain. One orientation of chain B is pointing along the -CH_3 end of the original Ile338. An electrostatic interaction might be formed to the Arg345 backbone carbonyl O-atom (3.4 Å).

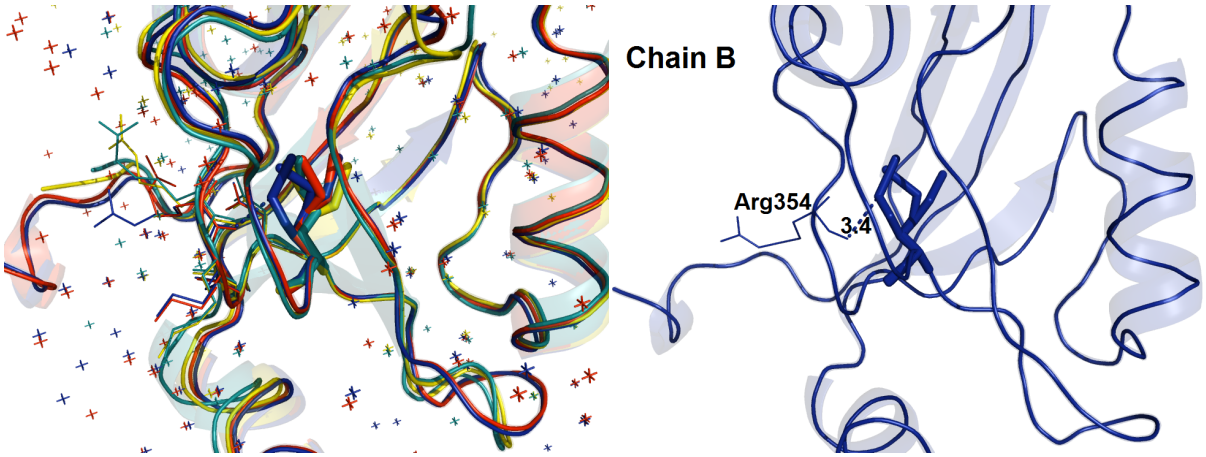

Figure 4.2.13: Right: C_α alignment of chain B-D of the X-ray structure of Ile338Aha with chain A at the mutation site. Chain A is colored red, chain B blue, chain C yellow, and chain D cyan. **Left:** Detailed view onto the Aha side chain interactions in chain B. Aha is depicted as sticks and non-covalent interactions of the Aha side chain with other groups of PDZ3 as dashed lines.

4.2.3.4 Crystal Structures Ala376Aha and Val386Aha

Crystal structures of Ala376Aha and Val386Aha were also determined by Deniz Üresin in course of his master thesis (not published yet). However, the resolution was not high enough (3.1 and 2.13 Å, respectively) to resolve Ahas side chain orientation, but the overall folding of PDZ3 seems not to be perturbed by the Aha mutation.

4.2.3.5 Crystal Structures Discussion

Overall the protein fold of PDZ3 seems to be highly conserved upon incorporation of Aha. Flexible elements like the two loops L1 and L2 and the α3-helix show the largest deviations. These deviations are not caused by the mutation. Only minor changes can be found around the mutation sites. Crystal structure data fit the data

determined with CD spectroscopy. For the only mutant, which exhibits a changed CD signal, unfortunately no X-ray structure is available. In all other mutants Aha incorporation is only minimally invasive at the majority of positions.

Multiple different Aha orientations are occurring in the individual mutants. The azido group can form an intramolecular electrostatic interaction with the carbonyl O-atom of its own backbone as it has been suggested by QM/MM MD simulations of Aha in NTL9 [177]. Furthermore, similar interactions were found with the backbone carbonyl O-atom of opposing AA residues. To the best of our knowledge this is the first time these types of interactions were discovered. In addition, the azido group is able to form these two types of electrostatic interactions simultaneously. Moreover, intermolecular hydrogen bonding to internal water molecules was observed. The capabilities of possible conformations and non-covalent interactions of the Aha side chain to other atoms are found to be more versatile in a protein fold than in solvent.

4.2.4 FTIR Spectroscopy PDZ3-Aha

4.2.4.1 FTIR Ligand Binding and Reproducibility PDZ3-Aha

FTIR spectra of azido's asymmetric stretching band of Aha were measured for the 15 mutants, for the unbound PDZ3 and for ligand bound PDZ3 (to Hepta) (**figure 4.2.14**). Some of the detected IR bands are much broader than the bands of the Ahas in solvent and show conspicuous sub structures consisting of multiple sub bands. Despite the small total structural change of PDZ3 upon ligand binding [210], remarkable changes of the Aha IR band upon ligand binding are obtained for some mutants. Since the detected Aha IR bands are very tiny (between 3 and 23 mOD) compared to the corrected solvent background, it has to be tested how reproducible the band shape between different measurements of the same sample is in order to be able to judge if a change in the band shape is ligand induced or just caused by measurement uncertainties. Therefore, in total 73 IR spectra of the PDZ3-Aha mutants with and without ligand were analyzed. Two independent spectra of several samples are compared, respectively (**figure 4.2.15**). For the samples being measured more than twice, the two strongest differing spectra are depicted.

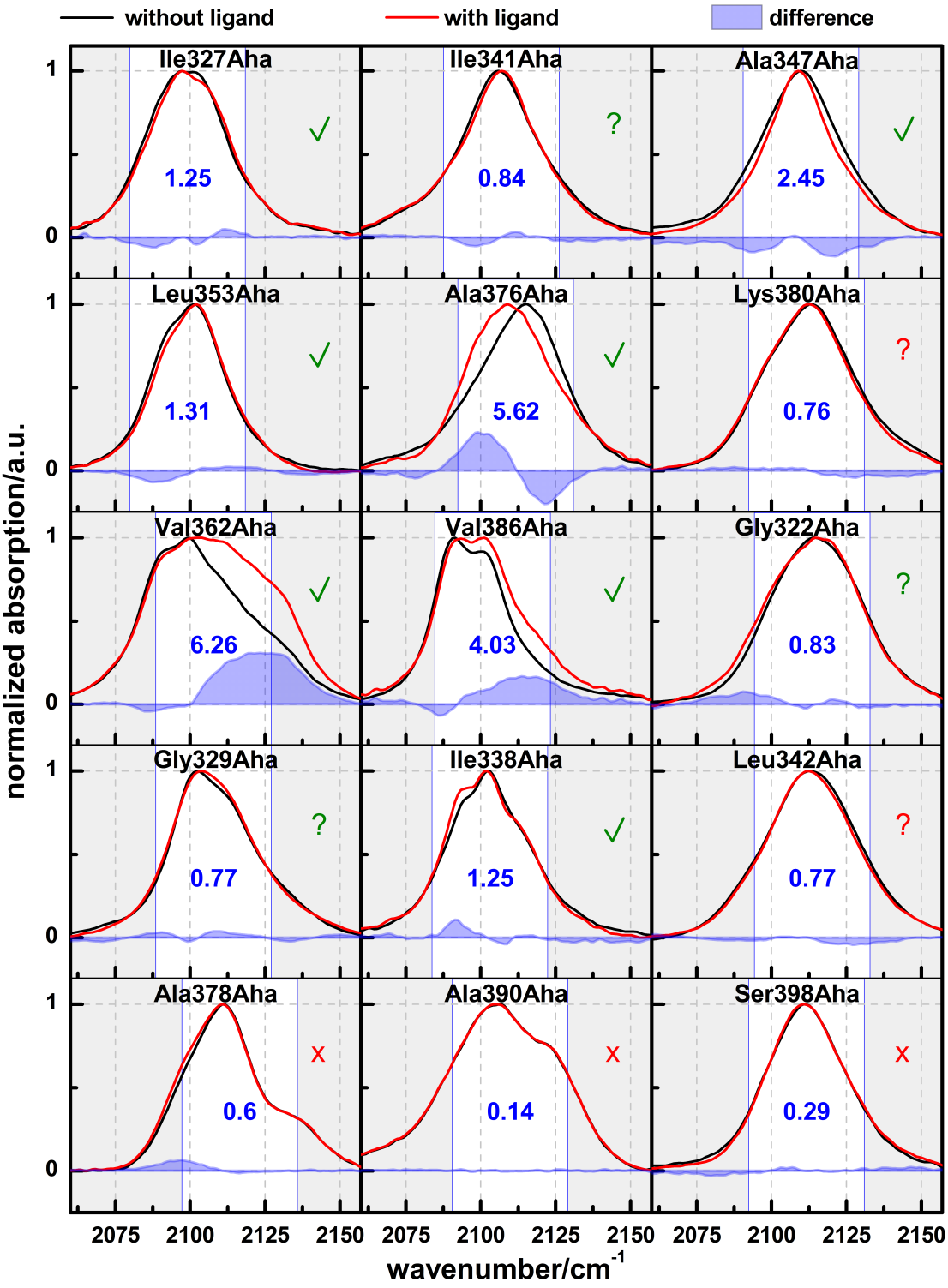

Figure 4.2.14: FTIR spectra of azido's asymmetric stretching band of 15 PDZ3-Aha mutants, unbound (black) and bound (red) to the Hepta ligand. The spectra are normalized to 1. The difference spectra of the bound and unbound state is colored blue. The white box with the blue borders gives the integration range for the difference area (blue number). The symbols (✔, ?, X) mark PDZ3-Aha mutants with similar characteristics regarding the difference spectra between the bound and unbound state.

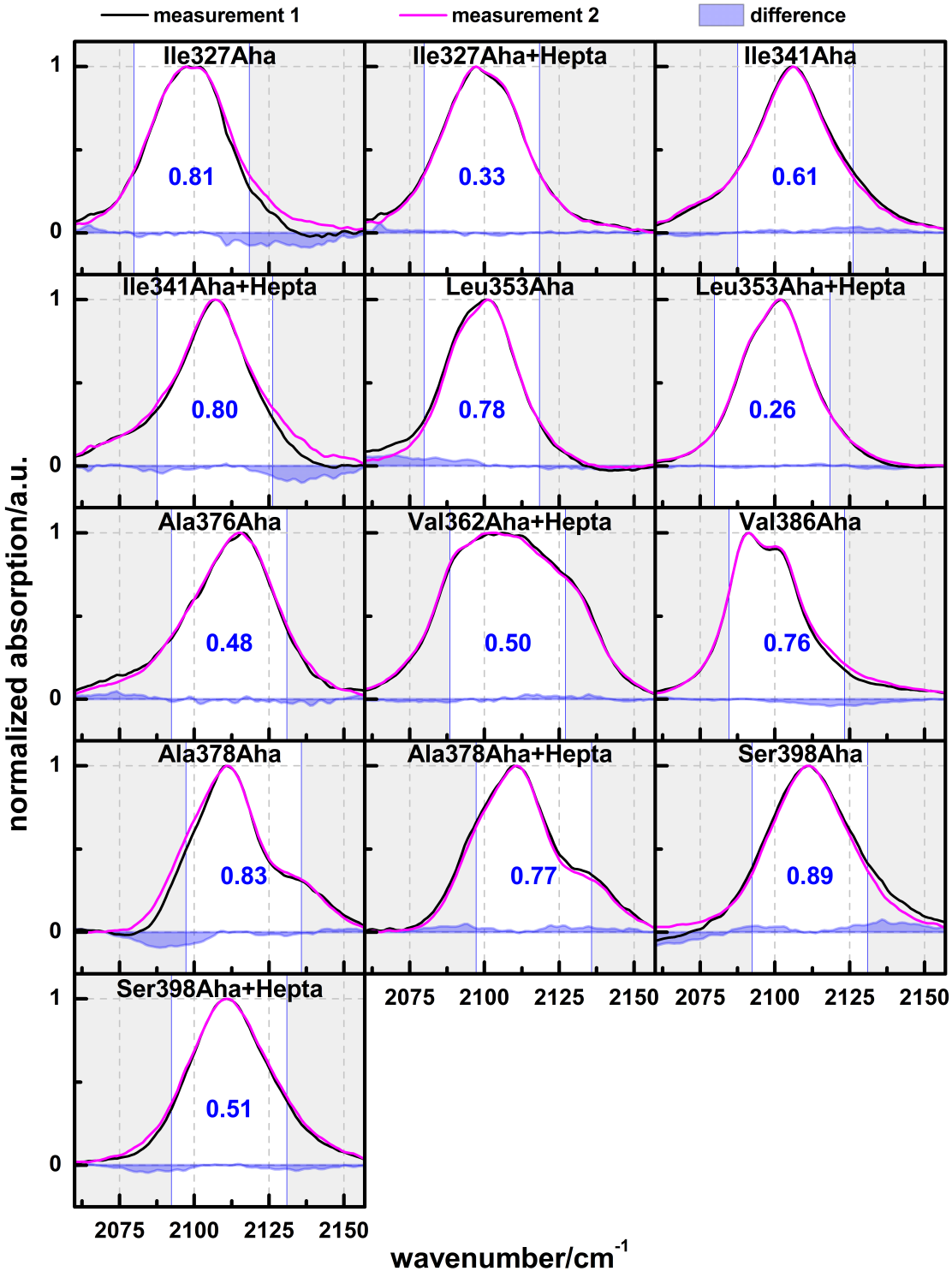

Figure 4.2.15: FTIR spectra of azido's asymmetric stretching band of some PDZ3-Aha mutants deriving from two independent measurements (black and magenta). The spectra are normalized to 1. The difference spectra of the two spectra is colored blue. The white box with the blue borders gives the integration range for the difference area (blue number).

Overall the reproducibility is very good for such a small band. In order to compare the ligand induced spectral changes and spectral changes caused by measurement uncertainties, the difference spectra of the two independent measurements were calculated as well as the ones between the unbound and bound spectra (blue curves in **figure 4.2.14** and **4.2.15**). In contrast to the ligand binding difference spectra, the reproducibility difference spectra show rather non zero signals at the outer flanks of the Aha bands than at Aha band maximum. Differences in the flanks are likely to be caused by the correction of the water background signal, which is several orders of magnitude larger than the Aha band. Even though the IR spectra of the PDZ3-Aha samples were directly measured against buffer background in the same sample cell, the buffer concentration is lower in the protein sample than in pure buffer because of the high protein concentration. Therefore, an inverse water signal remains, for which was corrected by a 5th order polynomial function. This correction seems to work much better in the middle of the Aha band than at its flanks, where the signal size is of course even smaller than at the maximum. Indeed, bands with a very small signal used to show stronger deviations in their flanks.

In order to incorporate this observation and allow a simplified way to compare the particular effects, the difference spectra were integrated in the signal range excluding the flanks. For this an integration window of 38.5 cm^{-1} was set covering the Aha band (white box with blue borders) and the absolute difference area in this range was calculated. As the choice of the integration window was set at discretion, the calculated difference areas have to be considered very carefully. They cannot be understood to be absolute; they are just a way to comprise observed effects and to be able to correlate them with other parameters in a graphical manner. Furthermore, it has to be considered, that all spectra were normalized to 1 at the band maximum prior to the analysis because the exact labeling efficiency and the accurate concentration of PDZ3-Aha were not known. Therefore, ligand induced spectral changes caused by a change in the extinction coefficient are not visible in our analysis. Due to the normalization on the total band maximum the difference spectrum is also modified if the ratio of the sub bands changes.

Comparing the ligand induced difference areas (blue) with the difference areas caused by reproducibility issues (grey) (**figure 4.2.16**) three different groups of PDZ3-Aha mutants evolve. The first group (Val362Aha, Ala376Aha, Val386Aha, Ala347Aha, Leu353Aha, Ile338Aha, and Ile327Aha; marked with a green hook in **figure 4.2.14**) shows a significant ligand induced spectral change clearly being larger than the reproducibility level. The second group (Ile341Aha, Gly322Aha, Leu342Aha, Gly329Aha, and Lys380Aha; marked with an orange or green ? (see below) in **figure 4.2.14**) exhibits a difference area of a similar size as the largest difference areas caused by reproducibility issues. Their spectra have to be analyzed separately in more detail to determine if a ligand induced spectral shift is observed. The difference area of the third group (Ala378Aha, Ser398Aha, Ala390Aha;

marked with a red X in **figure 4.2.14**) is much smaller than the reproducibility level and, therefore, no ligand induced shift is detectable. They are denoted as showing no ligand induced shift, even if effects smaller than the reproducibility level are possible.

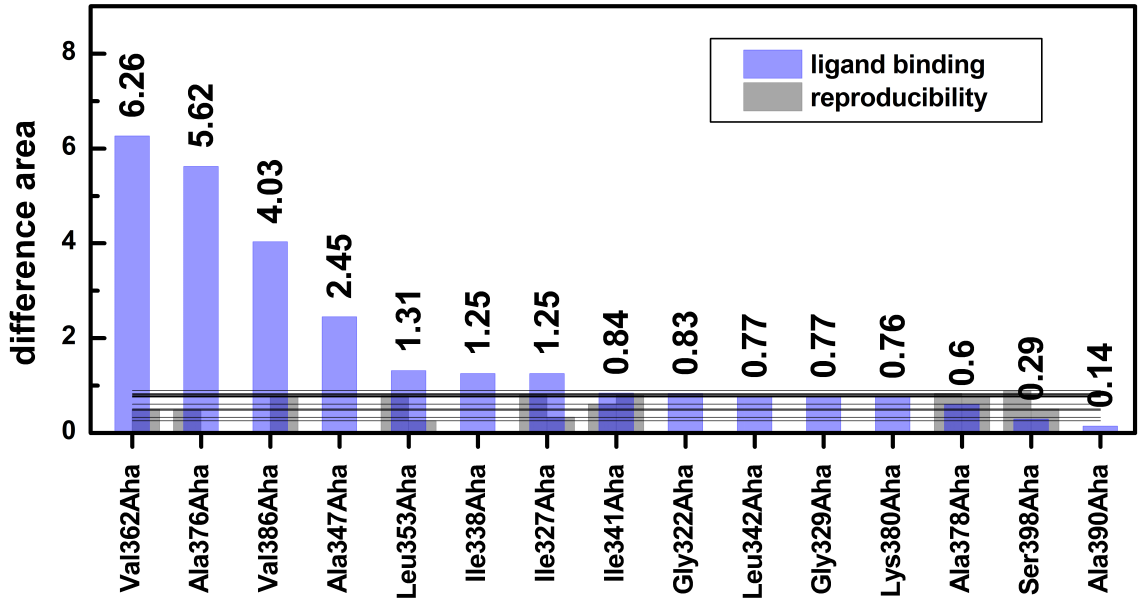

Figure 4.2.16: PDZ3-Aha FTIR difference areas deriving from ligand binding (blue) compared to the difference areas caused by reproducibility issues (grey). The levels of the latter are marked with black lines.

For the second group a closer look has to be taken on the spectral features of the difference spectra. As mentioned above reproducibility issues prone to cause a difference signal rather at the flanks than in the middle. Furthermore, these difference spectra seem to be noisier compared to the ligand induced spectral changes. The difference spectra of ligand bound/unbound Ile341Aha exhibits a smooth signal with a pronounced shape in the middle range of the Aha signal. The clear difference to the spectral feature of the reproducibility difference spectra suggests that the spectral change in Ile341Aha upon ligand binding is ligand induced and not caused by measurement uncertainties. Similar behavior is observed for the spectra of Gly329Aha and Gly322Aha. Therefore, their question mark is colored green, because it is likely that a ligand induced spectral change is observed. In contrast, the difference spectra of Lys380Aha and Leu342Aha rather exhibit signals in the flank region, which are noisier. They cannot be clearly distinguished from the difference spectra caused by measurement uncertainties. Therefore, they are assigned not to show ligand induced spectral changes in the reproducibility level of the measurements and the question marks are colored red.

4.2.4.2 FTIR Multiple Bands PDZ3-Aha

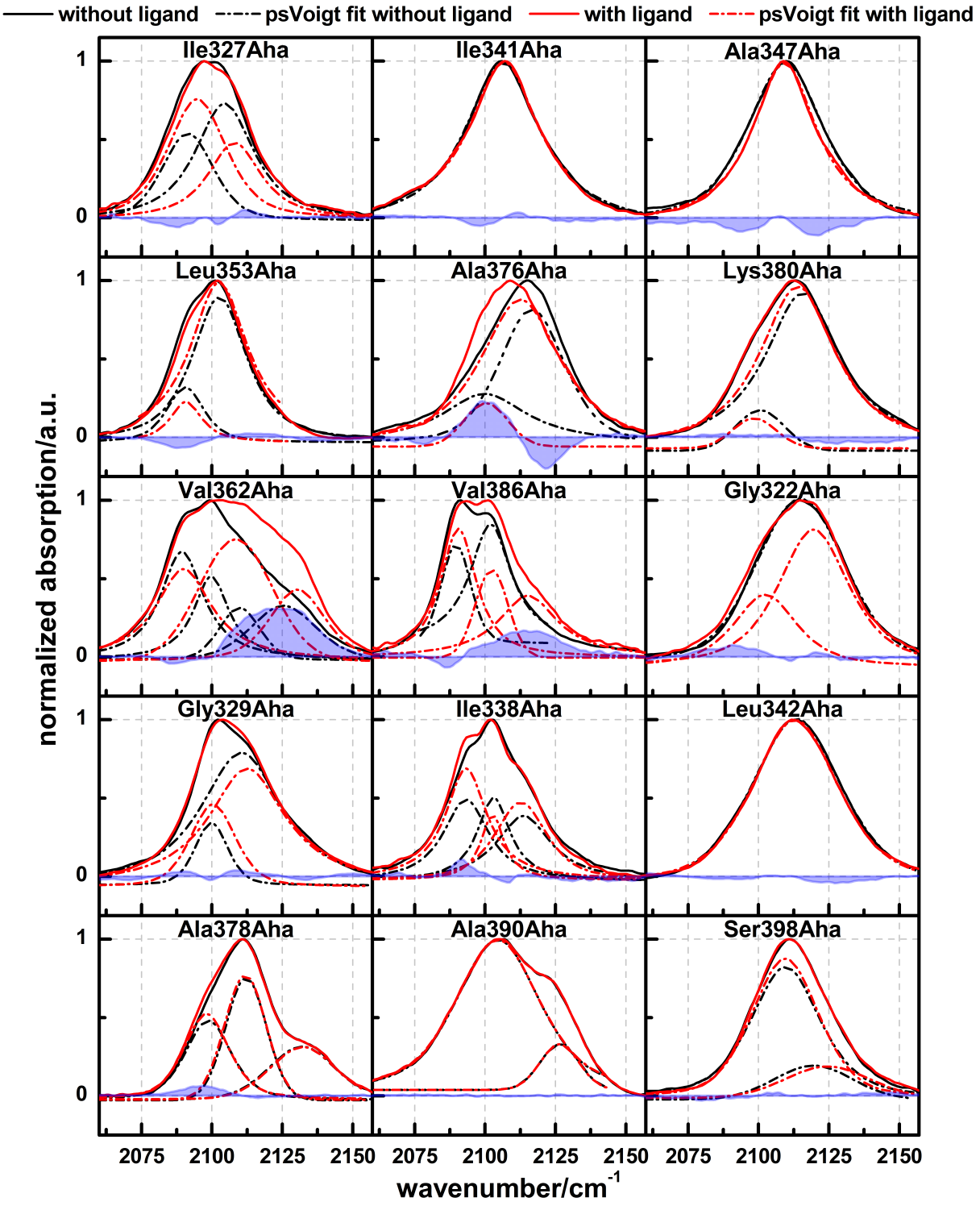

Figure 4.2.17: Fit of multiple (1-4) psVoigt functions (dashed lines) to the Aha bands (solid line) of ligand bound (red) and unbound (black) PDZ3-Aha. The overall fit to the spectra, which is the sum of the multiple psVoigt functions, and the fit parameters can be seen in the appendix (**figure A.0.2**, **figure A.0.3**, and **table A.2**).

The crystal structures of the three PDZ3-Aha mutants show multiple possible Aha side chain orientations, which can be understood as different conformational states. Similarly, the azido's asymmetric stretching band seems to consist of a number of sub bands, which can emerge from the Aha side chain being exposed to different local environments.

To further investigate the Aha IR absorption, the bands were fitted by a sum of 1-4 psVoigt functions (**equation 3.2.1**) (**figure 4.2.17**, **figure A.0.2**, and **figure A.0.3**; fit parameters in **table A.2**). The number of assumed sub bands was determined by counting the minima of the second derivative of the Aha band.

In several PDZ3-Aha mutants with multiple sub bands (Ile327Aha, Leu353Aha, Ile338Aha, Gly329Aha, and Lys380Aha) ligand binding seems to rather change the relative population of the bands to each other than shifting them. In Val386Aha not only the population ratio between two sub states changes, but also a third sub band arises upon ligand binding. Consequently, the difference signal follows the shape of sub bands for several of the mutants. A changed conformational equilibrium upon ligand binding is a feature of the conformational selection mechanism (see **chapter 2.1**) [1, 2, 4]. Explicit solvent MD simulations on PDZ3 found 3 sub states (A-C) in the in absence of the ligand, from which one (A) is selected upon ligand binding via conformational selection [17]. In the crystal structures only the A state is populated. As the Aha side chain shows different orientations even in its crystal structure, the visible sub bands might not reflect the different protein states, but rather Aha orientations and altered non-covalent interactions to surrounding atoms. However, the distinct protein conformations can exhibit different population ratios of the Aha side chain sub states. The large shift of the band of Ala376Aha upon ligand binding might be caused by water being expelled out of the binding pocket and, thus, changing the environment of the Aha side chain dramatically.

The band maximum of the single psVoigt peaks (**table 4.15**) ranges from 2089.4 cm^{-1} in Val362Aha to 2132.3 cm^{-1} in Ala378Aha. Latter is higher than the formerly published highest value of 2128.9 cm^{-1} for Aha in a protein [106]. In combination with the lowest measured wavenumber of 2084.0 cm^{-1} [106] a new total range of 48.3 cm^{-1} arises for possible band maxima of Aha incorporated into a protein. Several of the found bands in PDZ3-Aha are significantly red shifted compared to bocAha/fmocAha in aprotic solvents and some are even more blue shifted compared to bocAha/fmocAha in strong protic solvents. Therefore, additional contributions to the band maximum of the azido moiety must play an important role in proteins compared to solution.
MD simulations predicted that for distinct non-ideal hydrogen bond angles between the azido group and surrounding water molecules a red shift of the Aha band occurs and that the Aha can be forced to bind water molecules in these angles in a protein environment due to constricted space. Also a coulomb interaction between

the central N-atom of the Aha and its backbone carbonyl O-atom was proposed to strongly blue shift the Aha band [176, 177]. A polar contact with the negatively charged side chain carbonyl O-atom of a Glu has also been suggested by an MD simulation approach to induce a red shift [103]. Hydrogen bonding to the protic side chains of other residues, which might also occur in non-ideal angles, would be a possible effect in a protein environment, as well.

Table 4.15: Band maximum of the distinct psVoigt functions from the multiple psVoigt fit of the PDZ3-Aha bands.

mutant	ligand	band1 max /cm^{-1}	band2 max /cm^{-1}	band3 max /cm^{-1}	band4 max /cm^{-1}
Ala347Aha	**without**	2109.5			
	Hepta	2109.2			
Ala376Aha	**without**	2099.7	2116.6		
	Hepta	2100.3	2112.6		
Ala378Aha	**without**	2098.7	2112.1	2132.0	
	Hepta	2098.1	2111.9	2132.3	
Ala390Aha	**without**	2104.5	2126.5		
	Hepta	2104.5	2126.4		
Gly322Aha	**without**	2114.9			
	Hepta	2102.4	2119.6		
Gly329Aha	**without**	2099.8	2110.5		
	Hepta	2100.4	2112.5		
Ile327Aha	**without**	2091.5	2104.5		
	Hepta	2094.8	2108.0		
Ile338Aha	**without**	2093.2	2103.0	2113.7	
	Hepta	2093.3	2102.6	2112.7	
Ile341Aha	**without**	2106.2			
	Hepta	2106.7			
Leu342Aha	**without**	2113.5			
	Hepta	2113.1			
Leu353Aha	**without**	2090.6	2102.6		
	Hepta	2090.2	2102.3		
Lys380Aha	**without**	2100.6	2115.6		
	Hepta	2098.5	2114.0		
Ser398Aha	**without**	2109.6	2119.5		
	Hepta	2109.5	2124.5		
Val362Aha	**without**	2089.4	2099.8	2109.9	2125.4
	Hepta	2090.0	2108.5	2130.4	
Val386Aha	**without**	2089.7	2102.0		
	Hepta	2090.5	2102.4	2115.3	

In none of the PDZ3-Aha mutants any acidic AA side chain is in the close proximity of the Aha side chain. In addition, only a few mutants exhibit protic side chains, which can serve as a hydrogen bond donor, in the surrounding of the Aha side chain (Leu353Aha, Ala376Aha, Gly329Aha, Val362Aha, and Gly322Aha). In Val362Aha no hydrogen bond to another side chain was found in the crystal structure and Ala376Aha is located at the protein surface and is, therefore, highly water exposed making other hydrogen bonds unlikely. The other three exhibit band max-

ima within the range of the bocAha/fmocAha in solvent. However, electrostatic contacts with the carbonyl O-atom of the own backbone and/or with an opposing backbone carbonyl O-atom of another residue as found in the crystal structure and non-ideal hydrogen bonds to internal water molecules might be a reason for the significantly larger range of the Aha band position in a protein compared to solvent. The influence of the angle of these electrostatic interactions on the band position of the Aha band needs to be further investigated by MD simulations. Also the orientation of the transition dipole moment and the change in dipole moment could be different in a protein compared to solution, which might also affect solvatochromic wavenumber shifts caused by the solvent field.

4.2.4.3 FTIR Band vs. SASA PDZ3-Aha

The SCN vibrational wavenumber was shown to correlate with the SASA as a measure of water exposure of the mutation site, even if other factors like polarity, electrostatic field, and internal hydrogen bonding have to be taken into account as well [142, 150].

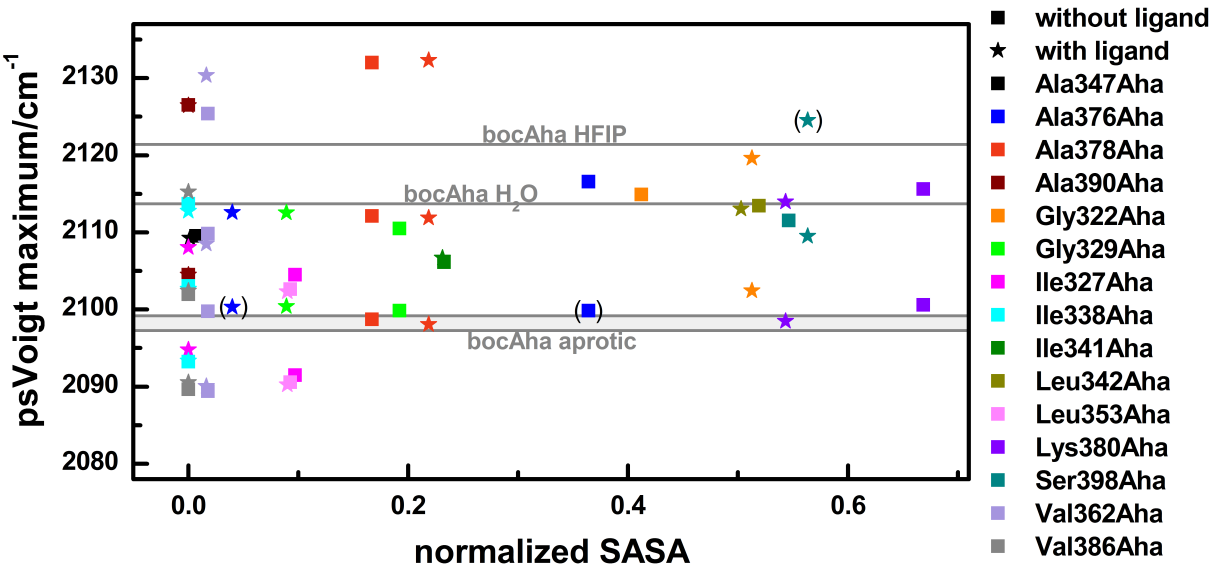

Figure 4.2.18: Correlation of the psVoigt band maximum with the normalized SASA. The band position range of bocAha in solvents is depicted as grey lines for comparison.

The correlation of solvent exposure and the Aha band maximum in a protein has not been investigated before. The band maximum of the psVoigt peaks was plotted against the normalized SASAs of the 15 PDZ3-Aha mutation sites (**table 4.8** and **figure 4.2.18**). The grey lines give the range of the band maximum found for bocAha in solvents. The psVoigt fits of the bands at the flank of the Aha band, which show only a very small signal, are bracketed, because they might derive from the

background correction. At moderate and high solvent water exposure the band maximum wavenumbers are all within the range of possible band positions of boc-Aha in solvent. At SASAs > 0.3 the strongest psVoigt band of each mutant exhibits a band maximum close to the one of bocAha in H_2O. But at low SASAs a broader wavelength variation than in any solvent is obtained for Aha in a protein. Additionally, pronounced multiple band structures are rather found at moderate and low SASAs being linked to restricted space at these positions, which leads to more distinct conformational sub states. As discussed above, electrostatic interactions to backbone carbonyl O-atoms and hydrogen bonds to internal water molecules at non-ideal angles might be the reason for this phenomenon. It is conceivable that for a protein in solution also internal water molecules are present, which are not considered by the SASA calculation on the crystal structure.

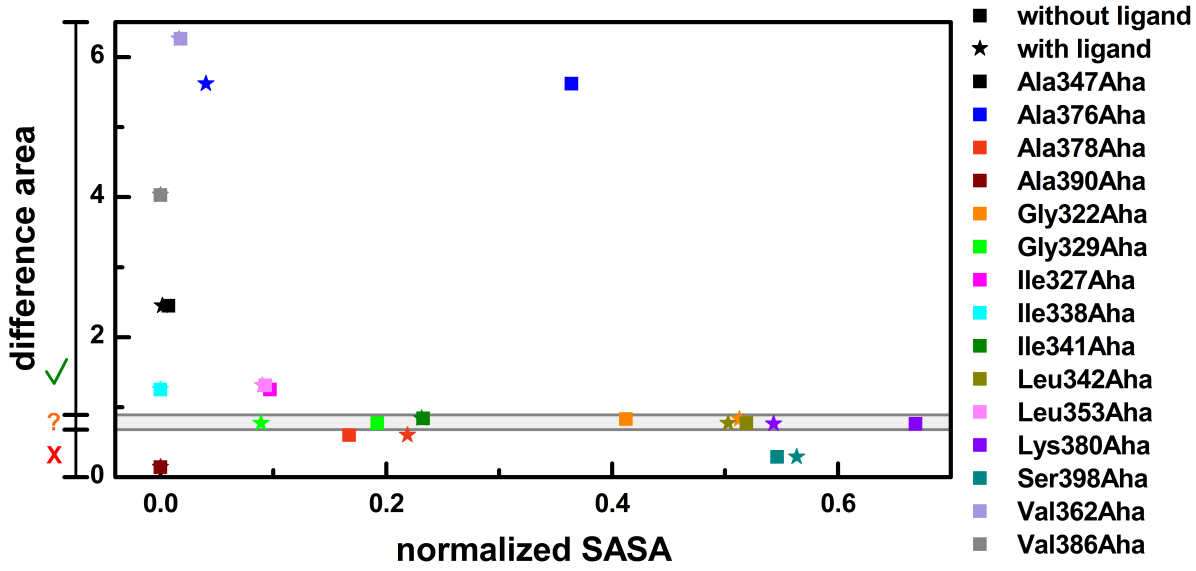

Figure 4.2.19: Correlation of the difference area of PDZ3-Aha with/without Hepta with the normalized SASA. The reproducibility range is depicted in grey. The range of the three groups of PDZ3-Aha is marked on the y-axis with a green hook, an orange question mark, and a red X.

Looking at the relation between the difference area between bound and unbound PDZ3-Aha and the normalized SASA, large ligand induced difference signals can be found only at a low solvent exposure of Aha. The value for Ala376Aha without ligand is standing out because in this mutant a very high change of the solvent accessibility upon ligand binding proceeds and a low SASA is reached when the ligand is bound. Therefore, it also fits the trend. The Aha label seems to get much more sensitive to subtle structural changes at low SASAs. This is not surprising as solvent exposed Aha forms ideal hydrogen bonds to water and subtle structural changes of the protein might not perturb these interactions. Only one mutant with a very low SASA and a pronounced double band structure does not show a ligand induced spectral change (Ala390Aha). In the model of Lockless and Ranganathan [5] and Ota and Agard [6] this residue position is off-pathway. By contrast, the

other in this sense off-pathway mutant (Ile338Aha) with a very low SASA and a pronounced triple band structure exhibits a clear ligand induced spectral change. Unfortunately, the other 3 off-pathway mutants are moderately or highly solvent exposed (Ala378Aha, Leu342Aha, Ser398Aha), whereas most of the selected on-pathway mutants from [5, 6] have a low SASA value. That makes the chosen set of mutants less suited for investigating allostery on PDZ3 in detail at this point, but the properties of the Aha label in proteins can be revealed, which is essential to exploit Aha's full potential as an IR sensor for protein function. The set of mutants needs to be expanded by further off-pathway mutants, which exhibit a low solvent accessibility.

4.2.4.4 FTIR Shift vs. ITC Data PDZ3-Aha

Comparing the determined $\triangle H$ and $\triangle S$ values deriving from ligand binding in the ITC experiments with the detected IR difference area between the bound and unbound PDZ3-Aha, a weak correlation between a large difference area and a $\triangle H$ and $\triangle S$ value, which is strongly differing from the WT PDZ3 value, is obtained (**figure 4.2.20**). Since this correlation is not given between the dissociation constant and the IR difference area (**figure A.0.4**) it seems to be a compensation between $\triangle H$ and $\triangle S$, solely. If and why the ratio between the enthalpic and entropic contribution to the Gibbs free energy really changes with a higher probability in mutants, which show a larger change in the Aha IR band upon ligand binding, might be interesting to further investigate with a broader set of mutants, particularly because this compensating behavior has been discovered before for PDZ3 with double mutations of an artificial ligand [214]. A connection to protein allostery is conceivable.

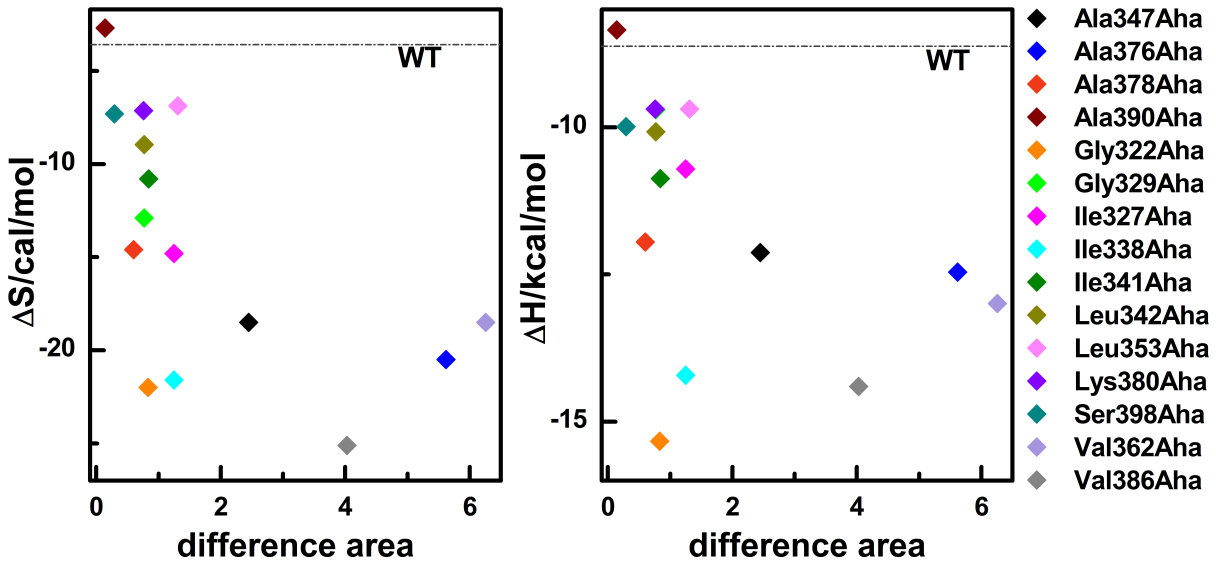

Figure 4.2.20: $\triangle S$ and $\triangle H$ in dependency on the IR difference area between bound and unbound PDZ3-Aha. The $\triangle S$ / $\triangle H$ value of the WT is marked by a dashed grey line.

4.2.5 2D-IR Spectroscopy PDZ3-Aha

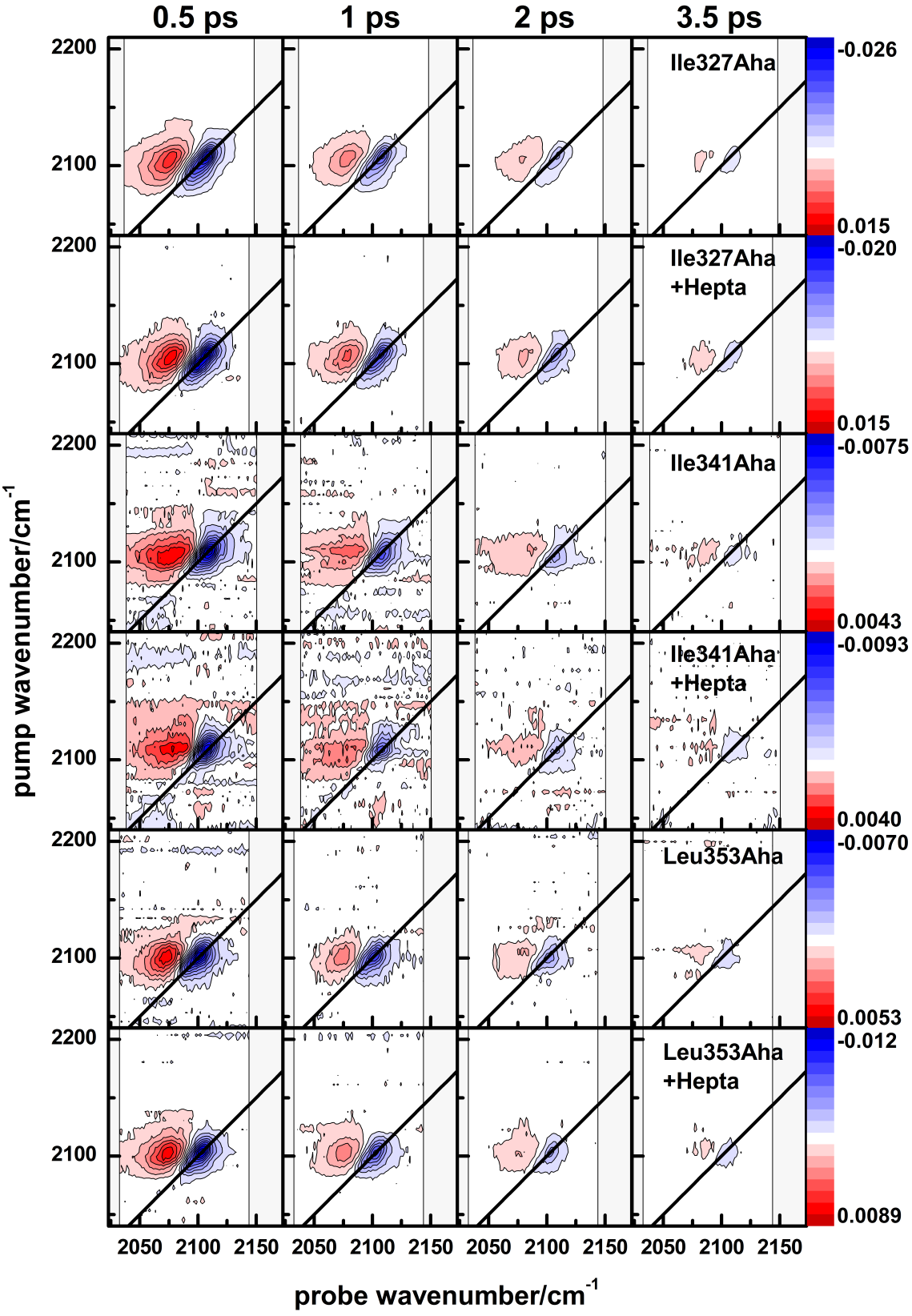

Figure 4.2.21: 2D-IR spectra of different PDZ3-Aha mutants at 0.5, 1, 2, and 3.5 ps population time. The black line gives the diagonal. The thin vertical lines mark the borders of the spectrum.

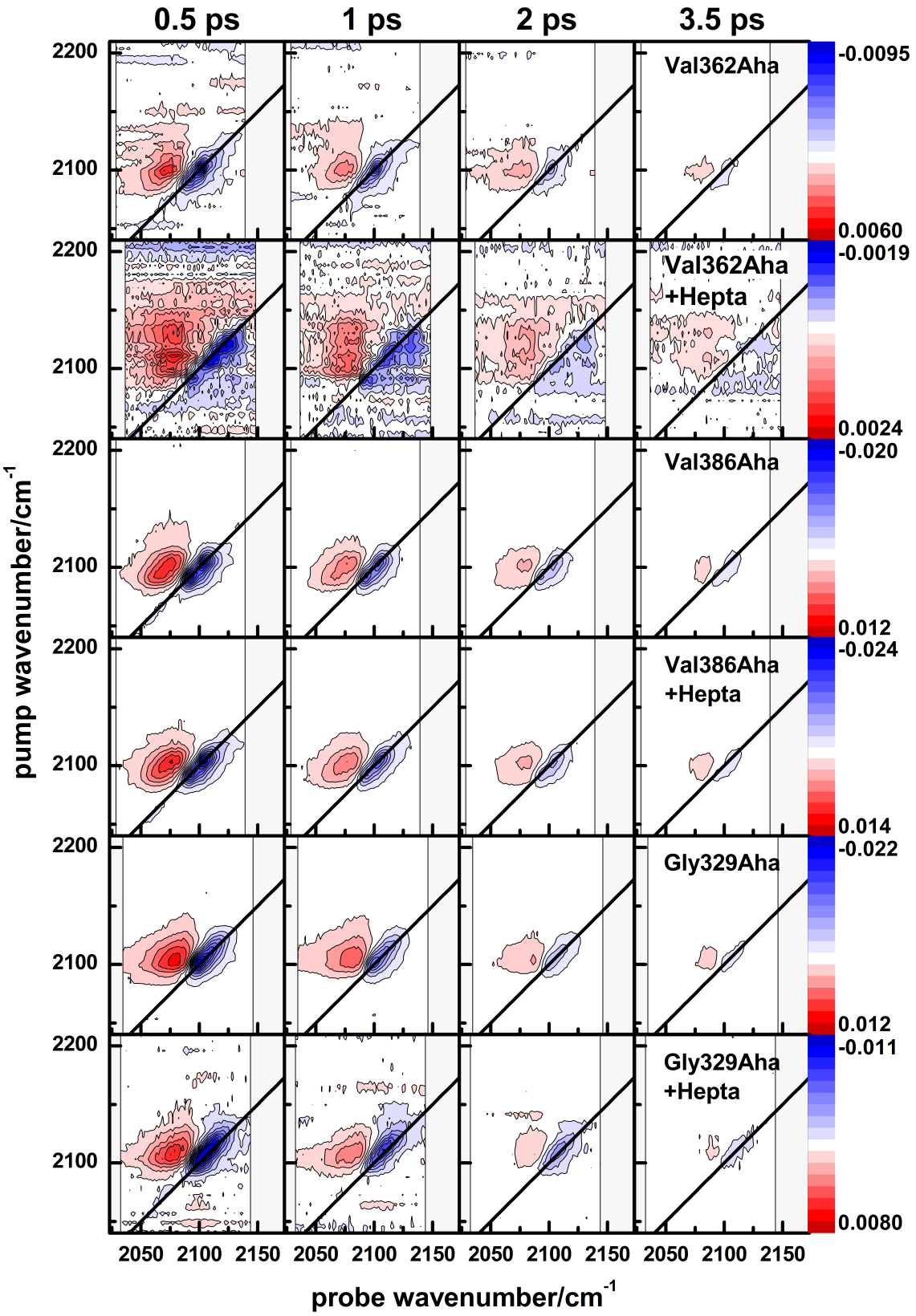

Figure 4.2.22: 2D-IR spectra of different PDZ3-Aha mutants at 0.5, 1, 2, and 3.5 ps population time. The black line gives the diagonal. The thin vertical lines mark the borders of the spectrum.

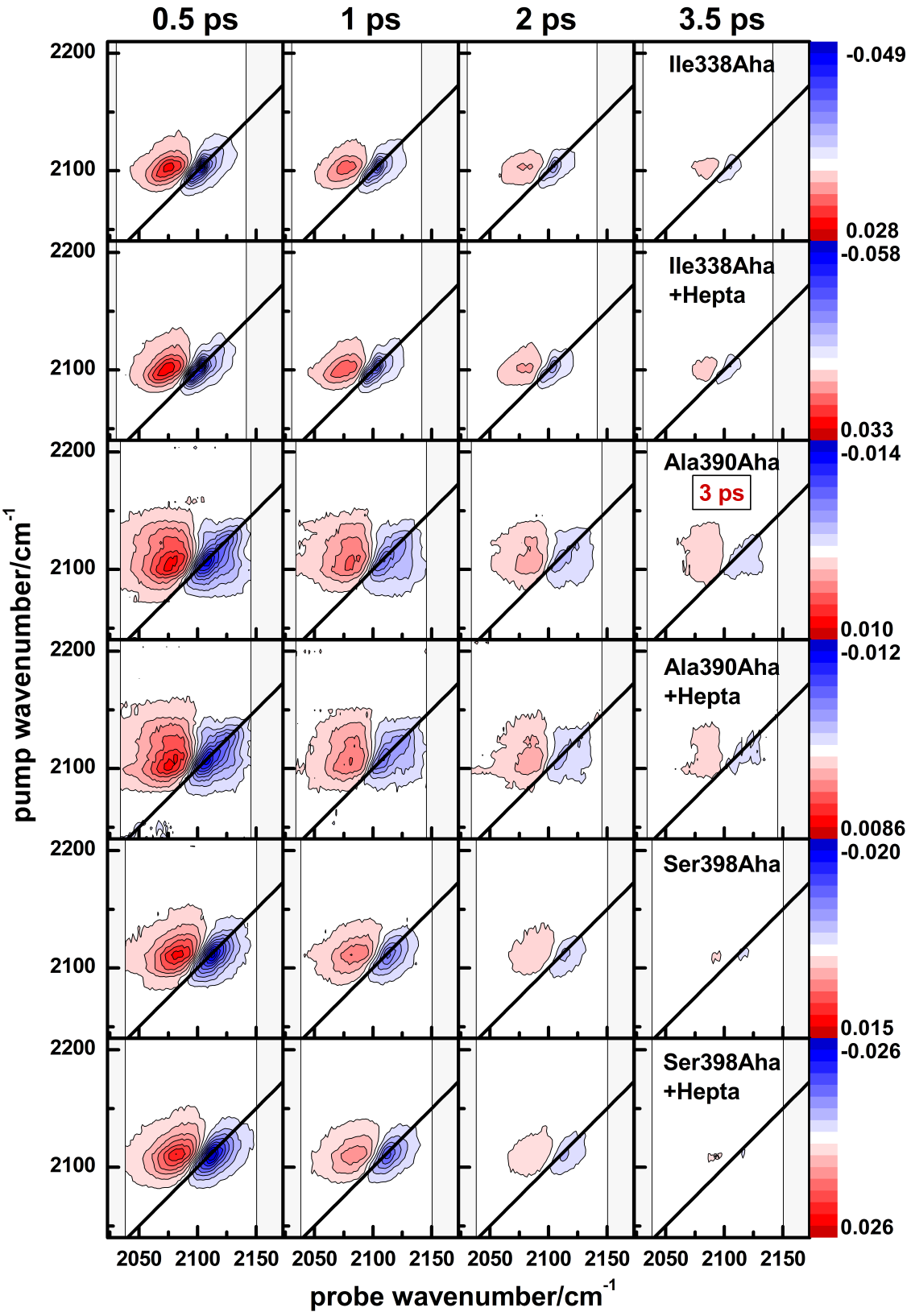

Figure 4.2.23: 2D-IR spectra of different PDZ3-Aha mutants at 0.5, 1, 2, and 3/3.5 ps population time, respectively. The black line gives the diagonal. The thin vertical lines mark the borders of the spectrum.

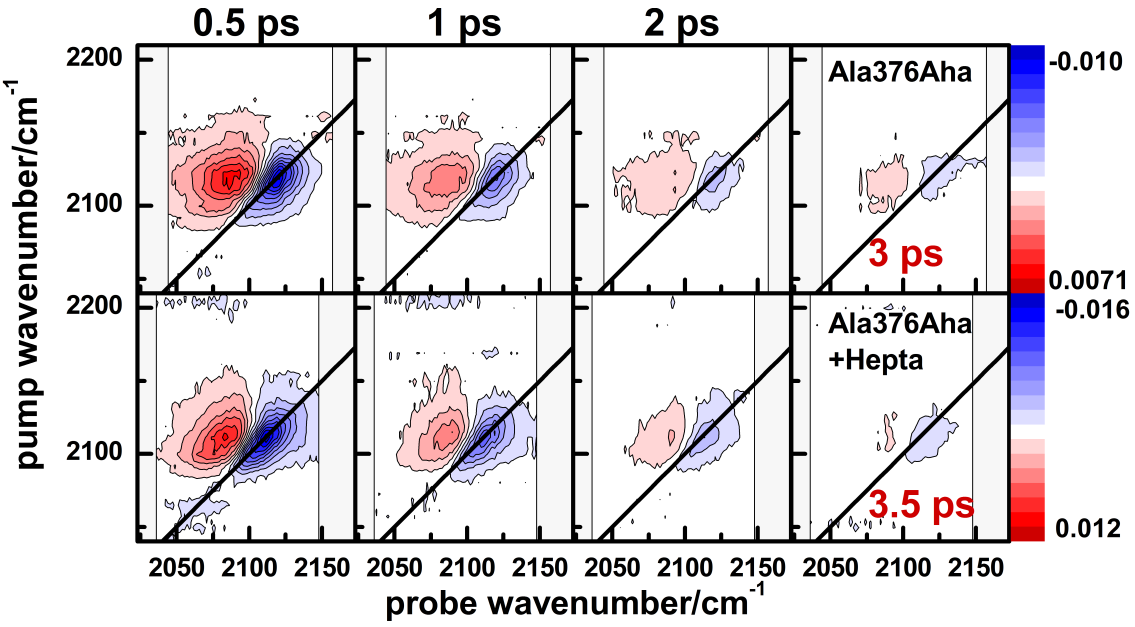

Figure 4.2.24: 2D-IR spectra of different PDZ3-Aha mutants at 0.5, 1, 2, and 3/3.5 ps population time, respectively. The black line gives the diagonal. The thin vertical lines mark the borders of the spectrum.

Fourier Transform 2D-IR spectra of 10 selected unbound and bound PDZ3-Aha mutants were measured (**figure 4.2.21**, **4.2.22**, **4.2.23**, and **4.2.24**) to study the vibrational lifetime and time dependent solvent-solute fluctuations of Aha in a protein. The spectra are composed of the typical negative (blue) (ground state bleaching and stimulated emission) and positive (red) band (excited state absorption) (see **chapter 2.2.3**). No exchange between the different conformational states on the timescale of the experiment is detected. The Ala376Aha+Hepta spectrum needed to be excluded from further analysis because of problems with the polarization upon the experiment and the resulting lack of comparability.

4.2.5.1 Vibrational Lifetime Analysis PDZ3-Aha

The vibrational lifetimes of the Aha bands of PDZ3-Aha were analyzed by a global analysis with four components and a sequential model equally to the Aha/solvent 2D-IR data. Due to the multi band structure the pump pixel cuts closest to the maximum of the sub bands were extracted and analyzed (**figure 4.2.25**, **4.2.26**, and **4.2.27**; fit parameters in **table A.3**). Due to the smaller signal sizes the global analysis was more difficult and less stable for the PDZ3-Aha samples compared to the Aha/solvent samples. For some of the pump cuts the signal was too low for the fit, so they were excluded. For the small side maximum of the Ser398Aha and Ile341Aha+Hepta band the amplitude seems to be too small to estimate the vibrational lifetime of component *4* correctly. Therefore, it is bracketed in the figures and tables.

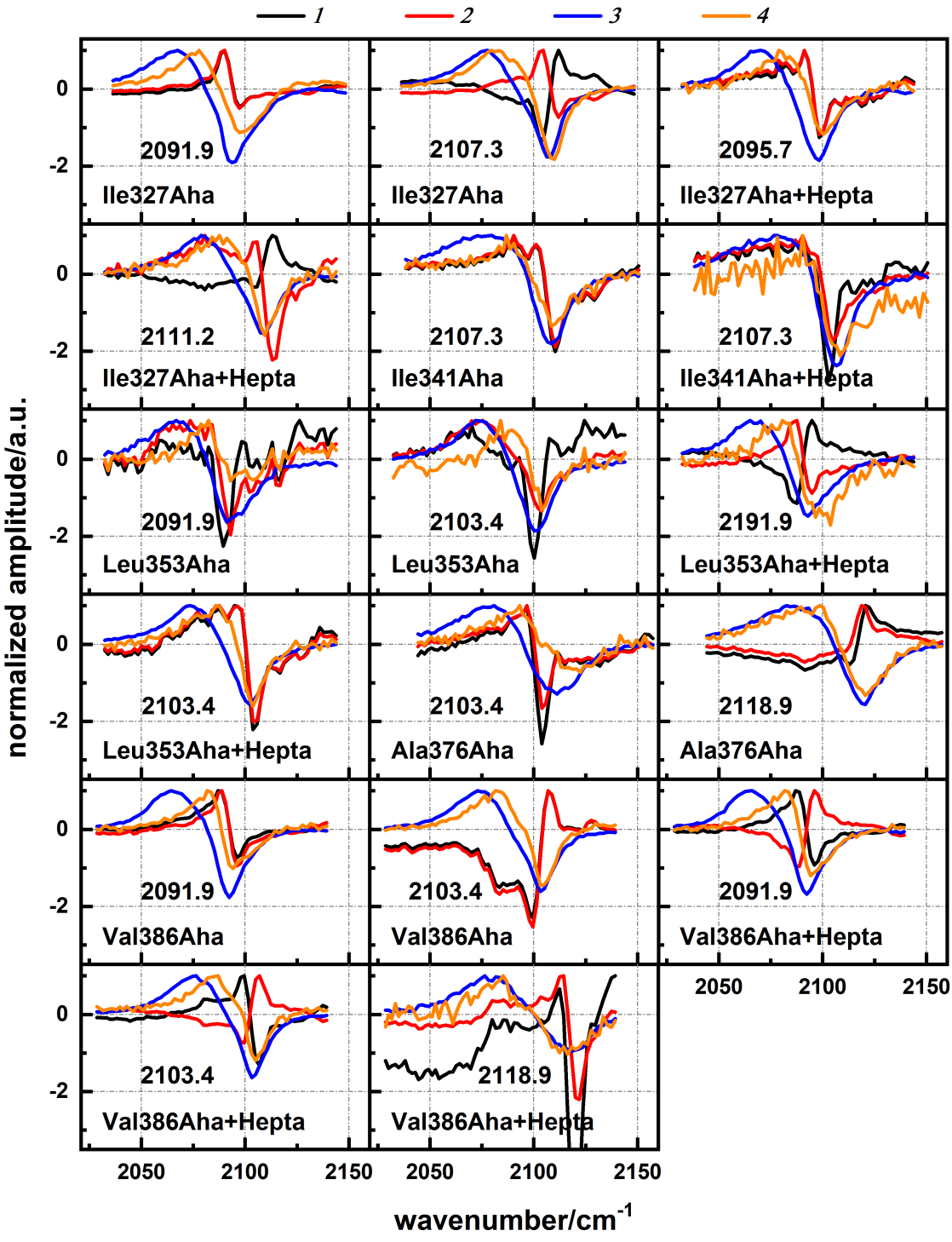

Figure 4.2.25: Global analysis spectra of the four components of the PDZ3-Aha 2D-IR cuts at the pump frequency the psVoigt maxima of the sub bands. The amplitude of the positive absorption was normalized to 1 (normalization factor, amplitudes, and lifetimes in **table A.3**).

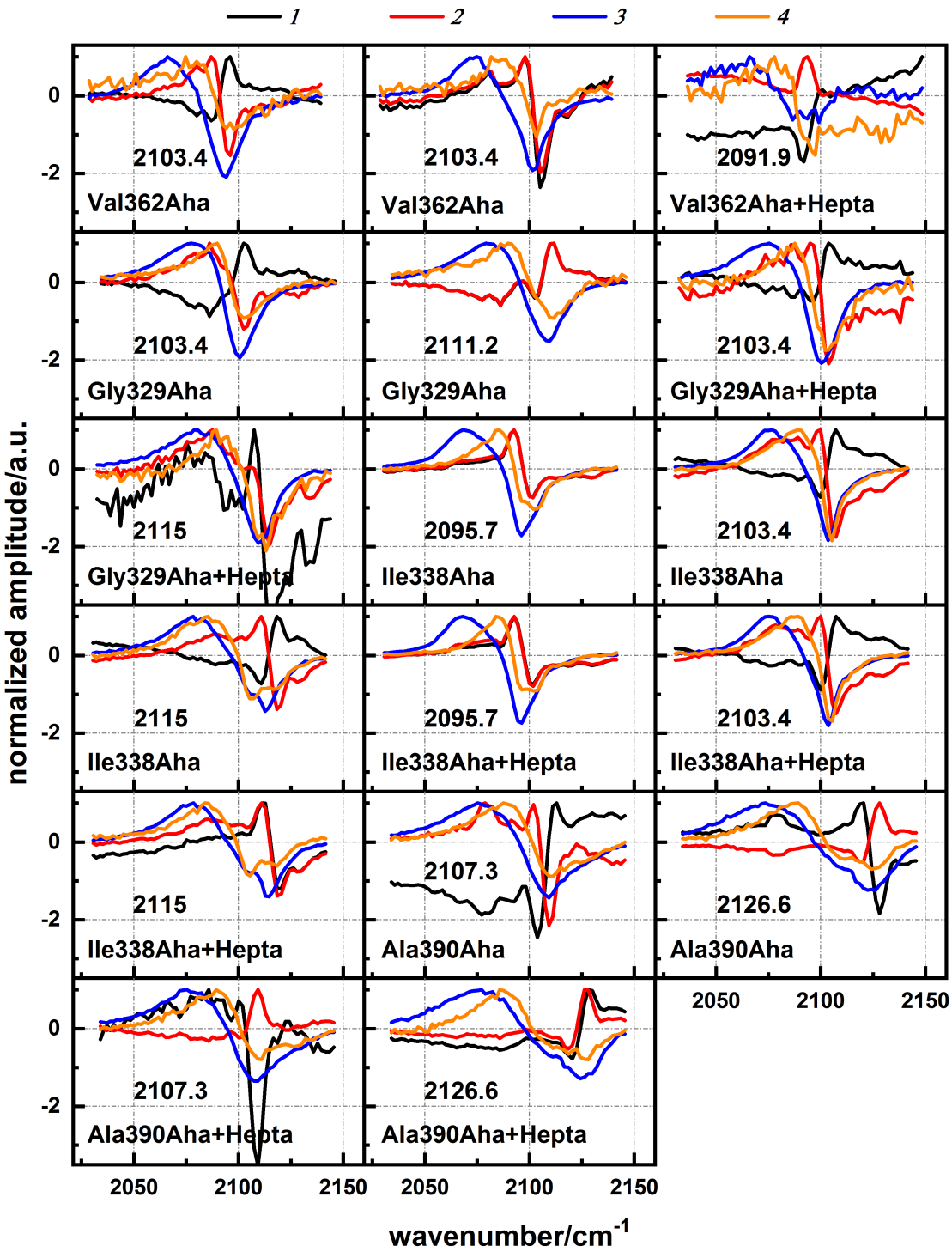

Figure 4.2.26: Global analysis spectra of the four components of the PDZ3-Aha 2D-IR cuts at the pump frequency of the psVoigt maxima of the sub bands. The amplitude of the positive absorption was normalized to 1 (normalization factor, amplitudes, and lifetimes in **table A.3**).

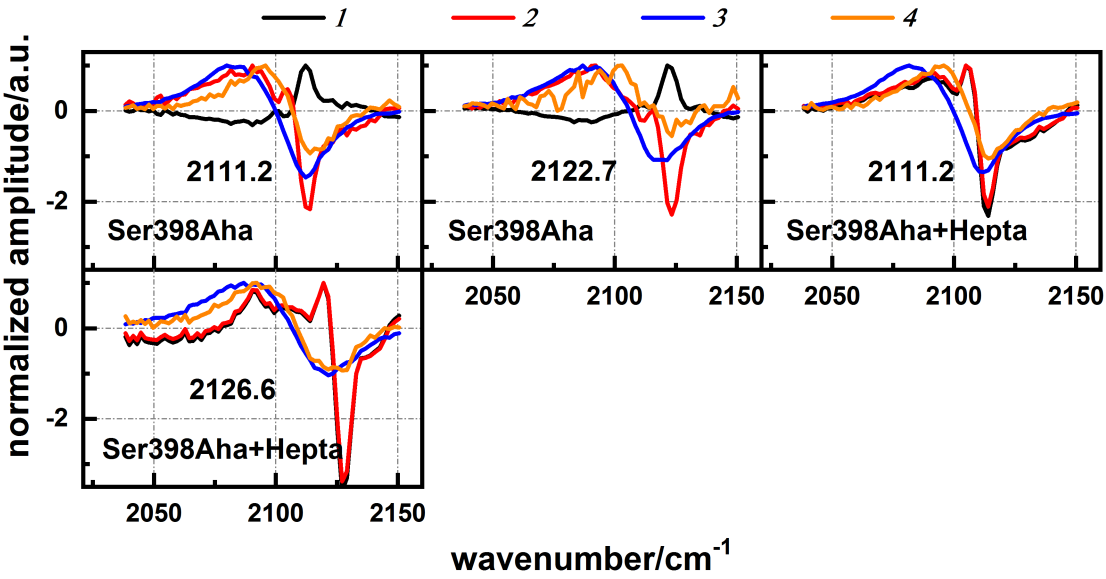

Figure 4.2.27: Global analysis spectra of the four components of the PDZ3-Aha 2D-IR cuts at the pump frequency of the psVoigt maxima of the sub bands. The amplitude of the positive absorption was normalized to 1 (normalization factor, amplitudes, and lifetimes in **table A.3**).

Due to the much smaller signal size and the different sample type, τ_1 and τ_2, which are assigned to perturbed free induction decay, are differing more for Aha in PDZ3 than for the Ahas in solvents. τ_3 and τ_4 describe the vibrational lifetime of azido's asymmetric stretching vibration and the cooling of the hot ground state, respectively (**table 4.16**) and present a similar spectral shape compared to free Aha in solvent. A much broader variation in τ_3 of Aha is obtained in protein compared to solution. In solution a shortest vibrational lifetime of 0.70 ps in H_2O and a longest vibrational lifetime of 1.1 ps in CCl_4 was observed (**chapter 4.1.2**). For PDZ3-Aha values between 0.4 and 1.2 ps were measured. The cooling of the hot ground state τ_4 of the Aha band in protein, by contrast, is rather in the range of the cooling found for bocAha/Aha in aqueous solution than in any other solvent. It ranges from 1.6-3.0 ps in protein compared to 1.8-2.1 ps in H_2O, 2.9 ps in D_2O and 3.3-6.5 ps in all other measured solvents. The ratio between the amplitudes of the spectra of component *3* and *4* (A_4/A_3) are also found to exhibit a broader range of variation (0.18-0.46) in protein compared to in solution (0.17-0.29). Correlations of these observations are analyzed in detail in this chapter.

Table 4.16: Lifetimes of component *3* and *4* from the global analysis fit of the PDZ3-Aha samples and their amplitude ratio. Values deriving form an inaccurate fit due to small signal sizes are bracketed.

sample	pump $\tilde{\nu}$ /cm^{-1}	τ_3/ps	τ_4/ps	A_4/A_3
Ala376Aha	2103.4	0.77	2.4	0.25
	2118.9	0.59	2.4	0.19
Ala390Aha	2107.3	0.58	2.2	0.34
	2126.6	0.61	2.5	0.39
Ala390Aha+Hepta	2107.3	0.63	2.2	0.38
	2126.6	0.67	2.6	0.36
Gly329Aha	2103.4	0.76	2.5	0.27
	2111.2	0.90	2.9	0.18
Gly329Aha+Hepta	2103.4	0.63	2.5	0.20
	2115.0	0.80	2.9	0.18
Ile327Aha	2091.9	0.40	2.1	0.25
	2107.3	0.55	2.1	0.26
Ile327Aha+Hepta	2095.7	0.58	2.2	0.33
	2111.2	0.85	2.2	0.25
Ile338Aha	2095.7	0.88	2.7	0.28
	2103.4	0.93	3.0	0.24
	2115.0	0.47	2.5	0.31
Ile338Aha+Hepta	2095.7	0.90	2.6	0.29
	2103.4	0.92	2.8	0.24
	2115.0	0.50	2.7	0.34
Ile341Aha	2107.3	0.71	2.5	0.27
Ile341Aha+Hepta	2107.3	1.03	(8)	(0.15)
Leu353Aha	2091.9	0.89	2.0	0.40
	2103.4	1.20	2.7	0.27
Leu353Aha+Hepta	2091.9	0.71	2.3	0.19
	2103.4	0.74	2.5	0.22
Ser398Aha	2111.2	0.72	1.7	0.24
	2122.7	0.86	(6)	(0.09)
Ser398Aha+Hepta	2111.2	0.68	1.8	0.19
	2126.6	0.53	1.6	0.23
Val362Aha	2091.9	0.82	2.1	0.46
	2103.4	1.12	2.2	0.35
Val362Aha+Hepta	2091.9	0.40	1.7	0.37
Val386Aha	2091.9	0.80	2.1	0.33
	2103.4	0.64	2.0	0.36
Val386Aha+Hepta	2091.9	0.76	2.1	0.33
	2103.4	0.91	3.0	0.20
	2118.9	0.80	3.0	0.19

Lifetime vs. Wavenumber and SASA PDZ3-Aha

There seems to be only a weak relation between the wavenumber and the vibrational lifetime τ_3 for specific cases (**figure 4.2.28 top**). All bands with a more blue shifted band maximum than in any solvent show a shorter Aha vibrational lifetime than in solvent, simultaneously. This probably means that the non-covalent interactions of the Aha, which are responsible for the very strong blue shift, shorten the

vibrational lifetime. The peaks with a longer vibrational lifetime than in any solution have their band maxima within the solvent range. Neither peaks with vibrational lifetimes shorter than in any solvent show a correlation to their wavenumbers nor peaks with a red shifted maximum compared to solution are correlated to their vibrational lifetimes.

No correlation between the cooling of the hot ground state τ_4 and the wavenumber was detected (**figure 4.2.28 bottom**).

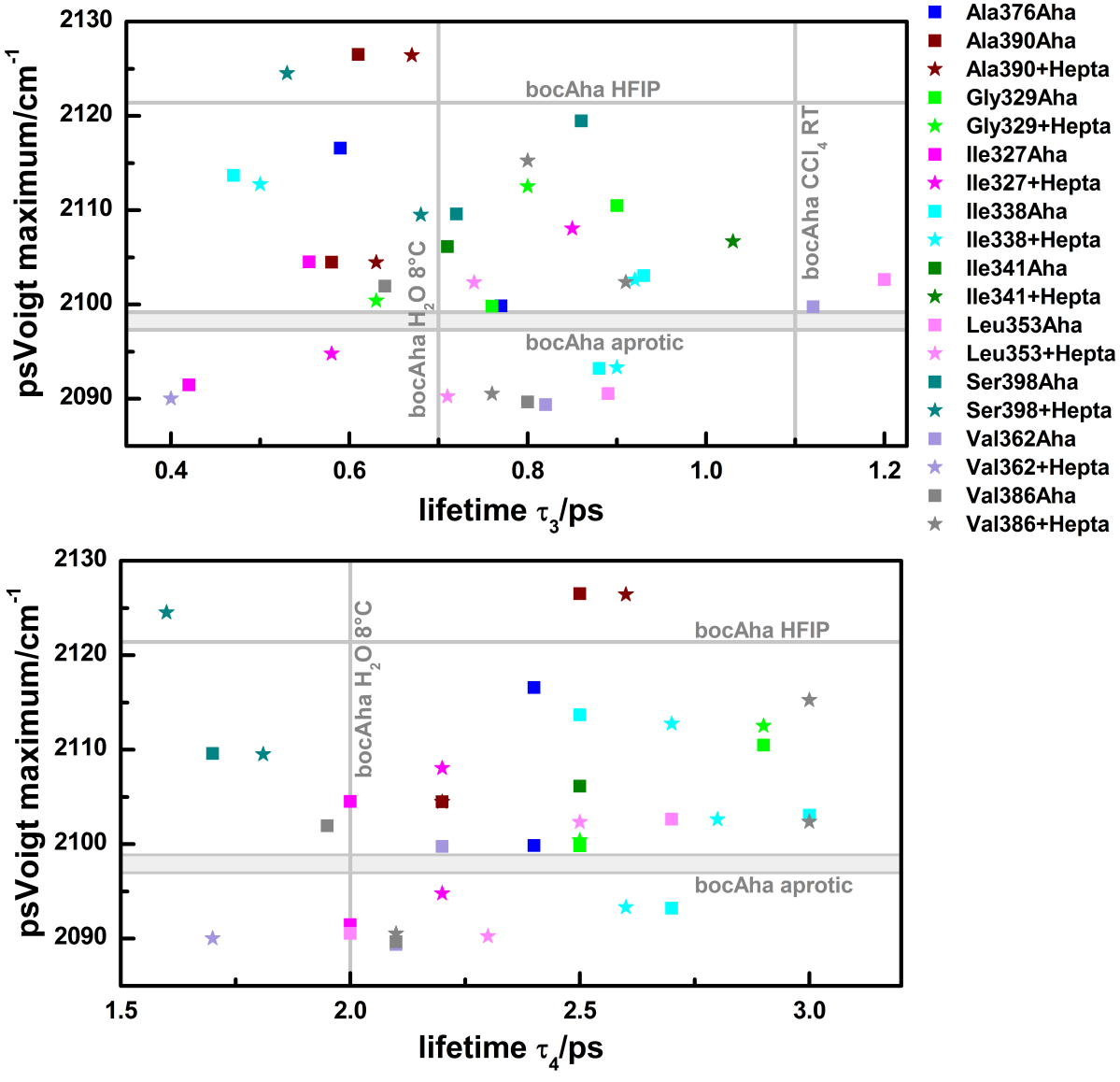

Figure 4.2.28: Top:Correlation between the psVoigt maximum and the vibrational lifetimes τ_3 for Aha in PDZ3. **Bottom:** Correlation between the psVoigt maximum and the cooling of the hot ground state τ_4 for Aha in PDZ3. The most extreme values of the bocAha/solvent samples are marked with grey lines.

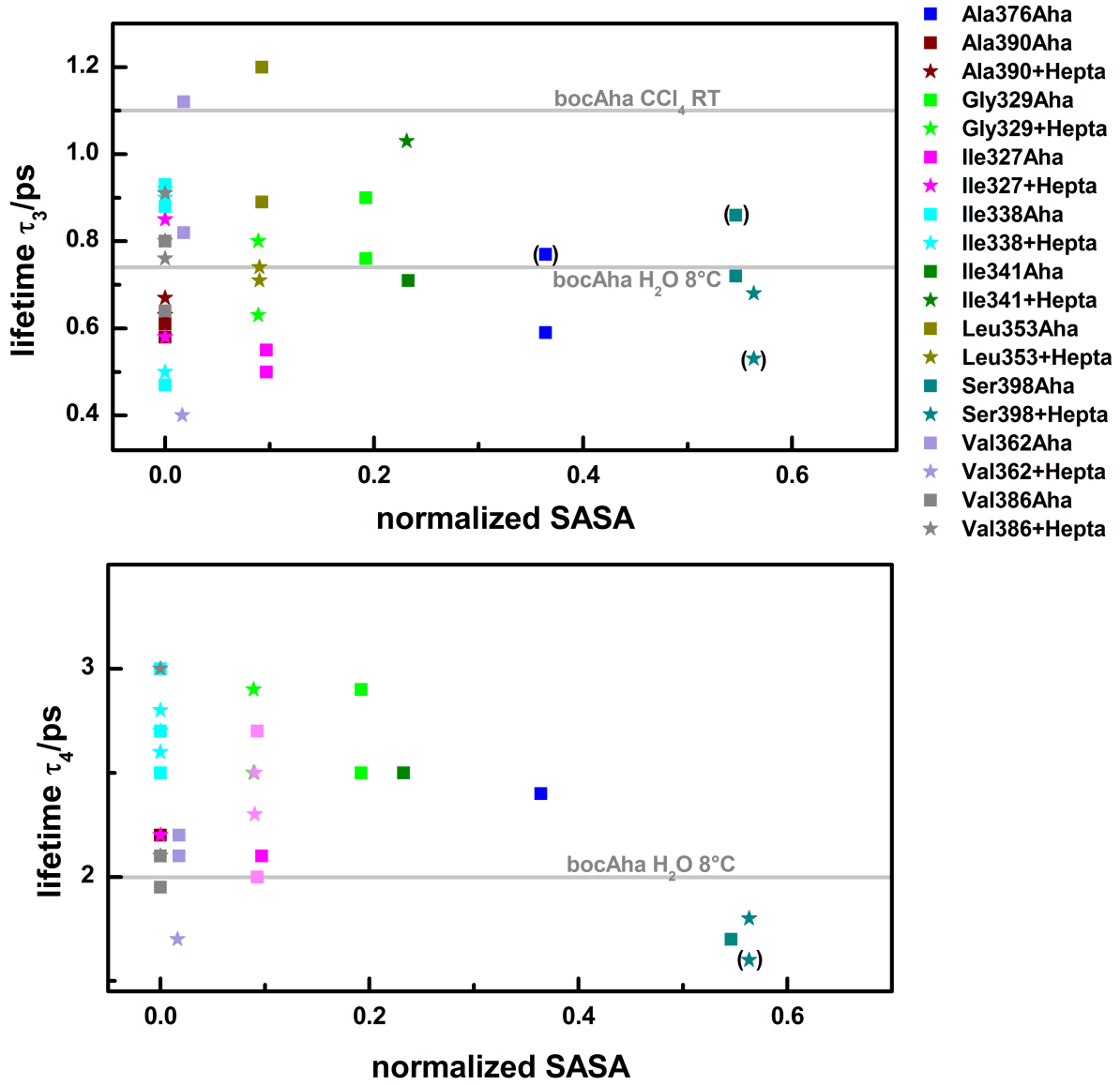

Figure 4.2.29: Correlation between the vibrational lifetimes τ_3 **(top)**/τ_4 **(bottom)** and the normalized SASA. The most extreme values of the bocAha/solvent samples are marked with grey lines.

Looking at the dependency of τ_3 on the normalized SASA, a similar behavior as for the band maximum in correlation to SASA is observed (**figure 4.2.29 top**). At low SASAs the vibrational lifetime of Aha exhibits a broader distribution than in any solvent. For high SASA it seems to be close to the Aha's vibrational lifetime in water. However, only a few mutants with a high SASA were measured. The vibrational lifetime, which is shorter than in any solvent for the most cases, might also be caused by non-covalent interactions unique for the protein environment compared to in solvent, like electrostatic interactions with backbone carbonyl O-atoms or hydrogen bonding to H_2O in non-ideal angles. For N_3Pro in $CHCl_3$ an elongated vibrational lifetime was obtained for the backbone interacting conformational state [171]. However, for N_3Pro relaxation also interactions with the low

frequency modes of its pyrolidine ring play a role [171] and it is conceivable that at different conditions backbone interactions might also shorten the vibrational lifetime. Despite Ahas vibrational lifetime was found to be not very sensitive to solvent properties, a much higher variation in vibrational lifetime was observed in proteins at low SASAs. That makes Aha a much more sensitive 2D-IR label in proteins compared to in solution.

τ_4 of PDZ3-Aha for highly solvent exposed Aha is similar to bocAha in water. At lower SASAs higher variations are found but they are less significant than these of τ_3. However, at low SASAs τ_4 is still more similar to bocAha in H_2O than to any other solvent. This means that the cooling of the heated environment around the Aha in PDZ3 occurs with a velocity closer to the one in H_2O than to other solvents, even in mutants with very low SASA. This could be a hint for internal water being hydrogen bonded to Aha and not considered by the SASA calculation or that the cooling of PDZ3 has a similar time constant as water.

Vibrational Lifetime and Ligand Binding PDZ3-Aha

The differences between the lifetimes of the bound state and the unbound state were calculated (**table 4.17** and **figure 4.2.30**) for the sub bands with mainly conserved band positions upon ligand binding to investigate the influence of ligand binding on the vibrational lifetime.

Table 4.17: Difference in vibrational lifetimes τ_3 and τ_4 between unbound and ligand bound (to Hepta) PDZ3-Aha.

sample	pump $\tilde{\nu}$ /cm^{-1}	$\triangle\tau_3$/ps	$\triangle\tau_4$/ps
Ala390Aha	2107.3	-0.05±0.07	0±0.03
	2126.6	-0.08±0.14	-0.1±0.7
Gly329Aha	2103.4	+0.13±0.06	0±0.5
	2111.2	+0.1±0.08	0±0.7
Ile327Aha	2091.9	-0.18±0.05	-0.1±0.4
	2107.3	-0.30±0.09	-0.1±0.3
Ile338Aha	2095.7	-0.02±0.05	+0.1±0.2
	2103.4	+0.01±0.06	+0.2±0.4
	2115.0	-0.03±0.08	-0.2±0.4
Ile341Aha	2107.3	-0.32±0.14	(-6±3)
Leu353Aha	2091.9	+0.18±0.14	-0.3±0.7
	2103.4	+0.46±0.3	+0.2±0.6
Ser398Aha	2111.2	+0.04±0.05	-0.1±0.2
Val362Aha	2091.9	+0.4±0.2	+0.4±0.4
Val386Aha	2091.9	+0.04±0.08	0±0.4
	2103.4	-0.27±0.08	-1.1±0.4

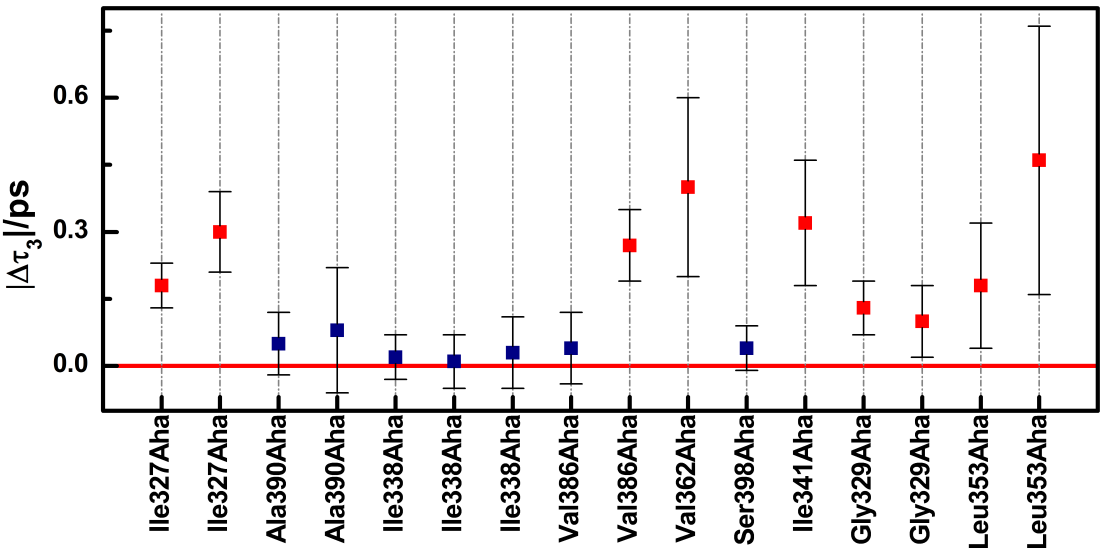

Figure 4.2.30: Vibrational lifetime difference of Aha in PDZ3 upon ligand binding. The $|\triangle\tau_3|$ which are larger than zero within their error range are colored red and the others are colored blue.

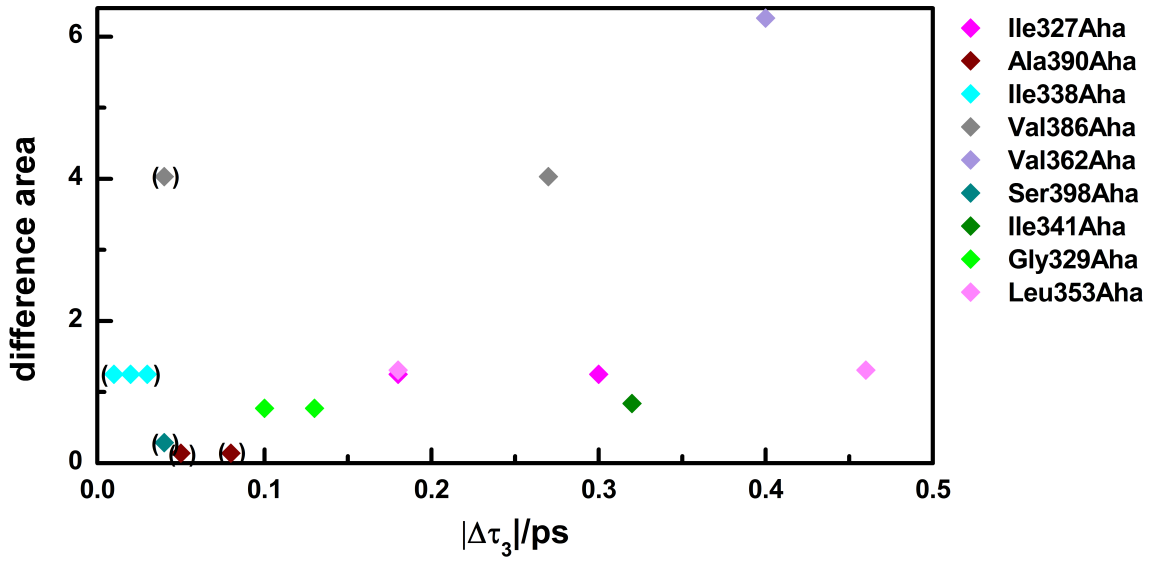

Figure 4.2.31: Correlation between the ligand induced difference area and $|\triangle\tau_3|$. The mutants with a $|\triangle\tau_3|$ which is not significantly larger than zero are bracketed.

For several bands a significant change in the vibrational lifetime of Aha ($\triangle\tau_3$) upon ligand binding was observed (red squares in **figure 4.2.30**). τ_4 changes in only one case more than its error range. Bloem *et al.* investigated binding of an Aha labeled ligand to PDZ2 from hTPT-1E with time resolved 2D-IR spectroscopy, but did not detect a change in the vibrational lifetime upon ligand binding [91]. To the best of our knowledge, the 2D-IR data displayed here show the first ligand induced change in Aha's vibrational lifetime ever measured. Generally speaking, the PDZ3-Aha

mutants showing a ligand induced spectral shift in the FTIR measurements tend to also change their vibrational lifetime in this course. Only Ile338Aha seems to be an exception and one of the two bands of Val386Aha. As Ile338Aha is an off-pathway mutant in definition of the pathways of Lockless and Ranganathan and Ota and Agard [5, 6], all off-pathway mutants investigated do not show a ligand induced change in τ_3, whereas the on-pathway mutants present a change in τ_3 (except one of two bands of Val386Aha). This is a very interesting observation, however, only a small set of off-pathway mutants was measured and a larger set of mutants needs to be investigated to verify this correlation.

Comparing the FTIR difference area with $|\triangle\tau_3|$ also reveals the trend of spectral changes upon ligand binding going along with changes in vibrational lifetime for the most mutants, even though no distinct correlation could be found between the amount of changes for both, which might be caused by the arbitrary choice of the difference area and the exclusion of changes in the extinction coefficients.

Amplitude Ratio PDZ3-Aha

The ratio between the spectral amplitudes of component *4* and *3* (**table 4.16**) (A_4/A_3) was also found to be in a broader range in protein compared to solution.

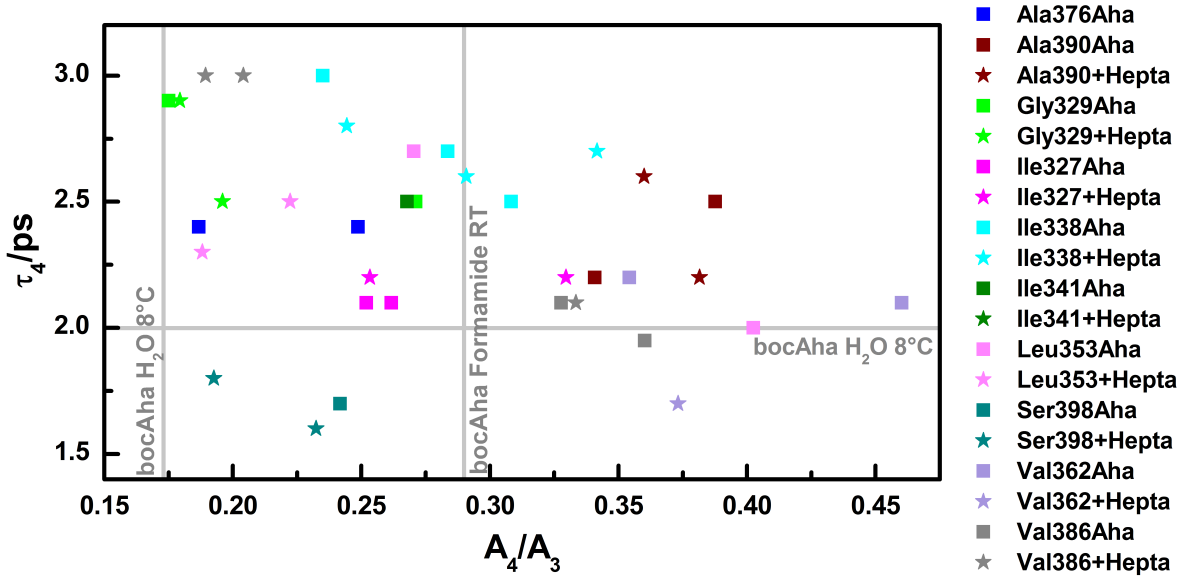

Figure 4.2.32: Correlation between the hot ground state cooling τ_4 and the amplitude ratio A_4/A_3. The most extreme values of the bocAha/solvent samples are marked with grey lines.

A smaller A_4/A_3 ratio than in solvent was only calculated for the two pump wavenumbers, at which the global analysis failed to estimate component *4*. Therefore, they are bracketed. For many mutants A_4/A_3 is larger than in solvent. Neither a correlation of A_4/A_3 with the maximum band (**figure A.0.5**) nor with the lifetimes

τ_3 (**figure A.0.6**) and τ_4 (**figure 4.2.32**) could be observed. But again, as for the band maximum and Aha's vibrational lifetime, the effect of higher A_4/A_3 variation in protein than in solvent is only observed for low solvent exposed Ahas (**figure 4.2.33**).

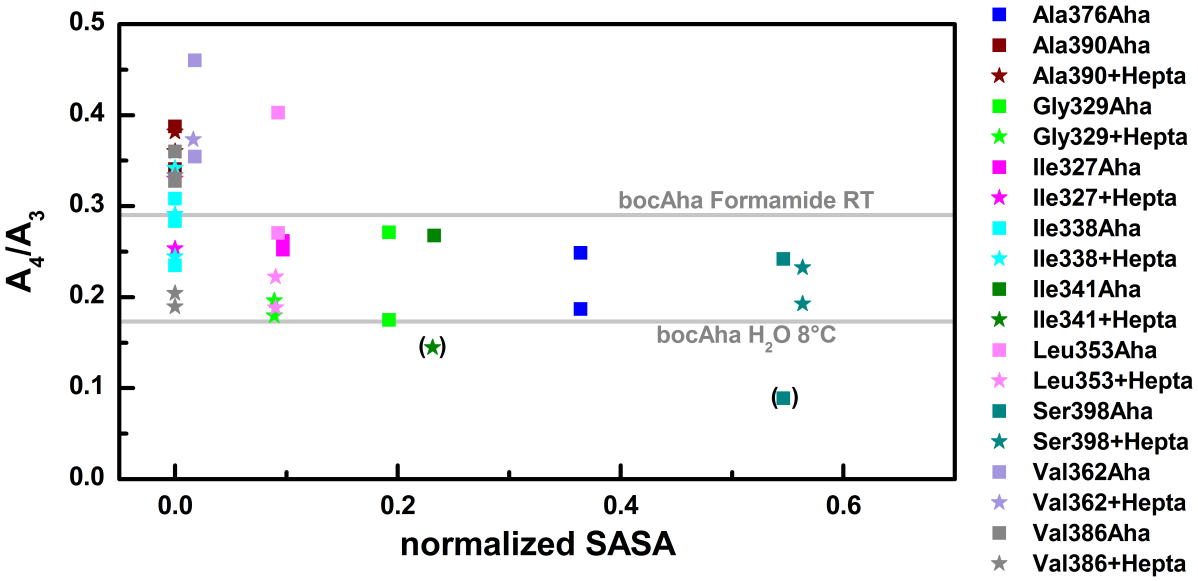

Figure 4.2.33: Correlation between the amplitude ratio A_4/A_3 and the normalized SASA. The most extreme values of the bocAha/solvent samples are marked with grey lines.

Component *4* was assigned to a hot ground state, which means, that a heated environment around the azido group slightly changes the anharmonic potential of its vibrational mode and, therefore, red shifts the absorption band. Diverse effects might contribute to an enlarged amplitude of this hot ground state. A slower cooling of the hot ground state τ_4 could be excluded to be the reason because of the lack of a correlation between τ_4 and A_4/A_3 (**figure 4.2.32**). Another possibility for an enlarged amplitude of component *4* is that the red shift of the anharmonic potential caused by heating is larger for some conformational states in a protein than in solvent. Stronger interactions of the azido group with its environment, for example in form of electrostatic interactions with backbone carbonyl O-atoms, might be a reason for a larger change in the anharmonic potential.

4.2.5.2 Line Shape Analysis PDZ3-Aha

Because line shape analysis on multi band structures is very difficult, it could only be performed for the mutants with a single or quasi single band shape. The CLS was fitted as described in the line shape analysis of the Aha/solvent samples (**chapter 4.1.2.2**). The combination of small signal size and short vibrational lifetime compared to a longer correlation time made the estimation of the CLS challenging. Only for the 2D-IR spectrum of Ser398Aha a sufficiently reliable fit

could be calculated (**figure 4.2.34** and **table 4.18**). The vibrational frequency correlation decay seems to be a bit faster in the protein compared to in H_2O. The inhomogeneous part of the line broadening $\delta+\Delta$ is found to be larger for the protein environment than for solution, which is mainly caused by an increased long living inhomogeneous component δ, as expected for a protein environment.

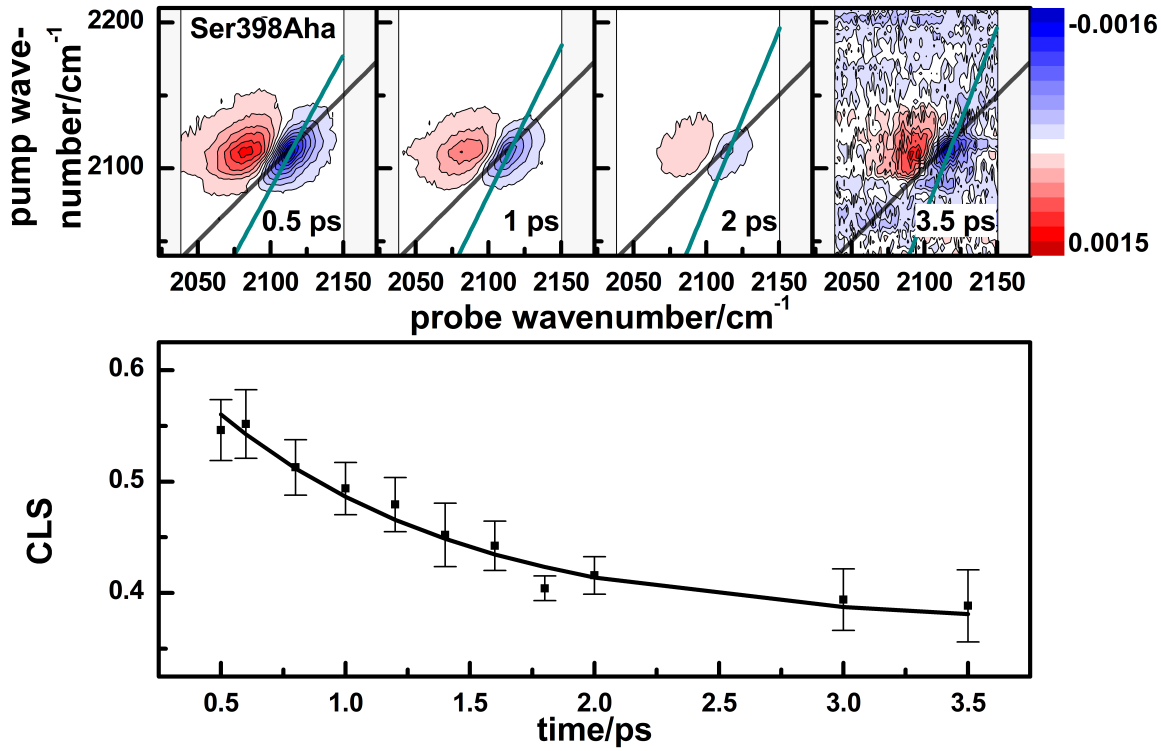

Figure 4.2.34: Top: 2D-IR spectra of Ser398Aha at 0.5, 1, 2, and 3.5 ps population time. The black line gives the diagonal and the blue line is the tilt of the bleach band. **Bottom**: CLS decay fitted by a monoexponential function.

Table 4.18: Fit parameters of the CLS decay of Ser398Aha and bocAha in H_2O in comparison with the vibrational frequency correlation decay τ_c, the amplitude Δ, the static offset δ, and the time range of the exponential fit Γ. Uncertainties are high and results need to be considered with care.

sample	τ_c/ps	δ	Δ	$\delta+\Delta$	Γ/ps
Ser398Aha 8 °C	1.0	0.37	0.31	0.68	0.5-3.5
bocAha H_2O 8 °C	1.5	0.14	0.37	0.51	0.5-3.5

4.2.6 Aha in PDZ3 Discussion

Incorporation of Aha into PDZ3 was shown to be only minimally invasive for the majority of mutation sites. The application of Aha in a broad set of PDZ3 mutants revealed that Aha shows a broader variation of its asymmetric stretching band position as well as its vibrational lifetime and the ratio of the signal size of its hot

ground state compared to any solvent. This increased sensitivity is achieved at mutation sites with low solvent exposure. Reasons for this increased sensitivity might be differing non-covalent interactions of the Aha, like electrostatic interactions with its own backbone carbonyl O-atom or opposing ones, as observed in the crystal structures, and hydrogen bonds to internal H_2O molecules in non-ideal angles. MD simulations are needed to further investigate these experimental observations. The IR absorption band of Aha in a protein exhibits multiple sub bands signifying different conformational states at several mutation sites. Both the band shape and the vibrational lifetime of Aha are highly sensitive to subtle changes upon ligand binding at distinct sites, which might be correlated with signaling pathways, and are worth to be studied with a broader set of buried mutation sites with low solvent exposure. Changes in the IR band upon ligand binding seem to arise rather from a change of population between conformational states than from a band shift for the majority of mutation sites.

The enormous variation of the band positions of Aha in proteins and its high sensitivity to even subtle changes caused by ligand binding emphasizes again Aha's great potential as an IR label of protein function. Even the observed small variation of Aha's vibrational lifetime in solvents seems to be overcome when it is incorporated into a protein and additional information can be gained by 2D-IR spectroscopy. However, CN and SCN are still more suitable 2D-IR labels because of their extremely long vibrational lifetimes in proteins of about 4 ps [153, 154] and 28-70 ps [164–166], respectively. A total range of 48.3 cm^{-1} for Aha's band maximum in proteins has been observed up to now including the data discussed here in combination with values provided by literature [100–103, 106], whereas for the SCN label in proteins only a wavenumber range of 18 cm^{-1} has been obtained up to now [142, 148–151, 158, 159, 163, 166]. This remarkably high spectral variation in proteins makes Aha an extremely sensitive IR label for protein function.

4.3 Vibrational Energy Transfer

The heater-sensor pair Azu-Aha combined with ultrafast transient IR spectroscopy (TRIR) was applied to measure vibrational energy transfer (VET). An ultrafast visible pump pulse of about 613 nm excites the Azu moiety to its first electronically excited state (see **figure 4.3.1**). The Azu moiety undergoes ultrafast internal conversion and converts the energy of the visible photon into vibrational energy. The vibrational energy is transferred along the molecule and into the solvent and its arrival at the sensor can be measured with a consecutive mid IR probe pulse.

First, the measurement setup was improved compared to previous experiments of Henrike M. Müller-Werkmeister [70, 78]. Then the heater-sensor pair was incorporated into small model peptides and intramolecular VET along the peptides was observed. Afterwards intermolecular VET between an Azu labeled ligand and an Aha in PDZ3 was mapped for seven different PDZ3-Aha mutants. The signal evolution and VET efficiencies for the different PDZ3-Aha mutants are compared. Later also the opposite scenario, VET from AzAla incorporated into PDZ3 at two distinct sites to an Aha labeled ligand was measured. The effect of the AzAla position on the observed VET signal is analyzed. Additionally, the influence of isotope labeling of solvent H_2O on VET in a small peptide is investigated.

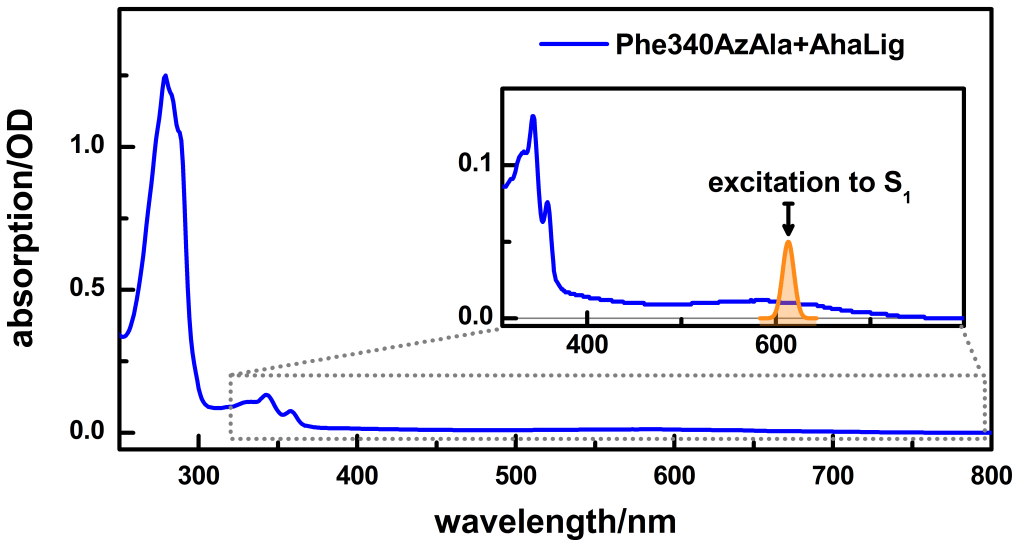

Figure 4.3.1: UV-Vis spectrum of AzAla in Phe340AzAla+AhaLig (blue). The insert gives an enlarged extract of the UV-Vis spectrum (blue) with the delineated visible pump pulse (orange), which is used for AzuCa/AzAla excitation in a VET experiment.

The data from the PDZ3-AzAla ITC, UV-Vis, and VET measurements have already been published by us in [105] and the first ITC data set of Ile341Aha with AzuLig in [104]. Parts of the VET measurements shown here were measured together with Erhan Deniz and Jan G. Löffler.

4.3.1 Setup Optimization

Henrike M. Müller-Werkmeister measured VET signals between an Azu and an Aha in small peptides, successfully, in course of her dissertation on the same laser setup as used for this thesis [70, 78].

Since the VET signal gets smaller at longer distances, several improvements of the setup had to be done in order to be able to observe VET signals in PDZ3-Aha mutants. First, a new sample holder was developed, which moves during the measurement with a vertical movement in combination with a rotational movement (**figure 4.3.2**). This ensures, that the sample volume, which is hit by the laser shot, is exchanged and the whole sample volume is used. This way, Azu bleaching and sample precipitation is prevented. Smaller protein amounts are needed compared to the formerly used flow cell. Moreover, the rotational cell worked more reliable than the flow cell.

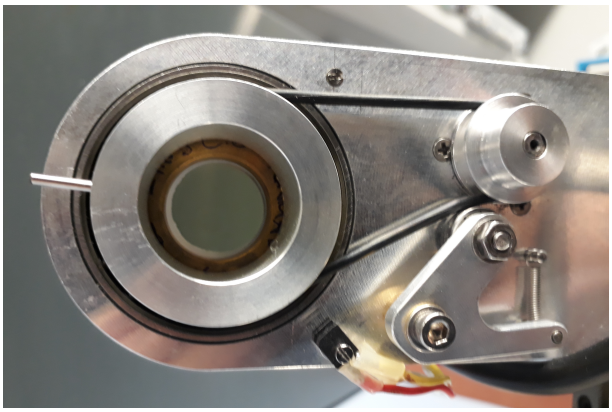

Figure 4.3.2: Rotational sample holder: The sample cell is rotated by a motor via an elastic band (black) while the whole arm is moved upwards and downwards by an additional motor.

The lens, which focuses the pump light into the sample was replaced by a lens with a larger focal length and the filter, which was used to separate the 610 nm light from the remaining *Signal* light, was exchanged by a series of dichroic mirrors (for detailed information on the devices see **chapter 3.4**). A larger amount of 610 nm pump light could reach the sample and the focus shape was optimized. A two times larger signal size was achieved by these additional improvements.

In an additional step of optimizations, the CaF_2 rods, which temporally stretched the pump pulse, were removed and a sharper pump pulse was gained. Furthermore, the probe path was reconstructed in order to get more probe light to the detector and improve the signal to noise ratio. In the previous path the main part of the mid IR light leaving the probe OPA was eliminated to serve as pump light in another experiment. Since this pump light was not needed in the VET experiments, the formerly used BaF_2 wedge was exchanged by a path with an IR beamsplitter to

divide the mid IR light into a probe part and a reference part (**figure 4.3.3**). This way, almost all mid IR light from the OPA could be used for the experiment (about 0.2 μJ per pulse).

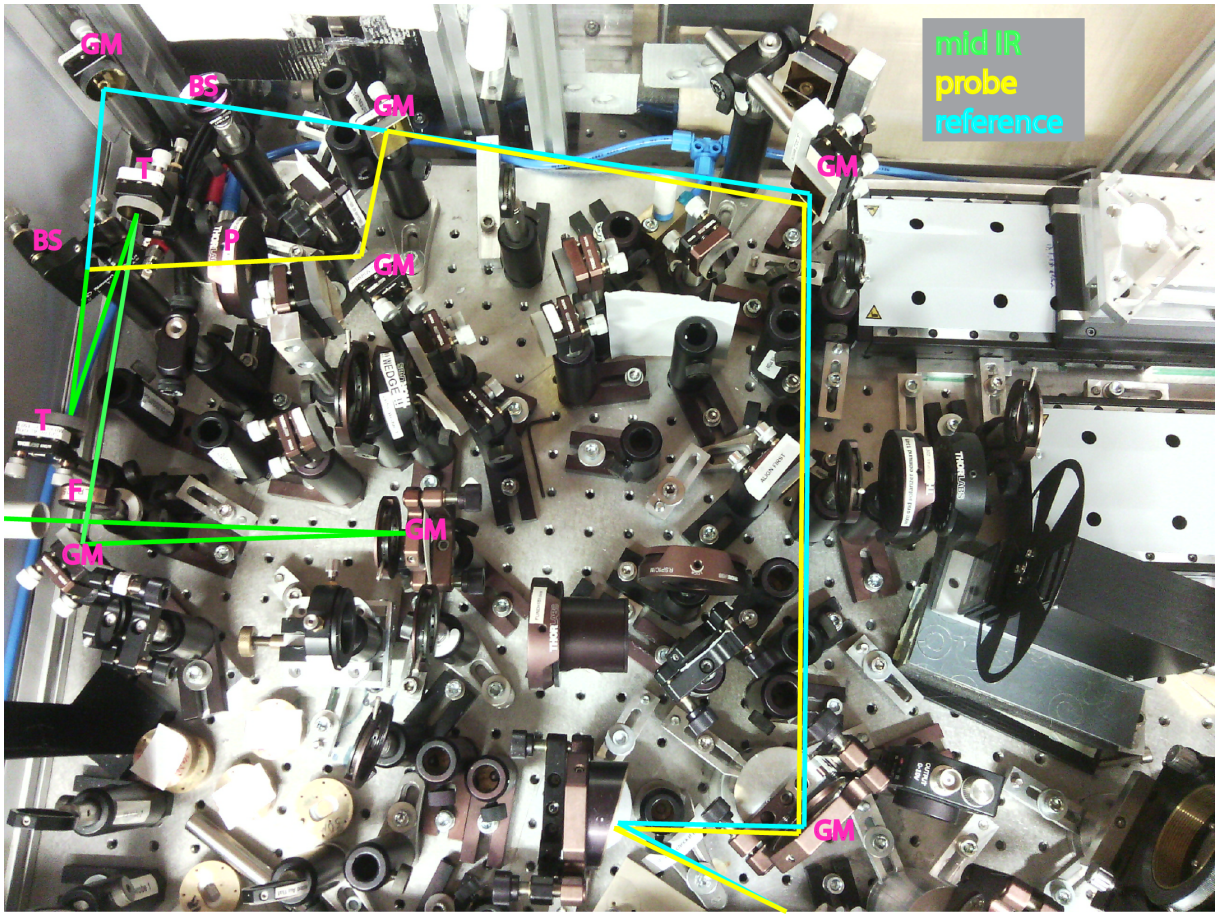

Figure 4.3.3: Beam path of the probe/reference beam in the laser setup used for the VET measurements after rebuilding. The mid IR light (green) leaves the OPA and is reflected by gold mirrors (GM) and guided through a telescope (T) to adjust the beam size. Afterwards a beamsplitter (BS) divides the mid IR light into the probe (yellow) and the reference (cyan) beam. The polarization of the probe beam is adjusted by a polarizer (P). A second beamsplitter clips a part of the reference beam so much, that the intensities of probe and reference beam are similar. Probe and reference are both guided above each other through the sample (not in the picture).

4.3.2 VET in the Amide Region

The VET after excitation of the Azu chromophore was tracked in the naturally occurring backbone and side chain absorption region for an Azu containing ligand (AzuLig) and a PDZ3 mutant plus AzuLig. The resulting TRIR spectra of the PDZ3 sample Ile341Aha+AzuLig is compared to the spectra of pure AzuLig (**figure 4.3.4**). Both are displaying largely the same spectral features in the amide region, which means, that the observed VET signals for the Ile341Aha+AzuLig samples almost completely originate from AzuLig. That shows that observation of VET in

the amide region is strongly limited to short distances and, thus, inappropriate for observing VET through a whole protein. It demonstrates the urgent need for the application of a VET sensor, which absorbs at a separate spectral position without superposition with other protein/peptide modes such as Aha.

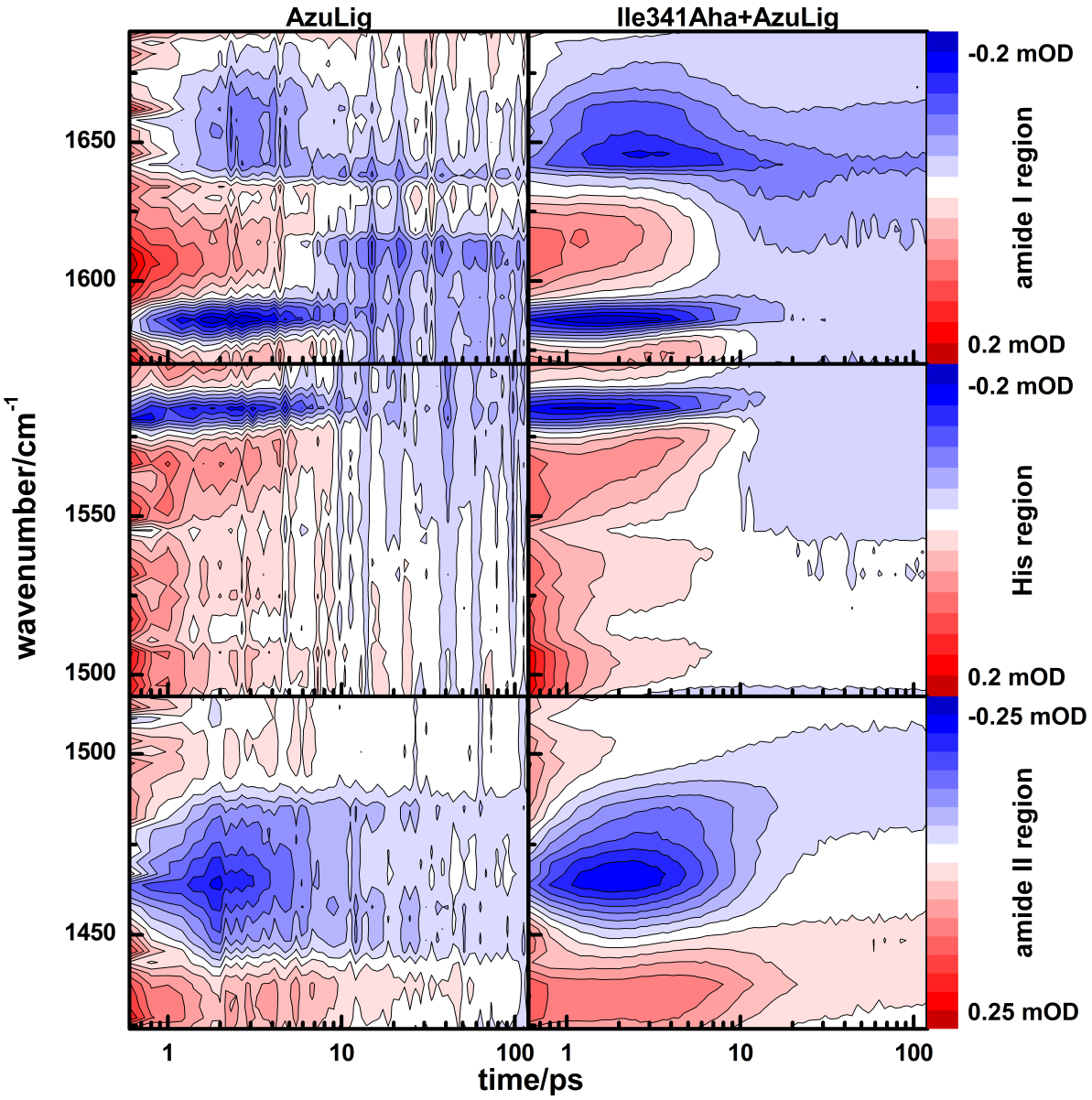

Figure 4.3.4: TRIR spectra of AzuLig (left column) and Ile341Aha+AzuLig (right column) in the amide I, histidine, and amide II region.

4.3.3 VET in Peptides

The heater-sensor pair Azu-Aha was applied to small peptides as test systems for the first VET measurements. The chemical structures of the used peptides are depicted in **figure 3.1.1** in **chapter 3**.

4.3.3.1 VET in DiPe

The first VET measurements with the heater-sensor pair were conducted on the most simple model system, a dipeptide consisting of only the ncAAs β-(1-azulenyl)-L-alanine (AzAla) and Aha (called DiPe) (**figure 4.3.5**).

Although the asymmetric stretching absorption of the azide in Aha is situated in a relatively spectrally clear region of the protein/water spectrum, a very broad combination band of H_2O libration and bending is centered at about 2000 cm^{-1} [120]. Even if the extinction coefficient of H_2O is very low for this mode, the vastly superior number of H_2O molecules compared to Aha residues leads to a much larger H_2O absorption in this region compared to the Aha absorption. The vibrational energy from the Azu heater is transferred to both, the peptide/protein and the solvent causing a large water heating background signal, which is overlapping with the azide signal (**figure 4.3.5 top**). Since the lifetime of this background signal is much longer than the one of the Aha signal, it can be easily corrected for it. A representative water heating signal was calculated by averaging all spectra at late population times (data points after 54 ps). At these delay times the Aha signal has already vanished and the water background signal is nearly constant. This averaged water signal was fitted with an amplitude and an offset to the TRIR spectra at every single population time and was subtracted. The Aha VET signal remained consisting of a typical negative and positive spectral feature (**figure 4.3.5 middle**). This shape arises from a red shift of the azido stretching vibration due to anharmonic coupling to low-frequency modes that received vibrational energy. The pumped/unpumped difference spectrum results in this typical spectra shape.

In order to summarize the information of the Aha VET signal and to reduce noise, the pixels on the probe axis containing the Aha VET signal were summed to get a time dependent azide transient. To prevent signal cancellation, the probe pixels with a positive Aha signal (in the dotted range marked with a red +) were summed up and the probe pixels with a negative Aha signal (in the dotted range marked with a blue -) were subtracted from them. The resulting azide transient gives the time evolution of the Aha VET signal (**figure 4.3.5 bottom**). To extract the maximum peak time, meaning the population time at which the VET signal is maximal, the azide transient was fitted by a biexponential function and its maximum value was picked. The estimated lifetimes of the two exponential components are containing large errors for several of the VET measurements pointing

out that a biexponential model with a monoexponential rise of the VET Aha signal and a monoexponential decay afterwards falls short. Considering the structure of PDZ3-Aha+AzuLig, several slightly different pathways between the heater and the sensor can be found. If the vibrational energy takes multiple pathways the growth of the arising VET signal will be a combination of these pathways and, thus, no longer monoexponential. The same applies to the decay of the VET signal. The biexponential fit of the azide transient can, therefore, only be used to determine the maximum peak time and not the time constants. However, when analyzing the different peak times, it has to be kept in mind, that the peak time depends not only on the transfer time of vibrational energy from the heater to the sensor, but also on the VET cooling time at the sensor, which depends on the position of the sensor in the molecule.

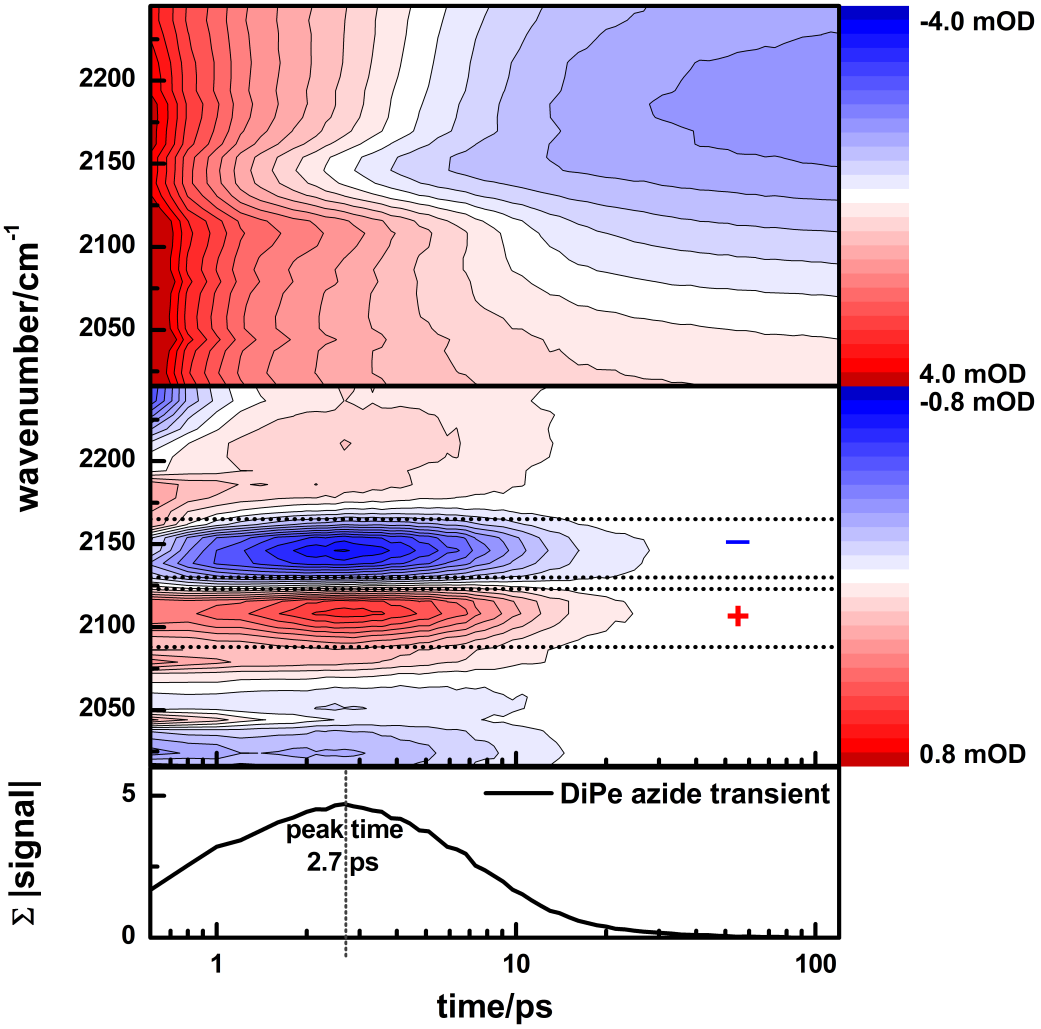

Figure 4.3.5: VET measurement of DiPe. **Top**: TRIR spectrum of a DiPe VET measurement probed in the Aha region before the background correction. **Middle**: The same DiPe TRIR spectrum after subtracting a scaled water heating background. All probe pixels in the dotted positive Aha signal range (marked with a red +) are added and the probe pixels in the dotted negative Aha signal range (marked with a blue -) are subtracted in order to calculate the azide transient (**bottom**).

In DiPe the along bond distance between the ring of the Azu and the first N-atom of the azido moiety in Aha comprises 8 covalent bonds (**table 4.19**). For a linear conformation, which might not be true for a DiPe in solution, a direct through-space distance between the Azu ring and the azide moiety of 8.5 Å is obtained. This value is, therefore, bracketed in the table. The Aha VET signal reaches its maximum 2.7 ps after the AzAla excitation.

Table 4.19: Distance between the heater and the sensor and the peak time of the VET signal for DiPe.

sample	**bonds Σ**	covalent bonds	H-bonds	**direct distance /Å**	**peak time /ps**
DiPe	8	8	-	(8.5)	2.7

4.3.3.2 VET in VETLig

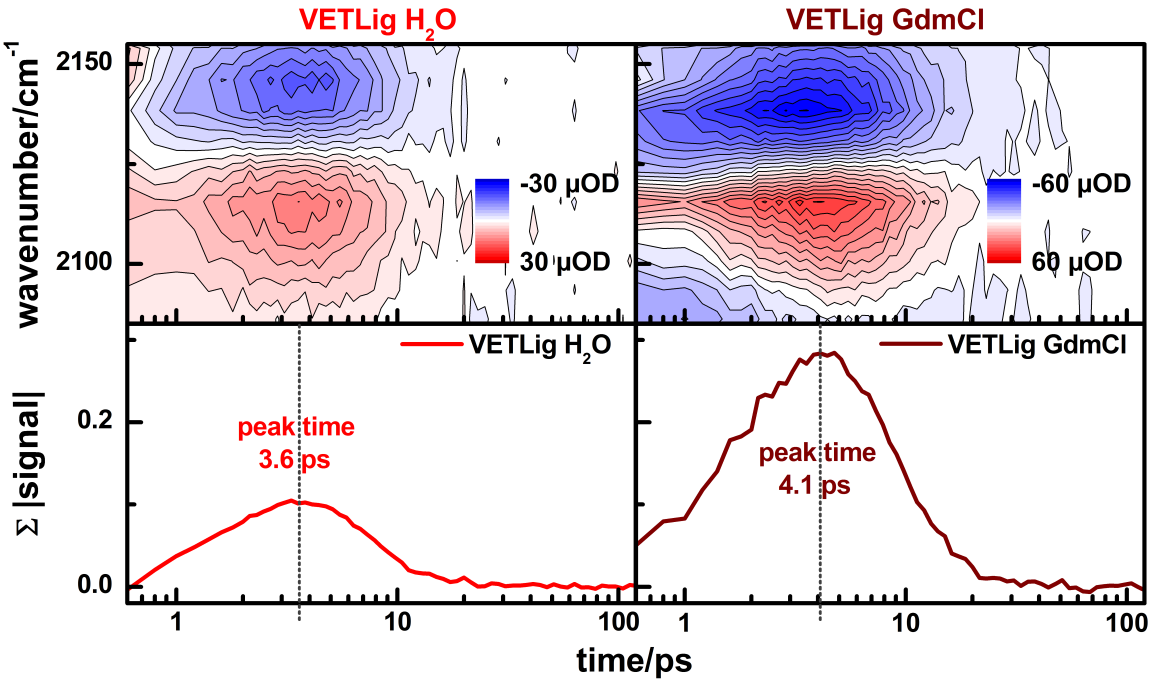

Figure 4.3.6: Left column: VET measurements of VETLig in H_2O. **Right column:** VET measurements of VETLig in H_2O with 8 M GdmCl. **Top row:** Background corrected TRIR spectra. **Bottom row:** Azide transients of VETLig.

Next, VET in a longer PDZ3 ligand-like peptide containing both AzAla and Aha with the sequence AzuAla-KQ-Aha-SV (VETLig) (structure in **figure 3.1.1**) is investigated (**figure 4.3.6 left**). Due to the larger distance (15 covalent bonds; **table 4.20**) between AzAla and Aha, the maximum peak time is reached later than for DiPe at 3.6 ps. In comparison to the distances the peak time of VETLig appears to be quite fast. Simulations of our collaboration partners in the Gerhard Stock group,

Physikalisches Institut, Albert-Ludwigs-Universität Freiburg, Germany, indicated that VETLig might be bended in solution (not published yet). Intramolecular non-covalent contacts seem to be available forming shortcuts for VET. To proof this finding, 8 M guanidine hydrochloride (GdmCl) serving as a strong denaturant were added to a VETLig sample to interrupt these intramolecular non-covalent contacts. Indeed, a later peak time of 4.1 ps was detected for the unfolded VETLig (**figure 4.3.6 right** and **figure 4.3.7**). The Aha VET signal of DiPe with 8 M GdmCl remained unperturbed (data not shown) confirming that the change in peak time of VETLig is not caused by a changed VET transfer rate to the solvent. These results demonstrate that vibrational energy is also transferred efficiently across non-covalent contacts like hydrogen bonds.

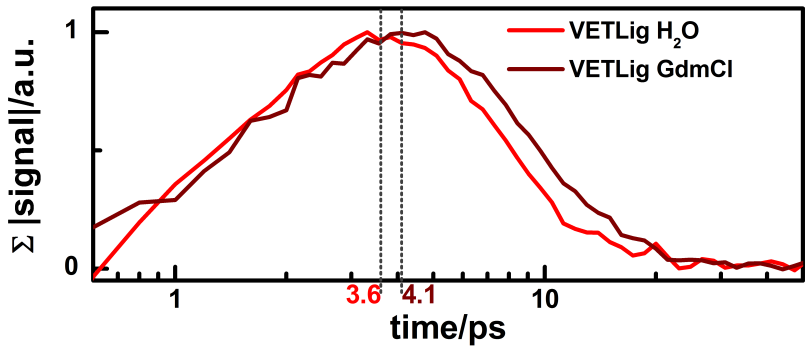

Figure 4.3.7: Normalized transients of the Aha VET signal of VETLig in H_2O and in H_2O containing 8 M GdmCl in comparison.

Table 4.20: Distance between the heater and the sensor and the peak time of the VET signal for VETLig.

sample	**bonds Σ**	covalent bonds	H-bonds	**direct distance /Å**	**peak time /ps**
VETLig	(15)	(15)	(-)	(15.6)	3.6
VETLig GdmCl	15	15	-	15.6	4.1

4.3.4 VET in PDZ3-Aha

In order to observe VET in an allosteric protein, an Azu was incorporated into a PDZ3 ligand (AzuCa-KQTSV called AzuLig; structure in **figure 3.1.1**). Azulene-1-yl-acetic-acid (AzuCa) was used as the Azu containing residue in this case. It comprises one C-C bond less on the way to the peptide bond to the next AA compared to AzAla, but exhibits similar properties in inducing VET [70]. When AzuLig is bound to PDZ3-Aha, intramolecular VET between the heater in the ligand and the sensor in the protein can be observed for several PDZ3-Aha mutants.

4.3.4.1 ITC PDZ3-Aha with AzuLig

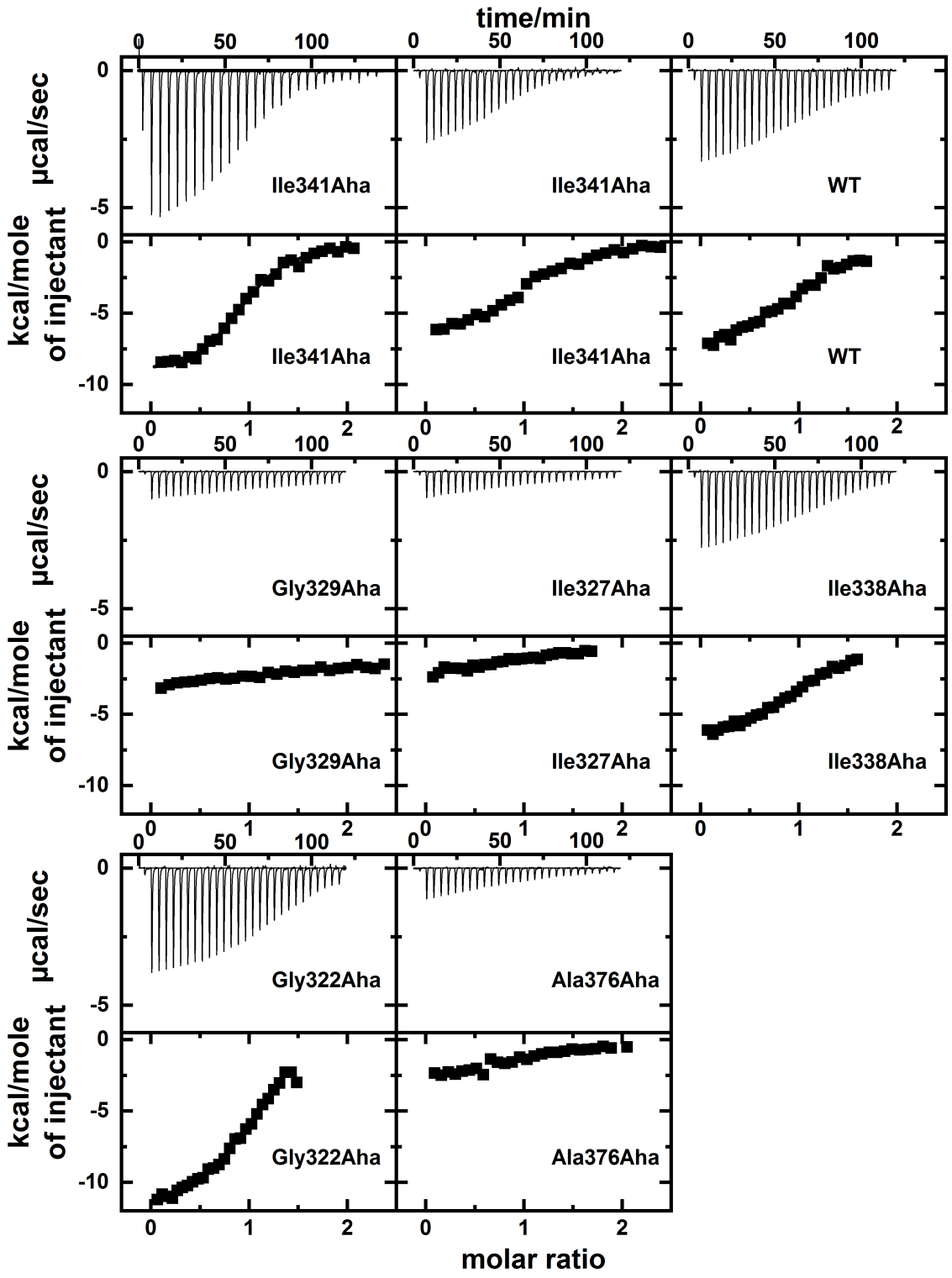

Figure 4.3.8: ITC data of different PDZ3-Aha mutants with AzuLig. The first Ile341Aha measurement was conducted with a pure AzuLig (top left). The concentration of the impure AzuLig used for the other measurements was normalized according to it.

ITC measurements of WT PDZ3 and the used PDZ3-Aha mutants were performed to proof that AzuLig binds with a sufficient binding affinity (**figure 4.3.8**). The concentration of AzuLig could not be determined because of the impurity with shorter fragments of the N-terminus. Therefore, an older ITC measurement with a former batch of pure AzuLig (old ligand) with Ile341Aha (**figure 4.3.8 top left**) is used to estimate the concentration of the new AzuLig by matching it to the binding parameters of the former ITC measurements. The AzuLig concentration for the other mutants are adjusted to this value via comparing UV-Vis absorptions. In total, significantly smaller binding affinities are found for AzuLig compared to native Hepta (a factor 7-20 less) (**table 4.21**). Here again, the same trend of which mutant binds with a lower/higher affinity compared to the WT PDZ3 as for the native ligand is found. Ile327Aha, Ala376Aha, and Gly329Aha bind AzuLig with a significantly lower affinity than WT PDZ3 and Gly322Aha binds it with a higher affinity. However, the ratios between the binding constants of the PDZ3-Aha mutants and WT with AzuLig are not exactly the same as for Hepta. Gly329Aha binds AzuLig that poorly, that the quality of the ITC measurement is very low and the value for stoichiometry needs to be fixed to N=1 in order to perform a fit. However, despite the lower binding affinity, AzuLig can be assumed to be bound to a ratio of more than 90 % for the applied concentrations in the VET measurements. Solely for the Gly329Aha+AzuLig VET measurement the ratio of bound AzuLig can be supposed to be a bit lower with just 79 %. Due to the bad data quality of the ITC PDZ3-Aha+AzuLig measurements and the uncertainty with the ligand concentration, it would be useful to repeat ITC measurements when pure AzuLig is available. For determining better data quality a ligand displacement strategy could be applied [256, 258].

Our collaboration partner Florian Lehner from the Harald Schwalbe group, Institut für Organische Chemie, Johann Wolfgang Goethe-Universität Frankfurt, Germany, measured NMR spectra of Ile341Aha with Hepta and also with AzuLig. The data showed that AzuLig binds to Ile341Aha in a very similar way than the native ligand Hepta [104]. Only the residues Gly329 and Gly330 in the L2-loop are affected by the bulky hydrophobic azulene moiety of AzuLig, which might explain the particular low binding affinity of Gly329Aha to AzuLig.

Table 4.21: Binding parameters of WT PDZ3 and PDZ3-Aha mutants with AzuLig determined by ITC.

	k_a /μM^{-1}	k_d /μM	N	ΔH/cal/mol	ΔS/cal/mol
WT	0.043±0.006	23±4	1.05±0.02	-8000±300	-5.77
Ala376Aha	0.026±0.009	40±20	1.09±0.08	-3200±400	9.43
Gly322Aha	0.077±0.008	13±2	1.07±0.02	-12000±200	-17.8
Gly329Aha	0.0011±0.0002	900±200	1.0 fixed	-32000±4000	-92.1
Ile327Aha	0.011±0.004	90±40	1.1±0.2	-3300±700	7.29
Ile338Aha	0.048±0.004	21±2	1.07±0.02	-6900±200	-184
Ile341Aha	0.073±0.007	14±2	0.96±0.02	-9400±200	-9.29
	0.074±0.008	14±2	1.07±0.02	-6900±200	-0.705

4.3.4.2 VET Measurements PDZ3-Aha with AzuLig

VET in WT

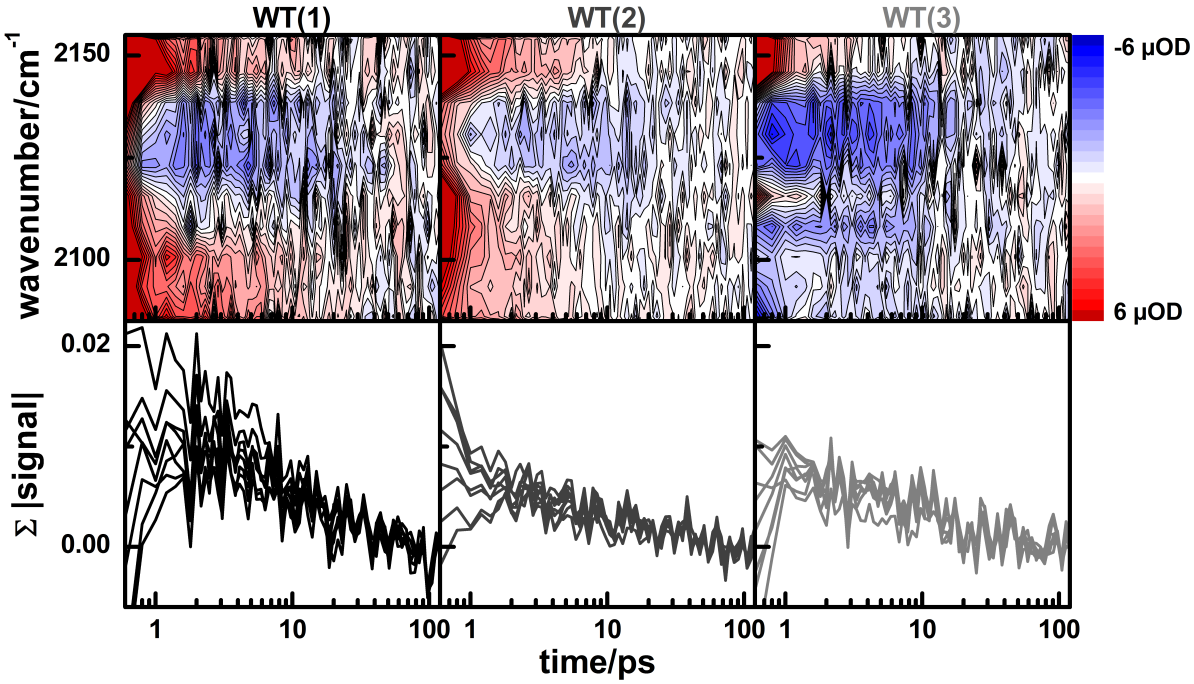

Figure 4.3.9: Three distinct WT+AzuLig VET measurements (**left** WT(1), **middle** WT(2), and **right** WT(3)). **Top:** Background corrected TRIR spectra. **Bottom:** Depicted transients of WT+AzuLig are calculated using the sum of the same probe pixels as for the individual PDZ3-Aha measurements to give the level of background signal.

The Aha VET signal is expected to decrease with increasing distance between the heater and the sensor due to VET to the solvent and along other pathways in the ligand/protein. Therefore, the underlying background spectrum after the water heating background correction needs to be proofed. To get the sensor free spectrum remaining after the water heating background correction, VET measurements of WT PDZ3 with AzuLig were conducted for three individual WT+AzuLig samples (**figure 4.3.9**). In these measurements without sensor the TRIR spectrum after background correction should be smooth and without any signal. However, very small signal like structures were detected exhibiting similarities to the Aha VET signals. Since some of these structures in the spectrum do not shift spectrally when the spectrometer is turned, they are assumed to arise from nonlinearities of the detector and uncertainties deriving from the background correction. Additionally, their shape and size is changing a bit between different measurements. Thus, they are assumed to be measurement artifacts. However, they limit up to which signal size an Aha VET signal can be distinguished explicitly from the background. The measured transients of the PDZ3-Aha+AzuLig samples, therefore, need to be compared to the transient of the WT+AzuLig measurements using the same probe

pixels for summation in order to judge if the observed signal is a real Aha VET signal and not an artifact.

VET in Gly329Aha

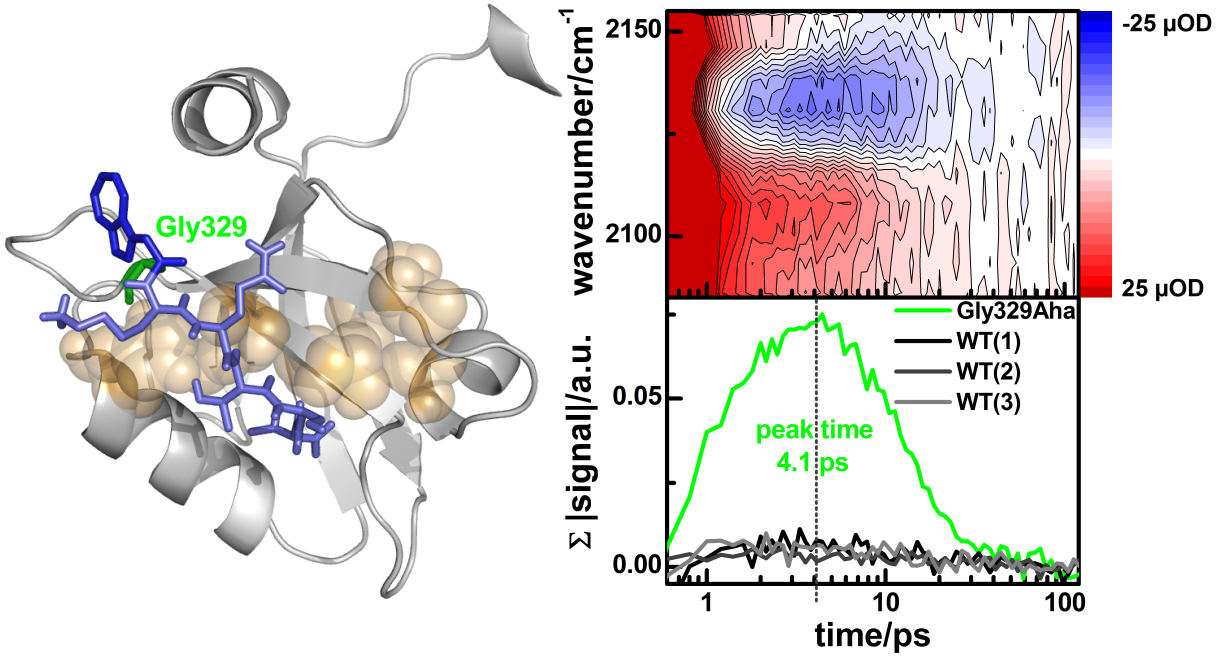

Figure 4.3.10: Left: Structure of PDZ3 (grey) with AzuLig (light blue). The structure derived from in silico docking experiments performed by Martin Essig [219] with the shortened PDB structure 1BE9. The position of Gly329 is marked green and the AzuCa in AzuLig is colored blue. The on-pathway residues of the simulation of Ota and Agard [6] are marked light yellow. **Right:** VET measurements. **Top:** Background corrected TRIR spectrum of Gly329Aha+AzuLig. **Bottom:** Azide transient of Gly329Aha+AzuLig (green) and the transients of 3 distinct WT+AzuLig measurements (grey) using the same probe pixels for summation.

Table 4.22: Distance between the heater and the sensor and the peak time of the VET signal for Gly329Aha+AzuLig.

sample	**bonds Σ**	covalent bonds	H-bonds	**direct distance /Å**	**peak time /ps**
Gly329Aha+AzuLig	(20)	(19)	(1)	(7)	4.1

A large Aha VET signal with a peak time of 4.1 ps, which is by several orders of magnitude larger than the background artifacts, is found for the Gly329Aha mutant (**figure 4.3.10**). Since the AzuCa and the Aha are very close in space and the exact orientation of the side chains of both is not known, the through bond and through space distance between both is difficult to estimate and, therefore, bracketed (**table 4.22**). The crystal structure of Gly329Aha+AzuLig is needed to be resolved for further analysis of VET in this mutant. It is conspicuous that the Aha

VET signal in this mutant is outstanding broad in time suggesting that multiple pathways with different traveling times are used by the vibrational energy on its way from AzuCa to Aha.

VET in Ile327Aha

In the Ile327Aha mutant the Aha is embedded into the βB-sheet in the binding pocket. The Aha side chain is expected to be orientated away from the ligand like the naturally occurring Ile327 side chain. An unambiguous Aha VET signal was detected (**figure 4.3.11**) with a peak time of 5.6 ps. The shortest along bond distance includes 15 covalent and 1 hydrogen bond (H-bond) and a direct distance of 9.9 Å (**table 4.23**).

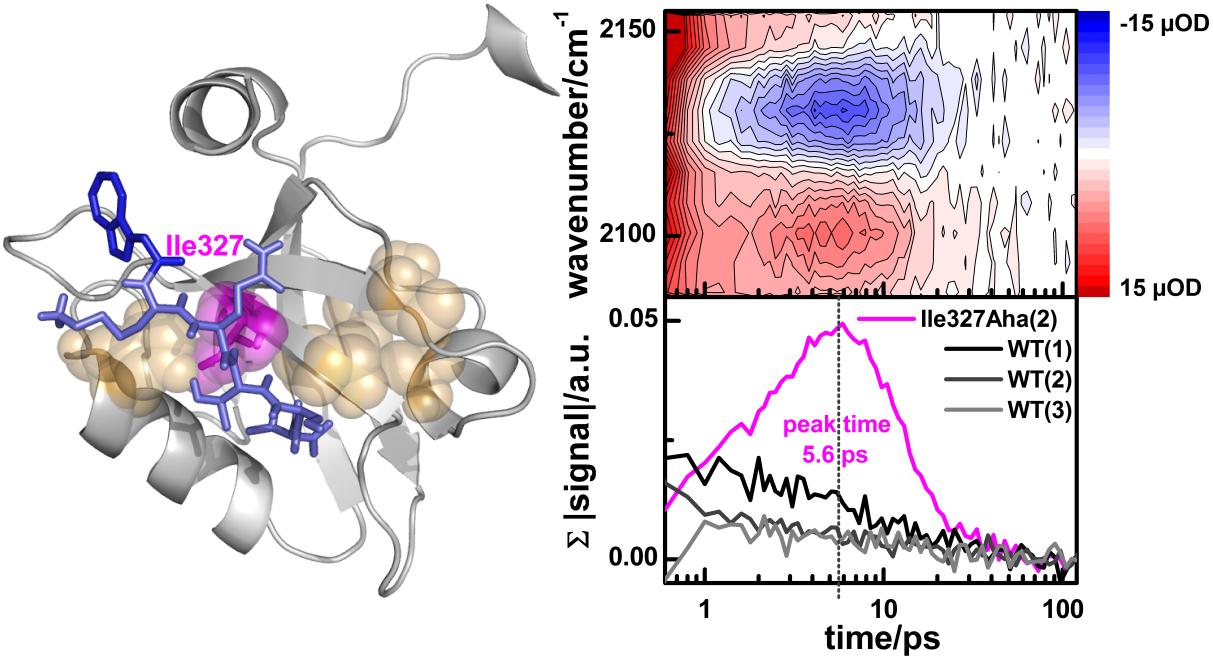

Figure 4.3.11: Left: Structure of PDZ3 (grey) with AzuLig (light blue). The structure derived from in silico docking experiments performed by Martin Essig [219] with the shortened PDB structure 1BE9. The position of Ile327 is marked magenta and the AzuCa in AzuLig is colored blue. The on-pathway residues of the simulation of Ota and Agard [6] are marked light yellow. **Right:** VET measurements. **Top:** Background corrected TRIR spectrum of Ile327Aha+AzuLig. **Bottom:** Azide transient of Ile327Aha+AzuLig (magenta) and the transients of 3 distinct WT+AzuLig measurements (grey) using the same probe pixels for summation.

Table 4.23: Distance between the heater and the sensor and the peak time of the VET signal for Ile327Aha+AzuLig.

sample	**bonds Σ**	covalent bonds	H-bonds	**direct distance /Å**	**peak time /ps**
Ile327Aha+AzuLig(2)	16	15	1	9.9	5.6

The transients the VET measurements of three different Ile327Aha+AzuLig samples at diverse experimental averaging times are compared in order to proof the reproducibility of the transient (**figure 4.3.12**) and the derived peak times (**table 4.24**). The early rise of the transients is strongly differing since the water heating background correction does not work well for early times because it is perturbed by the foothills of the large perturbed free induction decay signal at time zero at which the pump and the probe pulse are overlapping temporally. At times larger than 1.1 ps the measured transients are highly reproducible and also the estimated peak times are only differing maximally by 0.6 ps.

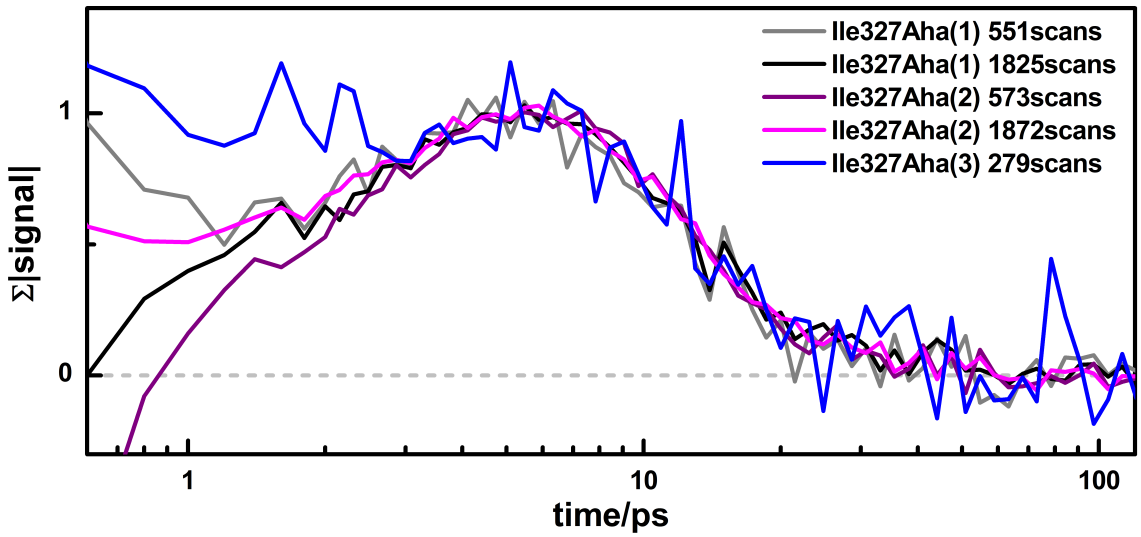

Figure 4.3.12: Aha transients of three different Ile327Aha+AzuLig measurements ((1)-(3)) after varying experimental averaging times (number of scans).

Table 4.24: Peak times of the Aha transients of three different Ile327Aha+AzuLig measurements ((1)-(3)) after varying experimental averaging times (number of scans).

data	number of scans	peak time/ps
(1)	551	5.0
	1825	5.3
(2)	573	5.6
	1872	5.6
(3)	279	5.2

VET in Ile338Aha

In the Ile338Aha mutant, in which Aha is placed in the βC-sheet, the vibrational energy needs to vertically cross two β-sheets to reach the Aha sensor. Nevertheless, a distinct temporally rather sharp Aha VET signal is obtained (**figure 4.3.13**) at a peak time of 7.8 ps after an through bond distance of 19 covalent and 2 H-bonds or a direct distance of 14.6 Å (**table 4.25**).

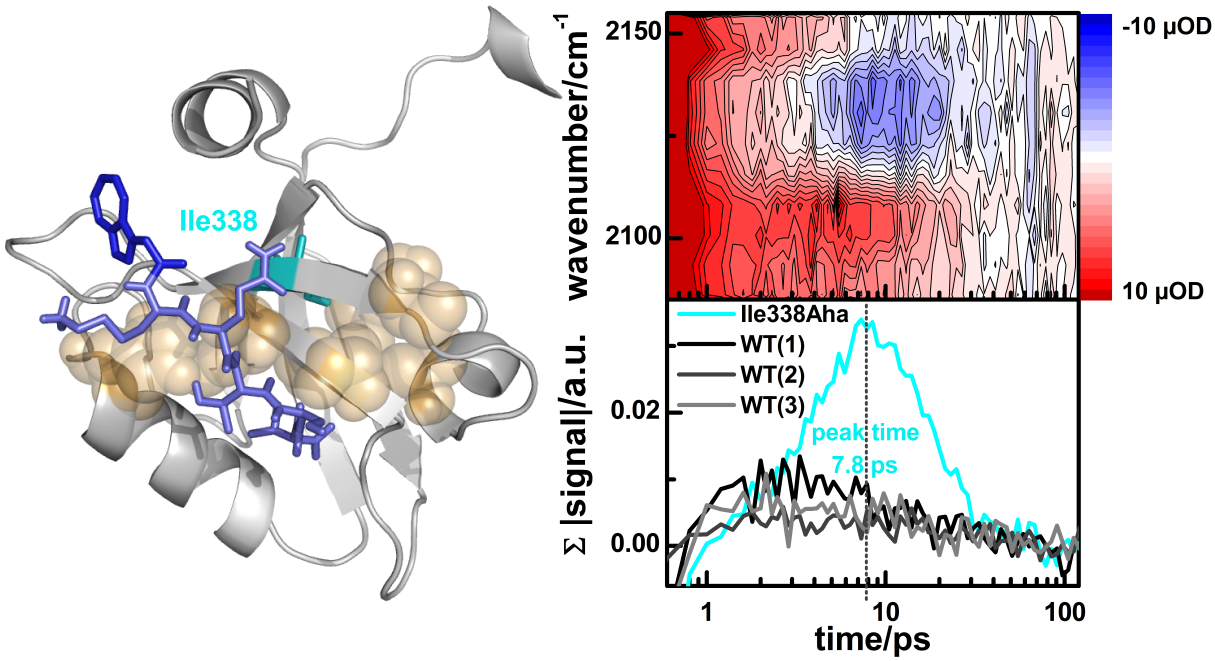

Figure 4.3.13: Left: Structure of PDZ3 (grey) with AzuLig (light blue). The structure derived from in silico docking experiments performed by Martin Essig [219] with the shortened PDB structure 1BE9. The position of Ile338 is marked cyan and the AzuCa in AzuLig is colored blue. The on-pathway residues of the simulation of Ota and Agard [6] are marked light yellow. **Right:** VET measurements. **Top:** Background corrected TRIR spectrum of Ile338Aha+AzuLig. **Bottom:** Azide transient of Ile338Aha+AzuLig (cyan) and the transients of 3 distinct WT+AzuLig measurements (grey) using the same probe pixels for summation.

Table 4.25: Distance between the heater and the sensor and the peak time of the VET signal for Ile338Aha+AzuLig.

sample	**bonds Σ**	covalent bonds	H-bonds	**direct distance /Å**	**peak time /ps**
Ile338Aha+AzuLig	21	19	2	14.6	7.8

VET in Ile341Aha

For the Ile341Aha mutant the distance between the Azu moiety in AzuLig and the Aha, which is placed at the opposite end of the βC-sheet, is even larger with 23 covalent bonds and 2 H-bonds for the shortest through bond distance and a direct through space distance of 16.5 Å (**table 4.26**). Accordingly, the signal in the VET transients gets very small and noisy (**figure 4.3.14**). It rises only little from the background artifact signal. At early times its temporal evolution is strongly perturbed by the foothills of the large perturbed free induction decay signal at time zero and the peak time of about 9.7 ps is difficult to estimate. The VET measurement of Ile341Aha+AzuLig was reproduced twice to ensure that the found signal is indeed arising from the Aha sensor and not a measurement artifact. In the first two

experiments (**figure 4.3.15 a** and **b**) the VET Aha transient rises from the background artifact and shows a similar curve shape at late population times, at which it is not perturbed by foothills from time zero signals (**4.3.15 d**). These findings suggest, that the observed signal in the transient is indeed an Aha VET signal. The third measurement was one of the last VET measurements performed at a time, when the laser setup was in an insufficient condition and the obtained VET signals were much smaller (see **chapter 3.4.1**). It is not surprising, that such a small VET Aha signal could not be detected under these suboptimal measurement conditions.

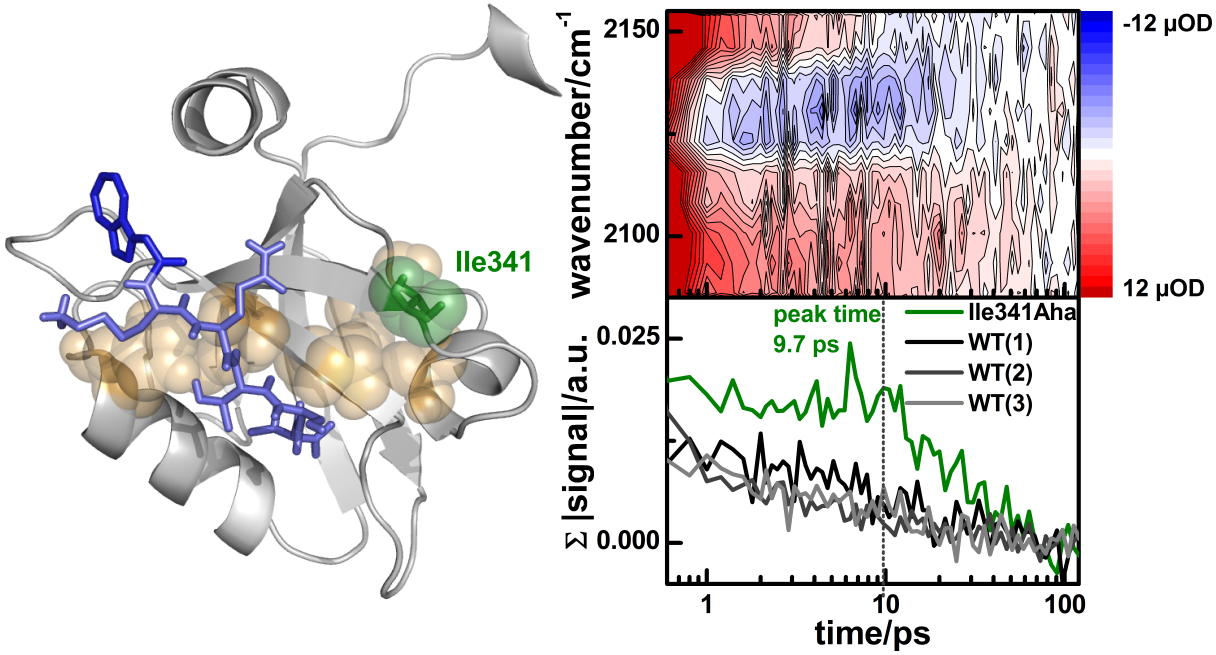

Figure 4.3.14: Left: Structure of PDZ3 (grey) with AzuLig (light blue). The structure derived from in silico docking experiments performed by Martin Essig [219] with the shortened PDB structure 1BE9. The position of Ile341 is marked olive green and the AzuCa in AzuLig is colored blue. The on-pathway residues of the simulation of Ota and Agard [6] are marked light yellow. **Right:** VET measurements. **Top:** Background corrected TRIR spectrum of Ile341Aha+AzuLig. **Bottom:** Azide transient of Ile341Aha+AzuLig (olive green) and the transients of 3 distinct WT+AzuLig measurements (grey) using the same probe pixels for summation.

Table 4.26: Distance between the heater and the sensor and the peak time of the VET signal for Ile341Aha+AzuLig.

sample	**bonds Σ**	covalent bonds	H-bonds	**direct distance /Å**	**peak time /ps**
Ile341Aha+AzuLig(2)	25	23	2	16.5	9.7

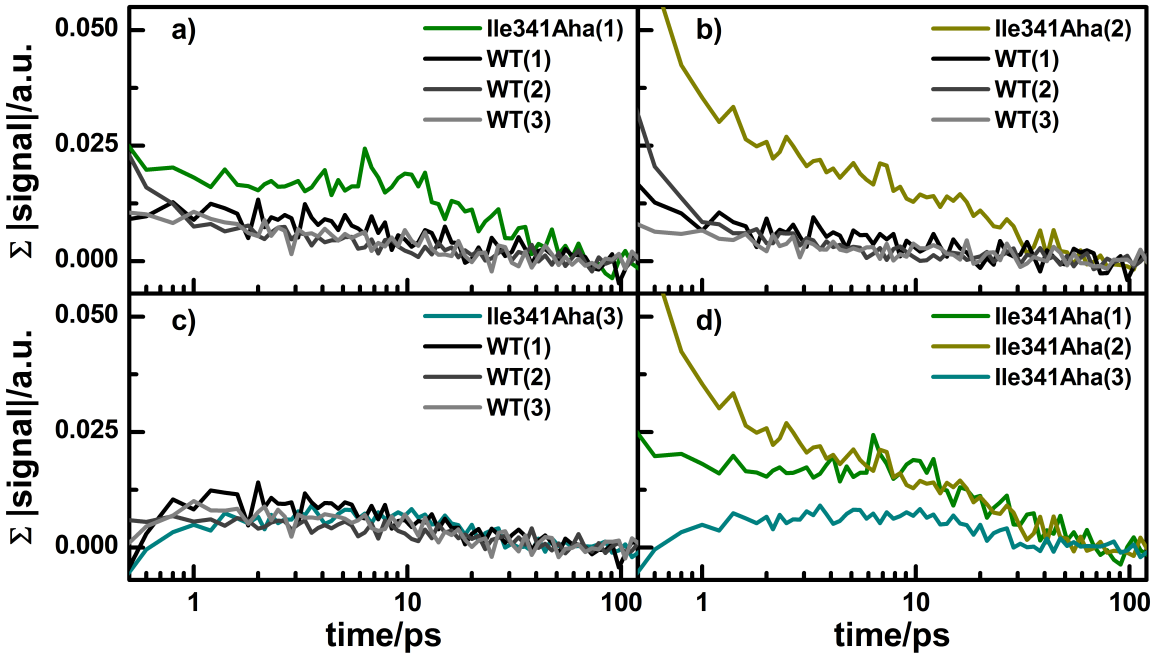

Figure 4.3.15: Azide transient of Ile341Aha+AzuLig and the transients of 3 distinct WT+AzuLig measurements (grey) summing the same probe pixels for three distinct Ile341Ah+AzuLig measurements (**a**, **b**, and **c**) and the three Ile341Aha+AzuLig transients in comparison (**d**).

VET in Gly322Aha

Despite also being measured with the described insufficient conditions of the laser setup, the VET transient of Gly322Aha+AzuLig seems to comprise a small Aha VET signal (**figure 4.3.16**). That this Aha VET signal can be seen even under the suboptimal setup conditions indicates that it might have been much clearer if it was detected under good measurement conditions. Due to the large perturbation caused by the time zero foothills and the large measurement noise, the peak time could not be estimated precisely. The Gly322Aha mutation is placed in the carboxylate binding loop at the opposing site of the ligand 24 bond or 19.2 Å away from the Azu moiety (**table 4.27**).

Table 4.27: Distance between the heater and the sensor and the peak time of the VET signal for Gly322Aha+AzuLig.

sample	**bonds Σ**	covalent bonds	H-bonds	**direct distance /Å**	**peak time /ps**
Gly322Aha+AzuLig	24	23	1	19.2	?

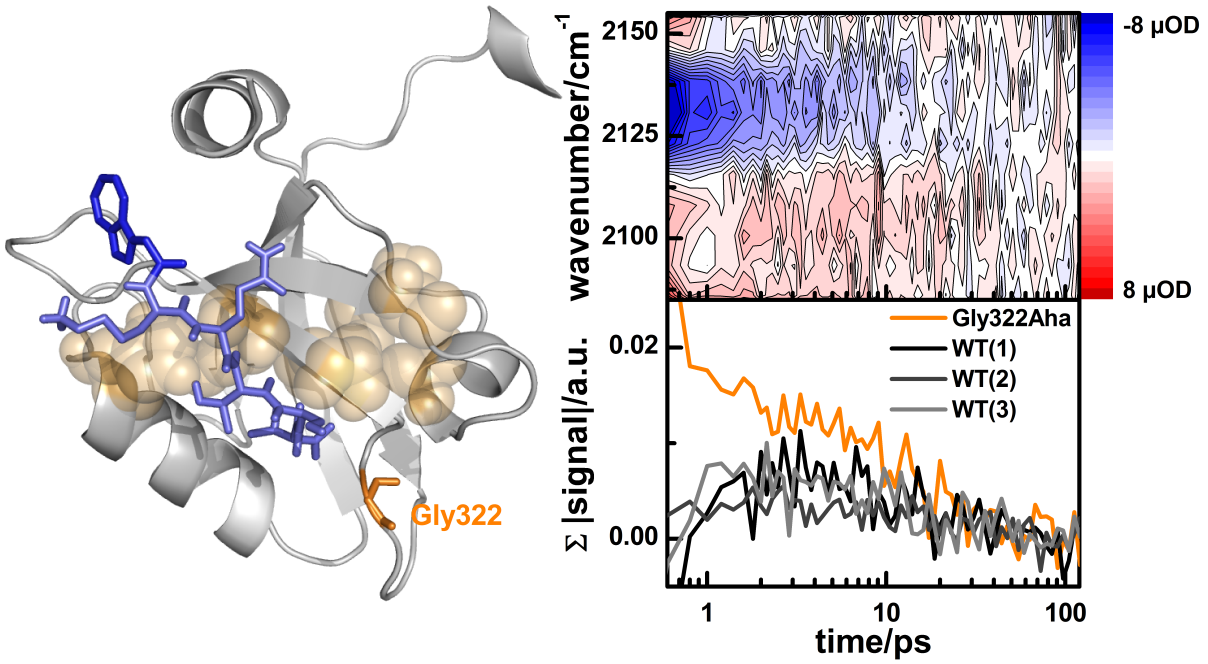

Figure 4.3.16: Left: Structure of PDZ3 (grey) with AzuLig (light blue). The structure derived from in silico docking experiments performed by Martin Essig [219] with the shortened PDB structure 1BE9. The position of Gly322 is marked orange and the AzuCa in AzuLig is colored blue. The on-pathway residues of the simulation of Ota and Agard [6] are marked light yellow. **Right:** VET measurements. **Top:** Background corrected TRIR spectrum of Gly322Aha+AzuLig. **Bottom:** Azide transient of Gly322Aha+AzuLig (orange) and the transients of 3 distinct WT+AzuLig measurements (grey) using the same probe pixels for summation.

VET in Ala376Aha

In the Ala376Aha mutant the sensor is placed on the other site of the ligand binding pocket in the αB-helix 24 covalent and 2 H-bond / 13.4 Å away from the Azu moiety (**table 4.28**). The VET transient of the Ala376Aha+AzuLig measurement hardly rises from the signal size of the background artifact (**figure 4.3.17**). It is difficult to judge, if the observed signal is an Aha VET signal or originates from the background artifact. The VET measurement was repeated, but with the described insufficient laser setup conditions, and, thus, no Aha VET signal was found for the second Ala376Aha+AzuLig measurement (**figure 4.3.18**).

Table 4.28: Distance between the heater and the sensor and the peak time of the VET signal for Ala376Aha+AzuLig.

sample	**bonds Σ**	covalent bonds	H-bonds	**direct distance /Å**	**peak time /ps**
Ala376Aha+AzuLig	26	24	2	13.4	?

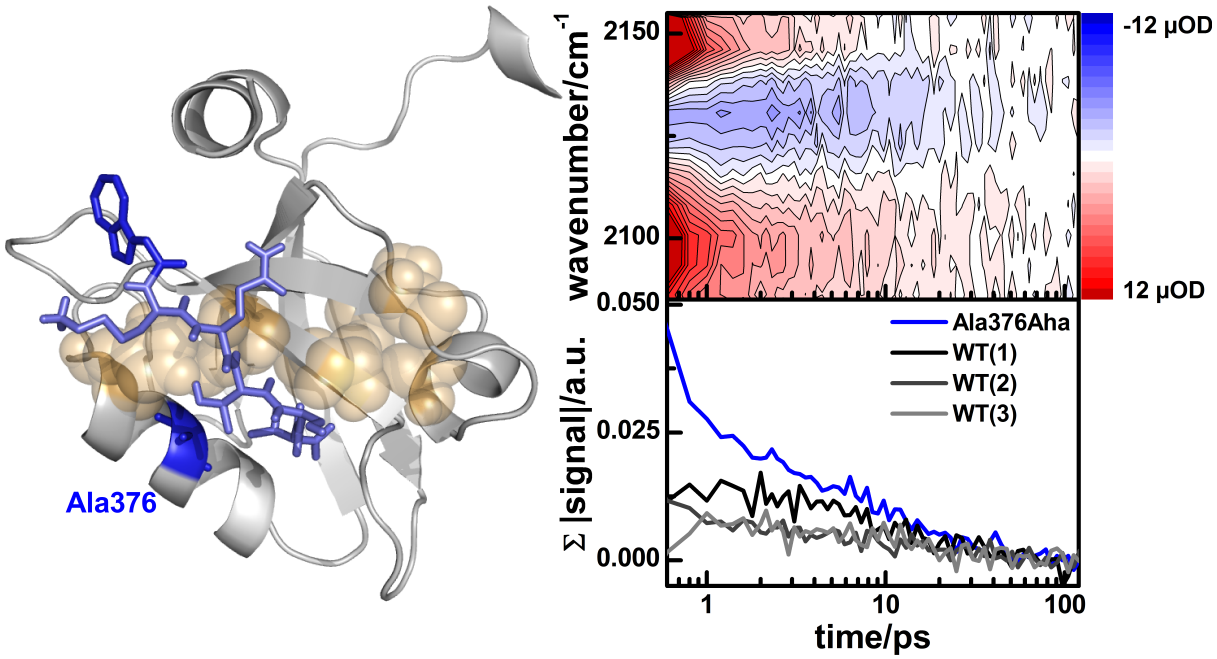

Figure 4.3.17: Left: Structure of PDZ3 (grey) with AzuLig (light blue). The structure derived from in silico docking experiments performed by Martin Essig [219] with the shortened PDB structure 1BE9. The position of Ala376 is marked blue and the AzuCa in AzuLig is also colored blue. The on-pathway residues of the simulation of Ota and Agard [6] are marked light yellow. **Right:** VET measurements. **Top:** Background corrected TRIR spectrum of Ala376Aha+AzuLig. **Bottom:** Azide transient of Ala376Aha+AzuLig (blue) and the transients of 3 distinct WT+AzuLig measurements (grey) using the same probe pixels for summation.

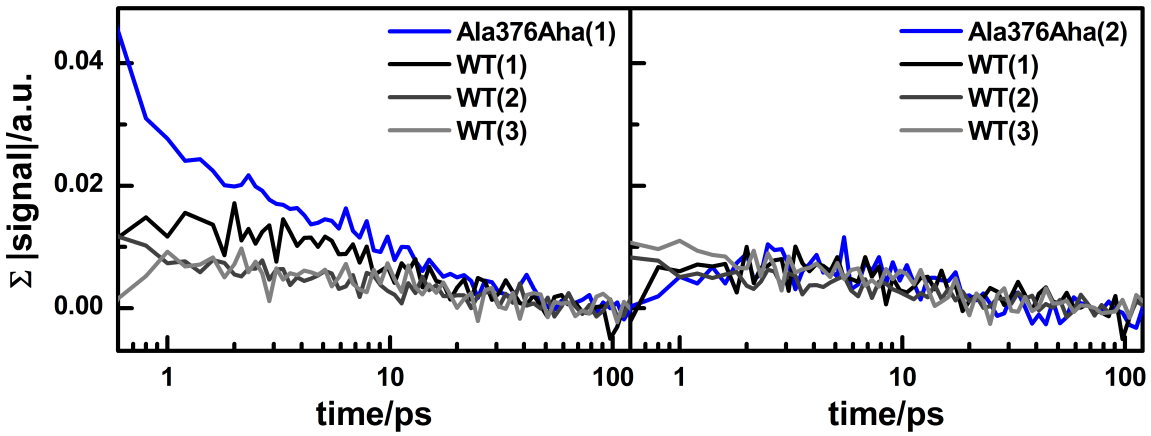

Figure 4.3.18: Azide transient of Ala376Aha+AzuLig with the transients of 3 distinct WT+AzuLig measurements (grey) (same probe pixels summed) for two distinct Ala376Aha+AzuLig measurements (**left** and **right**).

VET in Lys380Aha

For the Lys380Aha mutant, in which the Aha is placed further afar in the αB-helix, also no Aha VET signal could be observed using the suboptimal laser setup conditions (**figure 4.3.19**).

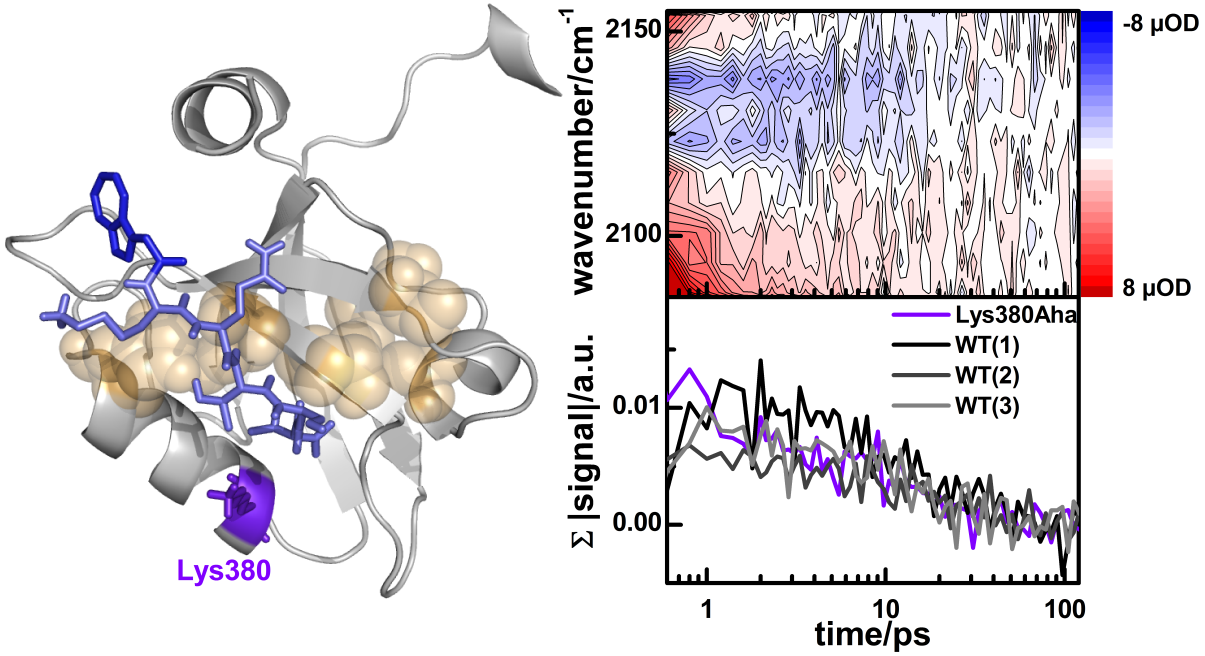

Figure 4.3.19: Left: Structure of PDZ3 (grey) with AzuLig (light blue). The structure derived from in silico docking experiments performed by Martin Essig [219] with the shortened PDB structure 1BE9. The position of Lys380 is marked violet and the AzuCa in AzuLig is colored blue. The on-pathway residues of the simulation of Ota and Agard [6] are marked light yellow. **Right:** VET measurements. **Top:** Background corrected TRIR spectrum of Lys380Aha+AzuLig. **Bottom:** Azide transient of Lys380Aha+AzuLig (violet) and the transients of 3 distinct WT+AzuLig measurements (grey) using the same probe pixels for summation.

4.3.4.3 VET Signal Evolution

Vibrational energy is transferred with a velocity of 1.7-1.9 Å/ps (through space direct distance) or 3.9-4.5 Å/ps (along bond distance) from the AzuCa in the ligand into PDZ3. This velocity corresponds to previously reported VET velocities of 1-14.4 Å/ps [10, 61, 63, 70, 135].

The time the vibrational energy needs to reach the sensor (peak time) increases with increasing distance between the heater and the sensor (**table 4.29**). This rise becomes obvious when comparing the normalized transients (**figure 4.3.20**). The width in time of the observed Aha VET peaks is strongly differing between the mutants. Two extreme scenarios are the Gly329Aha+AzuLig mutant, which is very broad and the Ile338Aha, which is very narrow in time. As discussed above

this might be due to the vibrational energy taking multiple pathways with variable transfer durations causing asynchronous arrival of vibrational energy at the sensor.

Table 4.29: Distance between the heater and the sensor and the peak times of the Aha VET signals in comparison.

sample	bonds Σ	covalent bonds	H-bonds	direct distance /Å	peak time /ps
DiPe	8	8	-	(8.5)	2.7
VETLig	(15)	(15)	(-)	(15.6)	3.6
VETLig GdmCl	15	15	-	(15.6)	4.1
Gly329Aha+AzuLig	(20)	(19)	(1)	(7)	4.1
Ile327Aha+AzuLig(1)	16	15	1	9.9	5.3
Ile327Aha+AzuLig(2)	16	15	1	9.9	5.6
Ile338Aha+AzuLig	21	19	2	14.6	7.8
Ile341Aha+AzuLig(2)	25	23	2	16.5	9.7
Ala376Aha+AzuLig(1)	26	24	2	13.4	?
Gly322Aha+AzuLig	24	23	1	19.2	?

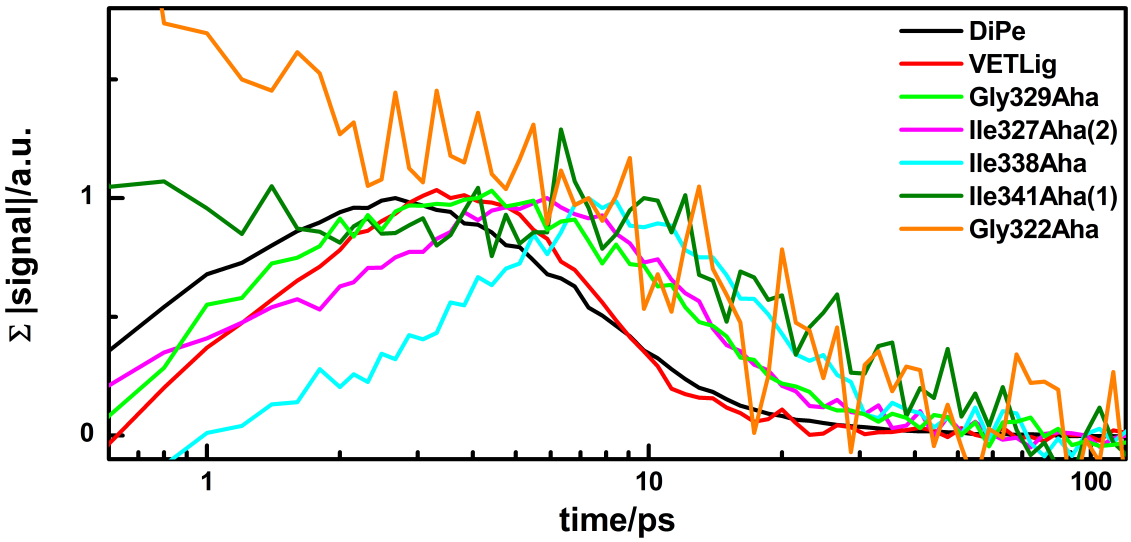

Figure 4.3.20: Normalized Aha transients of the peptides and the PDZ3-Aha mutants in comparison.

With increasing distance between the Azu heater and the Aha sensor not only the peak time increases but also the Aha VET signal size decreases (**figure 4.3.21**) due to the loss of vibrational energy to the solvent and to other branching off pathways in the PDZ3/ligand complex. Both the VET velocity along a distinct pathway in PDZ3-Aha and the Aha VET signal size in dependency on the distance between heater and sensor gives a scale of the vibrational energy throughput along this pathway. Comparing VET velocity and efficiency for PDZ3-Aha mutants spanning the whole protein will enable to reveal allosteric pathways of efficient VET.

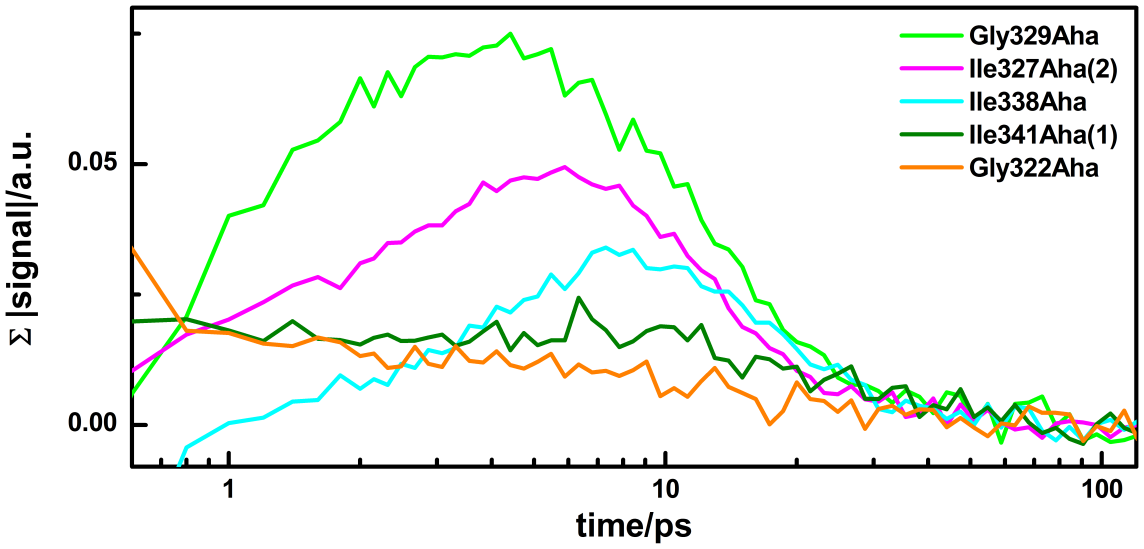

Figure 4.3.21: VET Aha transients of the PDZ3-Aha mutants in comparison.

4.3.4.4 VET Efficiency in PDZ3-Aha with AzuLig

Concentration Calculation

Knowledge of how much of the injected vibrational energy reaches the Aha sensor can give a scale for the efficiency of VET on the pathway between heater and sensor. VET efficiencies between different mutants/pathways can be compared.

For determining the VET efficiency of the PDZ3-Aha AzuLig measurements it is important to know the exact protein concentration and the ratio of AzuLig to PDZ3 of the used samples. As the protein concentration determined by Lowry assay before concentrating is not accurate enough, another method needs to be applied.

FTIR spectra of the VET samples were detected directly before the VET measurement with the VET sample already filled into its sample cell (**figure A.0.8**). The bands in the amide II and amide III region mainly reflect the spectrum of PDZ3 and not the ligand as the comparison with two separately measured FTIR spectra of WT PDZ3 without ligand (WT(1) and WT(2)) demonstrates (also in **figure A.0.8**). Small variations are due to a linear offset and a slightly different content of DMSO in the H_2O buffer (spectra of AzuLig compared to a DMSO/H_2O sample with circa 2 % DMSO). The region between 1500 and 1250 cm^{-1} might be a good scale for the protein concentration but not for AzuLig concentration.

The concentrations of the two WT without ligand reference samples are calculated from their UV-Vis spectra (**figure A.0.9**) and PDZ3's extinction coefficient at 280 nm of 2980 $M^{-1}cm^{-1}$ (determined by its sequence). WT(1) has a concentration of 10.4 mM and WT(2) one of 11.6 mM, which is close to the intended concentration

of 10 mM. To proof the utility of the FTIR amid II and III region for PDZ3 concentration determination, UV-Vis and FTIR spectra of a set of 8 PDZ3 mutant samples without ligand were measured and both WT spectra are fitted to the mutant spectra, separately, including a linear offset. Results are compared and a maximum deviation of 13 % is found with most of the values differing less. Concentration determination using the amid II and III FTIR bands of PDZ3 seems to be accurate.

The relative concentrations of all PDZ3 mutant samples in comparison to the two WT spectra are calculated. For this a linear combination of the scaled WT(1)/WT(2) spectra plus the scaled AzuLig/(DMSO/H_2O) spectra plus an offset is implemented (in the range between 1500 and 1250 cm^{-1}). A scaled AzuLig or DMSO/H_2O spectrum is needed to correct for differences in DMSO content. The calculated concentration of the VET PDZ3 mutant samples are similar for the different individually applied WT and AzuLig or DMSO/H_2O spectra. The mean value is formed (**table 4.30**). PDZ3-Aha concentrations in a range between 9 and 16.3 mM are found.

Table 4.30: Protein concentrations of the PDZ3-Aha VET samples determined by a linear combination in the amid II-III region of the IR spectrum and relative protein concentrations normalized to the concentration of Ala376Aha+AzuLig(1). The relative concentration of the AzuLig derived from a linear combination of the UV-Vis absorption. It is also normalized to the AzuLig concentration of the Ala376Aha+AzuLig(1) measurement. A relative ratio between the AzuLig and protein concentration is calculated. It is a normalized value which compares the ratio among the different samples and does not give an absolute value. The FTIR spectrum of Ile341Aha+AzuLig(1) is perturbed by air bubbles.

VET sample	c_{PDZ3}	relative c_{PDZ3}	relative c_{AzuLig}	$\frac{c_{AzuLig}}{c_{PDZ3}}$
Ile327Aha+AzuLig(1)	9.3	1.02	1.00	0.97
Ile327Aha+AzuLig(2)	9.9	1.09	1.03	0.95
Ala376Aha+AzuLig(1)	9.1	**1**	**1**	**1**
Ala376Aha+AzuLig(2)	10.7	1.17	0.83	0.70
Ile338Aha+AzuLig	16.3	1.79	1.04	0.58
Ile341Aha+AzuLig(1)			1.12	
Ile341Aha+AzuLig(2)	10.7	1.18	0.89	0.75
Gly329Aha+AzuLig	9.8	1.08	0.88	0.82
Gly322Aha+AzuLig	14.4	1.59	0.78	0.50
Lys380Aha+AzuLig	9.0	0.99	0.72	0.73

The shape of the UV-Vis spectra of PDZ3 with AzuLig (**figure A.0.9**) is strongly dominated by the Azu absorption. Therefore, it gives rather a scale for the AzuLig concentration and not for the protein concentration. Due to impurities of the used AzuLig sample, which are suspected to contain shorter N-terminal fragments with Azu, an absolute concentration determination is difficult. As a start the relative concentration of AzuLig (+PDZ3Aha) in the VET samples compared to a free AzuLig sample is identified applying a linear combination. The scaled UV-Vis spectrum of AzuLig plus the scaled UV-Vis spectrum of WT PDZ3 without ligand (again two different measurements tested: WT(1), WT(2)) plus an offset is fitted to the PDZ3-Aha+AzuLig spectra (in the range between 260 and 400 nm). The

determined relative concentrations of AzuLig in the VET samples compared to the pure AzuLig sample are normalized to the relative concentration of AzuLig in the Ala376Aha+AzuLig(1) sample (**table 4.30**). The normalization to Ala376Aha+AzuLig(1) is chosen because this sample gives the highest ratio of AzuLig compared to PDZ3-Aha.

VET Efficiency Models

In an ideal system, which means the same amount of AzuCa/AzAla and Aha is in the sample and ligand and protein are bound in a ratio of 1, a scale for the VET efficiency would be the ratio between the size of the Aha VET signal VET_{Aha} and the heated water background absorption VET_{BG}, ($Eff = \frac{VET_{Aha}}{VET_{BG}}$). Many deviations from this ideal system are complexing the calculation in the case of the PDZ3-Aha+AzuLig measurements: an Aha labeling efficiency of less than 100 %, a ratio between AzuCa and Aha unless 1, and AzuLig fragments in the sample containing AzuCa, which do not bind, but contribute to the VET_{BG} signal. Depending on which is present in excess, AzuCa or Aha, different correction terms need to be included into the formula for the VET efficiency.

In the case of AzuLig being available in excess, a part of the AzuLig, which is not bound to PDZ3, causes water background heating signal VET_{BG} without inducing a VET_{Aha} signal. A scaling on the ratio between the AzuLig concentration (UV-Vis absorption of Azu as a measure (Vis_{Azu})) and the concentration of Aha labeled PDZ3 (size of the FTIR Aha band ($FTIR_{Aha}$) as a measure) can be used to correct for this effect.

$$Eff = \frac{VET_{Aha}}{VET_{BG}} \cdot \frac{Vis_{Azu}}{FTIR_{Aha}} \tag{4.3.1}$$

In the opposite case, when Aha is present in excess the simple formula for the efficiency could in principle work, but it seems to be reasonable to correct for differences in the labeling efficiency of the PDZ3-Aha samples, because the Aha labeling efficiency was found to be in a range of 46 and 88 % only (**chapter 3.1.3.2**). As a corrective scale the ratio between the PDZ3 concentration (determined by the linear combination in the FTIR amid II-III region (c_{PDZ3})) and the size of the Aha FTIR absorption ($FTIR_{Aha}$) is used.

$$Eff = \frac{VET_{Aha}}{VET_{BG}} \cdot \frac{c_{PDZ3}}{FTIR_{Aha}} \tag{4.3.2}$$

To determine whether the Aha-PDZ3 or AzuLig was in excess in the performed VET measurements, advantage is taken of the ligand induced change in Aha's

IR absorption band as discussed in **chapter 4.2.4.1**. The ligand induced change caused by Hepta in excess are compared to the changes in the Aha band in the VET samples induced by AzuLig (**figure 4.3.22**). The ligand induced changes caused by AzuLig seem to be incomplete. Only Ala376Aha+AzuLig(1) shows a shift almost as strong as the shift induced by Hepta. In all three PDZ3+AzuLig samples depicted, PDZ3 seems not to be saturated by AzuLig, even if in the case of Ala376Aha+AzuLig(1) an almost saturation can be assumed. Fortunately, this sample is the sample which is found to have the highest ratio of AzuLig compared to PDZ3 using the UV-Vis and FTIR linear combinations (**table 4.30**). Consequently, AzuLig in all PDZ3+AzuLig ligand samples can be supposed to be in deficit. Therefore, **equation 4.3.2** needs to be applied for the VET efficiency calculation.

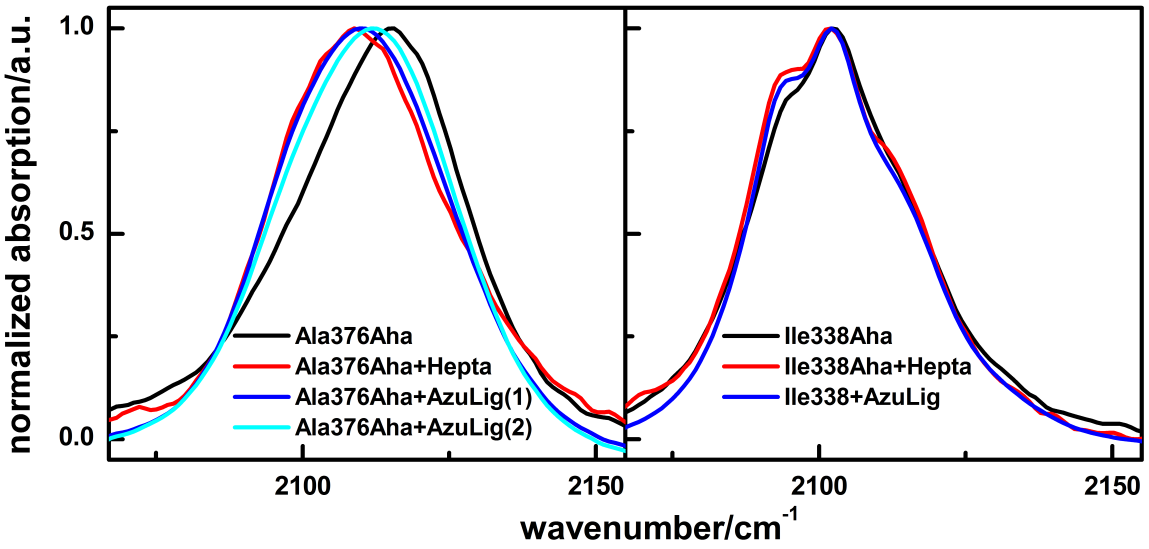

Figure 4.3.22: FTIR spectra of the Aha band of Ala376Aha and Ile338 each without ligand, with Hepta, and with AzuLig. The samples with AzuLig are the samples used in the VET experiments.

Validation of VET Efficiency Analysis

Five distinct VET measurements on Ile327Aha with AzuLig are used to test the reliability of the evolved model. For two of the data sets also the influence of the averaged scan number on the calculated efficiency is investigated to reveal effects of bleaching or precipitating protein and ligand. Different methods for analyzing the size of the Aha FTIR band, the VET Aha signal and the VET background signal are tested for giving the most reliable results.

For the size of the $FTIR_{Aha}$ signal, both the signal height and the area are applied. The height is found to give slightly better results, maybe because of being less affected by the FTIR water background absorption.

As a quantity for the VET_{Aha} signal size at the timepoint with maximum signal size four methods are tested: the amplitude between the maximum and minimum, the absolute area in the range between the maximum and the minimum, the absolute sum of the transients in the signal range, and the integral of the fit of two Gaussians with a biexponential temporal decay. The absolute area without fit gives the most reliable efficiency. For its calculation, the absolute integral in the range between the minimum and maximum of the Aha VET signal at every time point is estimated. These fitting borders are chosen to prevent the inclusion of broken detector pixels into the analysis, mainly in the induced absorption region. This way, an averaging of multiple pixels is possible without being too much affected by disturbing artifacts. The temporal progress of the signal area is fitted with a biexponential function to correct for noise. The absolute area at the biexponential function's maximum is used for the efficiency analysis.

The size of the VET_{BG} signal is analyzed in three ways: the amplitude of the negative signal at late timepoints, the amplitude of the total signal at late timepoints, and the amplitude of a fit of the spectrum (averaged last 5 timepoints) to the average of the late background spectra of all measurements. Despite using the negative amplitude is found to give the best results for this data set, the only slightly inferior calculation via the fit of an average spectrum is used to apply a more robust approach. One reason for its preference is that the zero-crossing of the background signal varies between the measurements.

Table 4.31: Validation of the efficiency analysis with 5 distinct VET experiments on Ile327Aha with AzuLig. For better comparison the calculated VET efficiencies are normalized to its mean (=1). The error is reported as the standard deviation of 6 %.

data	**scans**	$\mathbf{c_{PDZ3}}$**/mM**	$\boldsymbol{FTIR_{Aha}}$**/mOD**	$\boldsymbol{VET_{BG}}$	$\boldsymbol{VET_{Aha}}$	$\boldsymbol{Eff}$**/normalized**
(1)	551	9.3	16.2	0.840	0.145	1.06±0.06
	1825	9.3	16.2	0.734	0.127	1.06±0.06
(2)	573	9.9	21.3	1.055	0.204	0.95±0.06
	805	9.9	21.3	1.028	0.198	0.95±0.06
	1872	9.9	21.3	0.907	0.168	0.91±0.06
(3)	279	10.7	17.7	0.497	0.083	1.07±0.06
(4)	382	10.0	15.0	1.162	0.168	1.03±0.06
(5)	424	10.1	15.8	0.677	0.097	0.97±0.06

Applying the chosen methods to the Ile327Aha VET data set (**table 4.31**), PDZ3 concentrations in a range of 9.3-10.7 mM are obtained (**figure A.0.11**). The ratio between AzuLig and PDZ3 for all Ile327Aha VET measurements is lower than the ratio in the Ala376Aha(1) sample (UV-Vis spectra **figure A.0.12**). Therefore, Aha-PDZ3 can be assumed to be present in excess. The VET efficiencies of all 9 data sets are calculated (**table 4.31**, FTIR Aha band in **figure A.0.10**). Since numbers deriving from fitting are used for the calculation, the estimated efficiencies give only a relative efficiency of the Aha-PDZ3 VET measurements compared to each other. Therefore, the calculated efficiencies are normalized to their mean value. The cal-

culated VET efficiencies differ by a standard deviation of only 6 % and, thus, the efficiency analysis can be supposed to be highly reliable. However, some additional aspects needs to be considered when investigating other PDZ3-Aha mutants: *e.g.* the change in binding constant and the spectral shape of the Aha band.

VET Efficiencies of Different PDZ3-Aha Mutants

In a rough approximation a change in the bandwidth of the Aha FTIR band causes an alteration of a similar factor in the amplitude of the Aha VET signal. However, the area of the Aha VET signal remains mainly unconcerned by a change in the bandwidth of the IR band. This approximation holds for the range of found bandwidths for the Aha's IR asymmetric stretching vibrations. If a constant extinction coefficient is assumed for Aha's IR absorption, the amplitude of the FTIR signal will decrease with increasing bandwidth. Depending on which scales are used for the size of the $FTIR_{Aha}$ band and the Aha VET signal (VET_{Aha}) a correction for this impact is required. The amplitude is found to give the best results for $FTIR_{Aha}$, but in the case of the VET_{Aha} signal the absolute integral between the minimum and maximum amplitude, which is a scale of the area, performs best. Therefore, a correction for the bandwidth needs to be implemented into the calculation of the VET efficiency (**equation 4.3.4**). The FWHM is used as a scale. Even if its determination is bothered by the multiple band shape of Aha's IR band in some mutants, it gives a simple and coarse estimation.

For a second order kinetic reaction ($PDZ3 + AzuLig \rightarrow PDZ3AzuLig$) the concentration of the PDZ3AzuLig complex ($c_{PDZ3AzuLig}$) is given by:

$$c_{PDZ3AzuLig} = \frac{c_{AzuLig} + c_{PDZ3} + \frac{1}{k_a}}{2} \pm \sqrt{\frac{(c_{AzuLig} + c_{PDZ3} + \frac{1}{k_a})^2}{4} - c_{AzuLig} \cdot c_{PDZ3}} \tag{4.3.3}$$

The ratio of bound AzuLig ($\%Lig_{bound} = \frac{c_{PDZ3AzuLig}}{c_{AzuLig}} \cdot 100$) depends on the association constant k_a and consequently differs between the PDZ3-Aha mutants. Assuming a 1:1 ratio between protein and ligand concentration for the Ala376Aha+AzuLig(1) sample as a first approximation, the amount of bound ligand ($\%Lig_{bound}$) is found to be larger than 90 % for all mutants except Gly329Aha, which exhibits a significantly lower association constant (**table 4.32**). For the Ala376Aha+AzuLig(1) sample this means, that 93.7 % of Ala376Aha is bound to AzuLig, which might roughly estimate the FTIR spectrum of the Aha band. A correction factor for $\%Lig_{bound}$ is also incorporated into the extended equation for the VET efficiency (**equation 4.3.4**).

Table 4.32: Calculated normalized VET efficiencies (Eff) and applied parameters for the PDZ3-Aha mutants. The protein concentrations of the PDZ3-Aha VET samples are determined by a linear combination in the amid II-III region of the IR spectrum. The relative concentration of AzuLig derived from a linear combination of the UV-Vis absorption. It is normalized to the AzuLig concentration of the Ala376Aha+AzuLig(1) measurement. A relative ratio between AzuLig and protein concentration is calculated and the resulting amount of bound ligand ($\%Lig_{bound}$). The relative ratio was set to 1 for the Ala376Aha+AzuLig(1) sample based on the shift of Aha's FTIR band. $FTIR_{Aha}$ gives the size of the Aha IR band with its FWHM. VET_{Aha} is the area of the Aha VET signal. VET_{BG} is a scale for the size of the water background absorption in the VET measurements. (Total values for the Ile327Aha+AzuLig samples are differing from the values in **table 4.31** because the water background of all PDZ3 measurements was averaged. As relative values are considered, the relative efficiencies are not concerned.) The VET efficiencies are normalized to the efficiency of Gly329Aha+AzuLig.

VET sample	$\mathbf{c}_{PDZ3}$	$\frac{c_{AzuLig}}{c_{PDZ3}}$	$\boldsymbol{FTIR_{Aha}}$**/mOD**	$\boldsymbol{VET_{BG}}$	$\boldsymbol{VET_{Aha}}$	$\%\boldsymbol{Lig_{bound}}$	**FWHM/cm**$^{-1}$	$\boldsymbol{Eff}$**/normalized**
Gly329Aha+AzuLig	9.8	0.82	18	1.89	0.224	78.8	32.8	**1.00**
Ile327Aha+AzuLig(1)	9.3	0.97	16.2	1.05	0.127	91.8	29.6	**0.84**
Ile327Aha+AzuLig(2)	9.9	0.95	21.2	1.27	0.168	92.9	30.1	**0.74**
Ile338Aha+AzuLig	16.3	0.58	41.3	1.05	0.076	99.7	31.4	**0.33**
Ile341Aha+AzuLig(2)	10.7	0.75	16.5	1.08	0.050	99.5	31.0	**0.35**
Ala376Aha+AzuLig(1)	9.1	**1**	15.6	1.02	0.042	93.7	35.4	**0.34**
Gly322Aha+AzuLig	14.4	0.50	29	0.65	0.024	99.8	37.3	**0.25**

$$Eff = \frac{VET_{Aha}}{VET_{BG}} \cdot \frac{c_{PDZ3}}{FTIR_{Aha}} \cdot \frac{FWHM}{\%Lig_{bound}} \tag{4.3.4}$$

The relative VET efficiencies between the PDZ3-Aha mutants are calculated and normalized to the mutant with the highest VET efficiency (Gly329Aha) for better comparison (**table 4.32**). The two Ile327Aha+AzuLig measurements with high scan numbers are also listed in the table to depict the error range. As the assumed ratio of 1:1 for $\frac{c_{AzuLig}}{c_{PDZ3}}$ for Ala376Aha+AzuLig(1) was a coarse approximation, the ratio is set to 1.1:1 and 0.9:1 and VET efficiencies are calculated. However, it becomes apparent that VET efficiencies only differed by 1 % at a maximum when changing the ligand to protein ratio by this magnitude and the rough approximation of a ratio of 1:1 seems to be sufficient.

The background signal artifacts, which are placed partially below the VET_{Aha} signal in the TRIR spectrum, have a signal amplitude between 3.5 and 5.6 μOD. Consequently, the estimated VET efficiencies are expected to be overestimated because of including this background signal in parts. Spectra with very small VET_{Aha} signals are much more perturbed by these background signals than spectra with large VET signals. The same is true for the calculated efficiencies. The efficiencies of the samples with a very small VET signal (Ile341Aha+AzuLig(2), Ala376Aha+AzuLig(1), and Gly322Aha+AzuLig) are, thus, expected to be significantly smaller than estimated and the VET efficiency of Ile338Aha is supposed to be larger than the ones of those three mutants because of the much larger Aha VET signal in Ile338Aha+AzuLig.

Table 4.33: Distances between heater and sensor in the different PDZ3Aha mutants, maximum peak time of the VET signal, and VET efficiency.

VET sample	Σbonds	direct distance/Å	maximum/ps	Eff/norm.
Gly329Aha+AzuLig	(20)	(7)	4.1	1.00
Ile327Aha+AzuLig(1)	16	9.9	5.3	0.84
Ile327Aha+AzuLig(2)	16	9.9	5.6	0.74
Ile338Aha+AzuLig	21	14.6	7.8	0.33
Ile341Aha+AzuLig(2)	25	16.5	9.7	0.35
Ala376Aha+AzuLig(1)	26	13.4	?	0.34
Gly322Aha+AzuLig	24	19.2	?	0.25

The VET efficiency decreases with increasing distance between heater and sensor and also with increasing time, which the vibrational energy needs to reach the sensor. Comparing the direct distances, VET from the ligand into the βB-sheet seems to be a bit more efficient than into the αB-helix, but for the distance along bonds it seems to be similar. However, measurements with larger VET signals compared to the artifact background signals are needed to study VET efficiencies in samples with larger distances between AzuCa and Aha with a higher precision.

The evolved method gives a surprisingly good estimation of the VET efficiency despite the difficulties of concentration determination for PDZ3 and AzuLig and AzuLig's impurities. In combination with further improved data quality and a broader set of mutants it will enable studying the efficiency of VET along different pathways in PDZ3.

Concluding it should be remarked, that the size of the VET_{Aha} signal at maximum signal size depends on the time constant of VET to Aha, but also on the time constant of continuing energy transport giving the decay of the VET signal. If, for example, many pathways with different velocities contribute to the signal equally, the VET_{Aha} signal will get broader in time and, therefore, its amplitude decreases. Additional computational simulations reflecting the measured data are needed to further shed light on mechanisms and directionality of VET in PDZ3.

4.3.5 VET in PDZ3-AzAla

Tobias Baumann, Matthias Hauf, and Fabian Schildhauer from the group of Nediljko Budisa, Institut für Chemie, Technische Universität Berlin, Germany, incorporated AzAla into PDZ3 via amber stop codon suppression. Two mutation sites for the AzAla were chosen. In the Phe325AzAla mutant AzAla is placed in the βB-sheet in the ligand binding pocket. The naturally occurring Phe325 residue forms a backbone hydrogen bond to the V_0 residue of the ligand [210]. The second mutation site (Phe340AzAla) is placed in the adjacent βC-sheet. The side chain is located at the protein surface and is solvent exposed. The Aha sensor was placed into the ligand at a fixed position (YKQTAhaV, called AhaLig), which is natively not involved in binding interactions (structure in **figure 3.1.1**). Vice versa VET is observed now, from PDZ3 to a ligand altering the position of the heater AzAla instead of the sensor location.

4.3.5.1 ITC PDZ3-AzAla with Hepta & AhaLig

In order to determine the binding ability of the PDZ3-AzAla mutants to the native PDZ3 ligand Hepta compared to WT PDZ3 and also investigate the binding affinity of AhaLig, ITC was measured (**figure 4.3.23**). The depicted WT2+Hepta data set is the same as shown in **figure 4.2.3**. It was added for better comparison. The binding affinities of Phe325AzAla and Phe340AzAla to Hepta are only a bit lower than for WT PDZ3 (**table 4.34**). As expected, the effect of the mutation at the 325 position (in the binding pocket) is a bit larger than the effect at the 340 position (not in the binding pocket and solvent exposed). AzuLig binds to WT PDZ3 with a circa two times higher binding affinity compared to Hepta. This might be caused by the missing acetylation of the N-terminus [214]. Binding affinities of the PDZ3-AzAla mutants to AhaLig are again a bit lower than the one of the WT. However,

sufficient ligand binding of AhaLig to PDZ3-AzAla for the VET experiments can be assumed.

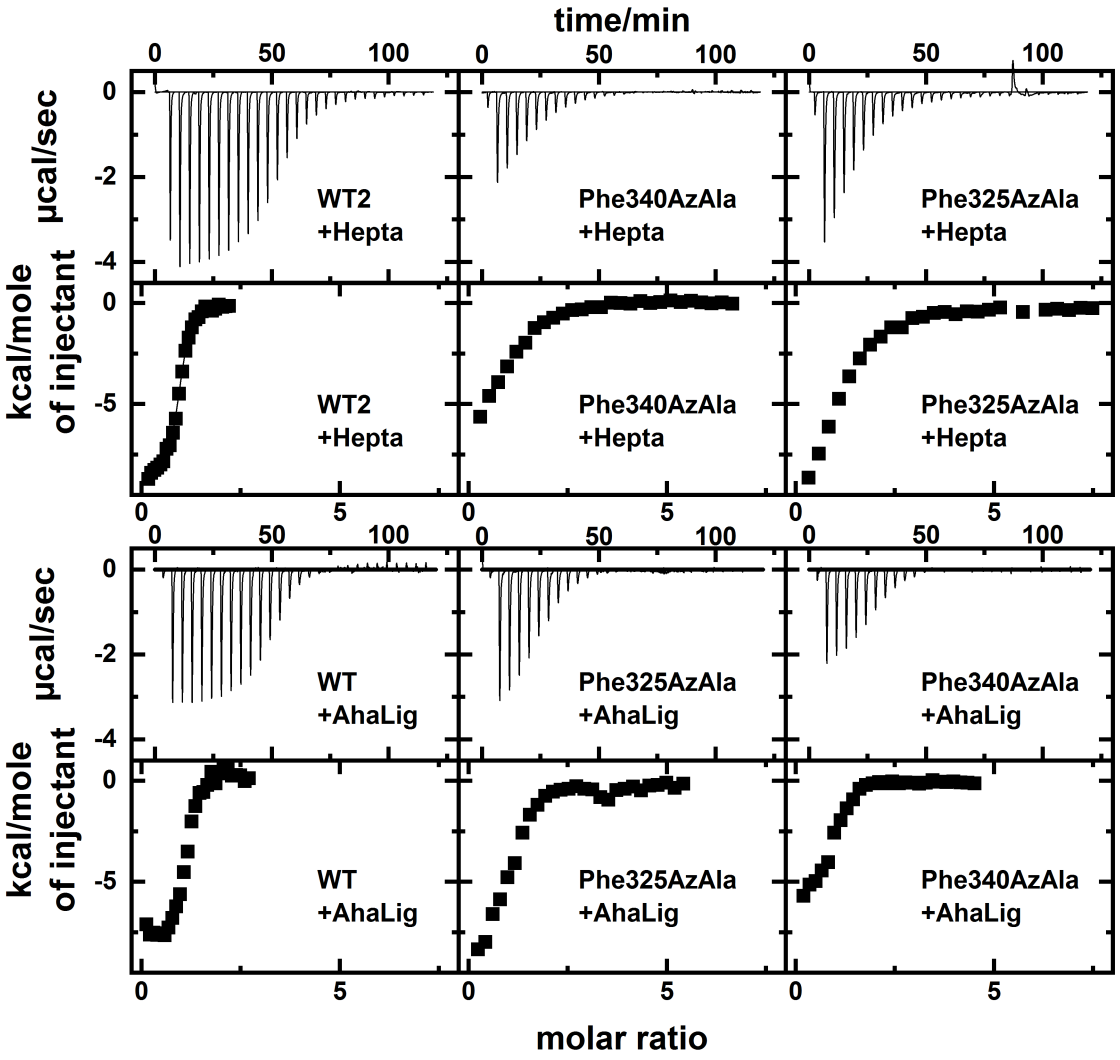

Figure 4.3.23: ITC data of the binding of the WT PDZ3 and the PDZ3-AzAla mutants to the native ligand Hepta and to the Aha containing AhaLig.

Table 4.34: Binding parameters of WT PDZ3 and the PDZ3-AzAla mutants to Hepta and to AhaLig determined by ITC.

	k_a /µM^{-1}	k_d /µM	N	ΔH/cal/mol	ΔS/cal/mol
WT+Hepta	0.35±0.02	2.9±0.2	1.00±0.002	-8550±30	-3.33
Phe325AzAla+Hepta	0.063±0.007	16±2	0.99±0.04	-13500±700	-23.3
Phe340AzAla+Hepta	0.11±0.02	9±2	0.99±0.04	-7000±400	-0.549
WT+AhaLig	0.8±0.2	1.3±0.4	1.09±0.02	-7600±200	1.42
Phe325AzAla+AhaLig	0.14±0.03	7±2	1.01±0.04	-9900±600	-9.56
Phe340AzAla+AhaLig	0.31±0.05	3.2±0.6	0.93±0.02	-5900±200	5.39

4.3.5.2 FTIR AhaLig with PDZ3-AzAla

The FTIR spectrum of free AhaLig and in combination with PDZ3-AzAla reveals a significant shift of the azido's asymmetric stretching vibration upon AhaLig binding to PDZ3 (**figure 4.3.24**). Deviations in the flanks of the band of the bound AhaLig are caused by background correction issues.

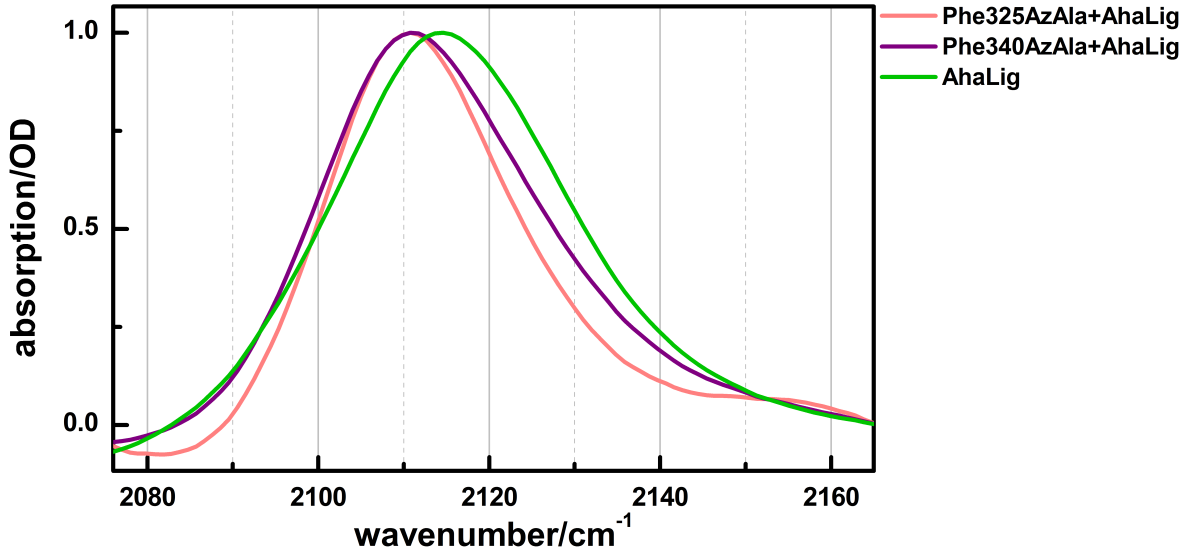

Figure 4.3.24: Normalized and background corrected FTIR spectra of the Aha's asymmetric stretching band of the different PDZ3-AzAla samples with AhaLig used for the VET experiments and of unbound AhaLig.

4.3.5.3 VET Measurements PDZ3-AzAla with AhaLig

VET Without Sensor

At first, again a VET control measurement without sensor was performed to determine the background noise/artifact level for this type of measurement. In this case it is a measurement of PDZ3-AzAla without AzuLig. The AzAla in the Phe325AzAla PDZ3 mutant was excited by the 613 nm pump pulse and the spectrum was probed in the Aha range. Since no Aha is in the sample, the water heat background corrected spectrum is expected to be clear of any signal (**figure 4.3.25**). Again, remaining background structures are observed. However, these perturbing signals are much smaller than in the case of the measurements with AzuLig and the background corrected spectrum is much smoother. A reason for this might be, that the water heating signal in the PDZ3-AzAla VET measurements is much smaller than in the experiments with AzuLig. Also the ratio between the Aha VET signal and the VET background signal is much better for the PDZ3-AzAla+AhaLig measurements. One reason for this might be the additional N-terminal fragments containing an Azu moiety in the impure AzuLig sample. These fragments are heating the

samples without contributing to the Aha VET signal and are, therefore, lowering the ratio of Aha VET signal to water background. The background artifacts remaining after the water heating background correction seem to scale with the size of the background signal in a rough approximation.

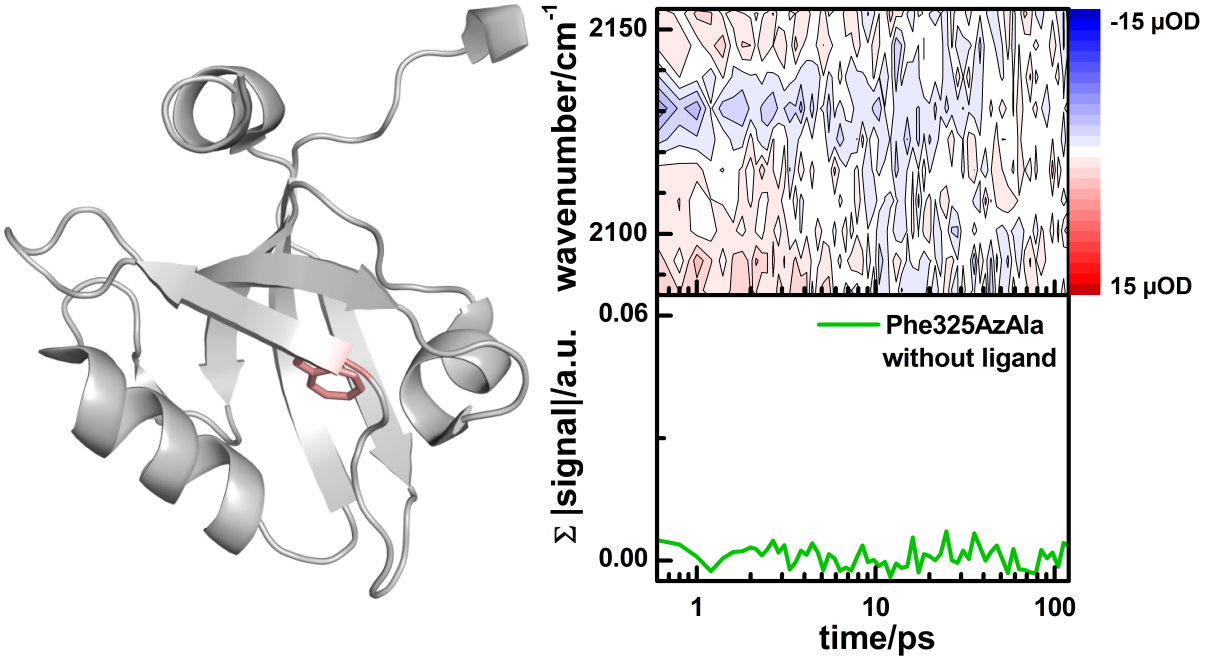

Figure 4.3.25: Left: Structure sketch of PDZ3 Phe325AzAla (grey) without ligand. The native side chains of the PDB structure 5HEB are replaced by those of the ncAAs retaining the backbone orientation. The AzAla is marked salmon. **Right:** VET measurements. **Top:** Background corrected TRIR spectrum of Phe325AzAla. **Bottom:** Transient of Phe325AzAla (green) using the same summed probe pixels as for the Phe325AzAla+AhaLig transient.

VET in Phe325AzAla

In the Phe325AzAla mutant the AzAla is located in the protein interior in the binding pocket. The AzAla side chain is expected to be oriented away from the ligand, like the naturally occurring Phe325 side chain. A large Aha VET signal of bound AhaLig was detected (**figure 4.3.26**) with a peak time of 4.4 ps. The shortest along bond distance includes 10 covalent and 1 H-bond and a direct distance of 8.4 Å (**table 4.35**).

Table 4.35: Distance between the heater and the sensor and the peak time of the VET signal for Phe325AzAla+AhaLig.

sample	**bonds Σ**	covalent bonds	H-bonds	**direct distance /Å**	**peak time /ps**
Phe325AzAla+AhaLig	11	10	1	8.4	4.4

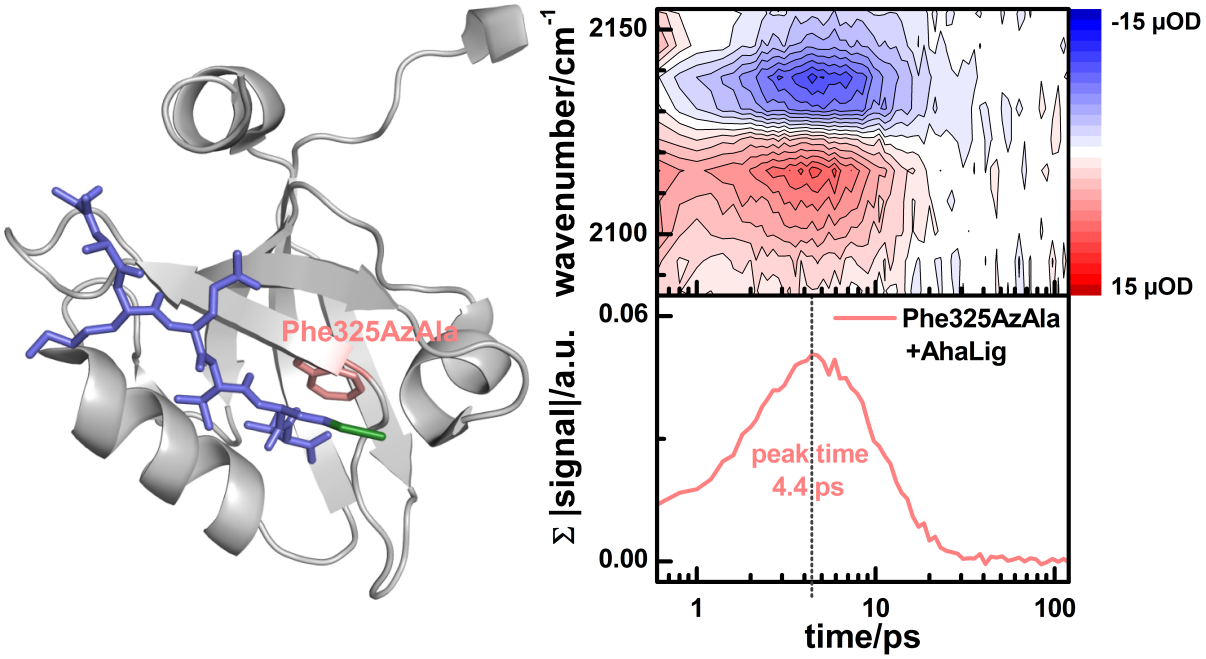

Figure 4.3.26: Left: Structure sketch of PDZ3 Phe325AzAla (grey) with AhaLig (light blue). The native side chains of the PDB structure 5HEB are replaced by those of the ncAAs retaining the backbone orientation. The AzAla is marked salmon and the Aha in AhaLig is colored green. **Right:** VET measurements. **Top:** Background corrected TRIR spectrum of Phe325AzAla+AhaLig. **Bottom:** Azide transient of Phe325AzAla+AhaLig (salmon).

VET in Phe340AzAla

An Aha VET signal with a peak time of 3.8 ps was observed for Phe340AzAla+AhaLig (**figure 4.3.27**), in which AzAla and Aha are separated by a through bond distance of 13 covalent and 2 H-bonds and a through space distance of 7.7 Å (**table 4.36**). In this mutant the AzAla side chain is expected to be solvent exposed at the protein surface.

Table 4.36: Distance between the heater and the sensor and the peak time of the VET signal for Phe340AzAla+AhaLig.

sample	**bonds Σ**	covalent bonds	H-bonds	**direct distance /Å**	**peak time /ps**
Phe340AzAla+AhaLig	15	13	2	7.7	3.8

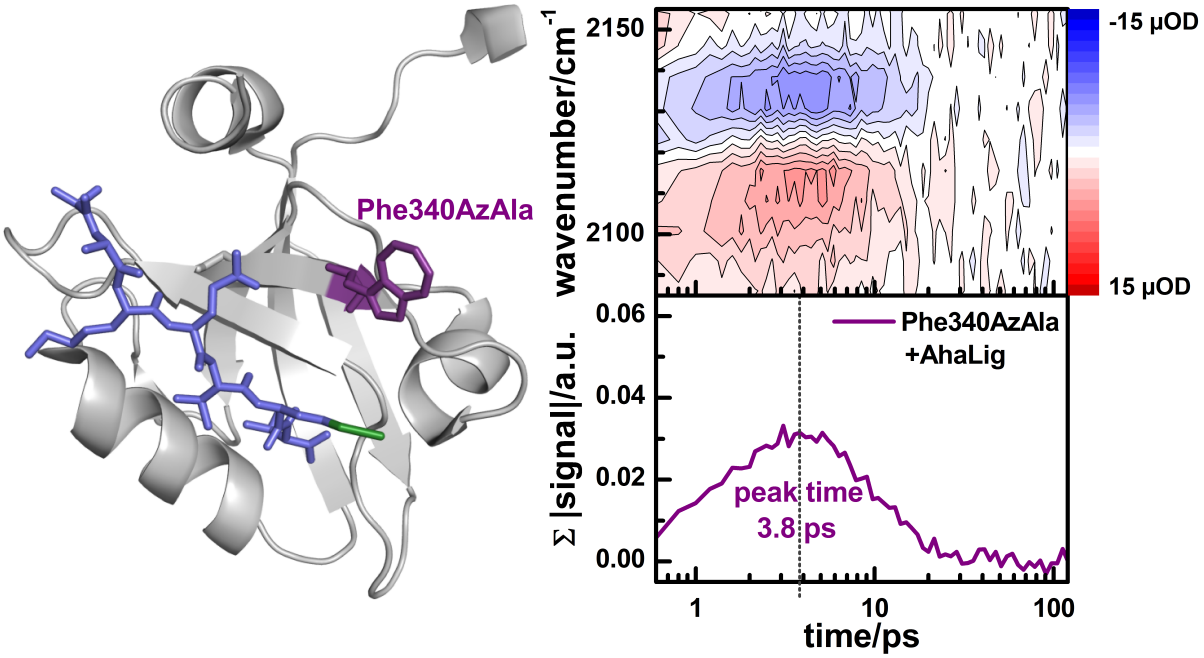

Figure 4.3.27: Left: Structure sketch of PDZ3 Phe340AzAla (grey) with AhaLig (light blue). The native side chains of the PDB structure 5HEB are replaced by those of the ncAAs retaining the backbone orientation. The AzAla is marked violetpurple and the Aha in AhaLig is colored green. **Right:** VET measurements. **Top:** Background corrected TRIR spectrum of Phe340AzAla+AhaLig. **Bottom:** Azide transient of Phe340AzAla+AhaLig (violetpurple).

4.3.5.4 VET Signal Evolution PDZ3-AzAla

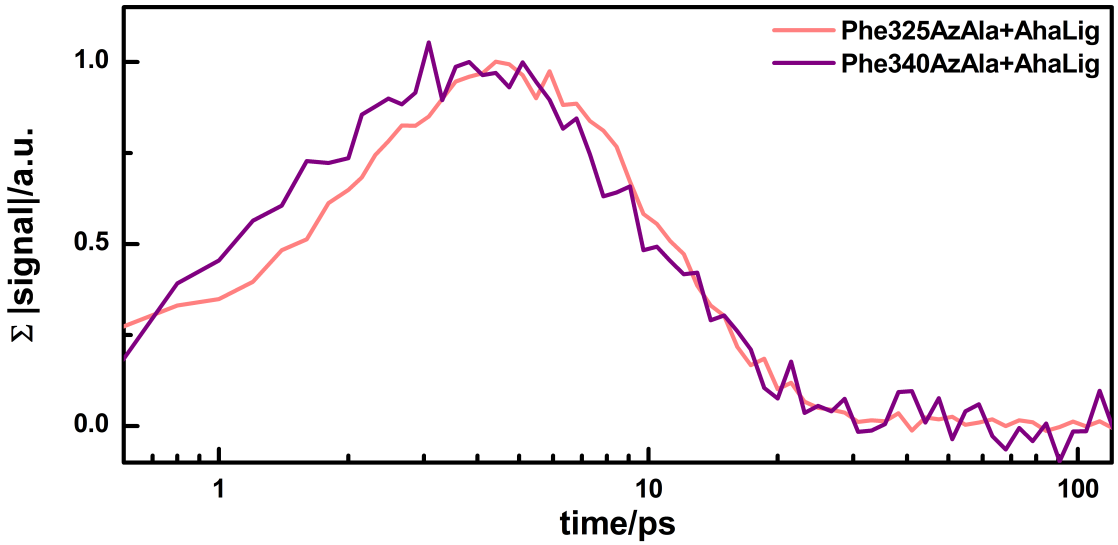

Figure 4.3.28: Normalized Aha transients of the PDZ3-AzAla mutants with AhaLig in comparison.

VET in Phe340AzAla+AhaLig is only slightly faster compared to VET in Phe325-AzAla+AhaLig (**figure 4.3.28** and **table 4.37**). This observation matches the similar through space direct distances but is contrary to the much longer through bond distance in Phe340AzAla+AhaLig. The observed VET velocities for the through space distance and also the through bond VET velocity of the Phe325AzAla+AhaLig totally fit the values observed for the PDZ3-Aha+AzuLig measurements. Only the through bond VET velocity of the Phe340AzAla+AhaLig is an outlier. Since neither the exact orientation of the AzAla side chain nor the orientation of the Aha side chain are known, the existence of a shorter through bond pathway along a non-covalent contact, which is not formed in the WT PDZ3 with native ligand, cannot be excluded. A knowledge of the exact molecular structure of Phe340AzAla+AhaLig would be necessary to shed light on this finding.

Table 4.37: Distance between the heater and the sensor and peak times of the Aha VET signals for the PDZ3-AzAla mutants with AhaLig in comparison.

sample	**bonds Σ**	covalent bonds	H-bonds	**direct distance /Å**	**peak time /ps**
Phe325AzAla+AhaLig	11	10	1	8.4	4.4
Phe340AzAla+AhaLig	15	13	2	7.7	3.8

4.3.5.5 VET Efficiency in PDZ3-AzAla with AhaLig

The PDZ3-AzAla VET samples were concentrated to about 10 mM according to the results of Lowry assays. The concentration of AhaLig is estimated using the size of the Aha IR absorption band in the FTIR spectrum (**figure A.0.13**), which was measured of the VET samples directly before the VET measurement, and an Aha extinction coefficient of 375 $cm^{-1}M^{-1}$ [235]. Concentrations of 3.5 and 5.5 mM are found, revealing that the AzAla containing protein was in excess (**table 4.38**). Therefore, **equation 4.3.1** is applied for calculating the relative VET efficiencies ($Eff = \frac{VET_{Aha}}{VET_{BG}} \cdot \frac{Vis_{Azu}}{FTIR_{Aha}}$). At these PDZ3 and AhaLig concentrations the ligand can be assumed to be completely bound. For the UV-Vis absorption of AzAla the band at 343 nm giving the S_2 electronic transition is chosen as a scale for the AzAla concentration (**figure A.0.14**). In this spectral region PDZ3 does not show any absorption.

Despite similar peak times and distances between AzAla and Aha, the VET efficiency is about a factor of 2.6 larger for the Phe325AzAla mutant compared to the Phe340AzAla mutant (**table 4.38**). This astonishing large difference in the relative VET efficiency is most likely caused by the increased dissipation of vibrational energy into the solvent in the more solvent exposed Phe340AzAla mutant. The calculated VET efficiencies of the PDZ3-AzAla and the PDZ3-Aha mutants cannot be compared because the assumptions needed for the calculation leaded to relative efficiencies and not absolute ones.

Table 4.38: Calculated normalized VET efficiency (Eff) and applied parameters for the PDZ3-AzAla+AhaLig VET measurements.

sample	$A_{343\,nm}$ /OD	$FTIR_{Aha}$ /mOD	c_{AhaLig} /mM	VET_{BG} /µOD	VET_{Aha} /µOD	Eff /normalized
Phe325AzAla +AhaLig	0.132	13.2	3.5	-139	21	1
Phe340AzAla +AhaLig	0.149	20.5	5.5	-127	12.8	0.38

4.3.6 VET to Solvent Dynamic

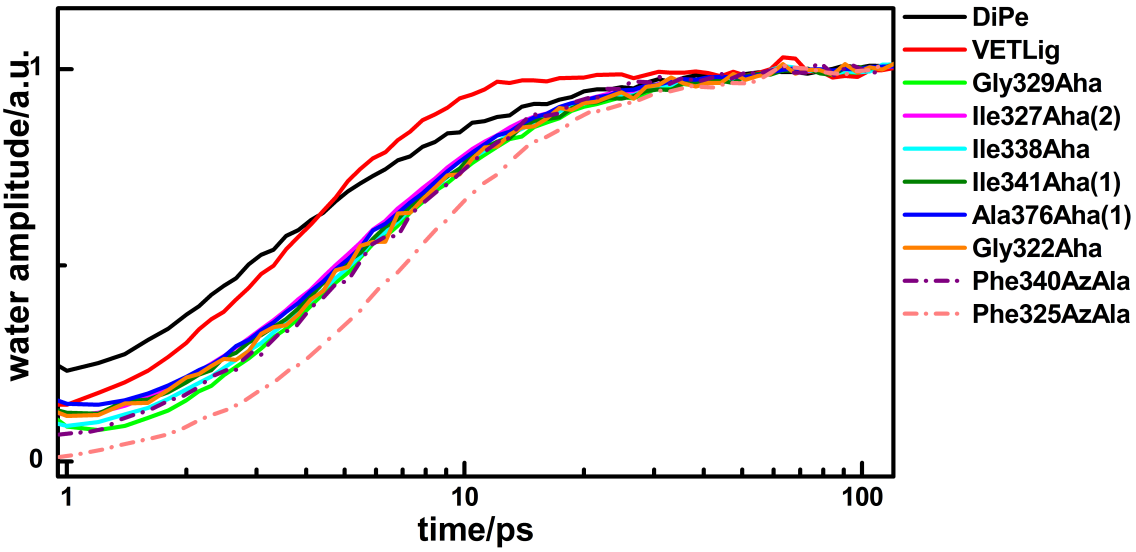

Figure 4.3.29: Evolution of the water heating signal amplitude with time for the different VET samples.

In order to investigate the dynamic of VET to the solvent in dependency on the AzuCa/AzAla position, the evolution of the water heating background signal is compared using the amplitude value of the background fit (**figure 4.3.29**). The shape of the water amplitude curve is very similar for all PDZ3-Aha+AzuLig samples and also for Phe340AzAla. In both, the Azu moiety is placed at the protein's surface. For a better comparison of the temporal evolution, the curves are fitted by a monoexponential function. The estimated VET to solvent transfer times are in a range of 3.8 and 8.5 ps and are strongly correlating with the solvent exposure of the AzuCa/AzAla (**table 4.39**). The solvent transfer time is very fast for strongly solvent exposed Azu moieties as it is the case for the peptides (3.8-4.8 ps) and very slow in the case of Phe325AzAla (8.5 ps) with the AzAla buried in the protein interior. A medium transfer rate is found for AzuCa/AzAla at the protein surface being partially solvent exposed (6.2-6.9 ps).

Table 4.39: Monoexponential fit of the amplitude of the water heating signal for the different VET samples in comparison.

Monoexp. Decay	τ[ps]
DiPe	4.8
VETLig	3.8
Gly329Aha+AzuLig	6.7
Ile327Aha+AzuLig(2)	6.2
Ile338Aha+AzuLig	6.6
Ile341Aha+AzuLig(1)	6.7
Ile341Aha+AzuLig(2)	6.5
Ala376Aha+AzuLig	6.6
Gly322Aha+AzuLig	6.8
Phe340Azu+AhaLig	6.9
Phe325Azu+AhaLig	8.5

4.3.7 VET in D_2O

The influence of solvent isotope labeling of H_2O to D_2O on the peak time and the VET to solvent transfer times is examined on the basis of VET measurements of VETLig (**figure 4.3.30**). With a peak time of 4.7 instead of 3.6 ps, the VET from AzAla to Aha is slowed down in D_2O compared to H_2O. The VET to solvent transfer times, however, are similar with 3.8 ps to H_2O and 4.0 ps to D_2O.

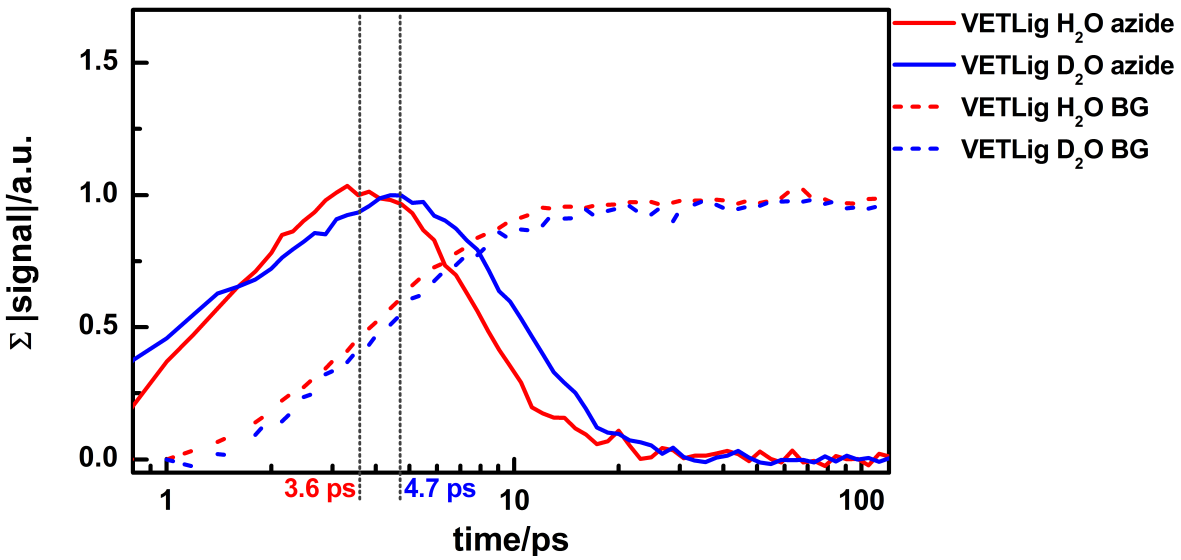

Figure 4.3.30: Normalized Aha transients of VETLig in H_2O and D_2O and the corresponding solvent background heating amplitudes in comparison.

4.3.8 VET Discussion

VET between the label pair AzuCa/AzAla-Aha was detected successfully in small peptides and between an allosteric protein and its ligand. The label pair combined with transient IR measurements is found to be an excellent tool to investigate VET in proteins. VET up to a distance of 19.2 Å in native environment was observed.

The vibrational energy can be assumed to be mainly transferred along the ligand/protein instead of across the solvent on the pathway from AzuCa/AzAla to Aha because the latter was figured out to be only low efficient in a previous study on VET in bridged azulene-anthrazen compounds [54] and was also found to negligibly contribute to the Aha signal in PDZ3-Aha+AzuLig in computational simulations by our collaboration partners in the group of Gerhard Stock, Physikalisches Institut, Albert-Ludwigs-Universität Freiburg, Germany (results not published yet).

The position of AzuCa/AzAla is found to have a major influence on the signal size of the Aha VET signal and on the velocity of VET to the solvent. AzAla incorporated into the protein interior is revealed to be the best position, because the vibrational energy is spread to the solvent slower and more vibrational energy is transferred into the protein. Therefore, resulting VET Aha signals are much larger and, accordingly, VET could be observed over larger distances. Fixing the AzAla position and changing the position of Aha is the preferable strategy for mapping VET through a protein in order to prevent troubles in comparing VET signal sizes caused by varying VET to the solvent.

In the VET simulations on PDZ3 of our collaboration partners in the Gerhard Stock group [46, 130] two possible orientations of the AzuCa residue were found, either turned to the βB-sheet or the αB-helix. The results of the experimental VET measurements showed much larger Aha VET signals in the βB-sheet and, thus, promote the orientation of AzuCa to the βB-sheet, just as the NMR results of our collaboration partners in the Harald Schwalbe group [104].

To be able to further analyze the experimental VET results and find pathways of efficient VET, knowledge of the exact molecular structure and orientation of the ncAA side chains is beneficial. Non-covalent contacts of the AzAla and the Aha side chain might form unexpected shortcuts for the pathway between them in some mutants. The observed electrostatic interactions of the azide moiety to carbonyl O-atoms of its own backbone or opposing backbone residues might also lead to unexpected changes in the VET efficiency or velocity. Therefore, associated computational studies would be required to reveal pathways of efficient VET. Furthermore, the determination of pathways of efficient VET would require characterization of the VET kinetics for all sites, which is too much effort with complex spectroscopic experiments [4]. Hence, combining spectroscopic measurements with computational approaches is very beneficial in order to reveal pathways of efficient VET

and connect them to allosteric pathways. In order to adopt the experimental VET results to reveal allosteric pathways it has to be considered, that the low-frequency modes used for transferring the vibrational energy depend on the heater applied for injecting the vibrational energy and the VET transport speed again depends on these transporting modes [55–57]. However, here too, computational simulations can help to connect experimental VET pathways to allosteric pathways.

Chapter 5

Summary & Outlook

The goal of this dissertation was the development, characterization, and first application of new tools and methods for the experimental investigation of allostery without big conformational changes in proteins using IR spectroscopy.

The azide containing ncAA Aha was chosen to serve as a highly sensitive and site-specific IR reporter in a protein being able to detect even subtle conformational changes upon ligand binding. In order to exploit the full potential of Aha as a site-specific FTIR and 2D-IR label, it is essential to understand the influence of electrostatics and hydrogen bonding on Aha's vibrational frequency, band shape, and vibrational dynamics (solvatochromism). The first part of the dissertation addresses the systematic investigation of the impact of these environmental properties on Aha's IR absorption features using a broad set of 16 solvents with distinct solvent characteristics and three different Aha derivatives: unprotected Aha (upAha), bocAha, and fmocAha with FTIR and 2D-IR spectroscopy. The position of the azide's asymmetric stretching vibration is found to shift in a range of 33 cm^{-1} (upAha), 24 cm^{-1} (bocAha), or 23 cm^{-1} (fmocAha) in different solvent environments. Applying two theoretical, linear solvation energy relationship models to the measured data, the band position turns out to be hardly sensitive to the dipolarity/polarizability of the solvent and the solvent field. Changes in the solvent field only causes a spectral shift of 2 cm^{-1}. The observed large solvatochromic shifts almost exclusively originate from hydrogen bonding to solvent molecules. Hydrogen bonding leads to blue shifting of the band maximum in solution. In proteins, the direction of the shift might vary, as hydrogen bonding geometries could occur in proteins that are not populated in solution. Different aliphatic azido compounds are found to show a variant solvatochromic behavior in protic solvents. Altered orientation, angle, and number of hydrogen bonds to solvent molecules or changes in the solute's intramolecular interactions caused by the different moieties bound to the aliphatic azide might be an explanation. Therefore, special diligence is required for choosing the right model system for an Aha in a protein. BocAha or fmocAha

seems to be the most suitable model system because they exhibit the most similar structure compared to an Aha in a protein and, additionally, both show very similar solvatochromic shifts. For the different Aha derivatives the solvatochromic shift caused by hydrogen bonding is found to rather scale with the strength of the hydrogen bond than with the density of hydrogen bonds.

In the analysis of the 2D-IR spectra of the different Aha derivatives in varying solvents, a relatively short vibrational lifetime of the azide's asymmetric stretching vibration between 0.7 and 1.1 ps is observed, which is not very sensitive to solvent properties. Due to heating of the solvent molecules around the azide, a hot ground state is formed, which decays with a time constant of 1.8-6.5 ps. The decay of the hot ground state is determined by solvent cooling and, thus, depends largely on the solvent properties and less on the nature of the interaction between the solvent and Aha. Therefore, it is faster in hydrogen bonding solvents and slower in nonpolar solvents. The correlation times of spectral diffusion are in a range of 2 ps, which is longer than Aha's vibrational lifetime. That makes the analysis of spectral diffusion of Aha challenging.

In summary, in the different Ahas a similarly broad range of band positions in various solvents like for other IR labels such as SCN is observed [166]. However, in the case of Aha this shift is almost exclusively caused by hydrogen bonding and not by a combination of competing contributions from hydrogen bonding and solvent field/dipolarity/polarizability as it is the case for the SCN [166] or the CN [183] label. That makes Aha, which is very sensitive to even slight changes in hydrogen bonding networks, a more sensitive hydrogen bond sensor than SCN or CN. Observed shifts in band position might also be easier to understand due to the lack of interference between the shifts caused by changes in hydrogen bonding and shifts caused by field changes. On the other hand this advantage makes Aha unsuitable as a vibrational sensor for the electric field in a protein. Despite its comparatively large extinction coefficient, Aha seems not to be the most suitable label for 2D-IR spectroscopy because of the short vibrational lifetime in solvents and the weak dependency of the lifetime on solvent properties. Since the vibrational lifetime of the CN and the SCN label in solvents is much larger (1-5 ps [86] and 32-158 ps [166]) and strongly sensitive to polarity and hydrogen bonding, they are more powerful 2D-IR labels than Aha.

In the next step, Aha was applied to FTIR and 2D-IR spectroscopy on an allosteric protein domain, the PDZ3 domain of PSD-95, which is a showcase example for allostery without big conformational changes [5, 6]. Aha was incorporated into the PDZ3 domain at 15 different positions (15 mutants) to cover a broad set of environmental conditions for the label. FTIR and 2D-IR spectra of PDZ3-Aha with and without its native ligand, a C-terminal sequence of the CRIPT peptide, were measured. Some of the mutation sites are part of theoretically predicted allosteric communication pathways [5, 6]. All mutants are characterized for correct folding by

CD-spectroscopy and their functionality in terms of ligand binding by ITC. Incorporation of Aha into PDZ3 is found to be only minimally invasive for the majority of mutation sites.

The crystal structures of three PDZ3-Aha mutants show multiple possible Aha side chain orientations displaying different conformational states. Similarly, the Aha's asymmetric stretching band in the IR spectrum of some mutants consists of a number of sub bands, which are proposed to originate from the Aha side chain being exposed to different local environments. In a protein, Aha shows a much broader variation of its asymmetric stretching band position as well as its vibrational lifetime and the ratio of the signal size of its hot ground state compared to the ensemble of all tested solvents in this thesis and the literature. This increased sensitivity of the Aha label for small changes of the protein is only found in mutants with a low solvent exposure of the mutation site. Reasons might be altered non-covalent interactions of the Aha in a protein compared to in solvents, like electrostatic interactions with Aha's own backbone carbonyl O-atom or with an opposing backbone carbonyl O-atom of another residue, as observed in the crystal structure, and hydrogen bonds to internal H_2O molecules being forced to non-ideal angles due to the lack of space. MD simulations are needed to further investigate these experimental observations.

A total range of 48.3 cm^{-1} for Aha's band position in proteins has been observed up to now including the data discussed here in combination with literature values [100–103, 106], whereas for the SCN label in proteins only a range of 18 cm^{-1} has been found yet [142, 148–151, 158, 159, 163, 166]. This enormous variation of Aha's band position, again, emphasizes Aha's great potential as an IR label to investigate protein function. Even the observed small variation of Ahas vibrational lifetime in solvents, seems to be overcome when Aha is incorporated into a protein and the vibrational lifetime can provide additional information.

The effect of ligand binding on the band shape and the vibrational lifetime of Aha is investigated. Due to the high reproducibility of the FTIR bands, even tiny changes in the band position and shape upon ligand binding could be detected for several of the Aha mutation sites. In the most cases, changes in the IR band upon ligand binding seem to arise from ligand induced population exchanges between the distinct conformational states. For several Aha bands also a significant change of the Aha's vibrational lifetime upon ligand binding could be observed. Spectral changes upon ligand binding are most often accompanied by changes in the vibrational lifetime. The high sensitivity of the Aha's IR band to subtle ligand induced changes is especially found for mutation sites with low solvent exposure. The mutation sites providing these ligand induced changes in the Aha's IR band might be correlated to signaling pathways and, thus, Aha's application for the investigation of allostery in proteins is highly promising. Due to the higher sensitivity of low solvent exposed Aha, only buried mutation sites can be compared. Effects on solvent exposed Aha

are overwhelmed by solvent effects. Unfortunately, most of the chosen off-pathway mutation sites are solvent exposed. Therefore, a broader set of PDZ3-Aha mutants will be worth to be studied in order to investigate allostery in PDZ3.

Possible new PDZ3-Aha mutants should have a low SASA and be preferably not involved in any of the predicted networks [5, 6, 10, 13–16, 18, 19, 26] in order to provide negative controls. Unfortunately, almost all AAs of PDZ3, which are not solvent exposed were proposed by at least one of these studies to be part of a coupled network (see **table 4.9**). Phe337 and Gly356 are exceptions providing low SASAs and being not involved in any of these networks and are, thus, interesting mutation sites. Ala382 might also be a worthwhile candidate because it is placed in proximity to the binding pocket and is not part of any predicted network. However, it is accompanied by the drawback of a moderate normalized SASA of about 0.18. Other residues exhibiting a low SASA and being in the proximity of the binding pocket are Leu323 and Leu379 and a bit further afar Ile359 and Ile388. All four are part of some of the predicted networks. Other possible mutation sites with a low SASA are Tyr392, Leu314, Ile316, and Asp357.

Since the exact Aha labeling efficiency is not known for the majority of used samples, the revealed ligand induced spectral changes of the normalized IR absorption bands do not include changes in the extinction coefficient. Applying mass spectrometry with ESI, the Aha labeling efficiencies can be determined and changes in Aha's extinction coefficient caused by ligand binding can be included in future analysis. Furthermore, resolving crystal structures of more PDZ3-Aha mutants in combination with additional MD simulations will be beneficial to further understand the influence of non-covalent interactions of the azido moiety with backbone carbonyl O-atoms and internal water molecules on the vibrational band shape and lifetime.

Since allosteric pathways were linked to pathways of efficient anisotropic energy flow by several theoretical studies [4, 6–8, 42], a new approach of measuring vibrational energy transfer (VET) in proteins using a heater-sensor pair consisting of an Azu moiety and an Aha in combination with ultrafast TRIR spectroscopy was applied to small model peptides and PDZ3 to evaluate the potential of this method. At first, the measurement setup was improved in order to be able to detect VET along larger distances compared to the preceding experiments with the heater-sensor pair on small peptides by Henrike M. Müller-Werkmeister [70, 78]. Afterwards, the heater-sensor pair was implemented into small model peptides and intramolecular VET along these peptides was measured. Then intermolecular VET between an Azu containing ligand and an Aha in PDZ3 was mapped for seven different PDZ3-Aha mutants. VET up to a distance of 19.2 Å on a picosecond timescale was detected successfully with PDZ3 being in a native environment. With increasing distance between the Azu heater and the Aha sensor the vibrational energy needs more time to reach the sensor and the Aha VET signal size decreases due

to the loss of vibrational energy to the solvent and to other branching off pathways in the PDZ3/ligand complex. Both the VET velocity along a distinct pathway in PDZ3-Aha and the amount of the vibrational energy reaching the Aha sensor (VET efficiency) give a scale of the vibrational energy throughput along this pathway. VET velocities of 1.7-1.9 Å/ps (through space direct distance) and 3.9-4.5 Å/ps (along bond distance) are found and an approach to calculate the VET efficiencies of the different mutants is developed.

Also the opposite scenario, VET from the Azu containing ncAA AzAla, incorporated into PDZ3 at two distinct sites, to an Aha labeled ligand was measured. The effect of the AzAla position on the observed VET to the Aha and to the solvent is analyzed. The found VET to solvent transfer times as obtained from the rise time of the water signal are in a range of 3.8 to 8.5 ps and are shortened with increasing solvent exposure of the Azu heater. Accordingly, the amount of vibrational energy reaching the Aha sensor is higher, when the Azu is buried in the protein interior and less energy is directly transferred to the solvent instead of to the protein. As a consequence, the best experimental strategy will be to place the Azu in the protein interior at a fixed position and alter the Aha position to get comparable VET results.

The heater-sensor pair combined with ultrafast TRIR spectroscopy is found to be a highly promising tool to investigate VET in proteins. Comparing VET velocities and efficiencies for a larger set of PDZ3 mutants extended over the whole protein will enable to reveal efficient VET pathways and allow to study their role for allostery. At the moment the limiting factors for PDZ3 VET measurements at longer distances are measurement artifacts in the background, which limit the minimum VET Aha signal size, which can be detected. These artifacts seem to scale with the signal size of the heated solvent water. They are assumed to be caused by nonlinearities of the detector and uncertainties deriving from the water solvent background correction. Exchanging the detector might improve the quality of the measured spectra. Furthermore, improving the ratio between the Aha VET signal and the solvent background heating signal would also help to improve the data quality. In the approach with the Azu in the ligand and the Aha in PDZ3, this means, that VET measurements with a pure AzuLig ligand, which is not contaminated by fragments containing Azu, are expected to have a smaller solvent background heating signal and, thus, much smaller artifacts. Also the Aha labeling efficiency of PDZ3 should be improved in order to get a better signal to background ratio. The best VET sample would be a completely labeled PDZ3 double mutant with AzAla and Aha simultaneously incorporated and the AzAla positioned in the protein interior. Since for both ncAAs different contranslational incorporation strategies are used, these approaches can be combined to gain a double mutated protein. For AzAla-Aha double mutants also the VET efficiency estimation would be easier. Moreover, the azido moiety could be isotope labeled in order to red shift its absorption band to a spectral position, at which the H_2O solvent absorption is smaller.

Knowledge of the molecular structure and orientation of the ncAA side chains is desirable, to further comprehend the experimental VET results and find pathways of efficient VET, since non-covalent contacts of the AzAla and the Aha side chain might form unexpected shortcuts between them. Furthermore, associated computational studies are needed to reveal pathways of efficient VET.

All in all, highly promising tools and experimental strategies to investigate allostery without big conformational changes using IR spectroscopy and ncAAs are developed and their potential is evaluated. They will help to shed light on hidden allosteric communication in proteins.

Chapter 6

Deutsche Zusammenfassung

Proteine sind die Maschinen der Zellen. Um die Funktionalität von zahlreichen zellulären Prozessen zu gewährleisten, müssen Kommunikationssignale zwischen verschiedenen Proteinen und innerhalb eines Proteins weitergeleitet werden. Die Weiterleitung einer Störung an einem Ort im Protein zu einer entfernten Stelle, an welcher sie strukturelle und/oder dynamische Änderungen auslöst, wird Allosterie genannt [1–4]. Zunächst wurde Allosterie hauptsächlich mit großräumigen Konformationsänderungen in Verbindung gebracht [1, 2], aber später entwickelte sich ein dynamischerer Blickwinkel auf Allosterie in Abwesenheit dieser großräumigen Konformationsänderungen [1–5]. Die Idee eines allosterischen Pfades bestehend aus konservierten und energetisch gekoppelten Aminosäuren, welche die Signalweiterleitung zwischen entfernten Stellen im Protein vermitteln, entstand [1]. Diese allosterischen Pfade wurden durch zahlreiche theoretische Studien in Zusammenhang mit Pfaden effizienten anisotropen Energieflusses gebracht [4, 6–9]. Der Energiefluss entlang dieser Netzwerke verknüpft allosterische Signalübertragung mit Schwingungsenergietransfer (VET - vibrational energy transfer) [2, 9]. Die Großzahl der Forschungsarbeiten über dynamische Allosterie basiert auf theoretischen Methoden, weil nur wenige geeignete experimentelle Verfahren existieren [5, 6, 8–37]. Um diesen essentiellen biologischen Prozess der Informationsübertragung besser verstehen zu können, ist die Entwicklung neuer und leistungsstarker experimenteller Instrumente und Techniken daher dringend erforderlich. Die vorliegende Dissertation setzt sich dies zum Ziel.

VET in Proteinen ist aufgrund der Proteingeometrie inhärent anisotrop [38–40]. Alle globulären Proteine besitzen Kanäle effizienten Energieflusses, von denen vermutet wird, dass sie wichtig für Proteinfunktionen, wie die schnelle Ableitung von überschüssiger Wärme, Regulation von chemischen Reaktionen, Ligandenbindung und allosterische Signalweiterleitung, sind [9, 38, 39, 41–46]. Der Transfer von Schwingungsenergie wird sowohl von kovalenten als auch von nicht-kovalenten Kontakten vermittelt [8, 9, 39, 46–50]. VET kann mit zeitaufgelöster Infrarot (IR)

Spektroskopie untersucht werden, bei welcher ein Femtosekunden Anregepuls eines Lasers Schwingungsenergie in ein molekulares System an einer bestimmten Stelle injiziert, entweder per direkter IR Anregung oder per UV-Vis Anregung, und ein, nach einem veränderbarem Zeitintervall folgender, IR Abfragepuls die Ausbreitung dieser Schwingungsenergie detektiert [41, 44, 47, 48, 51–70]. Die Weiterleitung der Schwingungsenergie durch das Molekül erfolgt entlang delokalisierter niederfrequenter Moden [38, 39, 71]. Um VET über größere Distanzen in einem Protein messen zu können muss eine große Menge Schwingungsenergie injiziert werden. Deshalb wird ein Chromophor, der die Energie eines sichtbaren Photons in Schwingungsenergie konvertiert, als Heizelement benötigt um langreichweitige VET Pfade in Proteinen kartieren zu können. Da nur wenige Proteine natürlich vorkommende Chromophore besitzen, wird ein künstlicher protein-kompatibler und universell einsetzbarer Chromophor gebraucht. Der Azulen (Azu) Chromophor eignet sich als Heizelement, weil er nach Photoanregung des ersten elektronischen Zustandes durch ultraschnelle interne Konversion fast die gesamte injizierte Energie innerhalb von einer Picosekunde in Schwingungsenergie umwandelt [41, 54, 70, 72–75]. Azu wurde bereits eingesetzt um VET in verbrückten Azu-Anthrazen Komponenten [41, 54, 72] und kleinen Peptiden zu messen [70]. Eingebettet in die nicht-kanonische Aminosäure (ncAA - non-canonical amino acid) β-(1-Azulenyl)-L-Alanine (AzAla), kann der Azu Rest in Proteine eingebaut werden [76, 77]. Die Ankunft der injizierten Schwingungsenergie an einer bestimmten Stelle im Protein kann mithilfe eines IR Sensors detektiert werden. Die Kombination aus Azu als VET Heizelement und Aha als VET Sensor mit transienter IR (TRIR) Spektroskopie wurde schon erfolgreich an kleinen Peptiden in der Dissertation von H. M. Müller-Werkmeister getestet, die der vorliegenden Dissertation in den Laboren der Bredenbeck Gruppe vorausging [70, 78].

Die Schwingungsfrequenz chemischer Bindungen ist strukturspezifisch und hochempfindlich auf selbst kleine Änderungen der Konformation und Dynamik in der unmittelbaren Umgebung [79] und kann mit IR Spektroskopie gemessen werden, z. B. mit Fourier Transform IR (FTIR) Spektroskopie [80, 81]. IR Spektroskopie bietet eine außergewöhnlich gute Zeitauflösung, die es ermöglicht, dynamische Prozesse in Molekülen auf einer Zeitskala von wenigen Picosekunden zu beobachten. Daher ist sie eine ausgezeichnete Methode, um die ultraschnelle Weiterleitung von Schwingungsenergie in molekularen Systemen und Proteinen zu untersuchen. Mit zweidimensionaler (2D)-IR Spektroskopie können die Relaxation von schwingungsangeregten Zuständen und strukturelle Fluktuationen um die schwingende Bindung detektiert werden [81–83]. Allerdings geht die herausragende Zeitauflösung mit verbreiterten Spektren und limitierter spektraler Auflösung einher [84]. In größeren Molekülen mit zahlreichen Bindungen überlagern sich die Schwingungsbanden und die Ortsauflösung geht verloren. In IR Spektren von Proteinen in wässrigen Lösungsmitteln (LM) dominieren die Absorptionen des Protein Rückgrats und des Wassers. Um diese Limitierung zu überwinden, können IR Marker

benutzt werden, chemische Gruppen, die in einer spektral durchsichtigen Region des Protein/Wasser Spektrums (1800 bis 2500 cm^{-1}) absorbieren. Als ncAA können sie kotranslational in Proteine an einer gewünschten Stelle eingebaut werden und so ortsspezifische Informationen aus dem Proteininneren liefern [79, 85–89]. Aufgrund ihrer geringen Größe, eines relativ großen Extinktionskoeffizientens (350-400 $M^{-1}cm^{-1}$) und einer hohen Empfindlichkeit auf Änderungen in der lokalen Umgebung sind organische Azide (N_3) wie zum Beispiel Azidohomoalanine (Aha) besonders geeignete IR Marker [90, 91]. Die asymmetrische Azid Streckschwingung von Aha absorbiert bei ca. 2100 cm^{-1} [70, 91–108]. Außerdem kann Aha als Methionin Analogon ins Protein eingebaut werden [100, 108] und eignet sich daher hervorragend um Allosterie in Proteinen zu untersuchen.

Die verschiedenen entwickelten Methoden zur experimentellen Untersuchung von dynamischer Allosterie in Proteinen basierend auf FTIR, 2D-IR und TRIR von Aha wurden im Zuge dieser Dissertation durch Anwendung an der PDZ3 Domäne des postsynaptischen Proteins PSD-95 validiert. PDZ3 ist eine kleine Protein-Protein-Interaktionsdomäne [109, 110] und ein Vorzeigebeispiel für Allosterie ohne großräumige Konformationsänderungen. Der Großteil der Studien zu Allosterie in PDZ3 basiert auf theoretischen Ansätzen [5, 6, 8–29], die teilweise recht unterschiedliche Netzwerke aus gekoppelten Aminosäuren als allosterische Pfade prognostizieren. Die wenigen vorhandenen experimentellen Arbeiten [5, 11, 22, 29–37] sind nicht in der Lage die verschiedenen theoretisch vorhergesagten Pfade zu bestätigen oder zu widerlegen. Neue Methoden werden deshalb dringend benötigt um allosterische Signalübertragung in PDZ3 zu verstehen.

Obwohl es nötig ist, den Einfluss von Elektrostatik und Wasserstoffbrückenbindungen auf Ahas Schwingungsfrequenz, Bandenform und Schwingungsdynamik zu verstehen (Solvatochromie), um das volle Potential von Aha als ortspezifischer IR Sensor in Proteinen nutzen zu können, wurde dies bis jetzt noch nicht systematisch untersucht. Der erste Teil dieser Dissertation umfasst deshalb die systematische Untersuchung des Einflusses der lokalen Umgebung auf die Schwingungsfrequenz, die Bandenform, die Schwingungslebensdauer und die spektrale Diffusion von drei verschiedenen Aha Derivaten (ungeschütztem Aha (upAha), bocAha und fmocAha) anhand von 16 LM mit verschiedenen Eigenschaften, unter Benutzung von FTIR und 2D-IR Spektroskopie.

Eine Variationsbreite der Azid Bandenposition im Bereich von 33 cm^{-1} (upAha), 24 cm^{-1} (bocAha) oder 23 cm^{-1} (fmocAha) konnte in den verschiedenen LM beobachtet werden. Die Anwendung zweier theoretischer linearer Solvatationsenergie Modelle ergab, dass die Bandenposition kaum von der Dipolarität/Polarisierbarkeit des LM oder von dem durch die LM Umgebung erzeugtem elektrischem Feld beeinflusst wird. Der Großteil der Bandenverschiebung wird durch Wasserstoffbrückenbindungen verursacht, welche die Bandposition blau verschieben. In Proteinen kann die Richtung der Verschiebung anders sein, weil dort die Geometrie der Was-

serstoffbrückenbindungen von der im LM abweichen kann. Die beobachteten Verschiebungen sind für die verschiedenen aliphatischen Azide unterschiedlich. Abweichende Orientierung, Winkel und Anzahl der Wasserstoffbrückenbindungen zu LM Molekülen oder veränderte intramolekulare Wechselwirkungen durch die unterschiedlichen Reste, die an das aliphatische Azid gebunden sind, sind mögliche Erklärungen dafür. Deshalb sollte ein Modell für Aha im Protein sorgfältig ausgewählt werden. BocAha und fmocAha scheinen als Modell am besten geeignet zu sein, weil sie die größten strukturellen Ähnlichkeiten mit Aha in einem Protein aufweisen und zusätzlich sehr ähnliche Bandenpositionsverschiebungen zeigen.

Die verschiedenen Ahas verfügen nur über eine relativ kurze Schwingungslebensdauer zwischen 0,7 und 1,1 ps, welche kaum von den LM Eigenschaften beeinflusst wird. Durch die Erwärmung von LM Molekülen um das Azid wird ein heißer Grundzustand gebildet, der mit einer Zeitkonstante im Bereich von 1,8 bis 6,5 ps wieder zerfällt. Der Zerfall dieses heißen Grundzustandes wird durch das Abkühlen des LM bestimmt. Das Abkühlen ist in wasserstoffverbrückten LM schneller und in nicht polaren langsamer. Die Korrelationszeit der spektralen Diffusion ist länger als die Schwingungslebensdauer und liegt im Bereich von 2 ps. Deshalb ist die Auswertung der spektralen Diffusion von Aha schwierig.

Insgesamt zeigt Aha einen ähnlich breiten Bereich von Bandpositionen in den verschiedenen LM wie andere IR Marker, z. B. SCN [166]. Allerdings ist im Fall von Aha diese Verschiebung fast ausschließlich durch Wasserstoffbrückenbindungen verursacht, und nicht durch eine Überlagerung mit zusätzlichen Beiträgen von Dipolarität/Polarisierbarkeit/Lösungsmittelfeld wie im Fall vom SCN [166] oder CN Marker [183]. Aha ist aufgrund der sehr kurzen Schwingungslebensdauer, die sich nur wenig durch LM Eigenschaften ändert, nur für wenige Anwendungen ein geeigneter 2D-IR Marker.

Anschließend wurde Aha in PDZ3 an 15 verschiedenen Stellen eingebaut (15 Mutanten). Einige der Mutationsstellen befinden sich auf und einige abseits verschiedener theoretisch prognostizierter Pfade allosterischer Kommunikation [5, 6]. Korrekte Faltung und Funktion in Bezug auf Ligandenbindung der Mutanten wurde mit CD Spektroskopie und ITC überprüft. Es konnte gezeigt werden, dass der Einbau von Aha in PDZ3 an den meisten Mutationsstellen nur minimalinvasiv ist.

FTIR und 2D-IR Spektren von den PDZ3-Aha Mutanten mit und ohne Ligand (C-terminale Sequenz des CRIPT Peptids) wurden aufgenommen und Schwingungsfrequenz, Bandenform und Schwingungslebensdauern in Zusammenhang zur LM Exposition von Aha gesetzt. Die Kristallstrukturen von drei PDZ3-Aha Mutanten weisen jeweils mehrere mögliche Aha Seitenkettenorientierungen auf, die verschiedene Konformationszustände darstellen. Die gemessene Aha Bande einiger Mutanten besteht aus mehreren Subbanden, welche vermutlich von verschiedenen lokalen Umgebungen des Azids verursacht werden. Sowohl die IR Bandenposition

als auch die Schwingungslebensdauer und die Signalgröße des heißen Grundzustandes von Aha im Protein sind wesentlich breiter verteilt als in allen getesteten LM. Diese erhöhte Empfindlichkeit des Aha Markers auf kleine Änderungen im Protein tritt nur in Mutanten auf, in denen Aha gegenüber dem LM wenig exponiert ist. Gründe hierfür könnten veränderte nicht-kovalente Wechselwirkungen von Aha im Protein im Vergleich zum LM sein, wie z. B. die in den Kristallstrukturen beobachteten elektrostatischen Wechselwirkungen mit dem eigenem Rückgrat Carbonyl O-Atom oder mit einem gegenüberliegendem Rückgrat Carbonyl O-Atom einer anderen Aminosäure oder Wasserstoffbrücken zu internen H_2O Molekülen, die durch Platzmangel in nicht-optimale Winkel gezwungen werden.

Unter Einbeziehung all dieser Daten und bereits veröffentlichter Daten anderer Forschungsgruppen wurden Aha Bandenpositionen im Protein in einem für einen IR Marker außergewöhnlich großem Bereich von 48,3 cm^{-1} gemessen [100–103, 106]. Für den SCN Marker im Protein hingegen ist der Bereich mit 18 cm^{-1} deutlich kleiner [142, 148–151, 158, 159, 163, 166]. Dies zeigt die herausragende Empfindlichkeit der Aha Bandenpostition auf die lokale Proteinumgebung. Die Schwingungslebensdauer von Aha im Protein variiert deutlich mehr als im LM und kann somit zusätzliche Informationen liefern.

Weil Ligandenbindung allosterische Effekte einleitet, wurde untersucht, in wie weit man mit der Hilfe von Aha winzige ligandeninduzierte strukturelle und dynamische Änderungen messen kann. Selbst geringe ligandeninduzierte Änderungen der Bandenposition und Bandenform konnten in mehreren PDZ3-Aha Mutanten entdeckt werden. In den meisten Fällen scheinen die ligandeninduzierten Veränderungen der Aha Bande von einer Verschiebung der Populationen zwischen den einzelnen Konformationszuständen zu stammen. Mehrere PDZ3-Aha Mutanten zeigten eine signifikante ligandeninduzierte Änderung in der Schwingungslebensdauer. Ligandeninduzierte spektrale Änderungen und Veränderungen der Schwingungslebensdauer traten meist gleichzeitig und insbesondere bei Mutanten mit niedriger LM Exposition von Aha auf. Aha scheint bei niedriger LM Exposition deutlich empfindlicher auf strukturelle und dynamische Änderungen zu reagieren. Deshalb können nur Daten von Mutationsstellen mit niedriger LM Exposition verglichen werden. Der Vergleich von den Positionen, die ligandeninduzierte IR Änderungen zeigen, mit den Positionen auf den prognostizierten allosterischen Pfaden erscheint ein vielversprechender Ansatz zu sein, um mehr Erkenntnisse über Allosterie in Proteinen zu gewinnen. Für eine ausreichende Datenmenge müssten zusätzliche geeignete PDZ3-Aha Mutanten untersucht werden.

Im dritten Teil der Dissertation wird die Anwendung des VET Heizelement-Sensor Paares Azu-Aha mit TRIR Spektroskopie zur Detektion von VET im Protein getestet. Zunächst wurden der Messaufbau und die Messroutine optimiert um VET Signale entlang größerer Distanzen als in den vorhergehenden Experimenten von H. M. Müller-Werkmeister [70, 78] messen zu können. Im Anschluss wurde das

Azu-Aha Paar in kleine Modellpeptide eingebaut und intramolekularer VET entlang dieser Peptide detektiert. Danach wurde intermolekularer VET zwischen einem Azu enthaltendem Liganden und einem Aha in PDZ3 für sieben verschiedene PDZ3-Aha Mutanten gemessen. VET bis zu einer Distanz von 19,2 Å konnte erfolgreich detektiert werden. Mit steigender Distanz zwischen dem Azu Heizelement und dem Aha Sensor braucht die Schwingungsenergie länger, um den Sensor zu erreichen, und das Aha VET Signal wird kleiner aufgrund des Verlustes von Schwingungsenergie ans LM und an abzweigende Pfade im PDZ3/Liganden Komplex. Sowohl die VET Geschwindigkeit entlang eines bestimmten Pfades in PDZ3-Aha als auch die Menge an Schwingungsenergie, die den Aha Sensor erreicht (VET Effizienz), ist ein Maß für den Schwingungsenergiedurchfluss entlang dieses Pfades. VET Geschwindigkeiten von 1,7-1,9 Å/ps (direkte Distanz) bzw. 3,9-4,5 Å/ps (Distanz entlang von Bindungen) wurden gemessen und eine Methode zur Berechnung der VET Effizienz wurde entwickelt.

Zusätzlich wurde das entgegengesetzte Szenario, VET von AzAla, eingebaut an zwei verschiedenen Stellen in PDZ3, zu einem Aha markierten Liganden gemessen und die Auswirkung der Position des AzAla auf den VET zum Aha und ins LM analysiert. Die Transferzeiten vom VET ins LM liegen im Bereich von 3,8 bis 8,5 ps mit schnellerem Transfer für LM exponierte Azus. Dementsprechend ist die Menge an Schwingungsenergie, die den Aha Sensor erreicht, größer, wenn sich das Azu im Proteininneren befindet und mehr Energie ins Protein statt direkt ins LM geleitet wird. Deshalb wäre die beste experimentelle Strategie, das Azu im Proteininneren an einer fixierten Stelle zu platzieren, und die Position von Aha zu variieren.

Die VET Experimente zeigen, dass TRIR Spektroskopie in Kombination mit dem Azu-Aha Paar sehr geeignet ist um Pfade effizienten VETs zu finden. Das Vergleichen von VET Geschwindigkeiten und Effizienzen vieler PDZ3 Mutanten, die über das gesamte Protein verteilt sind, wird es ermöglichen Pfade effizienten VETs aufzudecken und deren Rolle für die Allosterie von Proteinen zu untersuchen. Dafür sollte aber das Verhältnis von der VET Aha Signalgröße zu den Hintergrundartefakten weiter verbessert werden, damit noch kleinere VET Signale gemessen werden können. Auch hier wären begleitende MD Simulationen zur Interpretation der gemessenen Daten nützlich.

Die in dieser Dissertation entwickelten und erprobten Instrumente und experimentellen Strategien mit IR Spektroskopie und ncAA erweisen sich als sehr vielversprechend für die Untersuchung dynamischer Allosterie in Proteinen.

Appendix A

Additional Figures and Tables

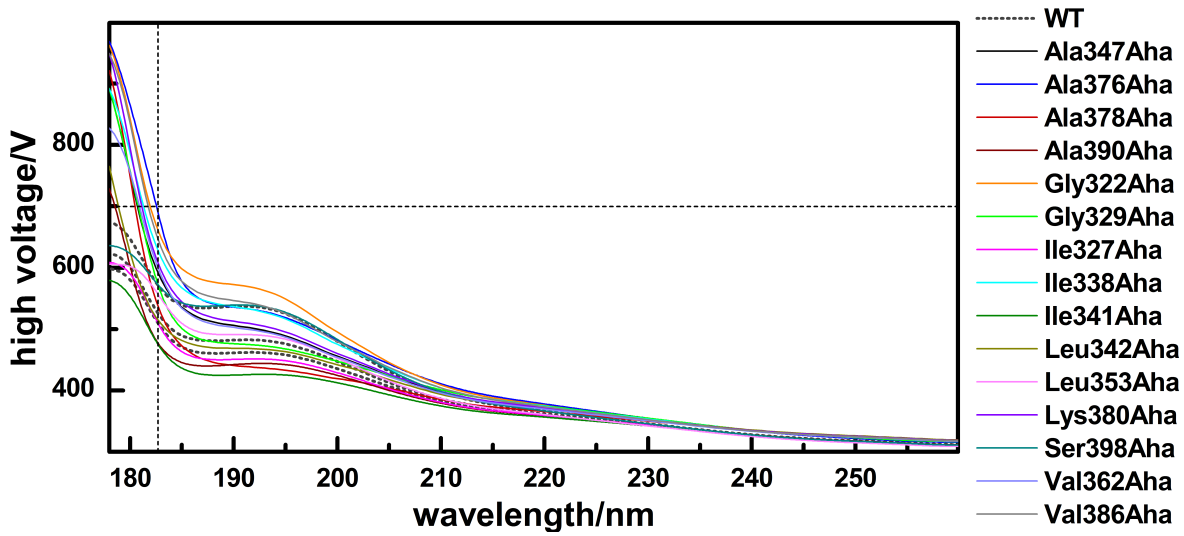

Figure A.0.1: High voltage of the CD measurements of the PDZ3 WT and Aha mutants. Spectra at voltages larger than 700 V (dotted lines) needs to be considered with care.

Table A.1: Parameters of the global analysis fits (sequential model) of the 2D-IR measurements on the Aha/solvent samples. The errors of the lifetimes τ of the four components derive from the fit. A gives the positive amplitude of the component spectra.

sample	T	τ_1/ps	τ_2/ps	τ_3/ps	τ_4/ps	SSE	A_1	A_2	A_3	A_4
upAha/H_2O	8 °C	5.6E-05	0.124±0.001	0.72±0.02	2.16±0.08	0.0050	3.6E08	0.53	0.21	0.037
upAha/D_2O	8 °C	5.8E-05	0.124±0.001	0.790±0.03	2.8±0.2	0.0049	5.5E08	0.35	0.16	0.033
bocAha/DMF	8 °C	4.2E-05	0.215±0.003	0.945±0.008	3.82±0.05	0.0015	1.3E07	1.0E07	0.41	0.12
bocAha/DMF	RT	1.8E-04	0.199±0.002	0.865±0.008	3.54±0.05	0.0020	2.1E05	1.1E07	0.40	0.11
bocAha/CCl_4	RT	5.2E-05	0.276±0.004	1.08±0.02	6.0±0.2	0.00019	1.2E06	0.27	0.11	0.027
bocAha/DMSO	RT	1.1E-04	0.131±0.004	0.87±0.01	5.1±0.2	0.0068	3.0E07	2.0E07	0.58	0.14
fmocAha/DMSO	RT	1.5E-04	0.113±0.005	0.911±0.009	5.0±0.2	0.0061	4.1E04	2.2	0.48	0.11
upAha/DMSO	RT	5.6E-05	0.082±0.002	0.890±0.008	5.06±0.08	0.0040	9.7E09	4.2E07	0.48	0.13
bocAha/H_2O	RT	1.1E-04	0.127±0.005	0.705±0.009	1.82±0.03	7.83E-05	4.7E07	0.31	0.079	0.020
bocAha/H_2O	8 °C	5.4E-05	0.10±0.02	0.73±0.02	2.02±0.07	0.0044	1.6E08	0.40	0.084	0.019
bocAha/$CHCl_3$	RT	2.4E-05	0.174±0.003	1.023±0.007	6.52±0.08	0.0066	4.2E08	1.7E07	0.57	0.15
bocAha/Formamide	RT	4.5E-05	0.146±0.001	0.912±0.007	3.32±0.04	0.0023	1.5E07	1.3E06	0.40	0.121
upAha/HFIP	RT	3.0E-05	0.113±0.006	0.886±0.008	4.56±0.08	0.028	7.3E07	3.5E06	0.88	0.21
bocAha/HFIP	RT	1.2E-04	0.103±0.001	0.868±0.008	4.23±0.09	0.0029	7.6E06	2.6E07	0.31	0.064
bocAha/Methanol	RT	2.4E-05	0.182±0.001	0.893±0.007	3.60±0.05	0.0046	9.4E07	1.8E06	0.51	0.13
fmocAha/Formamide	RT	2.6E-05	0.121±0.001	0.843±0.006	3.3±0.04	0.00087	2.1E08	1.1E07	0.26	0.057
bocAha/THF	RT	2.4E-05	0.173±0.005	0.894±0.005	5.34±0.05	0.0037	6.2E08	1.9E07	0.61	0.16

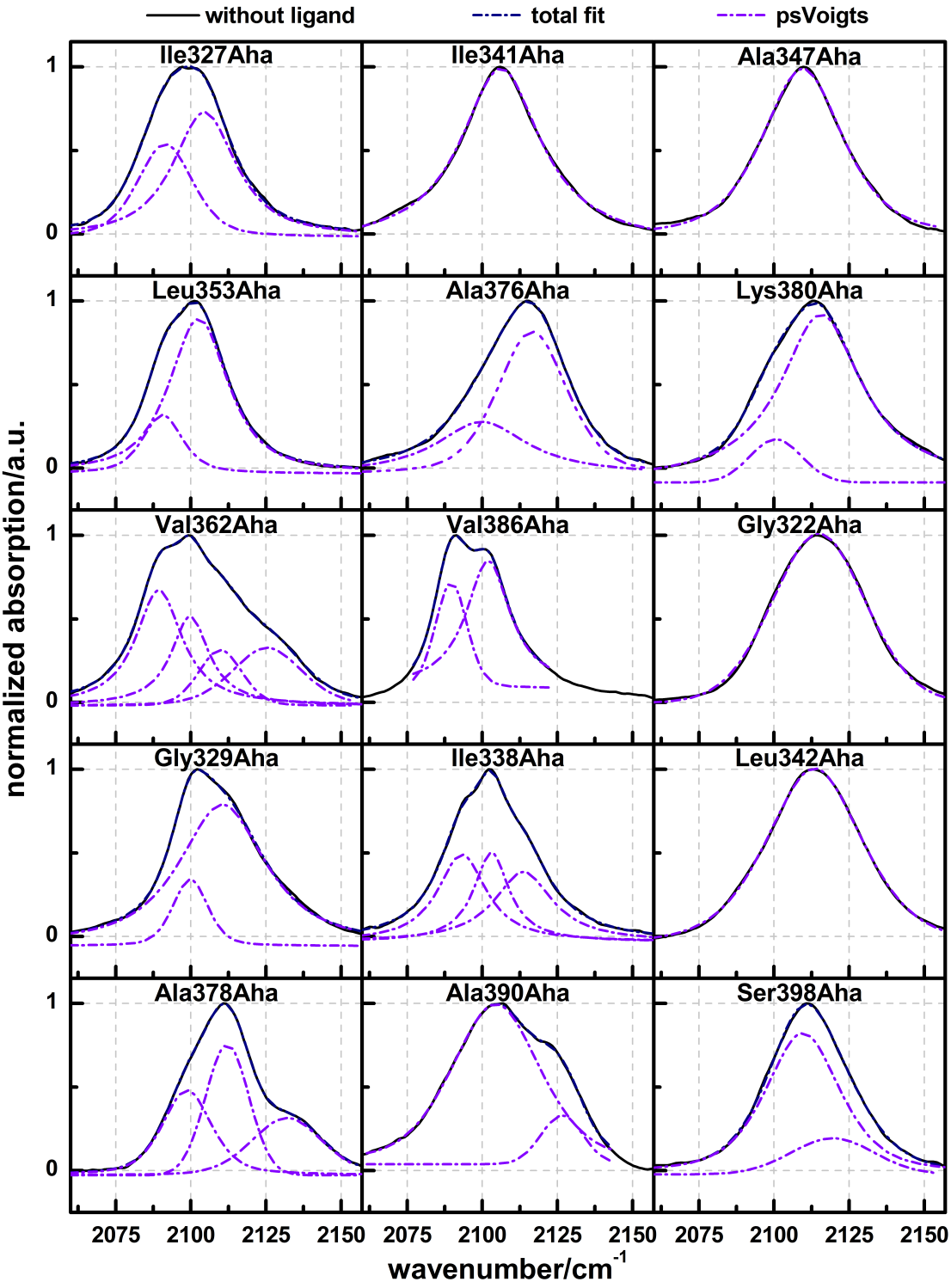

Figure A.0.2: Fit of multiple psVoigt functions (1-4) (violet dashed lines) to the Aha bands (solid line) of the unbound PDZ3-Aha (black). The overall fit to the spectra (dark blue dashed line) are the sums of the multiple psVoigt functions.

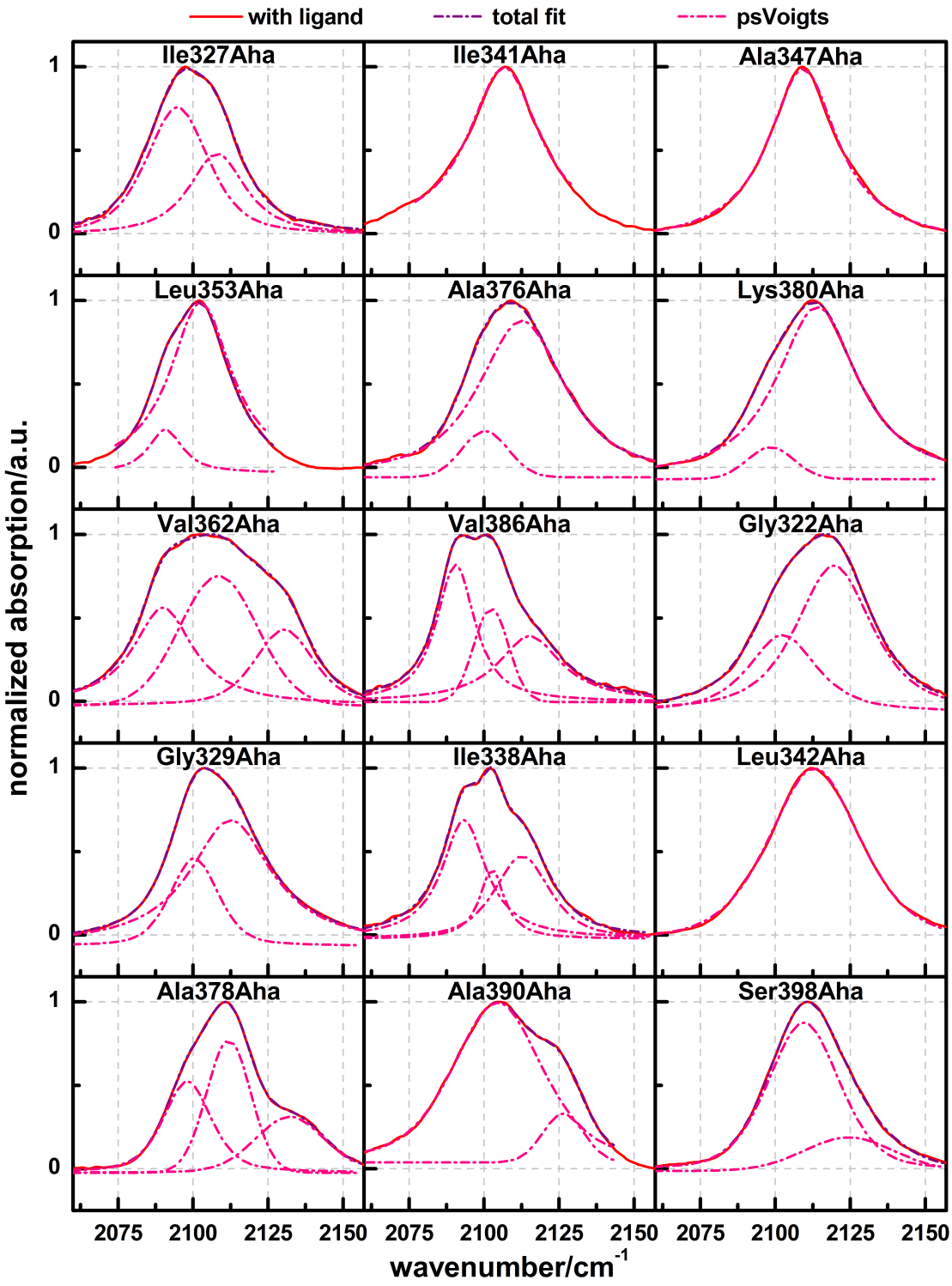

Figure A.0.3: Fit of multiple psVoigt functions (1-4) (pink dashed lines) to the Aha bands (solid line) of the bound PDZ3-Aha (red). The overall fit to the spectra (purple dashed line) are the sums of the multiple psVoigt functions.

Table A.2: Fit parameters of the psVoigt fit of azido's asymmetric stretching band of Aha in the PDZ3-Aha mutants with and without ligand. *Fitting borders were set to 0.1 **Fitting borders were set to 0.2

mutant	ligand	offset	area	FWHM/cm^{-1}	band maximum /cm^{-1}	Lorentz ratio
Ala347Aha	**without**	-0.03	45.71	32.32	2109.5	0.72
	Hepta	-0.06	46.34	28.13	2109.2	1.00
Ala376Aha	**without**	-0.04	18.40	36.94	2099.9	1.00
			29.82	27.48	2116.6	0.49
	Hepta	-0.06	47.05	34.14	2112.6	0.86
			5.35	18.16	2100.3	0.00
Ala378Aha	**without**	-0.03	11.06	27.68	2132.0	0.27
			12.76	19.31	2098.7	0.56
			14.07	16.93	2112.1	0.00
	Hepta	-0.02	10.36	27.24	2132.3	0.19
			13.46	18.88	2098.1	0.57
			14.63	17.32	2111.9	0.00
Ala390Aha	***without**	0.04	5.06	16.39	2126.5	0.00
			42.54	34.94	2104.5	0.51
	***Hepta**	0.04	5.01	16.17	2126.4	0.00
			43.30	35.09	2104.5	0.54
Gly322Aha	**without**	-0.01	42.54	36.68	2114.9	0.18
	Hepta	-0.07	17.82	26.97	2102.4	0.77
			37.31	30.11	2119.6	0.75
Gly329Aha	**without**	-0.06	43.41	34.42	2110.5	0.89
			6.78	13.72	2099.8	0.44
	Hepta	-0.07	39.29	33.13	2112.5	1.00
			12.63	18.95	2100.4	0.49
Ile327Aha	**without**	-0.02	27.81	25.03	2104.5	0.88
			15.22	21.79	2091.5	0.47
	Hepta	-0.01	16.30	22.38	2108.0	0.89
			25.15	24.63	2094.8	0.62
Ile338Aha	**without**	-0.03	15.45	23.51	2113.7	1.00
			15.64	19.44	2093.2	0.95
			11.87	14.14	2103.0	1.00
	Hepta	-0.02	14.96	21.75	2112.7	0.71
			19.85	17.72	2093.3	1.00
			6.51	9.86	2102.6	1.00
Ile341Aha	**without**	-0.07	54.05	32.46	2106.2	1.00
	****Hepta**	0.00	45.94	29.26	2106.7	1.00
Leu342Aha	**without**	-0.07	55.09	38.31	2113.5	0.62
	Hepta	-0.06	51.03	36.43	2113.1	0.62

mutant	ligand	offset	area	FWHM/cm^{-1}	band maximum /cm^{-1}	Lorentz ratio
Leu353Aha	**without**	-0.03	31.17	23.22	2102.6	0.82
			7.52	15.75	2090.6	0.67
	Hepta	-0.03	34.20	24.06	2102.3	0.81
			3.98	12.97	2090.2	0.62
Lys380Aha	**without**	-0.09	52.00	32.95	2115.6	1.00
			5.56	20.27	2100.6	0.00
	Hepta	-0.07	50.20	32.29	2114.0	0.91
			3.72	18.28	2098.5	0.00
Ser398Aha	**without**	-0.02	7.46	32.40	2119.5	0.00
			33.89	29.56	2109.6	0.67
	Hepta	-0.01	7.49	35.19	2124.5	0.00
			31.05	28.23	2109.5	0.43
Val362Aha	**without**	-0.02	11.52	27.42	2125.4	0.37
			6.58	17.12	2109.9	0.23
			12.82	15.25	2099.8	1.00
			19.89	18.65	2089.4	0.96
	Hepta	-0.03	13.68	23.29	2130.4	0.54
			25.26	30.59	2108.5	0.00
			22.38	24.27	2090.0	1.00
Val386Aha	****without**	0.09	21.33	17.82	2102.0	1.00
			9.12	12.39	2089.7	0.27
	Hepta	0.00	15.93	25.63	2115.3	1.00
			19.05	15.39	2090.5	0.91
			8.16	13.63	2102.4	0.00

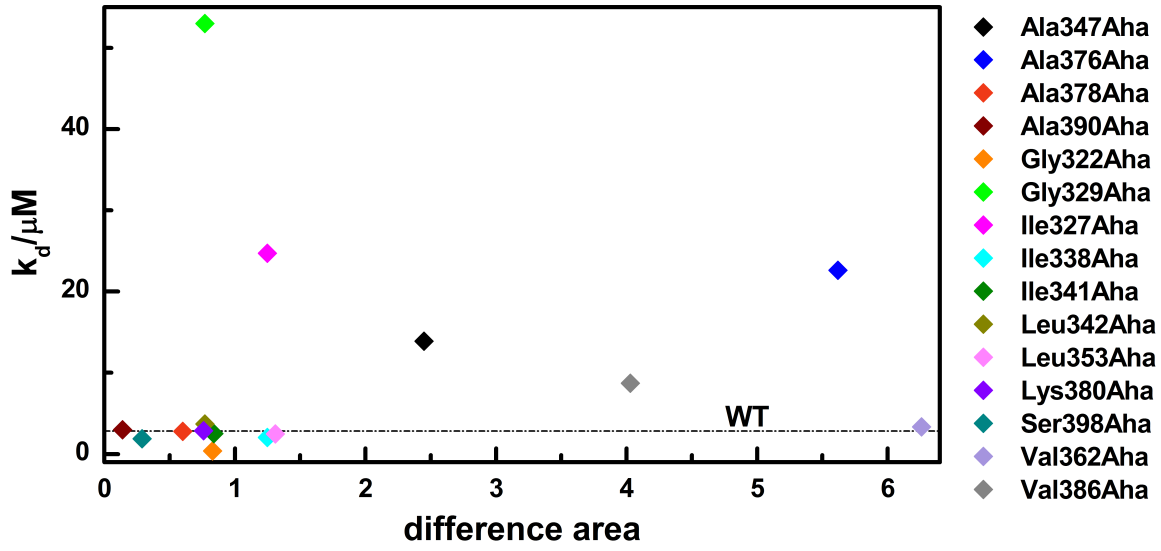

Figure A.0.4: Dissociation constant in dependency on the IR difference area between bound and unbound PDZ3-Aha. The k_d value of the WT is marked by a dashed grey line.

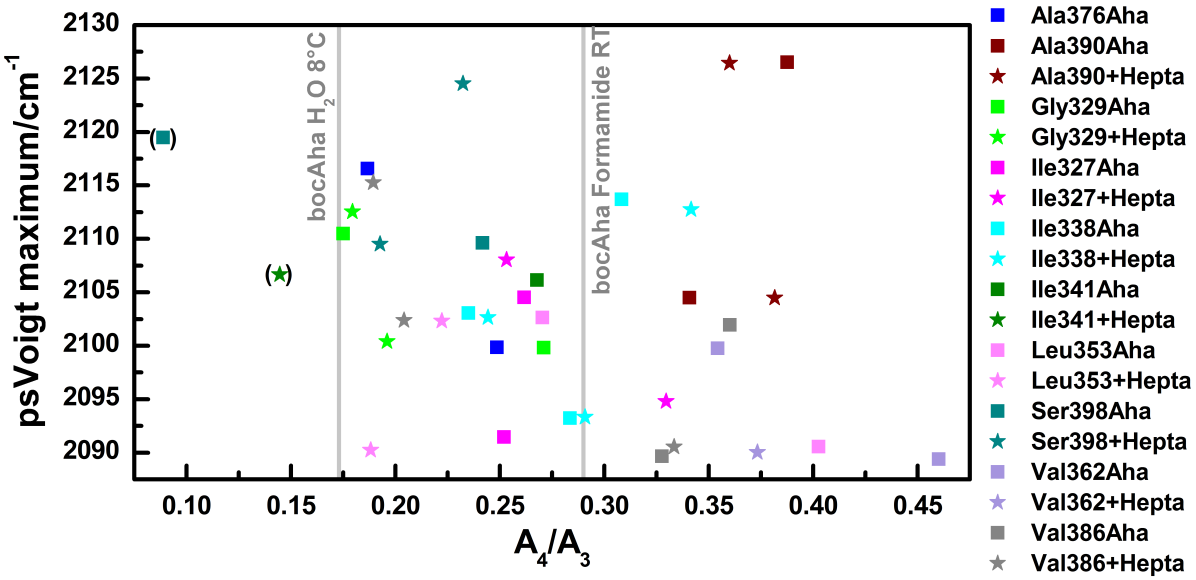

Figure A.0.5: Correlation between the wavenumber and the amplitude ratio A_4/A_3. The most extreme values of the bocAha/solvent samples are marked with grey lines.

Table A.3: Parameters of the global analysis fits (sequential model) of the 2D-IR spectra on the PDZ3-Aha samples. The errors of the lifetimes τ derive from the fit. A gives the positive amplitude of the component spectra.

sample	pump $\widetilde{\nu}$	τ_1/ps	τ_2/ps	τ_3/ps	τ_4/ps	SSE	A_1	A_2	A_3	A_4	A_4/A_3
Ile327Aha	2091.9	1.89E-05	0.058±0.006	0.40±0.02	2.1±0.2	0.0003	1.58E+07	8.95E-01	0.0199	0.0050	0.252
	2107.3	5.94E-05	0.048±0.002	0.55±0.03	2.1±0.1	0.000303	4.24E+09	2.00E+00	0.0263	0.0069	0.262
Ile327Aha+Hepta	2095.7	7.07E-05	0.08±0.02	0.58±0.03	2.2±0.2	0.0001	2.72E+07	3.58E-01	0.0181	0.0060	0.330
	2111.2	7.04E-05	0.066±0.008	0.85±0.06	2.2±0.2	0.000122	5.56E+07	4.69E-01	0.0204	0.0052	0.253
Ala376Aha	2103.4	2.01E-04	0.072±0.005	0.77±0.06	2.4±0.5	2.24E-05	1.92E+06	3.29E-01	6.46E-03	0.0016	0.249
	2118.9	2.92E-04	3.44E-04	0.59±0.03	2.4±0.3	3.21E-05	7.62E+08	5.08E+06	1.33E-02	0.0025	0.187
Ala390Aha	2107.3	5.88E-06	6.69E-05	0.58±0.03	2.2±0.2	2.17E-05	5.95E+11	2.60E+06	1.74E-02	0.0059	0.341
	2126.6	2.58E-05	2.67E-04	0.61±0.06	2.5±0.3	4.41E-05	4.38E+11	1.62E+05	1.06E-02	0.0041	0.388
Ala390Aha+Hepta	2107.3	5.07E-05	6.39E-04	0.63±0.04	2.2±0.1	4.58E-05	3.02E+09	2.22E+05	1.41E-02	0.0054	0.382
	2126.6	4.23E-05	4.96E-04	0.67±0.08	2.6±0.4	0.000124	2.23E+10	1.51E+04	0.0094	0.0034	0.360
Ile338Aha	2095.7	1.22E-04	0.057±0.002	0.88±0.03	2.7±0.02	0.000282	4.36E+07	1.24E+00	0.0314	0.0089	0.284
	2103.4	5.44E-05	0.089±0.003	0.93±0.03	3.0±0.2	0.000389	3.66E+07	1.43E-01	0.0388	0.0091	0.235
	2115	1.50E-04	0.09±0.02	0.47±0.04	2.5±0.2	0.000672	6.35E+05	1.34E-01	0.0187	0.0058	0.308
Ile338Aha+Hepta	2095.7	3.59E-04	0.069±0.001	0.90±0.02	2.6±0.1	0.000292	4.96E+05	8.73E-01	0.0449	0.0130	0.291
	2103.4	1.24E-04	0.095±0.003	0.92±0.03	2.8±0.2	0.000505	4.98E+08	1.79E-01	0.0462	0.0113	0.244
	2115	1.14E-04	0.11±0.02	0.50±0.04	2.7±0.2	0.000711	1.12E+05	1.06E-01	0.0228	0.0078	0.342
Val386Aha	2091.9	4.05E-05	1.78E-04	0.80±0.04	2.1±0.2	8.50E-05	2.64E+07	6.04E+05	1.78E-02	0.0058	0.328
	2103.4	2.53E-05	5.04E-05	0.64±0.05	1.95±0.08	6.16E-05	2.32E+10	5.33E+06	1.93E-02	0.0069	0.360
Val386Aha+Hepta	2091.9	1.05E-05	6.27E-04	0.76±0.04	2.1±0.2	7.04E-05	1.05E+10	1.03E+06	1.84E-02	0.0061	0.333
	2103.4	9.26E-07	5.78E-05	0.91±0.03	3.0±0.3	5.85E-05	3.32E+10	1.75E+07	2.23E-02	0.0046	0.204
	2118.9	1.84E-05	1.23E-04	0.8±0.2	3.0±0.9	9.15E-05	3.30E+09	1.59E+05	7.26E-03	0.0014	0.189
Val362Aha	2091.9	5.38E-05	0.047±0.001	0.82±0.08	2.1±0.2	3.45E-05	1.19E+09	3.08E+00	4.97E-03	0.0023	0.460
	2103.4	4.53E-06	9.89E-04	1.12±0.09	2.2±0.3	3.25E-05	1.02E+09	6.14E+03	6.70E-03	0.0024	0.354
Val362Aha+Hepta	2091.9	5.02E-05	3.33E-04	0.4±0.1	1.7±0.2	2.07E-05	3.55E+10	1.09E+05	2.83E-03	0.0011	0.373
Ser398Aha	2111.2	0.00117	0.088±0.009	0.72±0.03	1.69±0.09	3.56E-05	1.19E+04	1.65E-01	2.29E-02	0.0055	0.242
	2122.7	4.42E-0.5	0.10±0.01	0.86±0.03	(6±2)	4.15E-05	3.65E+07	1.21E-01	1.42E-02	0.0013	0.089
Ser398Aha+Hepta	2111.2	8.70E-05	0.08±0.02	0.68±0.02	1.81±0.09	6.17E-05	1.43E+07	5.07E-01	3.79E-02	0.0073	0.193
	2126.6	5.28E-05	0.058±0.001	0.53±0.05	1.6±0.2	5.00E-05	1.08E+08	9.39E-01	1.87E-02	0.0043	0.232
Ile341Aha	2107.3	5.30E-05	0.08±0.02	0.71±0.07	2.5±0.4	5.81E-05	1.56E+06	1.52E-01	6.61E-03	0.00177	0.268
Ile341Aha+Hepta	2107.3	5.14E-05	0.12±0.02	1.03±0.07	(8±2)	5.89E-05	1.97E+05	5.04E-02	4.53E-03	0.0007	0.145
Gly329Aha	2103.4	3.57E-05	5.22E-05	0.76±0.03	2.5±0.2	3.95E-05	2.62E+08	9.15E+07	1.95E-02	0.0053	0.271
	2111.2	4.62E-05	5.64E-05	0.90±0.04	2.9±0.3	3.97E-05	1.89E+08	2.84E+07	1.67E-02	0.0029	0.175
Gly329Aha+Hepta	2103.4	0.00194	0.066±0.003	0.63±0.03	2.5±0.3	0.000216	1.17E+03	1.14E-01	0.0114	0.0022	0.196
	2115	6.45E-05	0.10±0.02	0.80±0.04	2.9±0.4	0.000197	7.80E+06	2.38E-02	0.0097	0.0017	0.179
Leu353Aha	2091.9	3.76E-05	0.13±0.06	0.89±0.09	2.0±0.4	5.08E-05	3.94E+07	1.62E-02	4.51E-03	0.0018	0.403
	2103.4	5.43E-05	0.22±0.04	1.2±0.2	2.7±0.6	4.04E-05	1.07E+04	1.57E-02	4.63E-03	0.0013	0.270
Leu353Aha+Hepta	2091.9	1.12E-05	1.28E-05	0.71±0.06	2.3±0.3	5.56E-05	9.45E+09	3.78E+08	8.45E-03	0.0016	0.188
	2103.4	6.57E-06	0.08±0.02	0.74±0.04	2.5±0.3	5.84E-05	1.16E+11	1.25E-01	1.30E-02	0.0029	0.222

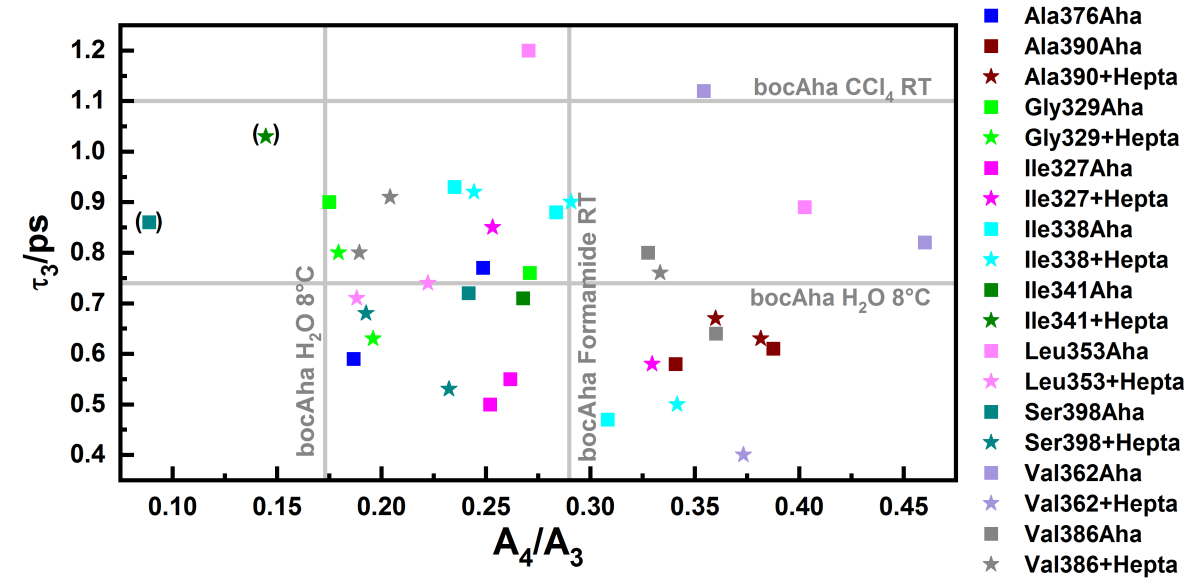

Figure A.0.6: Correlation between the vibrational lifetime τ_3 and the amplitude ratio A_4/A_3. The most extreme values of the bocAha/solvent samples are marked with grey lines.

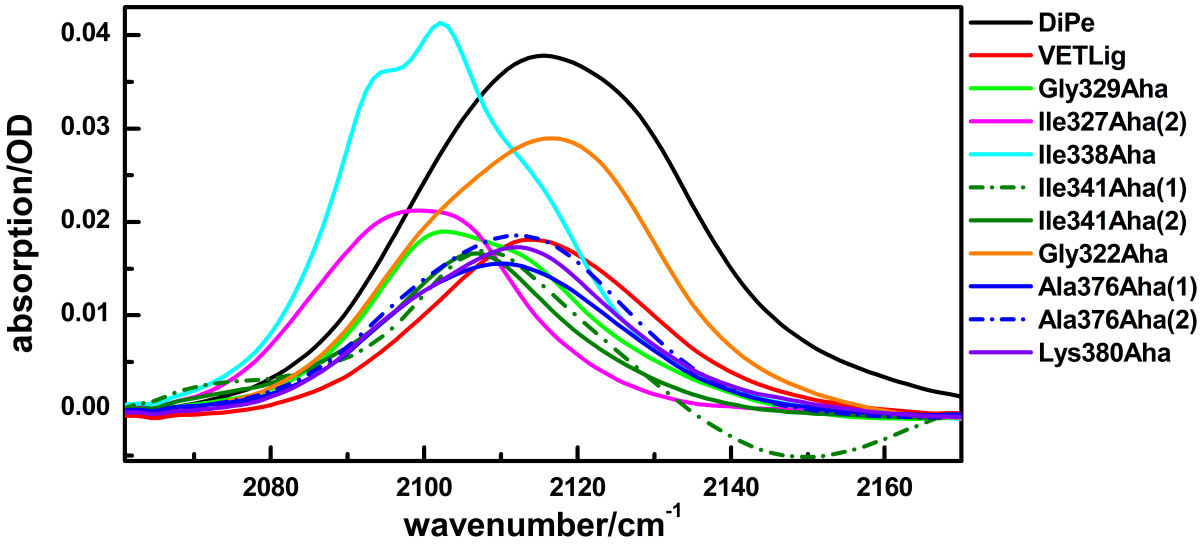

Figure A.0.7: Background corrected FTIR spectra of the Aha's asymmetric stretching band of the different samples used for the VET experiments. All PDZ3-Aha mutants are bound to AzuLig. The spectrum of the first Ile341Aha measurement is perturbed by air bubbles.

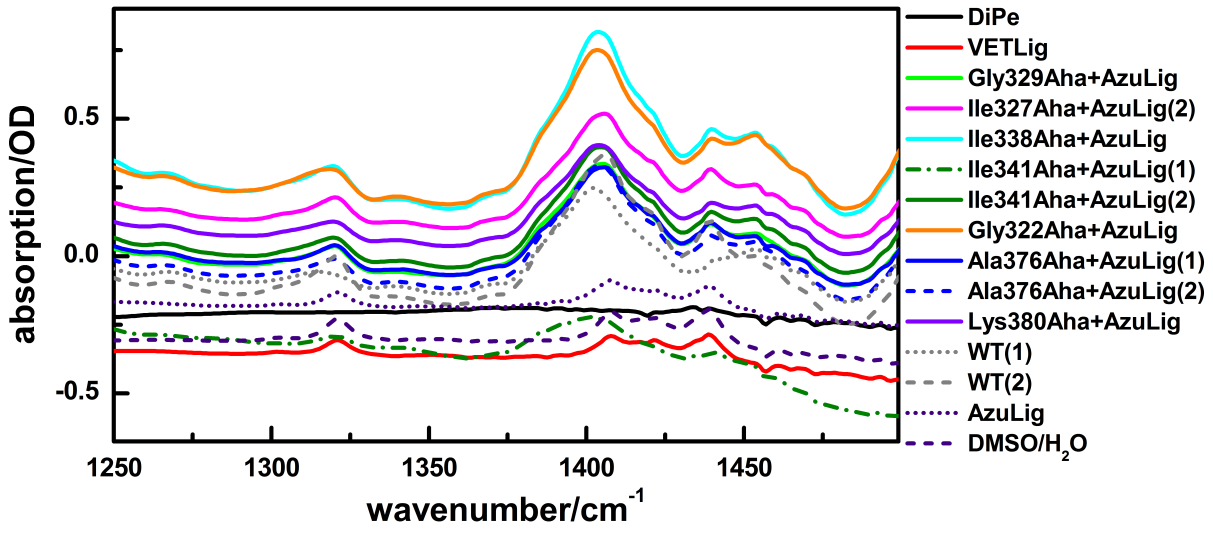

Figure A.0.8: FTIR spectra of the amide region, which were used for PDZ3-Aha concentration determination, of the different VET samples. The two WT spectra without ligand and the pure DMSO/H_2O and AzuLig spectrum were applied as basis for the implemented linear combination. The spectrum of the first Ile341Aha measurement is perturbed by air bubbles.

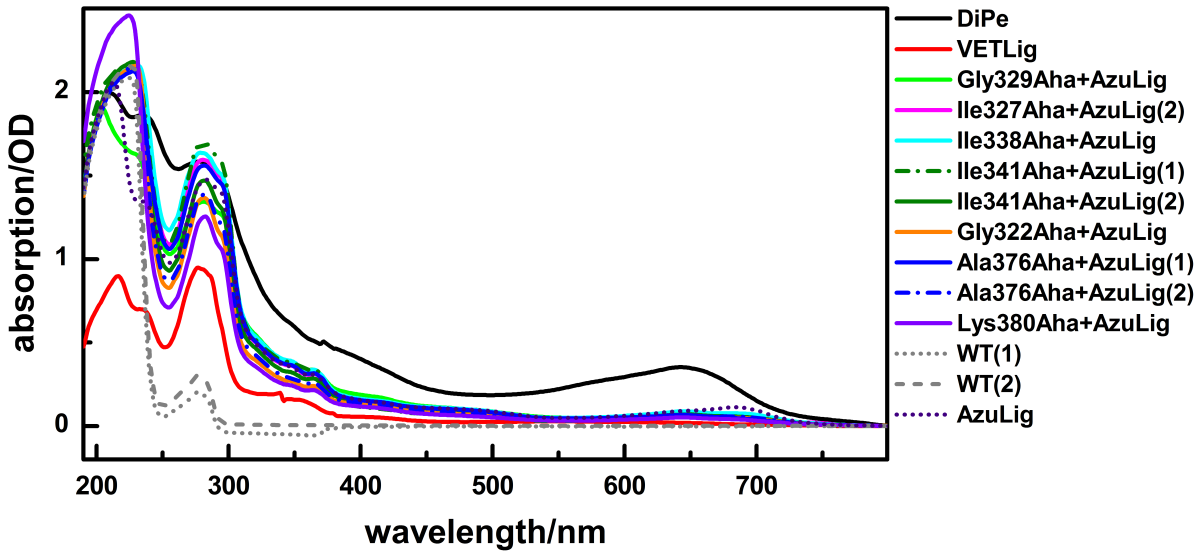

Figure A.0.9: UV-Vis spectra of the different PDZ3-Aha+AzuLig VET samples, which were used for AzuLig concentration determination. The two WT spectra without ligand and the AzuLig spectrum were applied as basis for the implemented linear combination.

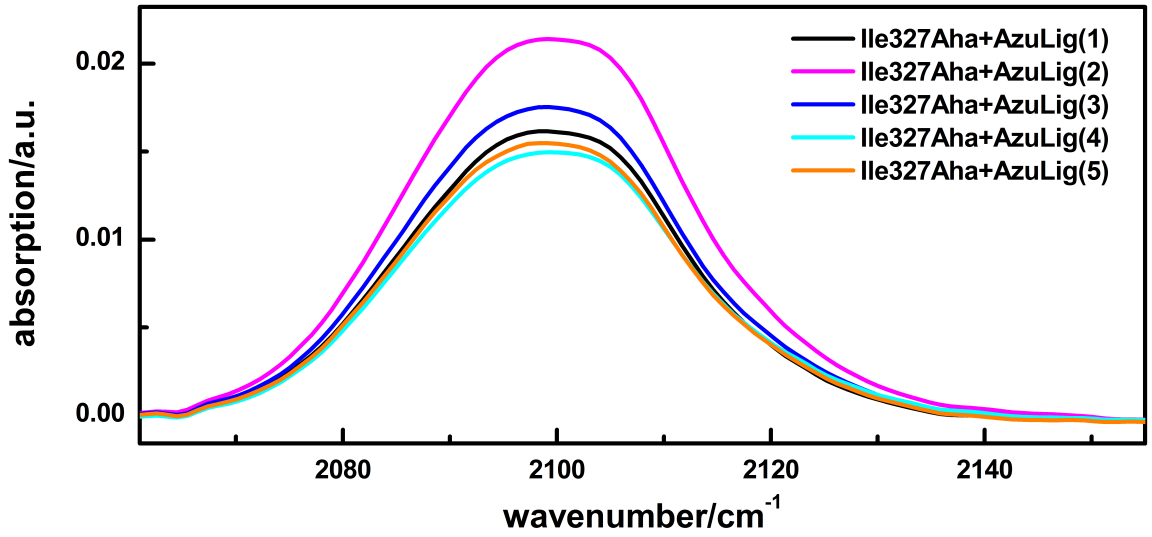

Figure A.0.10: Background corrected FTIR spectra of the Aha's asymmetric stretching band of the different Ile327Aha+AzuLig samples used for the VET experiments.

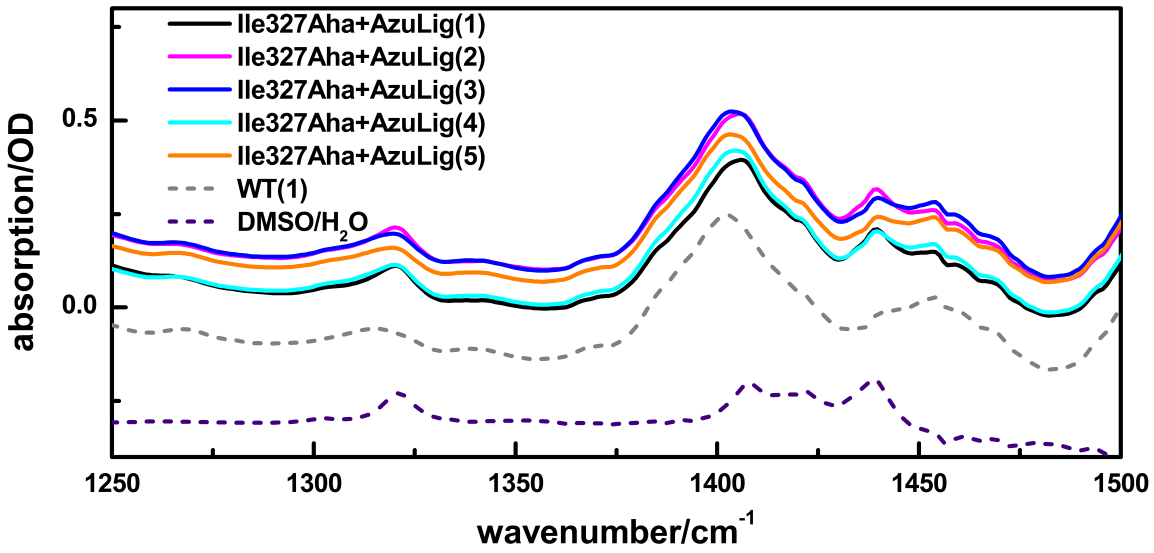

Figure A.0.11: FTIR spectra of the amide region, which were used for PDZ3-Aha concentration determination, of the different Ile327Aha+AzuLig VET samples. The WT spectrum without ligand and the pure DMSO/H_2O spectrum were applied as basis for the implemented linear combination.

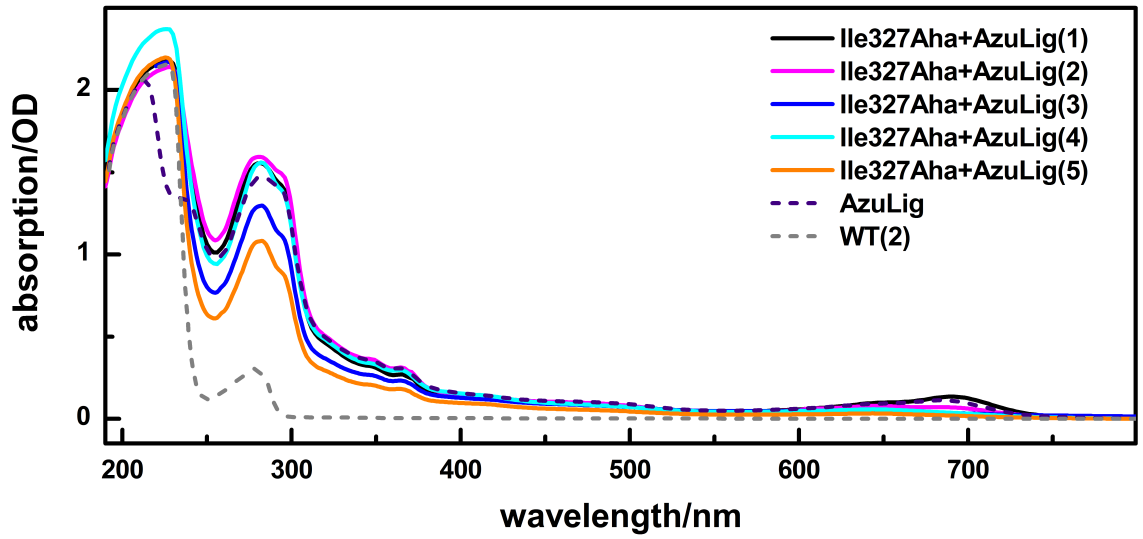

Figure A.0.12: UV-Vis spectra of the different Ile327Aha+AzuLig VET samples, which were used for AzuLig concentration determination. The WT spectrum without ligand and the AzuLig spectrum were applied as basis for the implemented linear combination.

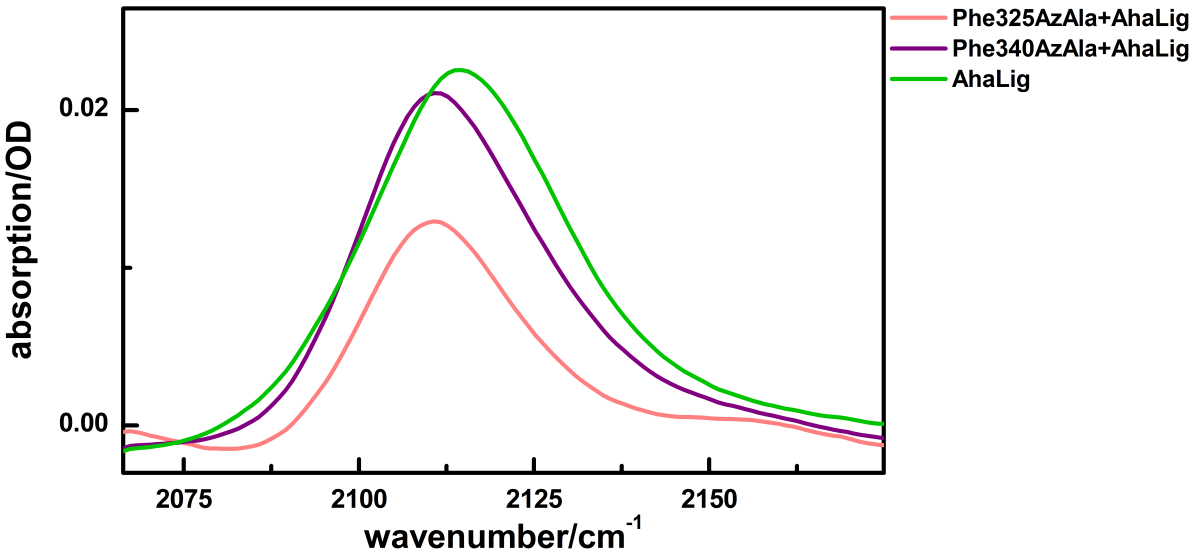

Figure A.0.13: Background corrected FTIR spectra of the Aha's asymmetric stretching band of the different PDZ3-AzAla samples with AhaLig used for the VET experiments and of unbound AhaLig.

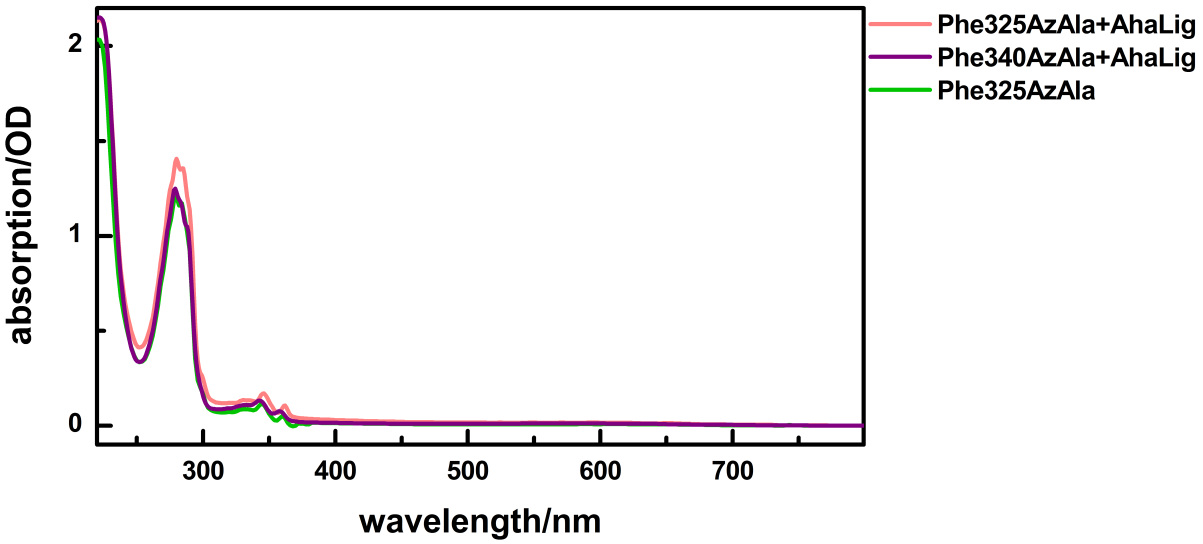

Figure A.0.14: UV-Vis spectra of the different PDZ3-AzAla VET samples.

Bibliography

[1] H. N. Motlagh, J. O. Wrabl, J. Li, and V. J. Hilser, "The ensemble nature of allostery," *Nature*, no. 508, pp. 331–339, 2014.

[2] D. Thirumalai, C. Hyeon, P. I. Zhuravlev, and G. H. Lorimer, "Symmetry, Rigidity, and Allosteric Signaling: From Monomeric Proteins to Molecular Machines," *Chemical Reviews*, no. 119, pp. 6788–6821, 2019.

[3] D. Kern and E. R. P. Zuiderweg, "The role of dynamics in allosteric regulation," *Current Opinion in Structural Biology*, vol. 13, no. 6, pp. 748–757, 2003.

[4] A. A. S. Ribeiro and V. Ortiz, "A Chemical Perspective on Allostery," *Chemical Reviews*, vol. 116, no. 11, pp. 6488–6502, 2016.

[5] S. W. Lockless and R. Ranganathan, "Evolutionarily Conserved Pathways of Energetic Connectivity in Protein Families," *Science*, vol. 286, no. 5438, pp. 295–299, 1999.

[6] N. Ota and D. A. Agard, "Intramolecular signaling pathways revealed by modeling anisotropic thermal diffusion," *Journal of Molecular Biology*, vol. 351, no. 2, pp. 345–354, 2005.

[7] S. Burendahl and L. Nilsson, "Computational studies of LXR molecular interactions reveal an allosteric communication pathway," *Proteins*, vol. 80, no. 1, pp. 294–306, 2012.

[8] G. A. Miño-Galaz, "Allosteric communication pathways and thermal rectification in PDZ-2 protein: a computational study," *The Journal of Physical Chemistry B*, vol. 119, no. 20, pp. 6179–6189, 2015.

[9] A. A. S. Ribeiro and V. Ortiz, "Energy Propagation and Network Energetic Coupling in Proteins," *The Journal of Physical Chemistry B*, vol. 119, no. 5, pp. 1835–1846, 2015.

[10] K. Sharp and J. J. Skinner, "Pump-probe molecular dynamics as a tool for studying protein motion and long range coupling," *Proteins*, vol. 65, no. 2, pp. 347–361, 2006.

[11] A. Dhulesia, J. Gsponer, and M. Vendruscolo, "Mapping of two networks of residues that exhibit structural and dynamical changes upon binding in a PDZ domain protein," *Journal of the American Chemical Society*, vol. 130, no. 28, pp. 8931–8939, 2008.

[12] Y. Kong and M. Karplus, "Signaling pathways of PDZ2 domain: a molecular dynamics interaction correlation analysis," *Proteins*, vol. 74, no. 1, pp. 145–154, 2009.

[13] Z. Liu, J. Chen, and D. Thirumalai, "On the accuracy of inferring energetic coupling between distant sites in protein families from evolutionary imprints: illustrations using lattice model," *Proteins*, vol. 77, no. 4, pp. 823–831, 2009.

[14] B. K. Ho and D. A. Agard, "Conserved tertiary couplings stabilize elements in the PDZ fold, leading to characteristic patterns of domain conformational flexibility," *Protein Science*, vol. 19, no. 3, pp. 398–411, 2010.

[15] Z. N. Gerek and S. B. Ozkan, "Change in allosteric network affects binding affinities of PDZ domains: analysis through perturbation response scanning," *PLoS Computational Biology*, vol. 7, no. 10, p. e1002154, 2011.

[16] B. Erman, "Relationships between ligand binding sites, protein architecture and correlated paths of energy and conformational fluctuations," *Physical Biology*, vol. 8, no. 5, p. 056003(9pp), 2011.

[17] S. Steiner and A. Caflisch, "Peptide binding to the PDZ3 domain by conformational selection," *Proteins*, vol. 80, no. 11, pp. 2562–2572, 2012.

[18] C. Kaya, A. Armutlulu, S. Ekesan, and T. Haliloglu, "MCPath: Monte Carlo path generation approach to predict likely allosteric pathways and functional residues," *Nucleic Acids Research*, vol. 41, pp. W249–W255, 2013.

[19] R. Kalescky, J. Liu, and P. Tao, "Identifying key residues for protein allostery through rigid residue scan," *The Journal of Physical Chemistry A*, vol. 119, no. 9, pp. 1689–1700, 2014.

[20] G. Morra, A. Genoni, and G. Colombo, "Mechanisms of Differential Allosteric Modulation in Homologous Proteins: Insights from the Analysis of Internal Dynamics and Energetics of PDZ Domains," *Journal of Chemical Theory and Computation*, vol. 10, no. 12, pp. 5677–5689, 2014.

[21] T. Ishikura, Y. Iwata, T. Hatano, and T. Yamato, "Energy exchange network of inter-residue interactions within a thermally fluctuating protein molecule: A computational study," *Journal of Computational Chemistry*, vol. 36, no. 22, pp. 1709–1718, 2015.

[22] A. S. Raman, K. I. White, and R. Ranganathan, "Origins of Allostery and Evolvability in Proteins: A Case Study," *Cell*, vol. 166, no. 2, pp. 468–480, 2016.

[23] A. Kumawat and S. Chakrabarty, "Hidden electrostatic basis of dynamic allostery in a PDZ domain," *PNAS*, vol. 114, no. 29, pp. E5825–E5834, 2017.

[24] V. C. Nibali, G. Morra, M. Havenith, and G. Colombo, "Role of Terahertz (THz) Fluctuations in the Allosteric Properties of the PDZ Domains," *The Journal of Physical Chemistry B*, vol. 121, no. 44, pp. 10200–10208, 2017.

[25] S. Buchenberg, F. Sittel, and G. Stock, "Time-resolved observation of protein allosteric communication," *PNAS*, vol. 114, no. 33, pp. E6804–E6811, 2017.

[26] W. B. Wang, Y. Liang, J. Zhang, Y. D. Wu, J. J. Du, Q. M. Li, J. Z. Zhu, and J. G. Su, "Energy transport pathway in proteins: Insights from non-equilibrium molecular dynamics with elastic network model," *Scientific Reports*, vol. 8, no. 1, p. 9487, 2018.

[27] G. Morra, M. Meli, and G. Colombo, "How the Ligand-Induced Reorganization of Protein Internal Energies Is Coupled to Conformational Events," *Journal of Chemical Theory and Computation*, vol. 14, no. 11, pp. 5992–6001, 2018.

[28] H. Zhou and P. Tao, "REDAN: relative entropy-based dynamical allosteric network model," *Molecular Physics*, vol. 117, no. 9-12, pp. 1334–1343, 2019.

[29] P. de Los Rios, F. Cecconi, A. Pretre, G. Dietler, O. Michielin, F. Piazza, and B. Juanico, "Functional dynamics of PDZ binding domains: a normal-mode analysis," *Biophysical Journal*, vol. 89, no. 1, pp. 14–21, 2005.

[30] B. Buchli, S. A. Waldauer, R. Walser, M. L. Donten, R. Pfister, N. Blöchliger, S. Steiner, A. Caflisch, O. Zerbe, and P. Hamm, "Kinetic response of a photoperturbed allosteric protein," *PNAS*, vol. 110, no. 29, pp. 11725–11730, 2013.

[31] C. N. Chi, L. Elfström, Y. Shi, T. Snäll, Å. Engström, and P. Jemth, "Reassessing a sparse energetic network within a single protein domain," *PNAS*, no. 105, pp. 4679–4684, 2008.

[32] C. N. Chi, A. Bach, K. Strømgaard, S. Gianni, and P. Jemth, "Ligand binding by PDZ domains," *BioFactors*, vol. 38, no. 5, pp. 338–348, 2012.

[33] E. J. Fuentes, C. J. Der, and A. L. Lee, "Ligand-dependent Dynamics and Intramolecular Signaling in a PDZ Domain," *Journal of Molecular Biology*, vol. 335, no. 4, pp. 1105–1115, 2004.

[34] E. J. Fuentes, S. A. Gilmore, R. V. Mauldin, and A. L. Lee, "Evaluation of energetic and dynamic coupling networks in a PDZ domain protein," *Journal of Molecular Biology*, vol. 364, no. 3, pp. 337–351, 2006.

[35] S. Gianni, S. R. Haq, L. C. Montemiglio, M. C. Jürgens, Å. Engström, C. N. Chi, M. Brunori, and P. Jemth, "Sequence-specific long range networks in PSD-95/discs large/ZO-1 (PDZ) domains tune their binding selectivity," *The Journal of Biological Chemistry*, vol. 286, no. 31, pp. 27167–27175, 2011.

[36] R. N. McLaughlin, F. J. Poelwijk, A. Raman, W. S. Gosal, and R. Ranganathan, "The spatial architecture of protein function and adaptation," *Nature*, vol. 491, no. 7422, pp. 138–142, 2012.

[37] C. M. Petit, J. Zhang, P. J. Sapienza, E. J. Fuentes, and A. L. Lee, "Hidden dynamic allostery in a PDZ domain," *PNAS*, vol. 106, no. 43, pp. 18249–18254, 2009.

[38] D. M. Leitner, "Energy Flow in Proteins," *Annual Review of Physical Chemistry*, vol. 59, no. 1, pp. 233–259, 2008.

[39] D. Leitner and T. Yamato, "Mapping energy transport networks in proteins," *Reviews in Computational Chemistry*, vol. 31, pp. 1–75, 2019.

[40] X. Yu and D. M. Leitner, "Heat flow in proteins: Computation of thermal transport coefficients," *The Journal of Chemical Physics*, vol. 122, no. 5, p. 054902, 2005.

[41] D. Schwarzer, C. Hanisch, P. Kutne, and J. Troe, "Vibrational Energy Transfer in Highly Excited Bridged Azulene-Aryl Compounds: Direct Observation of Energy Flow through Aliphatic Chains and into the Solvent," *The Journal of Physical Chemistry A*, vol. 106, no. 35, pp. 8019–8028, 2002.

[42] C. Riedel, R. Gabizon, C. A. M. Wilson, K. Hamadani, K. Tsekouras, S. Marqusee, S. Pressé, and C. Bustamante, "The heat released during catalytic turnover enhances the diffusion of an enzyme," *Nature*, vol. 517, no. 7533, pp. 227–230, 2015.

[43] Y. Zhang and H. Hess, "Enhanced Diffusion of Catalytically Active Enzymes," *ACS Central Science*, vol. 5, no. 6, pp. 939–948, 2019.

[44] G. Li, D. Magana, and R. B. Dyer, "Anisotropic energy flow and allosteric ligand binding in albumin," *Nature Communications*, vol. 5, no. 1, pp. 1–7, 2014.

[45] L. Martínez, A. C. M. Figueira, P. Webb, I. Polikarpov, and M. S. Skaf, "Mapping the Intramolecular Vibrational Energy Flow in Proteins Reveals Functionally Important Residues," *The Journal of Physical Chemistry Letters*, vol. 2, no. 16, pp. 2073–2078, 2011.

[46] A. Gulzar, L. V. Borau, S. Buchenberg, S. Wolf, and G. Stock, "Energy Transport Pathways in Proteins: A Non-equilibrium Molecular Dynamics Simulation Study," *Journal of Chemical Theory and Computation*, vol. 15, no. 10, pp. 5750–5757, 2019.

[47] N. Fujii, M. Mizuno, H. Ishikawa, and Y. Mizutani, "Observing Vibrational Energy Flow in a Protein with the Spatial Resolution of a Single Amino Acid Residue," *The Journal of Physical Chemistry Letters*, vol. 5, no. 18, pp. 3269–3273, 2014.

[48] S. Yamashita, M. Mizuno, D. P. Tran, H. Dokainish, A. Kitao, and Y. Mizutani, "Vibrational Energy Transfer from Heme through Atomic Contacts in Proteins," *The Journal of Physical Chemistry B*, vol. 122, no. 22, pp. 5877–5884, 2018.

[49] S. Buchenberg, D. M. Leitner, and G. Stock, "Scaling Rules for Vibrational Energy Transport in Globular Proteins," *The Journal of Physical Chemistry Letters*, vol. 7, no. 1, pp. 25–30, 2015.

[50] K. M. Reid, T. Yamato, and D. M. Leitner, "Scaling of Rates of Vibrational Energy Transfer in Proteins with Equilibrium Dynamics and Entropy," *The Journal of Physical Chemistry B*, vol. 122, no. 40, pp. 9331–9339, 2018.

[51] H. J. Bakker, P. C. M. Planken, and A. Lagendijk, "Role of solvent on vibrational energy transfer in solution," *Nature*, no. 347, pp. 745–747, 1990.

[52] Y. Mizutani and T. Kitagawa, "Direct observation of cooling of heme upon photodissociation of carbonmonoxy myoglobin," *Science*, vol. 278, no. 5337, pp. 443–446, 1997.

[53] A. Charvat, J. Aßmann, B. Abel, D. Schwarzer, K. Henning, K. Luther, and J. Troe, "Direct observation of intramolecular vibrational energy redistribution of selectively excited CH2I2 and C3H5I molecules in solution," *Physical Chemistry Chemical Physics*, vol. 3, no. 12, pp. 2230–2240, 2001.

[54] D. Schwarzer, P. Kutne, C. Schröder, and J. Troe, "Intramolecular vibrational energy redistribution in bridged azulene-anthracene compounds: Ballistic energy transport through molecular chains," *The Journal of Chemical Physics*, vol. 121, no. 4, pp. 1754–1764, 2004.

[55] V. Botan, E. H. G. Backus, R. Pfister, A. Moretto, M. Crisma, C. Toniolo, P. H. Nguyen, G. Stock, and P. Hamm, "Energy transport in peptide helices," *PNAS*, no. 104, pp. 12749–12754, 2007.

[56] D. V. Kurochkin, S. R. G. Naraharisetty, and I. V. Rubtsov, "A relaxation-assisted 2D IR spectroscopy method," *PNAS*, no. 104, pp. 14209–14214, 2007.

[57] I. V. Rubtsov, "Relaxation-Assisted Two-Dimensional Infrared (RA 2DIR) Method: Accessing Distances over 10 Å and Measuring Bond Connectivity Patterns," *Accounts of Chemical Research*, vol. 42, no. 9, pp. 1385–1394, 2009.

[58] N. Fujii, M. Mizuno, and Y. Mizutani, "Direct Observation of Vibrational Energy Flow in Cytochrome c," *The Journal of Physical Chemistry B*, vol. 115, no. 44, pp. 13057–13064, 2011.

[59] W. J. Schreier, T. Aumüller, K. Haiser, F. O. Koller, M. Löweneck, H.-J. Musiol, T. E. Schrader, T. Kiefhaber, L. Moroder, and W. Zinth, "Following the energy transfer in and out of a polyproline-peptide," *Biopolymers*, vol. 100, no. 1, pp. 38–50, 2012.

[60] H. M. Müller-Werkmeister, Y.-L. Li, E.-B. W. Lerch, D. Bigourd, and J. Bredenbeck, "Ultrafast hopping from band to band: assigning infrared spectra based on vibrational energy transfer," *Angewandte Chemie (International ed. in English)*, vol. 52, no. 24, pp. 6214–6217, 2013.

[61] Y. Yue, L. N. Qasim, A. A. Kurnosov, N. I. Rubtsova, R. T. Mackin, H. Zhang, B. Zhang, X. Zhou, J. Jayawickramarajah, A. L. Burin, and I. V. Rubtsov, "Band-Selective Ballistic Energy Transport in Alkane Oligomers: Toward Controlling the Transport Speed," *The Journal of Physical Chemistry B*, vol. 119, no. 21, pp. 6448–6456, 2015.

[62] N. I. Rubtsova and I. V. Rubtsov, "Vibrational energy transport in molecules studied by relaxation-assisted two-dimensional infrared spectroscopy," *Annual Review of Physical Chemistry*, vol. 66, pp. 717–738, 2015.

[63] N. I. Rubtsova, L. N. Qasim, A. A. Kurnosov, A. L. Burin, and I. V. Rubtsov, "Ballistic Energy Transport in Oligomers," *Accounts of Chemical Research*, vol. 48, no. 9, pp. 2547–2555, 2015.

[64] L. Chuntonov, "2D-IR spectroscopy of hydrogen-bond-mediated vibrational excitation transfer," *Physical Chemistry Chemical Physics*, vol. 18, no. 20, pp. 13852–13860, 2016.

[65] B. Dutta, B. E. Vos, Y. L. A. Rezus, G. H. Koenderink, and H. J. Bakker, "Observation of Ultrafast Vibrational Energy Transfer in Fibrinogen and Fibrin Fibers," *The Journal of Physical Chemistry B*, vol. 122, no. 22, pp. 5870–5876, 2018.

[66] O. Selig, A. V. Cunha, M. B. van Eldijk, J. C. van Hest, T. L. Jansen, H. J. Bakker, and Y. L. A. Rezus, "Temperature-Induced Collapse of Elastin-like Peptides Studied by 2DIR Spectroscopy," *The Journal of Physical Chemistry B*, vol. 122, no. 34, pp. 8243–8254, 2018.

[67] E. H. G. Backus, P. H. Nguyen, V. Botan, A. Moretto, M. Crisma, C. Toniolo, O. Zerbe, G. Stock, and P. Hamm, "Structural flexibility of a helical peptide regulates vibrational energy transport properties," *The Journal of Physical Chemistry B*, vol. 112, no. 48, pp. 15487–15492, 2008.

[68] E. H. G. Backus, P. H. Nguyen, V. Botan, R. Pfister, A. Moretto, M. Crisma, C. Toniolo, G. Stock, and P. Hamm, "Energy transport in peptide helices: a comparison between high- and low-energy excitations," *The Journal of Physical Chemistry B*, vol. 112, no. 30, pp. 9091–9099, 2008.

[69] E. H. G. Backus, R. Bloem, R. Pfister, A. Moretto, M. Crisma, C. Toniolo, and P. Hamm, "Dynamical Transition in a Small Helical Peptide and Its Implication for Vibrational Energy Transport," *The Journal of Physical Chemistry B*, vol. 113, no. 40, pp. 13405–13409, 2009.

[70] H. M. Müller-Werkmeister and J. Bredenbeck, "A donor-acceptor pair for the real time study of vibrational energy transfer in proteins," *Physical Chemistry Chemical Physics*, vol. 16, no. 7, pp. 3261–3266, 2014.

[71] X. Yu and D. M. Leitner, "Vibrational Energy Transfer and Heat Conduction in a Protein," *The Journal of Physical Chemistry B*, vol. 107, no. 7, pp. 1698–1707, 2003.

[72] D. M. Leitner, "Thermal boundary conductance and thermal rectification in molecules," *The Journal of Physical Chemistry B*, vol. 117, no. 42, pp. 12820–12828, 2013.

[73] B. D. Wagner, M. Szymanski, and R. P. Steer, "Subpicosecond pump–probe measurements of the electronic relaxation rates of the S1 states of azulene and related compounds in polar and nonpolar solvents," *The Journal of Chemical Physics*, vol. 98, no. 1, pp. 301–307, 1993.

[74] M. J. Bearpark, F. Bernardi, S. Clifford, M. Olivucci, M. A. Robb, B. R. Smith, and T. Vreven, "The Azulene S1 State Decays via a Conical Intersection: A CASSCF Study with MMVB Dynamics," *Journal of the American Chemical Society*, no. 118, pp. 169–175, 1996.

[75] A. J. Wurzer, T. Wilhelm, J. Piel, and E. Riedle, "Comprehensive measurement of the S1 azulene relaxation dynamics and observation of vibrational wavepacket motion," *Chemical Physics Letters*, no. 299, pp. 296–302, 1999.

[76] J. Shao, I. V. Korendovych, and J. Broos, "Biosynthetic incorporation of the azulene moiety in proteins with high efficiency," *Amino Acids*, vol. 47, no. 1, pp. 213–216, 2014.

[77] P. M. Gosavi, Y. S. Moroz, and I. V. Korendovych, "beta-(1-Azulenyl)-L-alanine - a functional probe for determination of pKa of histidine residues," *Chemical Communications*, vol. 51, no. 25, pp. 5347–5350, 2015.

[78] H. M. Müller-Werkmeister, *Unnatural Amino Acids as Novel Probes for Ultrafast 2D-IR Spectroscopy of Proteins*. Dissertation, Goethe University, Frankfurt, 2014.

[79] R. Adhikary, J. Zimmermann, and F. E. Romesberg, "Transparent Window Vibrational Probes for the Characterization of Proteins With High Structural and Temporal Resolution," *Chemical Reviews*, vol. 117, no. 3, pp. 1927–1969, 2017.

[80] C. Berthomieu and R. Hienerwadel, "Fourier transform infrared (FTIR) spectroscopy," *Photosynthesis Research*, vol. 101, no. 2-3, pp. 157–170, 2009.

[81] M. D. Fayer, ed., *An Introduction to Protein 2D IR Spectroscopy: Ch. 12 in Ultrafast Infrared Vibrational Spectroscopy*. New York: Taylor&Francis, 2013.

[82] K. Kwak, S. Park, I. J. Finkelstein, and M. D. Fayer, "Frequency-frequency correlation functions and apodization in two-dimensional infrared vibrational echo spectroscopy: a new approach," *The Journal of Chemical Physics*, vol. 127, no. 12, p. 124503, 2007.

[83] P. Hamm and M. T. Zanni, *Concepts and Methods of 2D Infrared Spectroscopy*. Cambridge: Cambridge University Press, 2011.

[84] K. L. Koziol, P. J. M. Johnson, B. Stucki-Buchli, S. A. Waldauer, and P. Hamm, "Fast infrared spectroscopy of protein dynamics: advancing sensitivity and selectivity," *Current Opinion in Structural Biology*, vol. 34, pp. 1–6, 2015.

[85] I. T. Suydam and S. G. Boxer, "Vibrational Stark effects calibrate the sensitivity of vibrational probes for electric fields in proteins," *Biochemistry*, vol. 42, no. 41, pp. 12050–12055, 2003.

[86] M. M. Waegele, R. M. Culik, and F. Gai, "Site-Specific Spectroscopic Reporters of the Local Electric Field, Hydration, Structure, and Dynamics of Biomolecules," *The Journal of Physical Chemistry Letters*, vol. 2, pp. 2598–2609, 2011.

[87] B. A. Lindquist, K. E. Furse, and S. A. Corcelli, "Nitrile groups as vibrational probes of biomolecular structure and dynamics: an overview," *Physical Chemistry Chemical Physics*, vol. 11, no. 37, pp. 8119–8132, 2009.

[88] H. Kim and M. Cho, "Infrared probes for studying the structure and dynamics of biomolecules," *Chemical Reviews*, vol. 113, no. 8, pp. 5817–5847, 2013.

[89] J. Ma, I. M. Pazos, W. Zhang, R. M. Culik, and F. Gai, "Site-Specific Infrared Probes of Proteins," *Annual Review of Physical Chemistry*, vol. 66, no. 1, pp. 357–377, 2015.

[90] X. S. Gai, E. E. Fenlon, and S. H. Brewer, "A Sensitive Multispectroscopic Probe for Nucleic Acids," *The Journal of Physical Chemistry B*, vol. 114, no. 23, pp. 7958–7966, 2010.

[91] R. Bloem, K. Koziol, S. A. Waldauer, B. Buchli, R. Walser, B. Samatanga, I. Jelesarov, and P. Hamm, "Ligand Binding Studied by 2D IR Spectroscopy Using the Azidohomoalanine Label," *The Journal of Physical Chemistry B*, vol. 116, no. 46, pp. 13705–13712, 2012.

[92] S. Ye, T. Huber, R. Vogel, and T. P. Sakmar, "FTIR analysis of GPCR activation using azido probes," *Nature Chemical Biology*, vol. 5, no. 6, pp. 397–399, 2009.

[93] D. D. Young, T. S. Young, M. Jahnz, I. Ahmad, G. Spraggon, and P. G. Schultz, "An evolved aminoacyl-tRNA synthetase with atypical polysubstrate specificity," *Biochemistry*, vol. 50, no. 11, pp. 1894–1900, 2011.

[94] M. C. Thielges, J. Y. Axup, D. Wong, H. S. Lee, J. K. Chung, P. G. Schultz, and M. D. Fayer, "Two-Dimensional IR Spectroscopy of Protein Dynamics Using Two Vibrational Labels: A Site-Specific Genetically Encoded Unnatural Amino Acid and an Active Site Ligand," *The Journal of Physical Chemistry B*, vol. 115, no. 38, pp. 11294–11304, 2011.

[95] E. M. Tookmanian, E. E. Fenlon, and S. H. Brewer, "Synthesis and Protein Incorporation of Azido-Modified Unnatural Amino Acids," *RSC Advances*, vol. 5, no. 2, pp. 1274–1281, 2015.

[96] A. Creon, I. Josts, S. Niebling, N. Huse, and H. Tidow, "Conformation-specific detection of calmodulin binding using the unnatural amino acid p-azidophenylalanine (AzF) as an IR-sensor," *Structural Dynamics*, vol. 5, no. 6, p. 064701, 2018.

[97] C. G. Bazewicz, M. T. Liskov, K. J. Hines, and S. H. Brewer, "Sensitive, site-specific, and stable vibrational probe of local protein environments: 4-azidomethyl-L-phenylalanine," *The Journal of Physical Chemistry B*, vol. 117, no. 30, pp. 8987–8993, 2013.

[98] E. M. Tookmanian, C. M. Phillips-Piro, E. E. Fenlon, and S. H. Brewer, "Azidoethoxyphenylalanine as a Vibrational Reporter and Click Chemistry Partner in Proteins," *Chemistry*, vol. 21, no. 52, pp. 19096–19103, 2015.

[99] S. Ye, E. Zaitseva, G. Caltabiano, G. F. X. Schertler, T. P. Sakmar, X. Deupi, and R. Vogel, "Tracking G-protein-coupled receptor activation using genetically encoded infrared probes," *Nature*, vol. 464, no. 7293, pp. 1386–1389, 2010.

[100] H. Taskent-Sezgin, J. Chung, P. S. Banerjee, S. Nagarajan, R. B. Dyer, I. Carrico, and D. P. Raleigh, "Azidohomoalanine: A Conformationally Sensitive IR Probe of Protein Folding, Protein Structure, and Electrostatics," *Angewandte Chemie (International ed. in English)*, vol. 49, no. 41, pp. 7473–7475, 2010.

[101] S. Nagarajan, H. Taskent-Sezgin, D. Parul, I. Carrico, D. P. Raleigh, and R. B. Dyer, "Differential ordering of the protein backbone and side chains during protein folding revealed by site-specific recombinant infrared probes," *Journal of the American Chemical Society*, vol. 133, no. 50, pp. 20335–20340, 2011.

[102] B. Stucki-Buchli, P. J. M. Johnson, O. Bozovic, C. Zanobini, K. L. Koziol, P. Hamm, A. Gulzar, S. Wolf, S. Buchenberg, and G. Stock, "2D-IR Spectroscopy of an AHA Labeled Photoswitchable PDZ2 Domain," *The Journal of Physical Chemistry A*, vol. 121, no. 49, pp. 9435–9445, 2017.

[103] C. Zanobini, O. Bozovic, B. Jankovic, K. L. Koziol, P. J. M. Johnson, P. Hamm, A. Gulzar, S. Wolf, and G. Stock, "Azidohomoalanine: A Minimally Invasive, Versatile, and Sensitive Infrared Label in Proteins To Study Ligand Binding," *The Journal of Physical Chemistry B*, vol. 122, no. 44, pp. 10118–10125, 2018.

[104] F. Lehner, D. Kudlinzki, C. Richter, H. M. Müller-Werkmeister, K. B. Eberl, J. Bredenbeck, H. Schwalbe, and R. Silvers, "Impact of Azidohomoalanine Incorporation on Protein Structure and Ligand Binding," *ChemBioChem*, vol. 18, no. 23, pp. 2340–2350, 2017.

[105] T. Baumann, M. Hauf, F. Schildhauer, K. B. Eberl, P. M. Durkin, E. Deniz, J. G. Löffler, C. G. Acevedo-Rocha, J. Jaric, B. M. Martins, H. Dobbek, J. Bredenbeck, and N. Budisa, "Site-Resolved Observation of Vibrational Energy Transfer Using a Genetically Encoded Ultrafast Heater," *Angewandte Chemie (International ed. in English)*, vol. 58, no. 9, pp. 2899–2903, 2019.

[106] R. Adhikary, J. Zimmermann, P. E. Dawson, and F. E. Romesberg, "IR probes of protein microenvironments: utility and potential for perturbation," *ChemPhysChem*, vol. 15, no. 5, pp. 849–853, 2014.

[107] P. J. M. Johnson, K. L. Koziol, and P. Hamm, "Quantifying Biomolecular Recognition with Site-Specific 2D Infrared Probes," *The Journal of Physical Chemistry Letters*, vol. 8, no. 10, pp. 2280–2284, 2017.

[108] K. L. Kiick, E. Saxon, D. A. Tirrell, and C. R. Bertozzi, "Incorporation of azides into recombinant proteins for chemoselective modification by the Staudinger ligation," *PNAS*, vol. 1, no. 99, pp. 19–24, 2002.

[109] C. Nourry, S. G. N. Grant, and J.-P. Borg, "PDZ Domain Proteins_Plug and Play," *Science's STKE*, no. 179, pp. 1–12, 2003.

[110] B. Z. Harris and W. A. Lim, "Mechanism and role of PDZ domains in signaling complex assembly," *Journal of Cell Science*, no. 114, pp. 3219–3231, 2001.

[111] G. Steiner and E. Koch, "Trends in Fourier transform infrared spectroscopic imaging," *Analytical and Bioanalytical Chemistry*, vol. 394, no. 3, pp. 671–678, 2009.

[112] A. Barth and C. Zscherp, "What vibrations tell about proteins," *Quarterly Reviews of Biophysics*, vol. 35, no. 4, pp. 369–430, 2002.

[113] R. Winter and F. Noll, *Methoden der Biophysikalischen Chemie*. Teubner Studienbücher: Chemie, 1998.

[114] Y. S. Kim and R. M. Hochstrasser, "Applications of 2D IR Spectroscopy to Peptides, Proteins, and Hydrogen-Bond Dynamics," *The Journal of Physical Chemistry B*, vol. 113, no. 24, pp. 8231–8251, 2009.

[115] W. Mäntele, *Biophysik*. Stuttgart: Eugen Ulmer KG, 2012.

[116] J. L. Koenig, "Fourier Transform Infrared Spectroscopy of Chemical Systems," *Accounts of Chemical Research*, vol. 1981, no. 14, pp. 171–178, 1981.

[117] C. Jung, "Insight into protein structure and protein-ligand recognition by Fourier transform infrared spectroscopy," *Journal of Molecular Recognition*, vol. 13, no. 6, pp. 325–351, 2000.

[118] A. Barth, "The infrared absorption of amino acid side chains," *Progress in Biophysics & Molecular Biology*, vol. 2000, no. 74, pp. 141–173, 2000.

[119] M. Wolpert and P. Hellwig, "Infrared spectra and molar absorption coefficients of the 20 alpha amino acids in aqueous solutions in the spectral range from 1800 to 500 cm(-1)," *Spectrochimica Acta Part A*, vol. 64, no. 4, pp. 987–1001, 2006.

[120] A. Morita and S. Kato, "Vibrational relaxation of azide ion in water: The role of intramolecular charge fluctuation and solvent-induced vibrational coupling," *The Journal of Chemical Physics*, vol. 109, no. 13, pp. 5511–5523, 1998.

[121] M. Di Donato, L. J. G. W. van Wilderen, I. H. M. van Stokkum, T. C. Stuart, J. T. M. Kennis, K. J. Hellingwerf, R. van Grondelle, and M. L. Groot, "Proton transfer events in GFP," *Physical Chemistry Chemical Physics*, vol. 13, no. 36, pp. 16295–16305, 2011.

[122] J. Helbing, "Spin state transitions upon visible and infrared excitation of ferric MbN3," *Chemical Physics*, vol. 396, pp. 17–22, 2012.

[123] L. J. G. W. van Wilderen and J. Bredenbeck, "From Ultrafast Structure Determination to Steering Reactions: Mixed IR/Non-IR Multidimensional Vibrational Spectroscopies," *Angewandte Chemie (International ed. in English)*, vol. 54, no. 40, pp. 11624–11640, 2015.

[124] J. Bredenbeck, J. Helbing, C. Kolano, and P. Hamm, "Ultrafast 2D-IR spectroscopy of transient species," *ChemPhysChem*, vol. 8, no. 12, pp. 1747–1756, 2007.

[125] V. Cervetto, J. Helbing, J. Bredenbeck, and P. Hamm, "Double-resonance versus pulsed Fourier transform two-dimensional infrared spectroscopy: an experimental and theoretical comparison," *The Journal of Chemical Physics*, vol. 121, no. 12, pp. 5935–5942, 2004.

[126] M. J. Tucker, X. S. Gai, E. E. Fenlon, S. H. Brewer, and R. M. Hochstrasser, "2D IRphoton echo of azido-probes for biomolecular dynamics," *Physical Chemistry Chemical Physics*, vol. 13, no. 6, pp. 2237–2241, 2011.

[127] P. Hamm, M. Lim, and R. M. Hochstrasser, "Structure of the Amide I Band of Peptides Measured by Femtosecond Nonlinear-Infrared Spectroscopy," *The Journal of Physical Chemistry B*, vol. 102, no. 31, pp. 6123–6138, 1998.

[128] S. Li, J. R. Schmidt, and J. L. Skinner, "Vibrational energy relaxation of azide in water," *The Journal of Chemical Physics*, vol. 125, no. 24, p. 244507, 2006.

[129] X. Dong, S. Wang, P. Yu, F. Yang, J. Zhao, L.-Z. Wu, C.-H. Tung, and J. Wang, "Ultrafast Vibrational Energy Transfer through the Covalent Bond and Intra- and Intermolecular Hydrogen Bonds in a Supramolecular Dimer by Two-Dimensional Infrared Spectroscopy," *The Journal of Physical Chemistry B*, vol. 124, no. 3, pp. 544–555, 2020.

[130] L. V. Borau, A. Gulzar, and G. Stock, "Master equation model to predict energy transport pathways in proteins," *The Journal of Chemical Physics*, vol. 152, no. 4, p. 045103, 2020.

[131] T. Ishikura and T. Yamato, "Energy transfer pathways relevant for long-range intramolecular signaling of photosensory protein revealed by microscopic energy conductivity analysis," *Chemical Physics Letters*, vol. 432, no. 4-6, pp. 533–537, 2006.

[132] M. Schade and P. Hamm, "Vibrational energy transport in the presence of intrasite vibrational energy redistribution," *The Journal of Chemical Physics*, vol. 131, no. 4, p. 044511, 2009.

[133] M. Kobus, P. H. Nguyen, and G. Stock, "Coherent vibrational energy transfer along a peptide helix," *The Journal of Chemical Physics*, vol. 134, no. 12, p. 124518, 2011.

[134] M. Schade and P. Hamm, "Transition from IVR limited vibrational energy transport to bulk heat transport," *Chemical Physics*, vol. 393, no. 1, pp. 46–50, 2012.

[135] S. L. Tesar, V. M. Kasyanenko, I. V. Rubtsov, G. I. Rubtsov, and A. L. Burin, "Theoretical Study of Internal Vibrational Relaxation and Energy Transport in Polyatomic Molecules," *The Journal of Physical Chemistry A*, vol. 117, no. 2, pp. 315–323, 2013.

[136] J. K. Agbo, R. Gnanasekaran, and D. M. Leitner, "Communication Maps: Exploring Energy Transport through Proteins and Water," *Israel Journal of Chemistry*, vol. 54, no. 8-9, pp. 1065–1073, 2014.

[137] Y. Xu and D. M. Leitner, "Vibrational Energy Flow through the Green Fluorescent Protein–Water Interface: Communication Maps and Thermal Boundary Conductance," *The Journal of Physical Chemistry B*, vol. 118, no. 28, pp. 7818–7826, 2014.

[138] N. Budisa, "Prolegomena to future experimental efforts on genetic code engineering by expanding its amino acid repertoire," *Angewandte Chemie (International ed. in English)*, vol. 43, no. 47, pp. 6426–6463, 2004.

[139] L. Wang and P. G. Schultz, "Expanding the genetic code," *Angewandte Chemie (International ed. in English)*, vol. 44, no. 1, pp. 34–66, 2005.

[140] C. C. Liu and P. G. Schultz, "Adding new chemistries to the genetic code," *Annual Review of Biochemistry*, vol. 79, pp. 413–444, 2010.

[141] F. Wang, W. Niu, J. Guo, and P. G. Schultz, "Unnatural Amino Acid Mutagenesis of Fluorescent Proteins," *Angewandte Chemie International Edition*, vol. 124, no. 40, pp. 10279–10282, 2012.

[142] L. Blankenburg, L. Schroeder, F. Habenstein, B. Błasiak, T. Kottke, and J. Bredenbeck, "Following local light-induced structure changes and dynamics of the photoreceptor PYP with the thiocyanate IR label," *Physical Chemistry Chemical Physics*, vol. 21, no. 12, pp. 6622–6634, 2019.

[143] T. S. Young and P. G. Schultz, "Beyond the canonical 20 amino acids: expanding the genetic lexicon," *The Journal of Biological Chemistry*, vol. 285, no. 15, pp. 11039–11044, 2010.

[144] P. M. Gosavi and I. V. Korendovych, "Minimalist IR and fluorescence probes of protein function," *Current Opinion in Chemical Biology*, vol. 34, pp. 103–109, 2016.

[145] L. Wang and P. G. Schultz, "A general approach for the generation of orthogonal tRNAs," *Chemistry & Biology*, no. 8, pp. 883–890, 2001.

[146] K. Kirshenbaum, I. S. Carrico, and D. A. Tirrell, "Biosynthesis of Proteins Incorporating a Versatile Set of Phenylalanine Analogues," *ChemBioChem*, vol. 2002, no. 02-03, pp. 235–237, 2002.

[147] K.-I. Oh, J.-H. Lee, C. Joo, H. Han, and M. Cho, "Beta-azidoalanine as an IR probe: application to amyloid Abeta(16-22) aggregation," *The Journal of Physical Chemistry B*, vol. 112, no. 33, pp. 10352–10357, 2008.

[148] K. N. Alfieri, A. R. Vienneau, and C. H. Londergan, "Using infrared spectroscopy of cyanylated cysteine to map the membrane binding structure and orientation of the hybrid antimicrobial peptide CM15," *Biochemistry*, vol. 50, no. 51, pp. 11097–11108, 2011.

[149] A. T. Fafarman, P. A. Sigala, J. P. Schwans, T. D. Fenn, D. Herschlag, and S. G. Boxer, "Quantitative, directional measurement of electric field heterogeneity in the active site of ketosteroid isomerase," *PNAS*, vol. 109, no. 6, pp. E299–308, 2012.

[150] A. J. Stafford, D. L. Ensign, and L. J. Webb, "Vibrational Stark effect spectroscopy at the interface of Ras and Rap1A bound to the Ras binding domain of RalGDS reveals an electrostatic mechanism for protein-protein interaction," *The Journal of Physical Chemistry B*, vol. 114, no. 46, pp. 15331–15344, 2010.

[151] C. G. Bischak, S. Longhi, D. M. Snead, S. Costanzo, E. Terrer, and C. H. Londergan, "Probing structural transitions in the intrinsically disordered C-terminal domain of the measles virus nucleoprotein by vibrational spectroscopy of cyanylated cysteines," *Biophysical Journal*, vol. 99, no. 5, pp. 1676–1683, 2010.

[152] H. Taskent-Sezgin, J. Chung, V. Patsalo, S. J. Miyake-Stoner, A. M. Miller, S. H. Brewer, R. A. Mehl, D. F. Green, D. P. Raleigh, and I. Carrico, "Interpretation of p-cyanophenylalanine fluorescence in proteins in terms of solvent exposure and contribution of side-chain quenchers: a combined fluorescence, IR and molecular dynamics study," *Biochemistry*, vol. 48, no. 38, pp. 9040–9046, 2009.

[153] S. Bagchi, S. G. Boxer, and M. D. Fayer, "Ribonuclease S dynamics measured using a nitrile label with 2D IR vibrational echo spectroscopy," *The Journal of Physical Chemistry B*, vol. 116, no. 13, pp. 4034–4042, 2012.

[154] D. C. Urbanek, D. Y. Vorobyev, A. L. Serrano, F. Gai, and R. M. Hochstrasser, "The Two Dimensional Vibrational Echo of a Nitrile Probe of the Villin HP35 Protein," *The Journal of Physical Chemistry Letters*, vol. 1, pp. 3311–3315, 2010.

[155] M. J. Tucker, Z. Getahun, V. Nanda, W. F. DeGrado, and F. Gai, "A new method for determining the local environment and orientation of individual side chains of membrane-binding peptides," *Journal of the American Chemical Society*, vol. 126, no. 16, pp. 5078–5079, 2004.

[156] W. Hu and L. J. Webb, "Direct Measurement of the Membrane Dipole Field in Bicelles Using Vibrational Stark Effect Spectroscopy," *The Journal of Physical Chemistry Letters*, vol. 2, no. 15, pp. 1925–1930, 2011.

[157] S. Mukherjee, P. Chowdhury, W. F. DeGrado, and F. Gai, "Site-specific hydration status of an amphipathic peptide in AOT reverse micelles," *Langmuir*, vol. 23, no. 22, pp. 11174–11179, 2007.

[158] A. T. Fafarman, L. J. Webb, J. I. Chuang, and S. G. Boxer, "Site-specific conversion of cysteine thiols into thiocyanate creates an IR probe for electric fields in proteins," *Journal of the American Chemical Society*, vol. 128, no. 41, pp. 13356–13357, 2006.

[159] A. T. Fafarman, P. A. Sigala, D. Herschlag, and S. G. Boxer, "Decomposition of vibrational shifts of nitriles into electrostatic and hydrogen-bonding effects,"

Journal of the American Chemical Society, vol. 132, no. 37, pp. 12811–12813, 2010.

[160] Z. Getahun, C.-Y. Huang, T. Wang, B. de León, W. F. DeGrado, and F. Gai, "Using nitrile-derivatized amino acids as infrared probes of local environment," *Journal of the American Chemical Society*, vol. 125, no. 2, pp. 405–411, 2003.

[161] J. T. First, J. D. Slocum, and L. J. Webb, "Quantifying the Effects of Hydrogen Bonding on Nitrile Frequencies in GFP: Beyond Solvent Exposure," *The Journal of Physical Chemistry B*, vol. 122, no. 26, pp. 6733–6743, 2018.

[162] L. J. G. W. van Wilderen, H. Brunst, H. Gustmann, J. Wachtveitl, J. Broos, and J. Bredenbeck, "Cyano-tryptophans as dual infrared and fluorescence spectroscopic labels to assess structural dynamics in proteins," *Physical Chemistry Chemical Physics*, vol. 20, no. 30, pp. 19906–19915, 2018.

[163] H. A. McMahon, K. N. Alfieri, K. A. A. Clark, and C. H. Londergan, "Cyanylated Cysteine: A Covalently Attached Vibrational Probe of Protein-Lipid Contacts," *The Journal of Physical Chemistry Letters*, vol. 1, no. 5, pp. 850–855, 2010.

[164] J. M. Schmidt-Engler, L. Blankenburg, B. Błasiak, L. J. G. W. van Wilderen, M. Cho, and J. Bredenbeck, "Vibrational Lifetime of the SCN Protein Label in H2O and D2O Reports Site-Specific Solvation and Structure Changes During PYP's Photocycle," *Analytical Chemistry*, vol. 92, no. 1, pp. 1024–1032, 2020.

[165] J. M. Schmidt-Engler, R. Zangl, P. Guldan, N. Morgner, and J. Bredenbeck, "Exploring the 2D-IR Repertoire of the -SCN Label to Study Site-Resolved Dynamics and Solvation in the Calcium Sensor Protein Calmodulin," *Physical Chemistry Chemical Physics*, pp. 1–12, 2020.

[166] L. J. G. W. van Wilderen, D. Kern-Michler, H. M. Müller-Werkmeister, and J. Bredenbeck, "Vibrational dynamics and solvatochromism of the label SCN in various solvents and hemoglobin by time dependent IR and 2D-IR spectroscopy," *Physical Chemistry Chemical Physics*, vol. 16, no. 36, pp. 19643–19653, 2014.

[167] Z. Ma, D. M. Cowart, B. P. Ward, R. J. Arnold, R. D. DiMarchi, L. Zhang, G. N. George, R. A. Scott, and D. P. Giedroc, "Unnatural amino acid substitution as a probe of the allosteric coupling pathway in a mycobacterial Cu(I) sensor," *Journal of the American Chemical Society*, vol. 131, no. 50, pp. 18044–18045, 2009.

[168] X. S. Gai, B. A. Coutifaris, S. H. Brewer, and E. E. Fenlon, "A direct comparison of azide and nitrile vibrational probes," *Physical Chemistry Chemical Physics*, vol. 13, no. 13, pp. 5926–5930, 2011.

[169] I. Peran, T. Oudenhoven, A. M. Woys, M. D. Watson, T. O. Zhang, I. Carrico, M. T. Zanni, and D. P. Raleigh, "General Strategy for the Bioorthogonal Incorporation of Strongly Absorbing, Solvation-Sensitive Infrared Probes into Proteins," *The Journal of Physical Chemistry B*, vol. 118, no. 28, pp. 7946–7953, 2014.

[170] C. R. Hall, J. Tolentino Collado, J. N. Iuliano, A. A. Gil, K. Adamczyk, A. Lukacs, G. M. Greetham, I. Sazanovich, P. J. Tonge, and S. R. Meech, "Site-Specific Protein Dynamics Probed by Ultrafast Infrared Spectroscopy of a Noncanonical Amino Acid," *The Journal of Physical Chemistry B*, vol. 123, no. 45, pp. 9592–9597, 2019.

[171] K.-K. Lee, K.-H. Park, C. Joo, H.-J. Kwon, J. Jeon, H.-I. Jung, S. Park, H. Han, and M. Cho, "Infrared probing of 4-azidoproline conformations modulated by azido configurations," *The Journal of Physical Chemistry B*, vol. 116, no. 17, pp. 5097–5110, 2012.

[172] K.-I. Oh, W. Kim, C. Joo, D.-G. Yoo, H. Han, G.-S. Hwang, and M. Cho, "Azido gauche effect on the backbone conformation of β-azidoalanine peptides," *The Journal of Physical Chemistry B*, vol. 114, no. 40, pp. 13021–13029, 2010.

[173] M. W. Nydegger, S. Dutta, and C. M. Cheatum, "Two-dimensional infrared study of 3-azidopyridine as a potential spectroscopic reporter of protonation state," *The Journal of Chemical Physics*, vol. 133, no. 13, p. 134506, 2010.

[174] J. Zhang, L. Wang, J. Zhang, J. Zhu, X. Pan, Z. Cui, J. Wang, W. Fang, and Y. Li, "Identifying and Modulating Accidental Fermi Resonance: 2D IR and DFT Study of 4-Azido-l-phenylalanine," *The Journal of Physical Chemistry B*, vol. 122, no. 34, pp. 8122–8133, 2018.

[175] J. S. Lipkin, R. Song, E. E. Fenlon, and S. H. Brewer, "Modulating Accidental Fermi Resonance: What a Difference a Neutron Makes," *The Journal of Physical Chemistry Letters*, vol. 2, no. 14, pp. 1672–1676, 2011.

[176] J.-H. Choi, K.-I. Oh, and M. Cho, "Azido-derivatized compounds as IR probes of local electrostatic environment: Theoretical studies," *The Journal of Chemical Physics*, vol. 129, no. 17, p. 174512, 2008.

[177] J.-H. Choi and M. Cho, "Vibrational solvatochromism and electrochromism of infrared probe molecules containing C≡O, C≡N, C=O, or C−F vibrational chromophore," *The Journal of Chemical Physics*, vol. 134, no. 15, p. 154513, 2011.

[178] A. Wang, N. Winblade Nairn, R. S. Johnson, D. A. Tirrell, and K. Grabstein, "Processing of N-terminal unnatural amino acids in recombinant human interferon-beta in Escherichia coli," *ChemBioChem*, vol. 9, no. 2, pp. 324–330, 2008.

[179] G. U. Bublitz and S. G. Boxer, "STARK SPECTROSCOPY: Applications in Chemistry, Biology, and Materials Science," *Annual Review of Physical Chemistry*, no. 48, pp. 213–242, 1997.

[180] A. Chattopadhyay and S. G. Boxer, "Vibrational Stark Effect Spectroscopy," *Journal of the American Chemical Society*, no. 117, pp. 1449–1450, 1995.

[181] S. S. Andrews and S. G. Boxer, "Vibrational Stark Effects of Nitriles I. Methods and Experimental Results," *The Journal of Physical Chemistry A*, vol. 104, no. 51, pp. 11853–11863, 2000.

[182] J.-H. Choi, D. Raleigh, and M. Cho, "Azido Homoalanine is a Useful Infrared Probe for Monitoring Local Electrostatistics and Side-Chain Solvation in Proteins," *The Journal of Physical Chemistry Letters*, vol. 2, no. 17, pp. 2158–2162, 2011.

[183] N. M. Levinson, S. D. Fried, and S. G. Boxer, "Solvent-Induced Infrared Frequency Shifts in Aromatic Nitriles Are Quantitatively Described by the Vibrational Stark Effect," *The Journal of Physical Chemistry B*, vol. 116, no. 35, pp. 10470–10476, 2012.

[184] M. P. Wolfshorndl, R. Baskin, I. Dhawan, and C. H. Londergan, "Covalently Bound Azido Groups Are Very Specific Water Sensors, Even in Hydrogen-Bonding Environments," *The Journal of Physical Chemistry B*, vol. 116, no. 3, pp. 1172–1179, 2012.

[185] M. Koziński, S. Garrett-Roe, and P. Hamm, "2D-IR spectroscopy of the sulfhydryl band of cysteines in the hydrophobic core of proteins," *The Journal of Physical Chemistry B*, vol. 112, no. 25, pp. 7645–7650, 2008.

[186] C. Fang, J. D. Bauman, K. Das, A. Remorino, E. Arnold, and R. M. Hochstrasser, "Two-dimensional infrared spectra reveal relaxation of the nonnucleoside inhibitor TMC278 complexed with HIV-1 reverse transcriptase," *PNAS*, no. 105, pp. 1472–1477, 2008.

[187] L. J. G. W. van Wilderen, C. N. Lincoln, and J. J. van Thor, "Modelling multipulse population dynamics from ultrafast spectroscopy," *PloS ONE*, vol. 6, no. 3, p. e17373, 2011.

[188] M. Okuda, K. Ohta, and K. Tominaga, "Vibrational dynamics of azide-derivatized amino acids studied by nonlinear infrared spectroscopy," *The Journal of Chemical Physics*, vol. 142, no. 21, p. 212418, 2015.

[189] M. Matěnová, V. L. Horhoiu, F.-X. Dang, P. Pospíšil, J. Alster, J. V. Burda, T. S. Balaban, and J. Pšenčík, "Energy transfer in aggregates of bacteriochlorophyll c self-assembled with azulene derivatives," *Physical Chemistry Chemical Physics*, vol. 16, no. 31, pp. 16755–16764, 2014.

[190] G. Loidl, H.-J. Musiol, N. Budisa, R. Huber, S. Poirot, D. Fourmy, and L. Moroder, "Synthesis of [beta]-(1-azulenyl)-L-alanine as a potential blue-colored fluorescent tryptophan analog and its use in peptide synthesis," *Journal of Peptide Science*, vol. 6, no. 3, pp. 139–144, 2000.

[191] T. Itoh, "Fluorescence and phosphorescence from higher excited states of organic molecules," *Chemical Reviews*, vol. 112, no. 8, pp. 4541–4568, 2012.

[192] T. Yamaguchi, Y. Kimura, and N. Hirota, "Vibrational energy relaxation of azulene in the S2 state. I. Solvent species dependence," *The Journal of Chemical Physics*, vol. 113, no. 7, pp. 2772–2783, 2000.

[193] E. P. Ippen, C. V. Shank, and R. L. Woerner, "Picosecond dynamics of azulene," *Chemical Physics Letters*, no. 46, pp. 20–23, 1977.

[194] Y. S. Moroz, W. Binder, P. Nygren, G. A. Caputo, and I. V. Korendovych, "Painting proteins blue: β-(1-azulenyl)-l-alanine as a probe for studying protein–protein interactions," *Chemical Communication*, vol. 49, no. 5, pp. 490–492, 2013.

[195] H.-J. Lee and J. J. Zheng, "PDZ domains and their binding partners: structure, specificity, and modification," *Cell Communication and Signaling*, vol. 8, pp. 1–18, 2010.

[196] T. Beuming, R. Farid, and W. Sherman, "High-energy water sites determine peptide binding affinity and specificity of PDZ domains," *Protein Science*, vol. 18, no. 8, pp. 1609–1619, 2009.

[197] M. van Ham and W. Hendriks, "PDZ domains - glue and guide," *Molecular Biology Reports*, no. 30, pp. 69–82, 2003.

[198] C. N. Chi, S. R. Haq, S. Rinaldo, J. Dogan, F. Cutruzzolà, Å. Engström, S. Gianni, P. Lundström, and P. Jemth, "Interactions outside the boundaries of the canonical binding groove of a PDZ domain influence ligand binding," *Biochemistry*, vol. 51, no. 44, pp. 8971–8979, 2012.

[199] P. Jemth and S. Gianni, "PDZ domains: folding and binding," *Biochemistry*, vol. 46, no. 30, pp. 8701–8708, 2007.

[200] G. Meyer, F. Varoqueaux, A. Neeb, M. Oschlies, and N. Brose, "The complexity of PDZ domain-mediated interactions at glutamatergic synapses: a case study on neuroligin," *Neuropharmacology*, vol. 47, no. 5, pp. 724–733, 2004.

[201] I. S. Yanez Orozco, F. A. Mindlin, J. Ma, B. Wang, B. Levesque, M. Spencer, S. Rezaei Adariani, G. Hamilton, F. Ding, M. E. Bowen, and H. Sanabria, "Identifying weak interdomain interactions that stabilize the supertertiary structure of the N-terminal tandem PDZ domains of PSD-95," *Nature Communications*, vol. 9, no. 1, p. 3724, 2018.

[202] Y. Qian and K. E. Prehoda, "INTERDOMAIN INTERACTIONS IN THE TUMOR SUPPRESSOR DISCS LARGE REGULATE BINDING TO THE SYNAPTIC PROTEIN GUKHOLDER," *Journal of Biological Chemistry*, no. 281, pp. 35757–35763, 2006.

[203] J. E. Brenman, R. J. Topinka, E. C. Cooper, A. W. McGee, J. Rosen, T. Milroy, H. J. Ralston, and D. S. Bredt, "Localization of Postsynaptic Density-93 to Dendritic Microtubules and Interaction with Microtubule-Associated Protein 1A," *The Journal of Neuroscience*, no. 18, pp. 8805–8813, 1998.

[204] L. C. J. van den Berk, E. Landi, T. Walma, G. W. Vuister, L. Dente, and W. J. A. J. Hendriks, "An allosteric intramolecular PDZ-PDZ interaction modulates PTP-BL PDZ2 binding specificity," *Biochemistry*, vol. 46, no. 47, pp. 13629–13637, 2007.

[205] G. Stock and P. Hamm, "A non-equilibrium approach to allosteric communication," *Philosophical Transactions B*, vol. 373, no. 1749, p. 20170187, 2018.

[206] Y. Li, J. Hu, K. Höfer, A. M. S. Wong, J. D. Cooper, S. G. Birnbaum, R. E. Hammer, and S. L. Hofmann, "DHHC5 interacts with PDZ domain 3 of postsynaptic density-95 (PSD-95) protein and plays a role in learning and memory," *The Journal of Biological Chemistry*, vol. 285, no. 17, pp. 13022–13031, 2010.

[207] J. H. Kim, D. Liao, L.-F. Lau, and R. L. Huganir, "SynGAP: a synaptic RasGAP that associates with the PSD-95/SAP90 protein family," *Neuron*, no. 20, pp. 683–691, 1998.

[208] A. Toto, S. W. Pedersen, O. A. Karlsson, G. E. Moran, E. Andersson, C. N. Chi, K. Strømgaard, S. Gianni, and P. Jemth, "Ligand binding to the PDZ domains of postsynaptic density protein 95," *Protein Engineering, Design & Selection*, vol. 29, no. 5, pp. 169–175, 2016.

[209] M. Irie, Y. Hata, M. Takeuchin, K. Ichtchenko, A. Toyoda, K. Hirao, Y. Takai, T. W. Rosahl, and T. C. Südhof, "Binding of neuroligins to PSD-95," *Science*, no. 277, pp. 1511–1515, 1997.

[210] D. A. Doyle, A. Lee, J. Lewis, E. Kim, M. Sheng, and R. MacKinnon, "Crystal Structures of a Complexed and Peptide-Free Membrane Protein–Binding Domain: Molecular Basis of Peptide Recognition by PDZ," *Cell*, vol. 85, no. 7, pp. 1067–1076, 1996.

[211] M. Niethammer, J. G. Valtschanoff, T. M. Kapoor, D. W. Allison, R. J. Weinberg, A. M. Craig, and M. Sheng, "CRIPT a novel postsynaptic protein that binds to the third PDZ domain of PSD-95/SAP90," *Neuron*, no. 20, pp. 693–707, 1998.

[212] W. Zhang, L. Vazquez, M. Apperson, and M. B. Kennedy, "Citron binds to PSD-95 at glutamatergic synapses on inhibitory neurons in the hippocampus," *The Journal of Neuroscience*, no. 19, pp. 96–108, 1999.

[213] M. Russwurm, N. Wittau, and D. Koesling, "Guanylyl cyclase/PSD-95 interaction: targeting of the nitric oxide-sensitive alpha2beta1 guanylyl cyclase to synaptic membranes," *The Journal of Biological Chemistry*, vol. 276, no. 48, pp. 44647–44652, 2001.

[214] D. Saro, T. Li, C. Rupasinghe, A. Paredes, N. Caspers, and M. R. Spaller, "A thermodynamic ligand binding study of the third PDZ domain (PDZ3) from the mammalian neuronal protein PSD-95," *Biochemistry*, vol. 46, no. 21, pp. 6340–6352, 2007.

[215] S. Gianni, A. Engström, M. Larsson, N. Calosci, F. Malatesta, L. Eklund, C. C. Ngang, C. Travaglini-Allocatelli, and P. Jemth, "The kinetics of PDZ domain-ligand interactions and implications for the binding mechanism," *The Journal of Biological Chemistry*, vol. 280, no. 41, pp. 34805–34812, 2005.

[216] S. Gianni, T. Walma, A. Arcovito, N. Calosci, A. Bellelli, A. Engström, C. Travaglini-Allocatelli, M. Brunori, P. Jemth, and G. W. Vuister, "Demonstration of long-range interactions in a PDZ domain by NMR, kinetics, and protein engineering," *Structure*, vol. 14, no. 12, pp. 1801–1809, 2006.

[217] C. N. Chi, A. Bach, A. Engström, H. Wang, K. Strømgaard, S. Gianni, and P. Jemth, "A sequential binding mechanism in a PDZ domain," *Biochemistry*, vol. 48, no. 30, pp. 7089–7097, 2009.

[218] J. Zhang, C. M. Petit, D. S. King, and A. L. Lee, "Phosphorylation of a PDZ domain extension modulates binding affinity and interdomain interactions in postsynaptic density-95 (PSD-95) protein, a membrane-associated guanylate kinase (MAGUK)," *The Journal of Biological Chemistry*, vol. 286, no. 48, pp. 41776–41785, 2011.

[219] M. Essig, *Ligandenoptimierung in silico mittels molecularem Docking*. Bachelor Thesis, Goethe University, Frankfurt, 2011.

[220] V. Raussens, J.-M. Ruysschaert, and E. Goormaghtigh, "Estimate secondary structure from CD spectra :: the concentration independent Raussens et al method," 2003.

[221] V. Raussens, J.-M. Ruysschaert, and E. Goormaghtigh, "Protein concentration is not an absolute prerequisite for the determination of secondary structure from circular dichroism spectra: a new scaling method," *Analytical Biochemistry*, vol. 319, no. 1, pp. 114–121, 2003.

[222] S. Mitternacht, "FreeSASA: An open source C library for solvent accessible surface area calculations," *F1000Research*, vol. 5, p. 189, 2016.

[223] S. Miller, J. Janin, A. M. Lesk, and C. Chothia, "Interior and Surface of Monomeric Proteins," *Journal of Molecular Biology*, no. 196, pp. 641–656, 1987.

[224] J. Bredenbeck and P. Hamm, "Versatile small volume closed-cycle flow cell system for transient spectroscopy at high repetition rates," *Review of Scientific Instruments*, vol. 74, no. 6, pp. 3188–3189, 2003.

[225] G. Cerullo and S. de Silvestri, "Ultrafast optical parametric amplifiers," *Review of Scientific Instruments*, vol. 74, no. 1, pp. 1–18, 2003.

[226] P. Hamm, R. A. Kaindl, and J. Stenger, "Noise suppression in femtosecond mid-infrared light sources," *Optics Letters*, vol. 25, no. 24, pp. 1798–1800, 2000.

[227] F. Seifert, V. Petrov, and M. Woerner, "Solid-state laser system for the generation of midinfrared femtosecond pulses," *Optics Letters*, no. 23, pp. 2009–2011, 1994.

[228] M. Bradler, P. Baum, and E. Riedle, "Femtosecond continuum generation in bulk laser host materials with sub-μJ pump pulses," *Applied Physics B*, vol. 97, no. 3, pp. 561–574, 2009.

[229] A. Brodeur and S. L. Chin, "Ultrafast white-light continuum generation and self-focusing in transparent condensed media," *Journal of the Optical Society of America B*, vol. 16, no. 4, pp. 637–650, 1999.

[230] A. L. Gaeta, "Catastrophic collapse of ultrashort pulses," *Physical Review Letters*, vol. 84, no. 16, pp. 3582–3585, 2000.

[231] E. Deniz, K. B. Eberl, and J. Bredenbeck, "Note: An automatic liquid nitrogen refilling system for small (detector) Dewar vessels," *Review of Scientific Instruments*, vol. 89, no. 11, p. 116101, 2018.

[232] J. Helbing and P. Hamm, "Compact implementation of Fourier transform two-dimensional IR spectroscopy without phase ambiguity," *Journal of Optical Society of America*, vol. 28, no. 1, pp. 171–178, 2011.

[233] R. Bloem, S. Garrett-Roe, H. Strzalka, P. Hamm, and P. Donaldson, "Enhancing signal detection and completely eliminating scattering using quasi phase-cycling in 2D IR experiments," *Optical Society of America*, vol. 18, no. 26, pp. 27067–27078, 2010.

[234] S. Lenz, *Entwicklung einer Toolbox zur Lineshape-Analyse in MATLAB*. Internship Report, Goethe University, Frankfurt, 2018.

[235] K. B. Eberl, *Biophysikalische Charakterisierung verschiedener azid-gelabelter Mutanten der PDZ-Domäne*. Bachelor Thesis, Johann Wolfgang Goethe Universität, Frankfurt, 2011.

[236] C. Bonifer, *Characterization of azidohomoalanine as an IR-sensor of the local electrostatic environment and H-bonding*. Report Practical Course, Goethe University, Frankfurt, 2018.

[237] M. J. Kamlet, J.-L. M. Abboud, M. H. Abraham, and R. W. Taft, "Linear solvation energy relationships. 23. A comprehensive collection of the solvatochromic parameters, pi*, alpha, and beta, and some methods for simplifying the generalized solvatochromic equation," *Journal of Organic Chemistry*, vol. 48, no. 17, pp. 2877–2887, 1983.

[238] R. W. Taft, J.-L. M. Abboud, and M. J. Kamlet, "Solvatochromic comparison method. 20. Linear solvation energy relationships. 12. The d delta term in the solvatochromic equations," *Journal of the American Chemical Society*, vol. 103, no. 5, pp. 1080–1086, 1981.

[239] M. J. Kamlet, A. Solomonovici, and R. W. Taft, "Solvatochromic comparison methods. 13. Linear solvation energy relationship. 5. Correlations between infrared DELTAnu values and the beta scale of hydrogen bond acceptor basicities," *Journal of the American Chemical Society*, vol. 101, no. 14, pp. 3734–3739, 1979.

[240] Y. Marcus, "The Properties of Organic Liquids that are Relevant to their Use as Solvating Solvents," *Chemical Society Reviews*, vol. 1993, pp. 409–416, 1993.

[241] L. Onsager, "Electric Moments of Molecules in Liquids," *Journal of the American Chemical Society*, no. 58, pp. 1486–1493, 1936.

[242] L. J. G. W. van Wilderen, D. Kern-Michler, H. M. Müller-Werkmeister, and J. Bredenbeck, "Correction: Vibrational dynamics and solvatochromism of the label SCN in various solvents and hemoglobin by time dependent IR and 2D-IR spectroscopy," *Physical Chemistry Chemical Physics*, vol. 19, no. 14, pp. 9676–9678, 2017.

[243] D. R. Lide, ed., *CRC Handbook of Chemistry and Physics: Edition 1996-1997*. 77 ed., 1996.

[244] J.-H. Choi, K.-I. Oh, H. Lee, C. Lee, and M. Cho, "Nitrile and thiocyanate IR probes: quantum chemistry calculation studies and multivariate least-square fitting analysis," *The Journal of Chemical Physics*, vol. 128, no. 13, pp. 1345061–1345068, 2008.

[245] M. Li, J. Owrutsky, M. Sarisky, J. P. Culver, A. Yodh, and R. M. Hochstrasser, "Vibrational and rotational relaxation times of solvated molecular ions," *The Journal of Chemical Physics*, vol. 98, no. 7, pp. 5499–5507, 1993.

[246] P. Hamm, M. Lim, and R. M. Hochstrasser, "Non-Markovian Dynamics of the Vibrations of Ions in Water from Femtosecond Infrared Three-Pulse Photon Echoes," *Physical Review Letters*, no. 81, pp. 5326–5329, 1998.

[247] Q. Zhong, A. P. Baronavski, and J. C. Owrutsky, "Vibrational energy relaxation of aqueous azide ion confined in reverse micelles," *The Journal of Chemical Physics*, vol. 118, no. 15, pp. 7074–7080, 2003.

[248] S. Li, J. R. Schmidt, A. Piryatinski, C. P. Lawrence, and J. L. Skinner, "Vibrational spectral diffusion of azide in water," *The Journal of Physical Chemistry B*, vol. 110, no. 38, pp. 18933–18938, 2006.

[249] M. Rozenberg and F. Tibika-Apfelbaum, "On the structure and the antisymmetric $\nu 3$ IR mode of covalent azide group," *Journal of Molecular Structure*, vol. 1035, pp. 267–270, 2013.

[250] H. Maekawa, K. Ohta, and K. Tominaga, "Spectral diffusion of the antisymmetric stretching mode of azide ion in a reverse micelle studied by infrared three-pulse photon echo method," *Physical Chemistry Chemical Physics*, vol. 6, no. 16, pp. 4074–4077, 2004.

[251] P. Quoika, *Biophysikalische Charakterisierung von IR-gelabelten Mutanten der PDZ3-Domäne und Untersuchung ihrer allosterischen Kommunikation*. Bachelor Thesis, Johann Wolfgang Goethe Universität, Frankfurt, 2015.

[252] S. M. Kelly, T. J. Jess, and N. C. Price, "How to study proteins by circular dichroism," *Biochimica et Biophysica Acta*, vol. 1751, no. 2, pp. 119–139, 2005.

[253] B. Ranjbar and P. Gill, "Circular dichroism techniques: biomolecular and nanostructural analyses - a review," *Chemical Biology & Drug Design*, vol. 74, no. 2, pp. 101–120, 2009.

[254] N. J. Greenfield, "Using circular dichroism spectra to estimate protein secondary structure," *Nature Protocols*, vol. 1, no. 6, pp. 2876–2890, 2006.

[255] O. H. Lowry, N. J. Rosebrough, L. A. Farr, and R. R. Randall, "PROTEIN MEASUREMENT WITH THE FOLIN PHENOL REAGENT," *The Journal of Biological Chemistry*, pp. 265–275, 1951.

[256] A. Velazquez-Campoy, H. Ohtaka, A. Nezami, S. Muzammil, and E. Freire, "Isothermal Titration Calorimetry," *Current Protocols in Cell Biology*, pp. 17.8.1–17.8.24, 2004.

[257] M. M. Pierce, C. S. Raman, and B. T. Nall, "Isothermal titration calorimetry of protein-protein interactions," *Methods*, vol. 19, no. 2, pp. 213–221, 1999.

[258] Y. Liang, "Applications of isothermal titration calorimetry in protein science," *Acta Biochimica et Biophysica Sinica*, vol. 40, no. 7, pp. 565–576, 2008.

[259] R. J. Falconer, A. Penkova, I. Jelesarov, and B. M. Collins, "Survey of the year 2008: applications of isothermal titration calorimetry," *Journal of Molecular Recognition*, vol. 23, no. 5, pp. 395–413, 2010.

[260] A. A. Saboury, "A review on the ligand binding studies by isothermal titration calorimetry," *Journal of the Iranian Chemical Society*, vol. 3, no. 1, pp. 1–21, 2006.

[261] S. W. Homans, "Dynamics and Thermodynamics of Ligand–Protein Interactions," *Top Curr Chem*, vol. 272, pp. 51–82, 2006.

Glossary

2D-IR two-dimensional infrared

a.u. arbitrary numbers

AA amino acid

aaRS aminoacyl-tRNA synthetase

AGS $AgGaS_2$

Aha azidohomoalanine

Ala alanine

Arg arginine

Asn asparagine

Asp aspartic acid

ATD anisotropic thermal diffusion

AzAla β-(1-azulenyl)-L-alanine

Azu azulene

BBO β-barium borate

bocAha Boc-protected azidohomoalanine

CCl_4 tetrachlormethane

CD circular dichroism

$CHCl_3$ chloroform

CLS center line slope

CRIPT cysteine-rich protein

CS conformational selection

Cys cysteine

DCM dichloromethane

DFG difference frequency generation

Dlg Disc Large

DMC double mutant cycle analysis

DMF dimethylformamide

DMSO dimethyl sulfoxide

ESA excited state absorption

FFCF frequency-frequency correlation function

fmocAha Fmoc-protected azidohomoalanine

fs femtosecond

FTIR Fourier transform infrared

FWHM full width at half maximum

GdmCl guanidine hydrochloride

Gln glutamine

Glu glutamic acid

Gly glycine

H-bond hydrogen bond

HFIP hexafluoroisopropanol

His histidine

IF induced fit

Ile isoleucine

IPTG isopropyl-β-D-1-thiogalactopyranoside

IR infrared

ITC isothermal titration calorimetry

IVR intramolecular vibrational energy redistribution

Leu leucine

Lys lysine

MAGUK membrane-associated guanylate kinase

MCT mercury cadmium telluride

MD molecular dynamic

MeSCN methyl thiocyanate

Met methionine

MM molecular mechanics

MSA multiple sequence alignment

N_3Ala azidoalanine

N_3Phe azidophenylalanine

N_3Pro azidoproline

ncAA non-canonical amino acid

Nlg Neuroligins

NMR nuclear magnetic resonance

nNOS neuronal nitric oxide synthetase

OD optical density

OPA optical parametric amplifier

PCE tetrachloroethylene

Phe phenylalanine

Pro proline

ps picosecond

psVoigt pseudo-Voigt

QM quantum mechanical

RMSD root mean square deviation

RT room temperature

SASA solvent accessible surface area

SCS stop codon suppression

Ser serine

SPI selective pressure incorporation

SPPS solid phase peptide synthesis

TFE 2,2,2-trifluoroethanol

THF tetrahydrofuran

Thr threonine

TRIR transient IR

Trp tryptophan

Tyr tyrosine

upAha unprotected azidohomoalanine

Val valine

VET vibrational energy transfer

VIS visible

WT wild type

List of Figures

List of Tables